Title
Galaxies at the Epoch of Reionization

Author
Mason, Charlotte

Publication Date
2018

Peer reviewed|Thesis/dissertation

UNIVERSITY OF CALIFORNIA
Los Angeles

Galaxies at the Epoch of Cosmic Reionization

A dissertation submitted in partial satisfaction
of the requirements for the degree
Doctor of Philosophy in Astronomy

by

Charlotte Ann Mason

2018

ABSTRACT OF THE DISSERTATION

Galaxies at the Epoch of Cosmic Reionization

by

Charlotte Ann Mason
Doctor of Philosophy in Astronomy
University of California, Los Angeles, 2018
Professor Tommaso L. Treu, Chair

The reionization of intergalactic hydrogen in the universe's first billion years was likely driven by the first stars and galaxies, so its history encodes information about their properties. But the timeline of reionization is not well-measured and it is still unclear whether galaxies alone can produce the required ionizing photons. In my thesis I have focused on two ways to use galaxies at our current observational frontiers to constrain reionization and high redshift galaxy evolution.

One tool is the UV luminosity function (LF), which traces the evolution of star-forming galaxies and their ionizing photons. Accurately measuring LFs and understanding their evolution are important for understanding the connections between galaxies and their dark matter halos. I developed a simple, but powerful, semi-analytic model for LF evolution assuming star formation is driven by dark matter accretion. This has proved remarkably consistent with observations, and implies the majority of star formation at high redshifts occurs in low mass galaxies. I also developed a technique to improve the accuracy of LF by accounting for gravitational lensing magnification bias.

Secondly, Lyman alpha (Lyα) emission from galaxies can probe the intergalactic medium (IGM) ionization state as Lyα photons are strongly attenuated by neutral hydrogen, but this requires disentangling physics on pc to Gpc scales. I developed a new forward-modeling Bayesian framework combining cosmological IGM simulations with interstellar medium models to infer the IGM neutral hydrogen fraction from observations of Lyα emission. My thesis

presents new measurements of the neutral fraction at $z \sim 7$ and $z \sim 8$, which, along with other independent constraints, provide increasing evidence for the bulk of reionization occurring at $z \sim 6-8$. This is consistent with reionization being driven by ultra-faint galaxies with a low average ionizing photon escape fraction. We also show that reionization impacts Lyα emission from different galaxy populations in different ways: UV bright galaxies living in overdense regions that reionize early have potentially visible Lyα even in a highly neutral IGM.

The upcoming James Webb Space Telescope was designed to observe galaxies at Cosmic Dawn. Throughout this thesis I have made predictions for what *JWST* may observe in the context of high redshift galaxy evolution.

The dissertation of Charlotte Ann Mason is approved.

Steven R. Furlanetto

Matthew A. Malkan

Smadar Naoz

Tommaso L. Treu, Committee Chair

University of California, Los Angeles

2018

TABLE OF CONTENTS

LIST OF FIGURES

LIST OF TABLES

ACKNOWLEDGMENTS

I owe thanks to many people who have enabled me to make my childhood dream of becoming an astrophysicist a reality.

Firstly to my family for their constant support, advice, and encouragement. To my parents for fostering an early love of science and exploration in me. To my sisters, for being fantastic and inspiring, and for always picking up the phone, no matter where we are in the world. And to my extended family, especially to my Grandad for many discussions about life, the universe, and everything, and always asking questions. I would also like to thank all of my friends, at graduate school and beyond, but especially past and current tenants of Casa Del Norte, who have made the last five years a lot of fun. And to Jon, thank you for sharing some of my happiest memories of life in California, and for being there in the most stressful times.

I would like to thank everyone who has taught me physics over the years, especially my tutors at Merton who gave me an excellent foundation in physics. A huge thanks to my mentors and collaborators for being wonderful to work with, and for teaching me so much about the universe. Particular thanks to Michele Trenti and Adriano Fontana for their guidance over the years, and introducing me to exciting new projects. Thanks to all past and current members of team TT with whom I shared an education in astronomy and gastronomy, particularly Kasper Schmidt, Anna Pancoast, and Anna Nierenberg for showing me the ropes and always being there when I need advice. Thank you to the UCSB Astronomy & Astrophysics group for their hospitality for the last three years, and to the department at UCLA for being so welcoming.

And finally to my advisor Tommaso for being pretty much the best advisor I could have imagined. Thank you for all of the guidance and encouragement, both in doing science and in learning how to be a scientist, and for always being available to Skype across many ever-changing time zones. Thank you for the opportunities you have given me during my PhD. Even if your attempts to make me a fully-fledged observer were a bit more painful than we

hoped, I am indebted to you for teaching me about data, and what we can and can't learn from it. It has been a pleasure working with and learning from you, and I look forward to many more future collaborations.

This thesis includes a number of chapters adapted from publications.

Chapter 2 was published as Mason et al. (2015a), ApJ, 813, 21, The Galaxy UV Luminosity Function Before the Epoch of Reionization (DOI: 10.1088/0004-637X/813/1/21). I acknowledge and thank my co-authors in this work: Tommaso Treu and Michele Trenti.

Chapter 3 was published as Mason et al. (2015b), ApJ, 805, 79, Correcting the $z \sim 8$ Galaxy Luminosity Function for Gravitational Lensing Magnification Bias (DOI: 10.1088/0004-637X/805/1/79). I acknowledge and thank my co-authors in this work: Tommaso Treu, Kasper B. Schmidt, Thomas E. Collett, Michele Trenti, Philip J. Marshall, Robert Barone-Nugent, Larry D. Bradley, Massimo Stiavelli, and Stuart Wyithe.

Chapter 4 was published as Mason et al. (2018a), ApJ, 856, 2, The Universe is Reionizing at $z \sim 7$: Bayesian Inference of the IGM Neutral Fraction Using Lyα Emission from Galaxies (DOI: 10.3847/1538-4357/aab0a7). I acknowledge and thank my co-authors in this work: Tommaso Treu, Mark Dijkstra, Andrei Mesinger, Michele Trenti, Laura Pentericci, Stephane de Barros, and Eros Vanzella.

Chapter 5 was published as Mason et al. (2018b), ApJL, 857, 11, The Universe is Reionizing at $z \sim 7$: Beacons into the Cosmic Dark Ages: Boosted transmission of Lyα from UV bright galaxies at $z \gtrsim 7$ (DOI: 10.3847/2041-8213/aabbab). I acknowledge and thank my co-authors in this work: Tommaso Treu, Stephane de Barros, Mark Dijkstra, Adriano Fontana, Andrei Mesinger, Laura Pentericci, Michele Trenti, and Eros Vanzella.

Chapter 6 was published as Mason et al. (2017), ApJ, 838, 14, First Results from the KMOS Lens-Amplified Spectroscopic Survey (KLASS): Kinematics of Lensed Galaxies at Cosmic Noon (DOI: 10.3847/1538-4357/aa60c4). I acknowledge and thank my co-authors in this work: Tommaso Treu, Adriano Fontana (KLASS PI), Tucker Jones, Takahiro Morishita, Ricardo Amorin, Maruša Bradač, Emily Quinn Finney, Claudio Grillo, Alaina Henry, Austin Hoag, Kuang-Han Huang, Kasper B. Schmidt, Michele Trenti, and Benedetta Vul-

cani.

Chapter 7 is in preparation for submission. I would like to acknowledge and thank my co-authors in this work: Adriano Fontana, Tommaso Treu, Kasper B. Schmidt, Austin Hoag, Louis Abramson, Ricardo Amorin, Lucia Guaita, Tucker Jones, Alaina Henry, Matthew Malkan, Laura Pentericci, Michele Trenti, and Eros Vanzella.

I acknowledge support from NASA Headquarters for my thesis through the NASA Earth and Space Science Fellowship Program, Grant NNX16AO85H. This work was supported by *HST* BoRG grants GO-12572, 12905, 13767 and 15212, and *HST* GLASS grant GO-13459.

VITA

2013	M.Phys. (Physics), Merton College, University of Oxford, UK.
2015	M.A. (Physics with Astrophysics Emphasis), UC Santa Barbara, California, USA.
2016	Awarded NASA Earth and Space Science Fellowship
2017	Awarded Dr. Pliny A. and Margaret H. Price Prize in Cosmology and AstroParticle Physics, *CCAPP, Ohio State University*
2018	Awarded CfA Fellowship, *Harvard-Smithsonian Center for Astrophysics* Awarded NASA Hubble Fellowship

FIRST AUTHOR PUBLICATIONS

Mason, C. A., et al. Beacons into the Cosmic Dark Ages: Boosted transmission of Lyα from UV bright galaxies at $z \gtrsim 7$. ApJL, 857, 11, 2018.

Mason, C. A., et al. The Universe is Reionizing at $z \sim 7$: Bayesian Inference of the IGM Neutral Fraction Using Lyα Emission from Galaxies. ApJ, 856, 2, 2018.

Mason, C. A., et al. First Results from the KMOS Lens-Amplified Spectroscopic Survey (KLASS): Kinematics of Lensed Galaxies at Cosmic Noon. ApJ, 838, 14, 2017.

Mason, C. A., Trenti, M., and Treu, T. The Galaxy UV Luminosity Function before the Epoch of Reionization. ApJ, 813, 21, 2015.

Mason, C. A., et al. Correcting the $z \sim 8$ Galaxy Luminosity Function for Gravitational Lensing Magnification Bias. ApJ, 805, 79, 2015.

CHAPTER 1

Introduction

Decades of cosmic microwave background (CMB) experiments (e.g., Mather et al., 1994; Hinshaw et al., 2012; Planck Collaboration et al., 2016a) have precisely measured the initial conditions for structure formation in our universe. But precisely when and how the first luminous sources formed in the universe, and evolved into the diverse galaxy population we observe today, is not known.

We cannot see the first stars and galaxies. Their light is diminished by $\gtrsim 50$ magnitudes as their photons travel across the expanding universe to our telescopes, too faint to be detected by current facilities. But we can infer their properties by studying young galaxies at our current observational frontiers, $\sim 0.4-1$ billion years after the Big Bang (redshifts $z \sim 6-10$). A key process to understand is the *reionization* of intergalactic hydrogen[1], driven by the first sources of UV photons, likely stars in nascent galaxies. By constraining reionization we can learn about these early sources, and vice versa.

Observations of distant galaxies are challenging due to their extremeness faintness (apparent magnitudes $m \gtrsim 26$) and compactness (most are unresolved even in *HST* imaging). Even with our most advanced telescopes, our observations of these galaxies are currently limited to counting them as a function of their luminosity, and obtaining spectra of the brightest emission lines in the brightest galaxies. Future observations with the upcoming James Webb Space Telescope (*JWST*) will finally enable spectroscopy of a wider range of these galaxies, allowing us to confirm their high-redshift status and learn more about their growth and chemical evolution.

[1] With the release of the CMB radiation at Recombination $z \sim 1100$, all intergalactic gas was atomic (previously in a highly ionized plasma). Absorption features in quasar spectra show the IGM is highly ionized by $z \lesssim 5$.

In this thesis I have used our frontier observations of high-redshift galaxies to constrain early galaxy evolution and the timeline of reionization. I have used two key observations as tools to study these early galaxies, and give an introduction to these tools below: galaxy UV luminosity functions, which trace the evolution of the star-forming galaxy population (Section 1.1); and Lyα emission from galaxies which can be used as a tracer of the reionizing IGM (Section 1.2).

1.1 Galaxy UV luminosity functions

The comoving number density of galaxies as a function of their absolute magnitude or luminosity is know as the 'galaxy luminosity function' (LF, e.g., Schechter, 1976). While we cannot directly observe the evolution of a single galaxy, observing changes in the LF with redshift allows us to see the evolution of the galaxy population in a statistical sense. Young star-forming galaxies emit the majority of their light in the rest-frame ultra-violet (UV), dominated by short-lived, massive, hot O and B stars. Thus the rest-frame UV luminosity function traces the evolution of star-forming galaxies.

Comparing the predicted comoving number density of dark matter halos (the halo mass function) in ΛCDM cosmology at any redshift to the observed galaxy LF reveals that galaxies are staggeringly less abundant than dark matter halos for the lowest and highest mass halos. Assuming gas is accreted with dark matter, this mismatch can be seen as an efficiency of converting baryons into stars, which peaks for halo masses $\sim 10^{12}\,M_\odot$ and declines at lower and higher halo masses. There is no accepted physical model for this star formation efficiency, but it is likely to due to a combination of effects which heat up and expel gas in forming galaxies making it harder to form stars, collectively referred to as 'feedback': e.g. heating of small halos due photoionization and supernova explosions, and the actions of active galactic nuclei (AGN) on high mass halos.

Characterizing the evolution of the galaxy LF over cosmic time is important because it enables us to see how the processes which govern star formation evolve with time, giving us more insight into their nature. As all of the feedback processes listed above are expected to have some redshift dependence: we can ask whether any observed change in shape of the LF indicates changing conditions for star formation at early times, e.g., perhaps AGN cannot sufficiently suppress star formation in massive halos in the early universe.

For galaxies at $z > 6$ their emitted UV light is redshifted to near infra-red (NIR, $\gtrsim 1\,\mu$m) wavelengths by the time it reaches Earth, generally requiring space telescopes to observe it due to strong OH emission in the NIR in the atmosphere. Revolutionary observations within the last decade, particularly aided by the installation of Wide Field Camera 3 on *HST* in 2009, have shown clear evolution in the LF over cosmic time: the number density of galaxies decreasing with increasing redshift at fixed luminosity (e.g., Bouwens et al., 2011; Grogin et al., 2011; Koekemoer et al., 2011; Trenti et al., 2011; Bradley et al., 2012; Dunlop et al., 2013; Illingworth et al., 2013; Yue et al., 2014; Schmidt et al., 2014b; Atek et al., 2015a; Lotz et al., 2017). Remarkably, the overall shape of the LF changes little with redshift, remaining well-described by a Schechter (1976) function out to $z \gtrsim 6$. However, recent observations (e.g., Bowler et al., 2015; Finkelstein et al., 2015b; Ono et al., 2017) have found some evidence of a deviation away from the Schechter form at the brightest end of the luminosity function at $z \sim 7$. Is this an indication of changing star formation procedures at high redshift?

Learning from the observations requires careful measurements. In this thesis I have developed a Bayesian method to account for a bias in observed luminosity functions due to the gravitational lensing magnification of high-redshift sources in our galaxy surveys, which can boost the bright end of the LF (Chapter 3, Mason et al., 2015b). This enables us to produce more accurate LFs, and account for how much of the observed bright end excess is due to lensing.

Calling on Occam's Razor to understand the evolution of the luminosity function in Mason et al. (2015a) (Chapter 2) I developed a simple, but powerful, semi-analytic model for the evolution of the UV LF, assuming halo mass accretion is the dominant driver of galaxy growth. We assume a mass-dependent, but redshift-independent star formation efficiency. This model reproduces observations remarkably well over a wide range of redshifts and luminosities. We used our model to forecast LFs at higher redshifts: upcoming observations with *JWST* will show whether this form for the star formation efficiency holds at even earlier times.

1.2 Lyman alpha emission from galaxies as a probe of reionization

Reionization of hydrogen is a significant milestone in the history of the universe, marking the last global phase transition. When and how reionization progressed is intimately linked to formation of the first luminous sources, which provide the ionizing photons. Young stars in early galaxies are thought to be the sources of the ionizing photons (e.g., Lehnert & Bremer, 2003; Bouwens et al., 2003; Yan & Windhorst, 2004; Bunker et al., 2004; Finkelstein et al., 2012a; Robertson et al., 2013; Schmidt et al., 2014a), but there may also be a contribution from AGN (Giallongo et al., 2015; Madau & Haardt, 2015; Onoue et al., 2017). Characterizing the sources of reionization requires a better understanding of the timing of reionization.

The timeline of reionization, i.e., the average fraction of the intergalactic medium (IGM) that is ionized as a function of redshift, is not well-measured. Planck Collaboration et al. (2016b) provides an integral measure reionization via the electron scattering optical depth from the CMB through the IGM, but it does not give information about the exact timing of the reionization process. Is it rapid or extended? When does it begin and end? Classic constraints on the ionization state of the IGM come from observations of absorption features in quasar spectra (e.g., Fan et al., 2006): rest-frame ionizing radiation emitted by the quasars is absorbed by intervening intergalactic gas. These observations have demonstrated that the IGM became predominantly ionized around $z \lesssim 6$ (e.g., Fan et al., 2006; McGreer et al., 2015). However, bright quasars are exceedingly rare at higher redshifts: as of May 2018, only two have been detected at $z > 7$, making such studies very challenging.

Galaxies, by contrast, have been discovered in the thousands at $z > 6$ (albeit mostly detected photometrically) and provide a statistical way to trace the IGM. Lyman alpha (Lyα) emission, produced in abundance by recombination in H II regions around massive stars, is absorbed and scattered by intervening neutral hydrogen gas, and reprocessed by dust, along the line of sight to our telescopes. As reionization progresses, more Lyα emission should be absorbed within the increasingly neutral IGM (e.g., Haiman & Spaans, 1999; Malhotra & Rhoads, 2004; Santos, 2004; Verhamme et al., 2006; McQuinn et al., 2007a; Mesinger & Furlanetto, 2008b; Dijkstra, 2014).

A declining fraction of Lyman Break selected galaxies emitting Lyα $z \gtrsim 6$ has been observed in the last 8 years (e.g. Fontana et al., 2010; Stark et al., 2010; Caruana et al., 2012; Treu et al., 2013; Caruana et al., 2014; Faisst et al., 2014; Tilvi et al., 2014; Schenker et al., 2014; Pentericci et al., 2014), plausibly attributed to an increasingly neutral IGM. However, making quantitative constraints on the IGM ionization state is challenging as it involves modeling physics on multiple scales: how are Lyα photons processed in the ISM and CGM of their source galaxies? How does this depend on galaxy properties? How are Lyα photons transmitted through the IGM? How does this depend on the local density environment of the source galaxy?

In Mason et al. (2018a) (Chapter 4) I developed a new forward-modeling Bayesian inference framework which enables us to compare observed spectral properties of galaxies to model galaxies emitting Lyα in different IGMs. Our framework combines cosmological reionization simulations with ISM models to encompass the multi-scale physics of Lyα radiative transfer to our telescopes. I then explored the significance of detection Lyα in UV bright galaxies at $z > 7.5$ in Mason et al. (2018b) (Chapter 5).

Significant observing time has been invested in imaging and spectroscopy of $z \gtrsim 6$ sources. Within the past few years, the Frontier Fields project (Lotz et al., 2017) has provided deep *HST* and Spitzer multi-band imaging of the fields of 6 massive galaxy clusters, using the clusters as cosmic magnifying glasses to observe intrinsically faint high redshift galaxies via gravitational lensing, and 6 parallel 'blank' fields. The Grism Lens-Amplified Survey from Space (GLASS, Treu et al., 2015) has obtained *HST* grism spectra of the Frontier Fields and 4 other massive cluster fields, with one science goal being to search for $z \gtrsim 6$ Lyα emission.

Ground-based high resolution spectroscopy is required to confirm the *HST* low resolution grism emission line candidates. As part of my thesis I have led the design, reduction and analysis of the first ESO Large Program on KMOS. KMOS is a multi-object near-IR IFU instrument on the VLT. The first results of our survey, KLASS, focusing on the kinematics of lensed $z \sim 1$ star-forming galaxies were presented by Mason et al. (2017) (Chapter 6). The final analysis of the KLASS Lyα candidate sample and its implications for the timeline of reionization at $z \sim 8$ is presented here in Chapter 7 and will be submitted with this thesis.

In this thesis I have asked what observations of galaxies at our current frontiers can tell use about galaxy formation in the early universe, and how and when the reionization of hydrogen occurred. I have found that the evolution of the star-forming galaxy population observed via the UV LF can be simply explained by assuming star formation is drive by halo mass accretion, with no redshift dependence on the conversion of baryons into stars. Using a forward-modeling inference framework I have found increasing evidence from observations of Lyα emission in galaxies that reionization was completed late (i.e. the IGM was still mostly neutral at $z \sim 8$). This is consistent with the majority of ionizing photons coming from ultra-faint galaxies, with a low average ionizing photon escape fraction.

My thesis is organized as follows: Chapter 3 presents a Bayesian method to account for a bias in high redshift galaxy UV luminosity functions due to gravitational lensing (published as Mason, Treu, Schmidt, Collett, Trenti, Marshall, Barone-Nugent, Bradley, Stiavelli, & Wyithe, 2015b, *ApJ, 805, 79*); Chapter 2 presents a semi-analytic model for the redshift evolution of high-redshift galaxy UV luminosity functions (published as Mason, Trenti, & Treu, 2015a, *ApJ, 813, 21*); Chapter 4 presents our flexible Bayesian framework for inferring the average neutral hydrogen fraction of the IGM during Reionization (published as Mason, Treu, Dijkstra, Mesinger, Trenti, Pentericci, de Barros, & Vanzella, 2018a, *ApJ, 856, 2*); Chapter 5 explores the significance of the detection of Lyα emission from UV bright galaxies at $z \gtrsim 7.5$ in the context of Reionization (published as Mason, Treu, de Barros, Dijkstra, Fontana, Mesinger, Pentericci, Trenti, & Vanzella, 2018b, *ApJL, 857, 11*); Chapter 6 describes the first results from the KLASS survey, focusing on the kinematics of lensed $z \sim 1$ star-forming galaxies (published as Mason, Treu, Fontana, Jones, Morishita, Amorin, Bradac, Finney, Henry, Hoag, Huang, Schmidt, Trenti, & Vulcani, 2017, *ApJ, 838, 14*); Chapter 7 describes our analysis of the Lyα candidate sample in KLASS. It will be submitted as Mason, Fontana, Treu, Schmidt, Hoag, Abramson, Amorin, Guaita, Jones, Henry, Malkan, Pentericci, Trenti & Vanzella. I present a summary of key results and conclusions, and future prospects, in Chapter 8.

CHAPTER 2

The Galaxy UV Luminosity Function Before the Epoch of Reionization

This paper was published as Mason, Trenti, & Treu (2015a), ApJ, 813, 21, and reproduced here with minor formatting changes.

We present a model for the evolution of the galaxy ultraviolet (UV) luminosity function (LF) across cosmic time where star formation is linked to the assembly of dark matter halos under the assumption of a mass dependent, but redshift independent, efficiency. We introduce a new self-consistent treatment of the halo star formation history, which allows us to make predictions at $z > 10$ (lookback time $\lesssim 500$ Myr), when growth is rapid. With a calibration at a single redshift to set the stellar-to-halo mass ratio, and no further degrees of freedom, our model captures the evolution of the UV LF over all available observations ($0 \lesssim z \lesssim 10$). The significant drop in luminosity density of currently detectable galaxies beyond $z \sim 8$ is explained by a shift of star formation toward less massive, fainter galaxies. Assuming that star formation proceeds down to atomic cooling halos, we derive a reionization optical depth $\tau = 0.056^{+0.007}_{-0.010}$, fully consistent with the latest Planck measurement, implying that the universe is fully reionized at $z = 7.84^{+0.65}_{-0.98}$. In addition, our model naturally produces smoothly rising star formation histories for galaxies with $L \lesssim L_*$ in agreement with observations and hydrodynamical simulations. Before the epoch of reionization at $z > 10$ we predict the LF to remain well-described by a Schechter function, but with an increasingly steep faint-end slope ($\alpha \sim -3.5$ at $z \sim 16$). Finally, we construct forecasts for surveys with *JWST* and *WFIRST* and predict that galaxies out to $z \sim 14$ will be observed. Galaxies at $z > 15$ will likely be accessible to *JWST* and *WFIRST* only through the assistance of strong lensing magnification.

2.1 Introduction

The rest-frame ultraviolet (UV) galaxy luminosity function (LF) and its evolution with redshift are crucial tracers of galaxy properties over cosmic time. In particular, UV light can be used efficiently to measure the star formation rate (SFR), because photons at rest-frame wavelengths around 1500 Å are primarily produced by young, massive, and short-lived stars. Current observations characterize the UV LF over the large majority of the history of the universe, ranging from studies in the local universe from *Galaxy Evolution Explorer* data (e.g., Burgarella et al. 2006 to *Hubble Space Telescope Wide Field Camera 3* (*HST*/WFC3) observations which now reach redshift $z \sim 8-10$, i.e. lookback times greater than 13 Gyr (e.g. Bouwens et al. 2015b). Transformational results on the rest-frame UV light from the epoch of reionization, when the universe was less than 0.8 Gyr old, have been made possible by large and dedicated community efforts that have identified a sample of more than 1000 galaxy candidates at $z > 7$, spanning a large range in luminosities. This progress is thanks to a variety of surveys, including ultradeep observations in blank fields with the HUDF09 and HUDF12 campaigns (Bouwens et al., 2011; Dunlop et al., 2013; Illingworth et al., 2013), the use of cluster-scale lensing to probe intrinsically faint objects (e.g., Yue et al., 2014; Atek et al., 2015a), the large area, panchromatic CANDELS survey (Grogin et al., 2011; Koekemoer et al., 2011), and wide-field random-pointing surveys to identify more luminous but rarer objects at the bright end of the LF (e.g., Trenti et al., 2011; Bradley et al., 2012; Schmidt et al., 2014b).

The picture emerging from these observations is that the number density of galaxies decreases with increasing redshift, while the LF remains consistent with a Schechter (1976) form, $\Phi(L) = \Phi^*(L/L^*)^\alpha \exp(-L/L^*)/L^*$ out to $z \sim 8$, albeit the uncertainty and co-variance in the best fitting parameters grows at high redshift (Schmidt et al., 2014b; Bouwens et al., 2015b). However, other studies find either an equally good fit with a double-power law at $z \sim 8$ (Finkelstein et al., 2015b), or a preference for the double power law at $z \sim 7$ (Bowler et al. 2014, 2015; but note that the $z \sim 7$ investigations are based on ground, rather than space observations). Irrespective of the form of the LF at the bright-end, whose evolution might be linked to changing astrophysical conditions of high-redshift galaxies, such as reduced feedback at early times (Somerville et al., 2008), it is clear that overall, the observed population of galaxies ($M_{AB} \lesssim -17$) at $z > 7$ does not produce sufficient photons to ionize the universe. This is consistent both with theoretical modeling (Trenti et al., 2010; Raičević et al., 2011; Robertson et al., 2015) and indirect probes, such as the lack of detections of gamma ray burst host galaxies (Trenti et al., 2012a; Tanvir et al., 2012), which suggest that even the deepest *HST* observations are seeing only the tip of the iceberg of the population of star-forming galaxies. Therefore, it is likely that a very faint population of unseen dwarf galaxies at $z \gtrsim 6$ is the main contributor to the UV luminosity density and in turn to the ionizing photon budget (e.g., see Alvarez et al. 2012). Indirect observational support for extrapolation of the UV LF is provided by the detection of ultrafaint galaxies behind gravitational lenses at $z \sim 2$ (Alavi et al., 2014). However, see Giallongo et al. (2015) and Madau & Haardt (2015) for a discussion of the potential contribution of active galactic nuclei to reionization.

HST is both wavelength and aperture limited to observations at $z \lesssim 11$, but future progress to characterize the properties of the UV LF at high redshift will be boosted by the upcoming James Webb Space Telescope (*JWST*; Gardner et al., 2006) and Wide-Field Infrared Survey Telescope (*WFIRST*; Spergel et al., 2013). These observatories are expected to extend the frontier of galaxy detection to before the epoch of reionization at $z > 10$, when the first generation of galaxies were being assembled and hydrogen in the universe was predominantly neutral.

Motivated by this upcoming improvement in discovery capabilities of high redshift galaxies, we aim here at predicting the UV LFs at $z > 10$. For this we use a simple, yet successful, semi-analytic framework introduced previously by Trenti et al. (2010, 2015); Tacchella et al. (2013) which assumes that the main driver of the evolution of the galaxy UV LF is the growth and hierarchical assembly of dark matter (DM) halos. Whilst this simple approach does not have the power of numerical hydrodyamic simulations (e.g., Gene et al., 2014; Furlong et al., 2015) to make predictions about galaxy properties such as morphology, and the role played by satellite galaxies, it provides a simple, robust and empirically calibrated method to make predictions for the evolution of global galaxy properties. In particular, the simplicity of our approach avoids the degeneracies of large multi-parameter numerical simulations, and allows us to calibrate at one reference redshift the complex physics that regulates the conversion of baryons into stars, and then to focus on investigating how DM halo assembly drives redshift evolution under the assumption that star formation efficiency is redshift independent at fixed halo mass.

The key assumptions of the framework are that, for star forming galaxies, the stellar mass content of a DM halo depends on the halo mass but not on redshift, and that the stellar mass built up has a characteristic timescale given by the halo assembly time. The mass dependent efficiency of converting halo mass into stellar mass is calibrated empirically at one redshift, where good observational constraints are available (e.g. $z = 4 - 5$), and then applied to predict the redshift evolution of the UV LF by combining evolution in the DM halo mass function (HMF) and halo assembly time with stellar population synthesis modeling. Since halos assembled more rapidly in the past, the SFR was higher at high redshift, explaining the general brightening of the luminosity versus halo mass relation found by abundance matching studies (e.g. Cooray & Milosavljevic 2005).

This simple strategy has been remarkably successful in describing the UV LF evolution with redshift (Tacchella et al., 2013), with results similar to those obtained by other studies based on matching DM halos to galaxy luminosity (e.g. Lacey et al. 2011; Muñoz 2012; Jaacks et al. 2013; Behroozi & Silk 2015; Dayal et al. 2014; Mashian et al. 2016). However, the earlier implementations had two limitations. First, the model took into account only the star formation happening in the second half of the halo assembly history: the time the halo took to grow from $M_h/2$ to M_h. In addition, the calibration of the star formation efficiency was not guaranteed to be internally self-consistent with the halo assembly history of a DM halo over redshift. Given that the UV luminosity of a galaxy is only weakly sensitive to the star formation history of stellar populations with ages greater than a few hundred Myr (Madau & Dickinson, 2014), these limitations had very little impact at $z \lesssim 8$. However the situation is potentially different at early times, when the assembly time goes below 100 Myr. Thus, the previous version of the model could not be trusted to formulate predictions at $z \geq 10$.

In this paper, we develop and present an improved and self-consistent model that describes the full star formation history of a DM halo, and we verify that (1) it continues to describe well the UV LF at $z \lesssim 8$; (2) it successfully reproduces the latest observations at $z \gtrsim 8$, providing an important validation of the approach introduced before such observations were available. In addition, we make detailed predictions for future surveys at $z \geq 10$ with the James Webb Space Telescope (*JWST*) and the Wide-Field Infrared Survey Telescope (*WFIRST*), and we discuss the implications of our results in the context of the ionizing photon budget.

This paper is organized as follows: in Section 2.2 we introduce our new model and its calibration; Section 2.3 describes our model results, and our predictions for future surveys; and we summarize and conclude in Section 2.4. All magnitudes are AB magnitudes and we use the Planck Collaboration et al. (2016a) cosmology, with $\Omega_{\rm m} = 0.315$, $\Omega_\Lambda = 0.685$, $\Omega_{\rm b} = 0.0490$, $h = 0.6731$, $\sigma_8 = 0.829$ and $n_s = 0.9655$.

2.2 Model Description

Our model considers the growth of DM halos to be the most important driving force in the growth of galaxies, and aims at predicting the evolution of the UV luminosity function with a minimal number of assumptions. We thus assume that the SFR is proportional to: (1) the halo mass, through a mass-dependent but redshift-independent efficiency $\varepsilon(M_h)$, which is the ratio of the stellar mass formed during the halo assembly time $t_a(M_h, z)$ to the final halo mass; and (2) to the inverse of the halo assembly time. The halo assembly time, $t_a(M_h, z)$, of a halo of mass M_h observed at redshift z is the lookback time at which the progenitor halo had mass $M_h/2$ (Lacey & Cole, 1993), and decreases at higher redshift. This implies that DM halos at fixed mass host star forming galaxies with stellar mass which is independent of redshift, but with stellar populations that are younger at higher redshift.

Since the HMFs and assembly times are fully defined by the cosmological model parameters, these assumptions allow us to calibrate our model at one redshift to derive $\varepsilon(M_h)$, and then construct predictions for the galaxy luminosity function at all other redshifts from the DM HMF and the halo assembly time.

2.2.1 Star formation prescription

The UV luminosity of a galaxy most strongly depends on its youngest stars, while stellar populations older than a few hundred Myr contribute little. However, at $z \lesssim 8$, the halo assembly time is less than 100 Myr, so to predict the UV luminosity at high redshift it is necessary to consider periods of star formation before the halo assembly time.

To include multiple epochs of star formation, as a halo grows in DM mass, we define the star formation history of a halo as a linear combination of constant bursts normalized by the length of each burst. Thus we define the SFR for a halo with mass M_h in each epoch between times t_i and t_{i+1} as:

$$SFR(t_i, t_{i+1}, M_h) = M_h \times \frac{\varepsilon(M_h/2^i)}{2^i(t_{i+1} - t_i)} \tag{2.1}$$

where we define t_0 as the lookback time for a halo observed at redshift $z_{\rm obs}$ and $t_{i>0} = t_a(M_h/2^{i-1}, z_{i-1})$, where t_a (z_a) is the halo assembly time (redshift). We similarly define $z_0 = z_{\rm obs}$ and $z_{i>0} = z_a(M_h/2^{i-1}, z_{i-1})$. We calculate the halo assembly time as defined by Lacey & Cole (1993)[1] in the extended Press-Schechter formalism (Bond et al., 1991) using an ellipsoidal collapse model (Sheth et al., 2001; Giocoli et al., 2007). We use the median of the probability distribution of assembly times for each halo. While this assumption does not take into account variations in the luminosity of individual galaxies, there is a minimal effect on the global LF from neglecting scatter in halo assembly times, as demonstrated by Tacchella et al. (2013).

We define the redshift-independent efficiency of star formation, $\varepsilon(M_h)$, as the ratio of the stellar mass formed during the halo assembly time to the final halo mass. Thus, to make predictions, we only need to calibrate $\varepsilon(M_h)$ at one redshift (see Section 2.2.3 and Figure 2.1) and can use the derived $\varepsilon(M_h)$ for all further predictions.

[1] The time it takes for a halo to double in mass

Figure 2.2 shows the star formation history of halos of fixed final mass $M_h = 10^{11}\ M_\odot$ observed at $z_0 = 2$, 6 and 10, calculated using the SFR in Equation (2.1). As $\varepsilon(M_h)$ is redshift independent, these halos will also have identical stellar masses at their observed redshifts. The SFR shown in Figure 2.2 increases in each epoch as the halo grows from $M_h/64$ to M_h, because $\varepsilon(M_h)$ decreases with decreasing halo mass (for $M_h \lesssim 10^{12}\ M_\odot$) more rapidly than the shortening of the halo assembly times as the lookback time grows. This behavior of our model is fully consistent with strong evidence of rising star formation histories with redshift from both numerical simulations and observations (Finlator et al., 2011; Papovich et al., 2011; Jaacks et al., 2012; Behroozi et al., 2013b; Lee et al., 2014). Thus the greatest contribution to the stellar mass is during the halo assembly time as the halo grows from $M_h/2$ to M_h. This figure also illustrates how the short halo assembly times at high redshift require a considerably higher SFR to form the same final stellar mass.

We include the contribution from star formation in successively smaller halo progenitors by summing the terms from Equation (2.1). The sum is truncated when the progenitor halo mass is below the cooling threshold, i.e. $\varepsilon(M_h \lesssim 10^8 M_\odot) = 0$.

Thus we can derive the stellar mass as:

$$M_\star(M_h) = M_h \times \sum_{i=0}^{i=\infty} \frac{\varepsilon(M_h/2^i)}{2^i} \tag{2.2}$$

which is redshift independent.

To compute the UV luminosity of a halo we populate every halo with a galaxy with a stellar population based on the simple stellar population (SSP) models of Bruzual & Charlot (2003). We assume a Salpeter initial mass function (IMF) between $0.1 M_\odot$ and $100 M_\odot$, as low mass stars do not contribute much to UV luminosity, and constant stellar metallicity $Z = 0.02 Z_\odot$. We neglect redshift evolution in metallicity as the UV luminosity does not depend strongly on metallicity under the assumption that current and future HST/JWST surveys detect galaxies living in relatively massive DM halos ($M_h \gtrsim 10^9$ M$_\odot$) where multiple generations of early star formation began enriching the gas at $z \gtrsim 20 - 40$ (Bromm et al., 2009; Trenti & Stiavelli, 2009; Smith et al., 2015), so that by $z \lesssim 16$ the metallicity has risen to $Z \gtrsim 0.01\ Z_\odot$. We define $\ell_{\rm BC}(t)$ as the luminosity at 1500 Å of an SSP of mass $1 M_\odot$ and

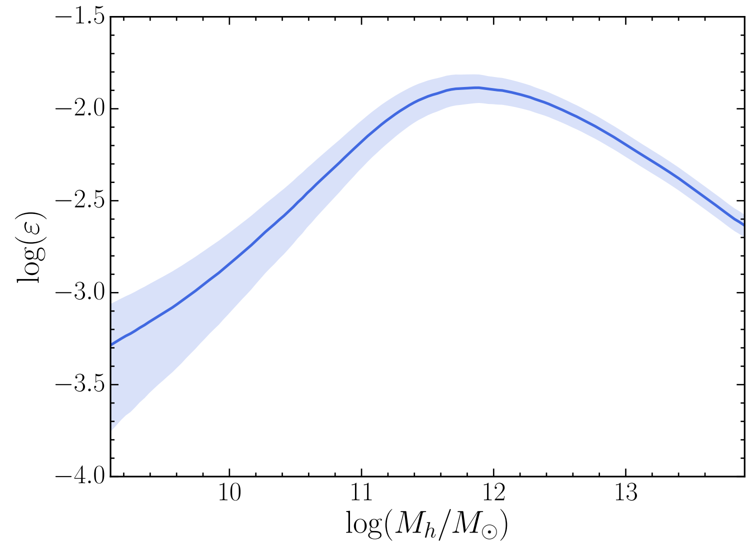

Figure 2.1: The efficiency of star formation, the ratio of stellar mass formed during the halo assembly time to halo mass, see Equation (2.2), derived at the calibration redshift $z \sim 5$, as described in Section 2.2.3. The shaded region shows 1σ confidence range.

age t. The total UV luminosity of a galaxy observed at redshift z is obtained by integrating over the SFR (Equation (2.1)) and SSP luminosity in each epoch of star formation:

$$L(M_h, z) = \sum_{i=0}^{i=\infty} \int_{t_i}^{t_{i+1}} SFR(t_i, t_{i+1}, M_h) \ell_{\rm BC}(t) dt \tag{2.3}$$

Where t_i are the halo assembly times for the half-mass progenitors defined above.

2.2.2 Dust extinction

The observed UV luminosity is significantly attenuation by dust extinction, particularly at $z \lesssim 4$. Thus, we include dust extinction in our model, following closely the procedure adopted in observations of Lyman-break galaxies. We assume a spectrum modeled as $f_\lambda \sim \lambda^\beta$, and extinction $A_{\rm UV} = 4.43 + 1.99\beta$ (Meurer et al., 1999). Following Trenti et al. (2015)

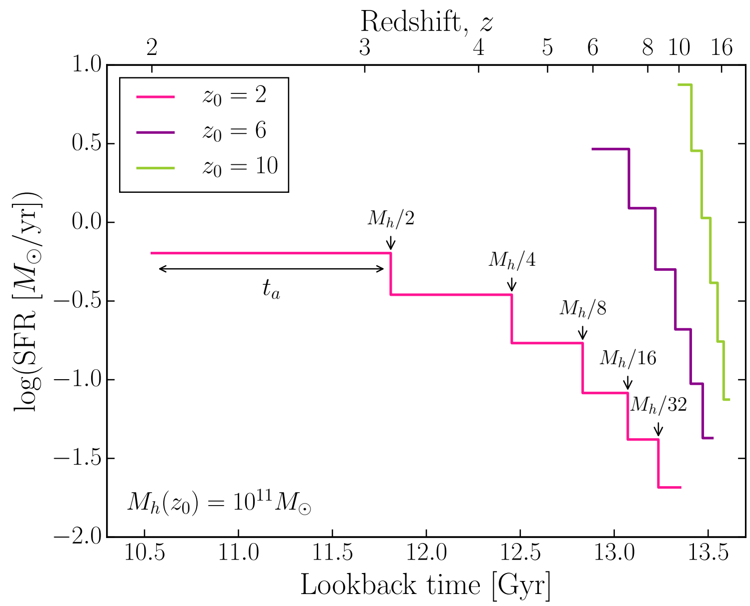

Figure 2.2: The star formation history, as described by Equation (2.1) in our model, of a halo of fixed mass 10^{11} $M_\odot$, if observed at $z_0 = 2$, $z_0 = 6$ or $z_0 = 10$. We label the halo assembly time for the $z_0 = 2$ halo and the mass of the halo progenitor at the start of each constant star formation epoch.

and Tacchella et al. (2013) we model the observations of β by Bouwens et al. (2014) as:

$$\langle\beta(z, M_{\rm UV})\rangle = \begin{cases} (\beta_{M_0}(z) - c)\exp\left[-\frac{\frac{d\beta}{dM_0}(z)[M_{\rm UV}-M_0]}{\beta_{M_0}(z)-c}\right] + c & M_{\rm UV} \geq M_0 \\ \frac{d\beta}{dM_0}(z)[M_{\rm UV} - M_0] + \beta_{M_0}(z) & M_{\rm UV} < M_0 \end{cases} \tag{2.4}$$

where $c = -2.33$, $M_0 = -19.5$, and the values of β_{M_0} and $d\beta/dM_0$ are taken from Table 3 in Bouwens et al. (2014) and linearly extrapolated to lower and higher redshifts. Using this linear plus exponential model for β we fit the Bouwens et al. (2014) observations well - which show evidence for a curved relation between β and $M_{\rm UV}$. The exponential fit at faint magnitudes avoids unphysical negative dust corrections.

We assume a Gaussian distribution for β at each $M_{\rm UV}$ value (with dispersion $\sigma_\beta = 0.34$), giving the average extinction $\langle A_{\rm UV}\rangle = 4.43 + 0.79\ln(10)\sigma_\beta^2 + 1.99\langle\beta\rangle$. We use this average extinction to calculate observed UV fluxes in our model.

2.2.3 Calibration

We calibrate the model by finding $\varepsilon(M_h)$ such that $L(M_h, z_c) = L^{\rm obs}(M_h, z_c)$, where z_c is the calibration redshift. To find $L^{\rm obs}(M_h, z_c)$ we derive an empirical relation between observed luminosity and halo mass by performing abundance matching (Mo et al., 1999) between the HMF, $n(M_h, z)$, and observed LF, $\Phi(L, z)$, assuming every halo hosts one galaxy:

$$\int_{M_h}^{\infty} n(M_h', z)\, dM_h' = \int_{L^{\rm obs}}^{\infty} \Phi(L', z)\, dL' \tag{2.5}$$

where we use the Sheth & Tormen (1999) HMF and calibrate at $z \sim 5$ using the Bouwens et al. (2015b) LF. We calibrate over the halo mass range $10^7 - 10^{14} M_\odot$, and therefore extrapolate the LF over $M_{\rm UV} = -7.5$ to $M_{\rm UV} = -24.5$ to perform the abundance matching.

We can then calculate the UV luminosity as a function of halo mass at any redshift using Equation (2.3). The largest contribution to the uncertainty in the predicted luminosity is from the uncertainty in the calibration LF; we plot 1σ confidence bounds from this uncertainty in the plots which follow.

2.3 Results

2.3.1 Stellar masses and ages

Figure 2.1 shows the efficiency of star formation as a function of halo mass, $\varepsilon(M_h)$, derived at the calibration redshift $z \sim 5$. Halos with mass $M_h \sim 10^{11} - 10^{12}\ M_\odot$ have the highest star formation efficiencies, which is consistent with the consensus picture that low-mass halos have lower efficiencies because of supernova feedback, while star formation in higher mass halos is affected by strong negative AGN feedback. Our derived $\varepsilon(M_h)$ is consistent, to first approximation, with the results obtained by Behroozi et al. (2013a) who calculated the ratio of stellar to halo mass at different redshifts ($z \leq 4$) by applying abundance matching techniques between the stellar mass function and HMF. We note that $\varepsilon(M_h)$ is redshift-independent in our model, but that the evolution of the HMF and halo assembly times allows to us predict the UV luminosity using Equation (2.3), via our rising star formation history (see Figure 2.2). Thus we find that with our simple redshift-independent $\varepsilon(M_h)$ the star formation at high redshift proceeds much more rapidly than at low redshift.

With Equation 2.1, we can derive the model predictions for average galaxy ages as a function of halo mass and redshift, which are shown in Figure 2.3. Galaxy ages are challenging to constrain observationally, due to the degeneracy between dust extinction, age and metallicity in spectral energy distribution (SED) fitting, which are especially severe at $z \gtrsim 4$ where *HST* covers only the rest-frame UV wavelengths. Our modeling results are consistent with the picture emerging from multiple recent studies that combine *HST* and Spitzer/IRAC data and find that the majority of $z \gtrsim 4$ galaxies to have old stellar populations (> 100 Myr) and relatively low specific SFR ($\sim 100\,M_\odot$ yr^{-1}) (Oesch et al. 2013; Straatman et al. 2014; see also González et al. 2011 for earlier studies reaching the same conclusion but without accounting for nebular emission lines). However, other independent studies based mostly on overlapping datasets reached the different conclusion that $z \gtrsim 4$ galaxies have a high chance of being young systems (ages < 50 Myr) with high specific SFRs (de Barros et al., 2014; Finkelstein et al., 2015a), suggesting that improved observational constraints are needed to evaluate the fidelity of stellar ages predicted by our model.

The contributions to the total UV luminosity at fixed halo mass from two epochs of star formation as a function of observed redshift are shown in Figure 2.4. We find that the earlier epoch of star formation, as the halo grows from $M_h/4$ to $M_h/2$ adds a negligible contribution to the total UV luminosity, suggesting that recent star formation is the most important contribution to the UV luminosity even at $z > 10$ when the assembly time is short. This is consistent with recent clustering studies (Barone-Nugent et al., 2014) which found a high duty cycle for galaxies at $z \geq 6.5$, possibly due to their bright, young stellar populations, and with the prediction of smoothly rising SFRs from numerical simulations (Finlator et al., 2011) and observations (Papovich et al., 2011; Behroozi et al., 2013b; Lee et al., 2014). Thus, we only consider the contribution from the first two terms in Equation (2.3) in predicting the UV luminosity.

The stellar mass density as a function of redshift, obtained by integrating our model stellar mass functions (using Equation (2.2) to derive stellar masses) to a stellar mass limit

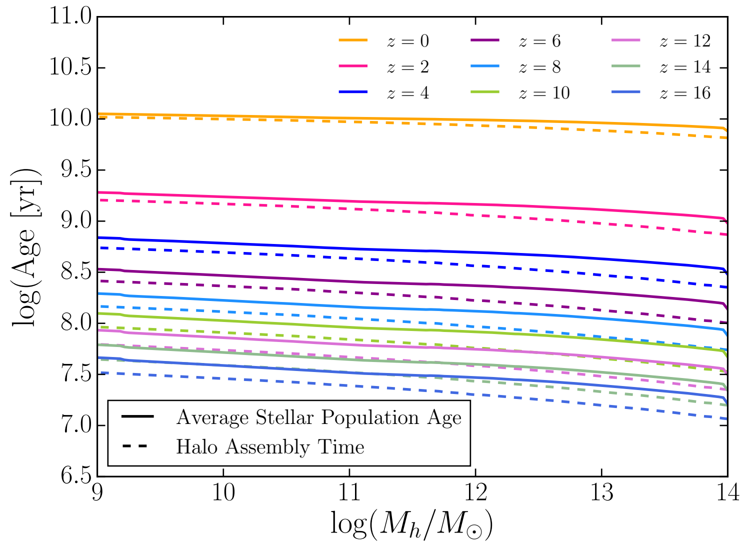

Figure 2.3: Average stellar population age in our model and halo assembly time (Lacey & Cole, 1993) as a function of halo mass and observed redshift.

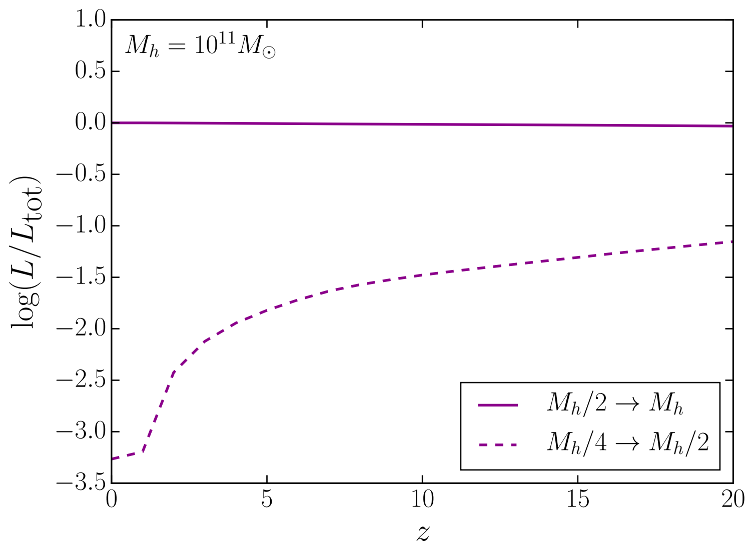

Figure 2.4: Contribution to predicted UV luminosity from the 0th and 1st order terms in Equation (2.3) as a function of observed redshift for fixed halo mass, $M_h = 10^{11} M_\odot$. The contribution from star formation during the halo assembly time (solid) dominates, with the contribution from the earlier star formation epoch (dashed) increasing with redshift. The SFR is constant in both epochs.

of $M_\star > 10^8 M_\odot$ is shown in Figure 2.5. We find good agreement with observations (Pérez-González et al., 2008; Stark et al., 2013; Tomczak et al., 2014; Grazian et al., 2015; Song et al., 2016) taking into account the scatter in observations at $z < 2$, and the uncertain but potentially significant contribution of massive quiescent galaxies at low redshift.

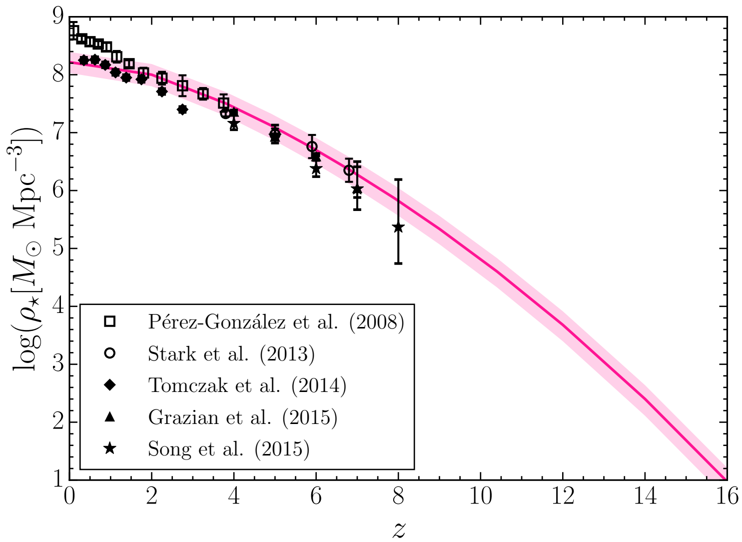

Figure 2.5: Stellar mass density ($\rho_\star$) obtained by integrating the stellar mass function derived from our model using Equation (2.2) to a stellar mass limit of $M_\star > 10^8 M_\odot$. We plot observations from Pérez-González et al. (2008); Stark et al. (2013); Tomczak et al. (2014); Grazian et al. (2015); Song et al. (2016). Shaded regions show the 1σ confidence range.

2.3.2 Luminosity functions and SFR density

The predicted observed $L(M_h, z)$ for a range of redshifts is plotted in Figure 2.6. Our model naturally provides redshift evolution of $L(M_h, z)$ through the evolution of the HMF and halo assembly times. Dust extinction (Section 2.2.2) significantly affects the high mass end of the relation at low redshift. At $z > 10$ we see the high mass end does not evolve much with redshift, motivating the model of Mashian et al. (2016) which uses an empirical redshift-independent $L(M_h)$. However, there is significant evolution at lower mass, which comprises the greatest contribution to the photon budget available to reionization because of the steep faint-end slope.

The model UV LFs at $z \leq 7$ and $z > 7$ are shown in Figures 2.7 and 2.8 respectively. The model is remarkably consistent with the observed data (Arnouts et al., 2005; Oesch et al., 2010, 2013, 2014; Alavi et al., 2014; Bowler et al., 2015; Finkelstein et al., 2015b; Bouwens et al., 2015b, 2016a), which is expected due to the success of our previous implementation of this class of models (Tacchella et al., 2013; Trenti et al., 2010, 2015). We find the model marginally overpredicts the bright end of the LF at $z \sim 0.3$ and $z \sim 2$ by ~ 0.1 dex due to the difficulty in modeling dust extinction at these redshifts, but the observations are still within 2σ of our model. In particular, our model predicts a steepening of the faint-end slope at higher redshifts, consistent with the observed trend (Bouwens et al., 2015b).

At $z > 7$, the model describes the most recent observed data (Oesch et al., 2013, 2014; Finkelstein et al., 2015b; Bouwens et al., 2015b, 2016a) well, validating our simple approach. Our model predicts the trend of steepening faint-end slope to continue at $z > 10$, and number densities to drop rapidly. With *JWST* capabilities, except in an extremely wide-field survey, the UV LF at $z > 10$ will be observed as a steep power-law function. This is agreement with the semi-analytic results of Behroozi & Silk (2015) who find a steepening power law slope at faint magnitudes and a significant drop in number densities.

For comparison, we also plot in Figure 2.9 the model LFs obtained by using the Finkelstein et al. (2015b) $z \sim 5$ LF for the calibration. The Finkelstein et al. (2015b) $z \sim 5$ LF has a lower value of M^* than that of Bouwens et al. (2015b), so it is not surprising that this calibration produces slightly lower number densities compared to our reference using the Bouwens et al. (2015b) LF. However, Figure 2.9 clearly shows that the overall evolution trends are unchanged and that the two calibrations produce LFs which are consistent within one standard deviation both between themselves and the observed data over $0 \lesssim z \lesssim 10$.

The best-fit Schechter (1976) function parameters for our LFs are shown in Table 2.1. The best-fit parameters are in good agreement with observations (Schmidt et al., 2014b; Bowler et al., 2015; Oesch et al., 2010; Finkelstein et al., 2015b; Bouwens et al., 2015b) given the large degeneracies in Schechter function parameters. Encouragingly, we find the evolution of the derived Schechter parameters is in excellent agreement with the observed evolution (Bouwens et al., 2015b; Bowler et al., 2015): we find $d\alpha/dz \sim -0.1$, $dM^*/dz \sim 0.1$, and $d\log(\Phi^*)/dz \sim -0.3$ between $z \sim 4$ and $z \sim 8$. We find the evolution of α and Φ^* between $z \sim 8$ and $z \sim 16$ to be more dramatic: $d\alpha/dz \sim -0.2$, $dM^*/dz \sim 0.1$, and $d\log(\Phi^*)/dz \sim -0.5$, consistent with the rapid evolution of $\sim 10^{10}\ M_\odot$ halos in the DM HMF at these redshifts.

Figure 2.10 shows the luminosity density and cosmic SFR density as a function of redshift.

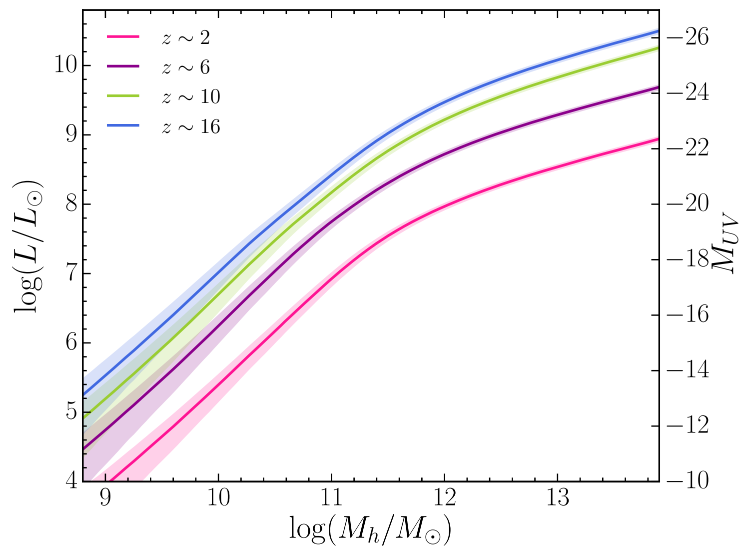

Figure 2.6: The relationship between observed galaxy luminosity and halo mass as a function of redshift, $L(M_h, z)$, plotted at $z = 2$, 6, 8, and 16. Shaded regions show the 1σ confidence range.

We calculate the luminosity density by integrating our model LFs down to a magnitude limit. We choose two fiducial limits of $M_{\rm lim} = -17$ (just fainter than current observational limits) and $M_{\rm lim} = -12$ (the theoretical mass limit for halos to cool). We calculate the SFR density, $\dot{\rho}_\star$ using the empirical relation from Madau et al. (1998) where $SFR[M_\odot/{\rm yr}] = 8.0 \times 10^{27} L[{\rm ergs/s/Hz}]$ at 1500 Å. We plot the densities and observations from Bouwens et al. (2015b) both with and without dust correction. At $z \leq 8$ the observations are consistent with both magnitude limits, however the observations at $z \sim 10$ suggests a significant steepening of the relation at high redshift, as do results from numerical simulations (Gene et al., 2014, though with large uncertainty), which is consistent with our model with $M_{\rm lim} = -17$. The sample at $z \sim 10$ is limited however; more observational data at $z > 8$ are needed to confirm this result.

2.3.3 Forecasts for *JWST* and *WFIRST*

We use our model to make forecasts for a representative set of *JWST* NIRCAM high-redshift dropout surveys using the 5 near-IR filters. The surveys (properties summarized in Table 2.2) include an ultra-deep (UD) survey of 4 pointings (~ 40 arcmin^2) exposed in 200 hours per

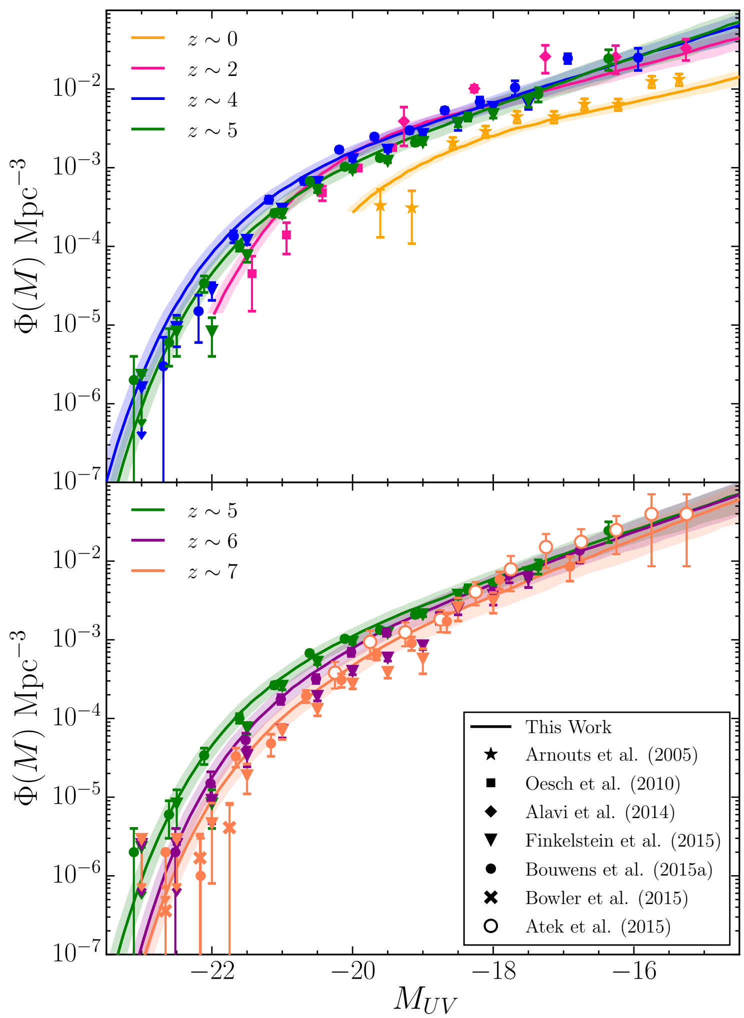

Figure 2.7: Predicted UV LFs at low (upper) and intermediate (lower) redshift. We show the LFs using the calibration (see Section 2.2.3) at $z \sim 5$ from Bouwens et al. (2015b), with Planck 2015 cosmology (Planck Collaboration et al., 2016a), with Planck 2015 cosmology (Planck Collaboration et al., 2016a). Points show the binned UV LFs and upper limits from Arnouts et al. (2005); Alavi et al. (2014); Oesch et al. (2010); Bouwens et al. (2015b); Finkelstein et al. (2015b); Bowler et al. (2015); Atek et al. (2015a). We note that the data from Atek et al. (2015a) was made public after our model was submitted and illustrates the consistency of our model with observations even at very low luminosity. Shaded regions show the 1σ confidence range.

pointing; a medium-deep (MD) survey of 40 pointings exposed in 20 hours per pointing; and a wide-field (WF) survey of 400 pointings exposed in 2 hours per pointing. We assume that the surveys will split the observing time so as to reach equal depth in all five filters, and estimate the limiting magnitude for an 8σ detection (in a single filter) using the *JWST* Exposure Time Calculator. We also include the effects of gravitational lensing magnification bias from

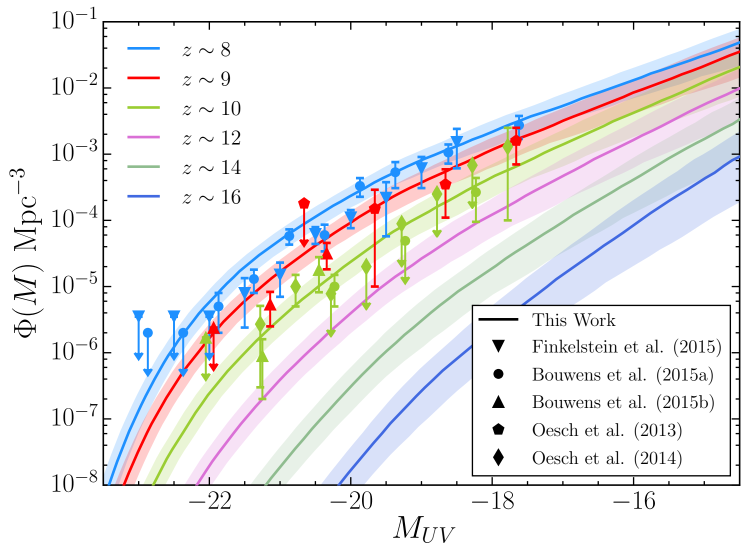

Figure 2.8: Predicted UV LFs at high redshift. We show the LFs using the calibration (see Section 2.2.3) at $z \sim 5$ from Bouwens et al. (2015b), with Planck 2015 cosmology (Planck Collaboration et al., 2016a). Points show the binned UV and upper limits LFs from Oesch et al. (2013, 2014); Finkelstein et al. (2015b); Bouwens et al. (2015b, 2016a). Shaded regions show the 1σ confidence range.

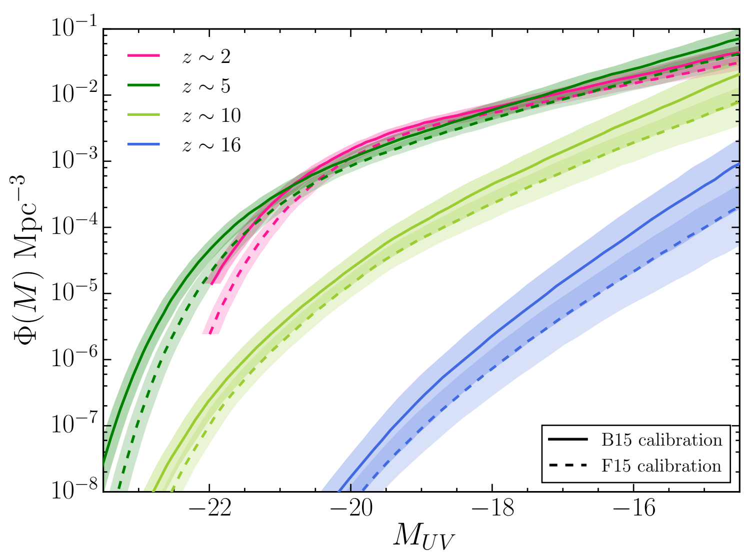

Figure 2.9: Predicted LFs at redshifts $z \sim 2$, 5, 10, 16 obtained by calibrating (see Section 2.2.3) our model with the Finkelstein et al. (2015b) LF at $z \sim 5$ (F15, dashed), compared to our reference calibration using the Bouwens et al. (2015b) LF at $z \sim 5$ (B15, solid). Shaded regions show the 1σ confidence range, highlighting that within the uncertainty of the calibrations, the two approaches yield consistent results.

strong lensing in blank fields, which is expected to distort the brightest end of high-redshift LFs (Mason et al., 2015b; Wyithe et al., 2011).

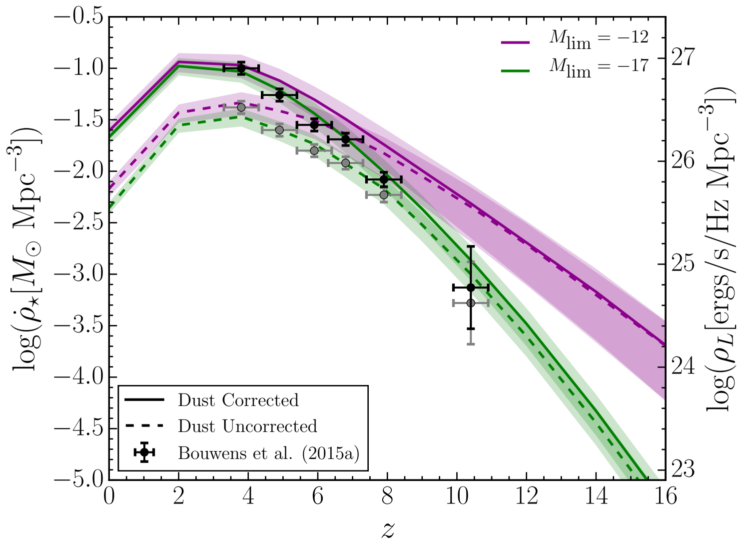

Figure 2.10: Luminosity density (ρ_L) and cosmic SFR density ($\dot{\rho}_\star$) as functions of redshift, derived by integrating the model UV LFs to magnitude limits of $M_{\rm AB} = -17$ (green lines) and $M_{\rm AB} = -12$ (purple lines). The dust corrected SFR densities for the two magnitude limits are shown as solid lines, dust uncorrected SFR densities are shown as dashed lines. The observed SFR densities from Bouwens et al. (2015b) are shown in black (dust corrected) and grey (dust uncorrected). Shaded regions show the 1σ confidence range.

Table 2.1: Best-fit Schechter parameters for model LFs

Redshift	α	M^*	$\log(\Phi^*[{\rm mag}^{-1}{\rm Mpc}^{-3}])$
$z \sim 0$	-1.68 ± 0.09	-19.9 ± 0.1	$-2.97^{-0.07}_{+0.08}$
$z \sim 2$	-1.46 ± 0.09	-20.3 ± 0.1	$-2.52^{-0.07}_{+0.09}$
$z \sim 4$	-1.64 ± 0.11	-21.2 ± 0.2	$-2.93^{-0.13}_{+0.19}$
$z \sim 5$	-1.75 ± 0.13	-21.2 ± 0.2	$-3.12^{-0.15}_{+0.24}$
$z \sim 6$	-1.83 ± 0.15	-20.9 ± 0.2	$-3.19^{-0.16}_{+0.25}$
$z \sim 7$	-1.95 ± 0.17	-21.0 ± 0.2	$-3.48^{-0.18}_{+0.32}$
$z \sim 8$	-2.10 ± 0.20	-21.3 ± 0.4	$-4.03^{-0.26}_{+0.72}$
$z \sim 9$	-2.26 ± 0.22	-21.2 ± 0.4	$-4.50^{-0.29}_{+1.36}$
$z \sim 10$	-2.47 ± 0.26	-21.1 ± 0.5	-5.12 ± 0.34
$z \sim 12$	-2.74 ± 0.30	-21.0 ± 0.5	-5.94 ± 0.38
$z \sim 14$	-3.11 ± 0.38	-20.9 ± 0.5	-7.05 ± 0.45
$z \sim 16$	-3.51 ± 0.46	-20.7 ± 0.6	-8.25 ± 0.51

NOTE. – Fit performed between $M_{\rm AB} = -17.5$ and $M_{\rm AB} = -22.5$

In Figure 2.11 we plot the predicted cumulative number counts for redshifts $8 \leq z \leq 16$ and the regions accessible to these mock *JWST* surveys, as well as the region accessible to *WFIRST* High-Latitude Survey (HLS, Spergel et al., 2013). The estimated number of dropouts are given in Table 2.2.

Our model predicts a significant drop in number density from $z \sim 8$ to $z \sim 10$ compared to lower redshifts (which is also seen in the observations, Bouwens et al., 2015b, 2016a). The drop continues to high redshift, thus we find that no $z \sim 16$ galaxies would be detected in our mock *JWST* surveys. To detect 1 galaxy at $z \sim 16$ in our UD survey would require ~ 40 pointings (~ 400 arcmin^2). We find that magnification bias in blank fields does not significantly affect our model even at the brightest observable magnitudes at $z > 10$. The magnification bias effect is only noticeable in the exponential part of the LF, which is within reach only at z 8, but too weak otherwise for power laws with slope in the range -2 to -3.5 (it is exactly neutral for faint end slope $\alpha = -2$). Mason et al. (2015b) showed the lensing effect was most significant for a Schechter function LF at high redshift (see also Barone-Nugent et al. 2015). Thus we expect that without significant strong lensing, i.e. using galaxy clusters as cosmic telescopes (e.g. the *Hubble Frontier Fields* Yue et al., 2014; Ishigaki et al., 2015; Coe et al., 2015; Atek et al., 2015a), $z > 15$ is beyond the reach of *JWST*.

2.3.4 Implications for reionization

The timeline of cosmic reionization depends on the balance between the recombination of free electrons with protons to form neutral hydrogen atoms, and the ionization of hydrogen atoms by Lyman continuum photons emitted by young stars. The UV luminosity density (and therefore, SFR density) at a given redshift allows us to calculate the number of photons available for reionization, and is most sensitive to the faint end of the LF. We can use this to infer the timeline of reionization by calculating the ionized hydrogen fraction, $Q(z)$, as a function of redshift given the following time-dependent differential equation:

$$\dot{Q} = \frac{\dot{n}_{ion}}{\langle n_{\rm H} \rangle} - \frac{Q}{t_{rec}} \qquad (2.6)$$

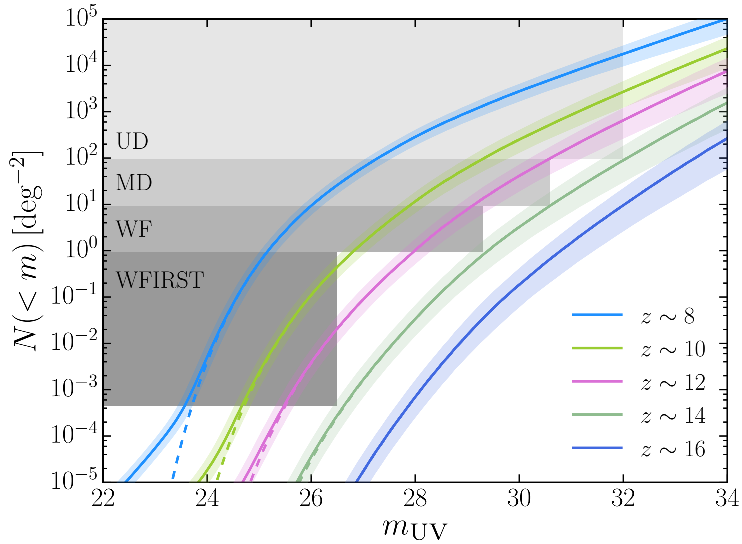

Figure 2.11: Predicted number counts of galaxies brighter than apparent magnitude $m_{\rm UV}$ (rest-frame UV) per square degree for a range of redshifts based on our model LFs. We plot the cumulative number counts including the boost from gravitational lensing magnification bias (Mason et al., 2015b; Wyithe et al., 2011) as solid lines, and without the magnification bias effect (dashed lines). We plot the estimated coverage of future surveys as shaded regions: 3 mock *JWST* surveys detailed in Section 2.3.3 and the *WFIRST* High-Latitude Survey (Spergel et al., 2013). The calculated number counts are given in Table 2.2.

where $\dot{n}_{ion}$ is the comoving number density of ionizing photons, $\langle n_{\rm H} \rangle$ is the comoving number density of hydrogen atoms, and the recombination time of the IGM (Stiavelli et al., 2004; Robertson et al., 2015, and references therein) is:

$$t_{\rm rec}(z) = \left[C \alpha_B(T) n_e (1+z)^3 \right]^{-1} \tag{2.7}$$

where $\alpha_B(T)$ is the case B recombination (i.e. opaque IGM) coefficient for hydrogen, $n_e = (1 + Y_p/4X_p)\langle n_{\rm H} \rangle$ is the comoving number density of electrons (assuming singly ionized He), X_p and Y_p are the primordial hydrogen and helium abundances respectively, and $C = \langle n_H^2 \rangle / \langle n_{\rm H} \rangle^2$ is the "clumping factor" which accounts for inhomogeneity in the IGM.

The production rate of ionizing photons can be related to the total UV luminosity density, ρ_L as

$$\dot{n}_{\rm ion} = f_{\rm esc} \xi_{\rm ion} \rho_L \tag{2.8}$$

where $f_{\rm esc}$ is the average fraction of photons which escape galaxies to affect the IGM, and $\xi_{\rm ion}$ is the rate of ionizing photons per unit UV luminosity, with units Hz/ergs, which depends on the initial mass function, metallicity, age and dust content of the stellar populations. There is an equivalent relation between $\dot{n}_{ion}$ and SFR density (Madau et al., 1999; Shull et al., 2012), which requires the same stellar population modeling.

All of the parameters involved are difficult to estimate, and may evolve with redshift as reionization progresses and the IGM evolves (Furlanetto & Oh, 2005; Shull et al., 2012). In this work, we follow Schmidt et al. (2014b) and use a distribution of parameters. For two limiting magnitudes ($M_{\text{AB}} = -17$, corresponding to currently observable galaxies, and $M_{\text{AB}} = -12$, corresponding to atomic cooling halos) we assume the escape fraction is uniformly distributed between $f_{\text{esc}} = 0.1 - 0.3$ (Ouchi et al., 2009), and we use a uniform distribution between $C = 1 - 6$ for the clumping factor. Finally we model ξ_{ion} as a log-normal distribution with mean $\log \xi_{\text{ion}} = 25.2$ and standard deviation 0.15 dex, which was the range obtained by Robertson et al. (2013) using the standard Bruzual & Charlot (2003) models and measurements of the UV spectral slope by Dunlop et al. (2012). We assume an IGM temperature of $20,000$ K.

Once the reionization history, $Q(z)$, is known, an important constraint is to compare the electron scattering optical depth with that inferred from CMB observations. The Planck Collaboration et al. (2016a) reported a reionization value of $\tau = 0.066 \pm 0.012$, consistent with instantaneous reionization at $z = 8.8^{+1.2}_{-1.1}$. The optical depth as a function redshift is:

$$\tau(z) = \int_0^z \sigma_T n_e (1+z')^2 Q(z') \frac{c}{H(z')} dz' \tag{2.9}$$

where c is the speed of light, σ_T is the Thomson scattering cross section and $H(z)$ is the Hubble parameter.

Figure 2.12 shows the reionization history: the ionized hydrogen fraction as a function of redshift, obtained by solving Equation (2.6) with our model luminosity density, sampling the distributions of input parameters. Figure 2.13 shows the electron scattering optical depth as a function of redshift. For the LF magnitude limit $M_{\text{AB}} = -17$, reionization is complete ($Q = 1$) by $z_{\text{reion}} = 6.86^{+0.32}_{-0.66}$, with $\tau(z_{\text{reion}}) = 0.042^{+0.008}_{-0.002}$. For the LF magnitude limit $M_{\text{AB}} = -12$, reionization is complete by $z_{\text{reion}} = 7.84^{+0.65}_{-0.98}$, with $\tau(z_{\text{reion}}) = 0.056^{+0.007}_{-0.010}$.

The fainter magnitude limit, corresponding to atomic cooling halos of mass $M_h \sim 10^9 M_\odot$,

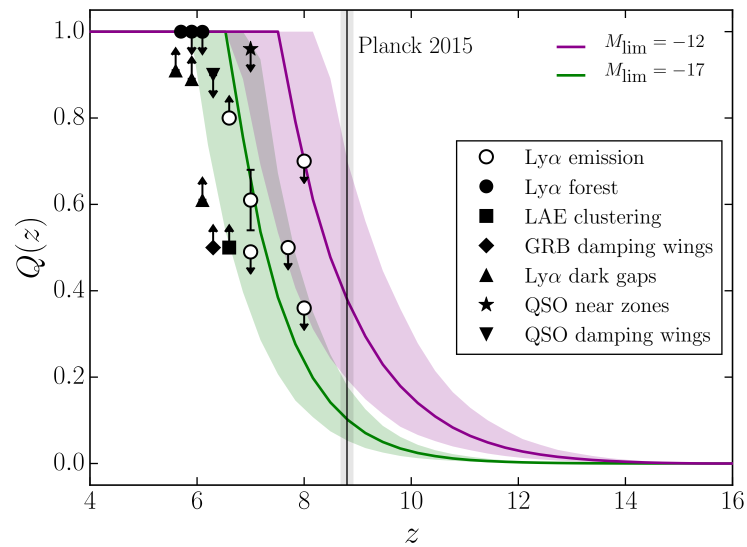

Figure 2.12: The fraction of ionized hydrogen as a function of redshift, obtained by solving Equation (2.6) with our model luminosity density. We plot our results from integrating the model UV LFs to two magnitude limits of $M_{\rm AB} = -17$ (green) and $M_{\rm AB} = -12$ (purple), with 1σ confidence regions as shaded regions. We also plot constraints derived from observations of: Lyα emission from galaxies (open circles, Ouchi et al., 2010; Pentericci et al., 2014; Tilvi et al., 2014; Faisst et al., 2014; Schenker et al., 2014); the Lyα forest (filled circles, Fan et al., 2006); the clustering of Lyα emitting galaxies (square, Ouchi et al., 2010); GRB spectra damping wings (diamond, McQuinn et al., 2008); dark gaps in the Lyα forest (upper triangles, McGreer et al., 2015); quasar near zones (star, Venemans et al., 2015); and quasar spectra damping wings (lower triangle, Schroeder et al., 2013). We also plot the Planck Collaboration et al. (2016a) redshift of instantaneous reionization. We note that the conversion from the Lyα escape fraction to the global ionized hydrogen fraction is uncertain and relies on several model assumptions (Mesinger et al., 2015).

is fully consistent with the Planck results, considering the uncertainty in the reionization model parameters. This calculation shows that ultrafaint galaxies can in principle provide enough photons to fully reionize the universe by $z \sim 6$ to match observations of the Lyα forest (Fan et al., 2006). Both magnitude limits are broadly consistent with a range of constraints from observations, within the reionization model uncertainty: UV luminosity densities (Finkelstein et al., 2012a) for observable galaxies; quasar near zones (Venemans et al., 2015); quasar spectra damping wings (Schroeder et al., 2013); GRB spectra damping wings (McQuinn et al., 2008); transmission (Fan et al., 2006) and dark gaps (McGreer et al., 2015) in the Lyα forest; and the clustering of Lyα emitting galaxies (Ouchi et al., 2010).

Qualitatively, the non-negligible neutral fraction predicted by our model at $z \gtrsim 7$ is con-

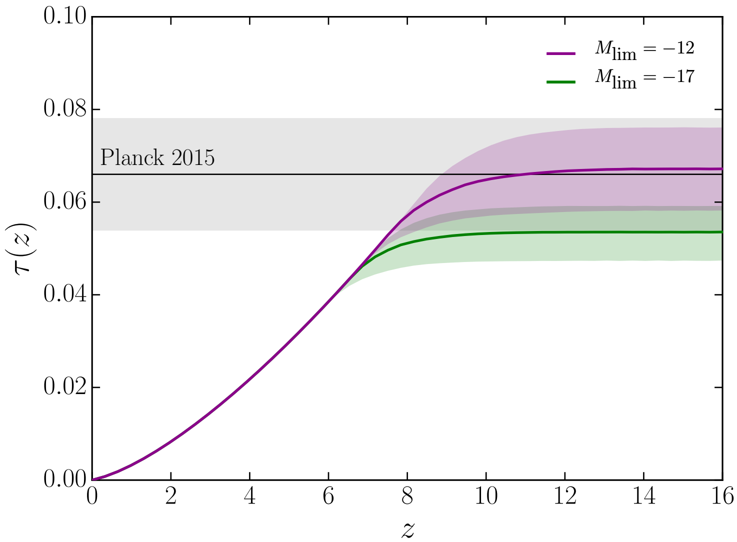

Figure 2.13: The electron scattering optical depth, calculated using Equation (2.9) from our derived Q(z). We plot our results from integrating the model UV LFs to two magnitude limits of $M_{\rm AB} = -17$ (green) and $M_{\rm AB} = -12$ (purple), with 1σ confidence regions as shaded regions. We show the reionization optical depth value and its 1σ confidence levels from Planck Collaboration et al. (2016a) in grey.

sistent with the observed high optical depth of Lyα (Ouchi et al., 2010; Treu et al., 2013; Pentericci et al., 2014; Tilvi et al., 2014; Faisst et al., 2014; Schenker et al., 2014, K. B. Schmidt et al. 2015, ApJ submitted), however the conversion from the Lyα emission fraction to the volume filling factor of ionized hydrogen is difficult and requires several assumptions (Mesinger et al., 2015). In particular, to make constraints on reionization it is generally assumed that there are no changes in galaxy and the Lyα emission line properties, which necessitates a rapid evolution of the global ionization fraction between $z \sim 6$ and $z \sim 7$. However, recent studies have shown that the rapid decline in the Lyα escape fraction at these redshifts cannot result only from the changing IGM attenuation (Mesinger et al., 2015) but could also be explained by the co-evolution of the escape fraction of ionizing photons, $f_{\rm esc}$, (Dijkstra et al., 2014). Thus, the uncertainties in the ionization fraction from the Lyα optical depth shown in our plot are likely underestimated, since they do not include these systematic effects.

2.4 Summary and Conclusions

We have presented a simple model for the evolution of the UV LF from $0 \lesssim z \lesssim 16$, assuming that the average star formation history of galaxies is set by their halo mass and by the redshift (through the halo assembly time), so that halos of the same mass have the same stellar mass content independent of redshift. Our model builds upon previous similar implementations, but here we extended our framework to construct a self-consistent model which is capable of following the evolution of the star formation even when the halo assembly times become very short (at $z \gtrsim 10$).

Our key findings are as follow:

1. Our model UV luminosity functions are very successful in matching observations at all redshifts where data are available ($0 \lesssim z \lesssim 10$). Overall, we find that the shape of the LF is well described by a Schechter function with faint-end slope increasing with redshift. This trend continues at higher redshift, and we use the model to make predictions for LFs at $z > 10$, finding a faint-end slope $\alpha \sim -3.5$ at $z = 16$.

2. Our model reproduces the observed cosmic SFR density well, indicating a sharp decline at $z > 8$ with a magnitude limit of $M_{\rm AB} = -17$, consistent with observed data at $z \sim 10$.

3. Compared to previous more basic models (Tacchella et al., 2013; Trenti et al., 2015), we find that the self-consistent inclusion of earlier periods of star formation does not significantly affect the total UV luminosity at a given halo mass and redshift, but it allows us to better reproduce the observed average stellar ages and stellar mass density of high redshift galaxies.

4. Taking advantage of the ability of the model to make predictions at the earliest times, we investigate the expected galaxy detections for future ultra-deep, medium-deep and wide-field surveys with *JWST*, and *WFIRST*. We predict that $z \sim 14$ galaxies over a range of luminosities are in reach of these surveys. However, significant strong lensing magnification will be needed to push beyond $z > 15$.

5. Finally, we investigate the implications of our model for the reionization process and find that reionization is complete by $z_{\rm reion} = 7.84^{+0.65}_{-0.98}$, under the assumption that the LF extends down to a minimum galaxy luminosity of $M_{\rm AB} = -12$ ($M_h \sim 10^9 M_\odot$), with $\tau(z_{\rm reion}) = 0.056^{+0.007}_{-0.010}$. Overall our model is consistent with the Planck Collaboration et al. (2016a) results and with ultrafaint galaxies being the dominant sources of reionization, despite the fact that this population is currently not detected via direct imaging (but inferred indirectly through GRB host galaxy searches at $z > 6$).

This work was supported by the *HST* BoRG grants GO-12572, 12905, and 13767, and the *HST* GLASS grant GO-13459. T.T. acknowledges support by the Packard Foundation through a Packard Fellowship.

Table 2.2: Predicted number counts for example *JWST* and *WFIRST* surveys

Redshift	Dropout Filter	UD ($m_{\rm lim} = 32.0$)	MD ($m_{\rm lim} = 30.6$)	WF ($m_{\rm lim} = 29.3$)	*WFIRST* ($m_{\rm lim} = 26.5$)
		~ 40 arcmin^2	~ 400 arcmin^2	~ 4000 arcmin^2	~ 2000 deg^2
$z \sim 8$	F115W	197^{+104}_{-92}	548^{+259}_{-225}	1335^{+595}_{-503}	61370^{+27995}_{-22029}
$z \sim 10$	F115W	30^{+21}_{-17}	52^{+33}_{-26}	102^{+64}_{-48}	1026^{+701}_{-473}
$z \sim 12$	F150W	6^{+5}_{-4}	10^{+8}_{-6}	13^{+10}_{-7}	47^{+41}_{-25}
$z \sim 14$	F150W	$0.3^{+0.4}_{-0.2}$	$0.4^{+0.4}_{-0.2}$	$0.4^{+0.4}_{-0.3}$	$0.4^{+0.4}_{-0.2}$
$z \sim 16$	F200W	0	0	0	0

NOTE. – Limiting magnitudes for a 8σ detection estimated with the *JWST* Exposure Time Calculator and *WFIRST*HLS. The mock surveys are described in Section 2.3.3. These estimates include the boost from gravitational lensing magnification bias in blank fields (Mason et al., 2015b; Wyithe et al., 2011).

CHAPTER 3

Correcting the $z \sim 8$ Galaxy Luminosity Function for Gravitational Lensing Magnification Bias

This paper was published as Mason, Treu, Schmidt, Collett, Trenti, Marshall, Barone-Nugent, Bradley, Stiavelli, & Wyithe (2015b), ApJ, 805, 79, and reproduced here with minor formatting changes.

We present a Bayesian framework to account for the magnification bias from both strong and weak gravitational lensing in estimates of high-redshift galaxy luminosity functions. We illustrate our method by estimating the $z \sim 8$ UV luminosity function using a sample of 97 Y-band dropouts (Lyman break galaxies) found in the Brightest of Reionizing Galaxies (BoRG) survey and from the literature. We find the luminosity function is well described by a Schechter function with characteristic magnitude of $M^\star = -19.85^{+0.30}_{-0.35}$, faint-end slope of $\alpha = -1.72^{+0.30}_{-0.29}$, and number density of $\log_{10} \Psi^\star[\mathrm{Mpc}^{-3}] = -3.00^{+0.23}_{-0.31}$. These parameters are consistent within the uncertainties with those inferred from the same sample without accounting for the magnification bias, demonstrating that the effect is small for current surveys at $z \sim 8$, and cannot account for the apparent overdensity of bright galaxies compared to a Schechter function found recently by Bowler et al. (2015, 2014) and Finkelstein et al. (2015b). We estimate that the probability of finding a strongly lensed $z \sim 8$ source in our sample is in the range $\sim 3 - 15\%$ depending on limiting magnitude. We identify one strongly-lensed candidate and three cases of intermediate lensing in BoRG (estimated magnification $\mu > 1.4$) in addition to the previously known candidate group-scale strong lens. Using a range of theoretical luminosity functions we conclude that magnification bias will dominate wide field surveys – such as those planned for the Euclid and WFIRST missions – especially at $z > 10$. Magnification bias will need to be accounted for in order to derive

accurate estimates of high-redshift luminosity functions in these surveys and to distinguish between galaxy formation models.

3.1 Introduction

Accurate measurements of the rest-frame UV luminosity function (LF) are crucial for studying the evolution of galaxies at high redshift and reconstructing the physics and timeline of cosmic reionization. In recent years, significant progress has been achieved in measuring the LF out to $z \sim 8$ and beyond based on images taken with the Hubble Space Telescope in the deep legacy fields, the Hubble Frontier Fields and through parallel programs (e.g., Bouwens et al., 2007, 2011; Bradley et al., 2012; Oesch et al., 2012; Robertson et al., 2013; McLure et al., 2013; Schenker et al., 2013b; Schmidt et al., 2014b; Bradley et al., 2014; Bouwens et al., 2015b; Finkelstein et al., 2015b; Zitrin et al., 2015a; Coe et al., 2015).

From many of these surveys it appears the LF at $z < 6$ is well fit by a Schechter (1976) function with a power-law slope at faint luminosities and an exponential drop at the bright end, where it is expected that feedback reduces star-formation in the most massive galaxies (Somerville et al., 2012) and dust extinction may reduce the UV flux of galaxies (Cai et al., 2014). The evolution of the LF is expected to be driven by these processes and the evolution of the underlying halo mass function. It is so far unestablished which processes dominate the evolution and whether there are signification changes in the physical conditions of galaxies forming at high redshifts.

Recent studies by Bowler et al. (2015, 2014) and Finkelstein et al. (2015b) claimed an over-abundance of galaxies at the bright end of the $z \geq 6$ LF when compared to the fit of a Schechter (1976) function, although Bouwens et al. (2015b) found no evidence for a departure from a Schechter-like form at $z \sim 4-8$, largely analyzing the same data sets. An over-abundance of bright galaxies may also be apparent in smaller surveys (e.g., Ono et al., 2012; Hathi et al., 2012; Finkelstein et al., 2013). If the departure from an exponential cutoff is confirmed by future observations, this may be an indication of the changing astrophysical conditions of high-redshift galaxies. However, another possible explanation is that the LF remains intrinsically with a Schechter form and the over-abundance of bright galaxies is caused by gravitational lensing magnification bias, which has been predicted to be significant for galaxies at $z \geq 8$ (Wyithe et al., 2011).

While it has long been recognized that the gravitational lensing effect can be exploited in order to probe intrinsically faint galaxies – in particular behind massive clusters of galaxies at moderate redshift – (e.g., Franx et al., 1997; Ellis et al., 2001; Schmidt et al., 2014a; Bowler et al., 2014; Zitrin et al., 2015a; Atek et al., 2015a; Coe et al., 2015), the effect in blank fields is much less well appreciated.

In fact, gravitational lensing affects all lines of sight, as the trajectory of every photon in the universe is perturbed by the inhomogeneous foreground mass distribution. Though the effect is generally not as strong as in the fields of massive clusters of galaxies, even so-called blank field surveys are affected by gravitational lensing (weak, intermediate, or strong). In practice, owing to the lensing effect, flux-limited surveys include sources that should be below the sample threshold, but have been magnified into the sample. Furthermore, gravitational lensing changes the relation between observed solid angle and cosmic volume with respect to that expected for a perfectly homogeneous universe. At fixed detector field-of-view the intrinsic solid angle observed is smaller for magnification $\mu > 1$ and vice versa. This phenomenon is called *magnification bias* (e.g., Turner et al., 1984; Wyithe et al., 2001, 2011) and it can change the shape of the observed LF. Thus, it needs to be accounted for in order to derive accurate intrinsic LFs from flux-limited samples.

The main aim of this paper is to improve the estimation of the intrinsic UV LF at high redshift by developing a formalism to take into account the magnification bias. Our new formalism improves on previous work in several ways: we extend the analytic strong lensing model of Wyithe et al. (2011) to include the redshift evolution of the deflector population, and we develop a technique to treat the intermediate lensing regime and introduce a framework to include weak lensing effects, neither of which have been systematically accounted for in any previous estimates of the LF. Furthermore, by providing probability distribution functions for the magnification of each dropout and empty field, our formalism can be directly included in any Bayesian LF parameter estimation, thus allowing for a rigorous derivation of the related uncertainties.

We present two applications of our formalism. The first application is the interpretation of the $z \sim 8$ dropouts found by the *Brightest of Reionizing Galaxies Survey*[1], (hereafter BoRG, Trenti et al., 2011). After estimating the fraction of sources in BoRG that are multiply imaged and presenting one strongly-lensed candidate and three candidate systems with magnification $\mu > 1.4$, we use the extended sample presented by Schmidt et al. (2014b) to derive the LF including the effects of magnification bias. For this we extend the Bayesian formalism introduced by Schmidt et al. (2014b) by including a term describing the likelihood for magnification of high-redshift sources for each field, and marginalize over the range of possible magnifications.

The second application of our formalism is a set of predictions for the modification of the LF at $8 < z \leq 16$, where JWST will detect dropouts (Gardner et al., 2006), by using a variety of possible LFs based on theoretical models (Muñoz, 2012; Behroozi & Silk, 2015) and extrapolations of lower redshift data (Bouwens et al., 2015b; Finkelstein et al., 2015b). With our formalism we can give a quantitative assessment of how magnification bias will affect future surveys.

The paper is organized as follows. In Section 3.2 we briefly describe the BoRG survey and the data used in this paper. In Section 3.3 we introduce the relevant theoretical background for gravitational lensing and magnification bias. In Section 3.4 we develop a semi-analytic framework, based on that in Wyithe et al. (2011) to study the magnification bias due to strong and intermediate gravitational lensing. In Section 3.5 we use the reconstruction of lines-of-sight in cosmological simulation data to investigate weak lensing. The Bayesian inference for the determination of the intrinsic LF is introduced in Section 3.6 and presented in more detail in Appendix 3.9. The results are presented and discussed in Section 3.7. A brief summary is given in Section 3.8.

All magnitudes are AB magnitudes and a standard concordance cosmology with $\Omega_m = 0.3$, $\Omega_\Lambda = 0.7$, and $h = 0.7$ is assumed. The Millennium Simulation uses a cosmology

[1]http://borg.physics.ucsb.edu

with $\Omega_m = 0.25$, $\Omega_\Lambda = 0.75$, and $h = 0.73$, which is used to estimate the weak lensing magnification. We assume the difference between these two cosmologies is negligible for our purposes.

3.2 Data

This paper estimates the $z \sim 8$ LF using 38 bright Lyman Break galaxies selected from the BoRG survey and 59 fainter dropouts taken from deep legacy fields (in HUDF09 and the WFC3/IR wide area Early Release Science). The BoRG survey is described briefly in Section 3.2.1, but we refer to Trenti et al. (2011, 2012b); Bradley et al. (2012) and Schmidt et al. (2014b) for further details. The deep legacy data are described by Bouwens et al. (2011). Additionally, we used data of galaxies with spectroscopically determined velocity dispersions to estimate the velocity dispersion of the foreground BoRG galaxies (described in Section 3.2.2). In Section 3.2.3 we give an overview of the simulated data used in the analysis of weak lensing.

3.2.1 The BoRG Survey

The ongoing BoRG survey is a pure-parallel imaging program with the HST WFC3. The current survey covers ~ 350 arcmin^2 divided into 71 independent fields located randomly on the sky. This reduces cosmic variance below the level of statistical noise (Trenti & Stiavelli, 2008; Bradley et al., 2012). The photometry is in the visual and near-infrared, primarily using the four HST WFC3 filters F606W, F098M, F125W, and F160W (commonly referred to as V-, Y-, J-, and H-bands respectively). The $z \sim 8$ BoRG survey consisted mainly of HST programs GO/PAR 11700 and GO/PAR 12572 (PI: Trenti) and includes a small additional number of coordinated parallels from COS-GTO. 53 core BoRG fields are complemented by other archival data including 8 fields from GO/PAR 11702 (PI: Yan, Yan et al., 2011) and 10 COS-GTO fields, which used the F600LP-band instead of the F606W-band. The BoRG survey is the largest current survey of Y-band dropouts by solid angle.

The $z \sim 8$ galaxy candidates were identified from Y-band dropouts, full details of the selection criteria used to find dropouts are described in Schmidt et al. (2014b). The BoRG survey detected 38 Lyman break galaxy (LBG) candidates at $z \sim 8$ with S/N > 5 in the J-band, of which 10 have S/N > 8 (Bradley et al., 2012; Schmidt et al., 2014b). We use the 5σ sample of objects in this work. Throughout this work we will assume 42% of the selected BoRG dropouts are contaminants (usually $z \sim 2$ interlopers, see e.g., Hayes et al., 2012; Bouwens et al., 2014). This is the fiducial contamination fraction for the BoRG sample and was shown to be robust in the estimation of the LF by Bradley et al. (2012); Schmidt et al. (2014b). By definition we cannot determine which specific sources are contaminants without further photometry and spectroscopy, but our rigorous Bayesian method to determine the LF allows us to accurately estimate the LF parameters accounting for the presence of random contaminants (Schmidt et al., 2014b).

3.2.2 Massive Foreground Galaxies Acting as Deflectors

In Section 3.4.2 we estimate the velocity dispersions of strong lens candidates in the BoRG fields by comparing their photometry with similar early-type galaxies which have both HST photometry and spectroscopically determined velocity dispersions (Treu et al., 2005; Belli et al., 2014b,a). We divided the galaxy samples into three large redshift bins in order to account for the position of the 4000Å break in the filters at higher redshifts.

In the range $z < 1$ we used a sample of 165 spheroidal galaxies from Treu et al. (2005) with photometry from the Great Observatories Origins Deep Survey North (GOODS-N, Bundy et al., 2005). For $z > 1$ we use a sample of 66 massive quiescent galaxies, presented by Belli et al. (2014b,a), which were selected from HST photometric catalogs of objects in the COSMOS, GOODS and Extended Groth Strip (EGS) fields (Grogin et al., 2011; Koekemoer et al., 2011; Windhorst et al., 2011). We used an aperture correction to rescale observed velocity dispersions, σ_{obs}, to σ_e, the velocity dispersion within one effective radius, R_e.

We follow Belli et al. (2014b) and used the model of van de Sande et al. (2013) which proposes a constant rescaling:

$$\sigma_e = 1.05\sigma_{\text{obs}} \tag{3.1}$$

For galaxies at $z < 1$ (the Treu et al. (2005) sample), we used the model of Cappellari et al. (2006):

$$\sigma_e = \left(\frac{R_e}{R}\right)^{-0.066} \sigma_{\rm obs} \tag{3.2}$$

where the slit size, R is the $1''$ aperture on Keck DEIMOS (Treu et al., 2005).

The reference photometry used for the individual samples differ. As listed in Table 3.1 we use HST F606W for galaxies at $z < 0.5$, HST F850LP from Treu et al. (2005) (converted to F098M through linear interpolation) for galaxies at $0.5 < z < 1.0$, and HST F160W for galaxies at $z > 1$.

3.2.3 The Millennium Simulation

In Section 3.5 we describe our method to generate weak lensing probability density functions (PDFs) by reconstructing simulation data along the line-of-sight to $z \sim 8$. Due to the very high redshift of our sources, it was necessary to use simulation data containing halos out to redshifts above 5.

We used 24 1.4×1.4 square degree simulated lightcones built by Henriques et al. (2012) from the Millennium Simulation (Springel et al., 2005) which contain halos out to $z \sim 12$. While the Millennium Simulation contains halos from very high redshift, it has a box length of only 500 Mpc h^{-1}. The comoving distance in the universe to $z = 1$ is 2390 Mpc h^{-1}, so it is necessary to build lightcones with the galaxies correctly distributed in comoving volumes (see Blaizot et al. (2005) and Kitzbichler & White (2007) for a thorough discussion of generating mock lightcones).

These lightcones were generated using the semi-analytical galaxy formation model of Guo et al. (2011), and photometric properties were calculated using the stellar population synthesis code by Maraston (2005) which can be applied at high redshift.

3.3 Theoretical Background

In this section we summarize the relevant theory for the galaxy LF, strong and weak gravitational lensing, and magnification bias.

3.3.1 Galaxy Luminosity Function

When a simply parametrized form is needed, we describe the LF by a Schechter function (Schechter, 1976):

$$\Psi(L) = \frac{\Psi^\star}{L^\star}\left(\frac{L}{L^\star}\right)^\alpha \exp\left(-\frac{L}{L^\star}\right) \tag{3.3}$$

where $L^\star$ marks the characteristic break in the LF, $\Psi^\star$ is the characteristic density at that luminosity and α is the power-law exponent slope of the faint end.

3.3.2 Strong Lensing

If the line-of-sight to a background source is closely aligned with a massive foreground object, e.g. a cluster or single massive galaxy, gravitational lensing can produce multiple observed images of the source (Schneider et al., 1992, 2006). Multiple imaging signifies the regime of strong gravitational lensing lensing.

3.3.2.1 Singular Isothermal Sphere

Strong gravitational lenses are commonly modeled as Singular Isothermal Spheres (SIS), which provides a convenient analytic form to describe the mass profiles of massive galaxies (e.g. Treu,Tommaso et al., 2010, and references therein). The scale of image separation is characterized by the *Einstein radius* of the lens:

$$\theta_{\mathrm{ER}}(\sigma, z) = 4\pi\frac{D_{ls}}{D_s}\left(\frac{\sigma}{c}\right)^2 \tag{3.4}$$

where D_{ls} and D_s are the angular diameter distances between the lens and source, and from the observer to the source respectively, σ is the velocity dispersion of the lens galaxy, and c

is the speed of light. Velocity dispersion is the most important property for determining the strength of a strong gravitational lens as it scales with the mass of the dark matter in the system (Turner et al., 1984; Schneider et al., 2006; Treu,Tommaso et al., 2010).

The magnification, μ, due to an SIS lens is given by:

$$\mu = \frac{|\theta|}{|\theta| - \theta_{\mathrm{ER}}} \tag{3.5}$$

where θ is the distance between the lens and the source in the image plane. An SIS lens can produce two images, with the brighter one having magnification $\mu > 2$, or one image with magnification $\mu < 2$. The case of multiple imaging is referred to here as strong lensing. In this paper we refer to images with $1.4 < \mu < 2$ as intermediate lensing.

3.3.2.2 Multiple Image Optical Depth

The optical depth τ_m is the cross-section for a galaxy at redshift z_S to be multiply imaged (i.e. strongly lensed) by a foreground galaxy at z_L: it is the fraction of the sky covered by the Einstein radii of all intervening deflectors at redshifts z_L. Following standard practice and assuming SIS deflectors, Wyithe et al. (2011) defines it as:

$$\tau_m = \int_0^{z_S} dz_L \int d\sigma \; \Phi(\sigma, z_L) \; (1+z_L)^3 \; c\frac{dt}{dz_L} \pi D_L^2 \; \theta_{\mathrm{ER}}^2(\sigma, z_L) \tag{3.6}$$

where $\Phi(\sigma, z_L)$ is the velocity dispersion function of the deflectors, D_L is the angular diameter distance to z_L, and t is time. Without the magnification bias, the optical depth gives the probability of a high-redshift source being multiply imaged.

3.3.3 Weak Lensing

Weak gravitational lensing is the deflection of light that causes the magnification and distortion of an observed source, but without producing multiple images. There are no empty lines-of-sight in the universe, so all light traveling to us has been deflected some amount by intervening mass (Hilbert et al., 2007). Whilst it is impossible to determine the exact effect on individual observed sources, it can be done in a statistical sense and is important to quantify this effect for our high-redshift sources.

The lens equation can be constructed for an arbitrary number of lens planes due to an ensemble of deflectors along the line-of-sight (Hilbert et al., 2009; McCully et al., 2014). The magnification of a source in a multiplane system is a function of the total convergence and total shear experienced. Hilbert et al. (2009) showed to first order that the total convergence and shear are the sum of the individual contributions from each object along the line-of-sight:

$$\mu = \frac{1}{(1 - \sum_i \kappa_i)^2 - |\sum_i \gamma_i|^2} \tag{3.7}$$

The convergence, κ_i, and shear, γ_i, of each object are determined by the lens model.

3.3.4 Magnification Bias

The gravitational lensing of a source with luminosity L in a solid angle Ω of sky has two effects. The observed luminosity is magnified by a factor μ and sources are now distributed over a magnified solid angle $\mu\Omega$. In a flux-limited sample intrinsically low luminosity sources can be magnified above the survey limit, while the number density of sources can decrease for a given observed solid angle.

Since the faint end of the LF of high-redshift LBG galaxies is so steep, in regions around large low-redshift deflectors we may observe an excess of intrinsically faint high-redshift sources. These effects are known as the *magnification bias* and will effect our inferences about the population and LF of high-redshift galaxies.

If it were possible to observe all galaxies in the universe without the magnification bias the probability of a high-redshift galaxy being strongly lensed is purely given by the optical depth, τ_m (Section 3.3.2.2). However, magnification of more numerous intrinsically faint sources into our surveys implies that we do not observe the true population of galaxies with luminosity. The magnification bias increases the probability that a sample of observed high-redshift sources have been gravitationally lensed.

The magnification bias for sources with observed luminosities above L_{lim} in a flux-limited sample is given by:

$$B = \frac{\int_{\mu_{\rm min}}^{\mu_{\rm max}} d\mu \, p(\mu) N \left(> \frac{L_{\rm lim}}{\mu}\right)}{N(> L_{\rm lim})} \tag{3.8}$$

assuming that each source could be magnified between $\mu_{\rm min}$ and $\mu_{\rm max}$. Where $p(\mu)$ is the probability distribution for magnification of a source and $N(> L_{\rm lim})$ is the integrated galaxy LF (Wyithe et al., 2011).

The true probability of a high-redshift source being multiply imaged is $B\tau_m$. Therefore, using B it is possible to find the fraction of galaxies at a given redshift in a flux-limited sample that are multiply-imaged:

$$F_{\rm mult} = \frac{B\tau_m}{B\tau_m + B'(1-\tau_m)} \tag{3.9}$$

We assume that B', the bias for galaxies to not be multiply imaged is close to unity.

If the survey limit is brighter than the characteristic apparent magnitude of the observed sample the magnification bias is expected to be large, as a large fraction of the observed sources are likely to be intrinsically fainter sources magnified above the detection threshold of the survey.

We can compute the gravitationally lensed LF, including strong and weak gravitational lensing:

$$\begin{aligned} \Psi_{\rm mod}(L) &= (1-\tau_m)\frac{1}{\mu_{\rm demag}}\Psi\left(\frac{L}{\mu_{\rm demag}}\right) \\ &+ \tau_m \int_0^\infty d\mu \, \frac{1}{\mu} p(\mu) \Psi\left(\frac{L}{\mu}\right) \end{aligned} \tag{3.10}$$

Where $\mu_{\rm demag} < 1$ is introduced such that the mean magnification over the entire sky is unity (Pei, 1995; Wyithe et al., 2011) and $p(\mu)$ is the full probability density for magnification of a high-redshift source, as above. For a Schechter LF, the gravitationally lensed LF is predicted to exhibit a 'kick' in the bright end (e.g., Wyithe et al., 2011) due to a pile-up of brightened galaxies, whereas at the faint end the magnification of flux is balanced by the loss of number density (for faint-end slope $\alpha \sim -2$, Blandford & Narayan, 1992) so there is no distortion, even if many strongly lensed faint sources are observed.

3.4 Strong and Intermediate Lensing

In this section we compute the probability that the $z \sim 8$ dropouts are affected by strong and intermediate lensing. First, in Section 3.4.1 we compute the strong lensing optical depth and the probability that a $z \sim 8$ source is multiply imaged by foreground massive elliptical galaxy deflectors. We account for evolution of the deflector population based on the observed stellar mass function. In Section 3.4.2 we describe our method to identify sources in the intermediate lensing regime ($1.4 < \mu < 2$). In order to identify these sources, we estimate the lensing strength of massive foreground galaxies based on HST photometry and an empirical calibration of the Faber & Jackson (1976) relation. A candidate strongly lensed dropout in the BoRG fields was presented by Barone-Nugent et al. (2015), in this paper one more candidate multiply-imaged dropout ($\mu > 2$) is found, and three dropouts may experience significant intermediate magnification. We detail their properties in Table 3.2.

3.4.1 Strong Lensing by an Evolving Deflector Population

In order to compute the strong lensing optical depth and multiple image probability, we follow Wyithe et al. (2011) and use a simple SIS lensing model (see Section 3.3.2.1) with a flat cosmology. Strong lenses are assumed to be uniformly distributed in the universe and we can calculate the probability of encountering a strong lens along the line-of-sight to a high-redshift source, i.e. the lensing optical depth (see Section 3.3.2.2). By considering the number of galaxies observed above a certain flux limit we can calculate the magnification bias factor, B, from Equation (3.8), assuming a Schechter luminosity function (Equation (3.3)). For these calculations we use the $z \sim 8$ LF inferred by Schmidt et al. (2014b), with a characteristic magnitude of $M^\star = -20.15^{+0.29}_{-0.38}$, faint-end slope of $\alpha = -1.87^{+0.26}_{-0.26}$, and number density of $\log_{10} \Psi^\star[\mathrm{Mpc}^{-3}] = -3.24^{+0.25}_{-0.24}$. We marginalize over the entire MCMC chain for each of the Schechter parameters.

In their calculation of the optical depth Wyithe et al. (2011) used the local velocity dispersion function as measured by SDSS (Choi et al., 2007). As most strong lenses occur at $z \lesssim 1.5$ (Fassnacht et al., 2004; Treu,Tommaso et al., 2010), Wyithe et al. (2011) assumed that the velocity dispersion function does not evolve with redshift for massive galaxies. This is consistent with studies of the velocity dispersion function out to $z \sim 1$ (e.g., Chae, 2010; Bezanson et al., 2012). However, significant galaxy growth and evolution is observed from $z > 1$ as structure forms (van de Sande et al., 2013; Belli et al., 2014b), and we can improve the accuracy of the model by allowing the parameters of the velocity dispersion function for massive ellipticals to evolve with redshift. Introducing redshift evolution is expected to reduce the optical depth (Barkana & Loeb, 1999).

The dashed blue line in the left panel of Figure 3.3 shows the probability that the source has been multiply imaged as a function of lens redshift for a source at $z \sim 8$, calculated using Equation (3.6). The distribution is strongly peaked at $z_L \sim 1$, but there is a significant probability that $z_L > 1.5$. Only 48% of the contribution to the optical depth for strong lensing occurs at $z_L < 1.5$. We find that 90% of lensing occurs within a lens redshift of $z_L \lesssim 3.5$. Therefore, in order to account for most of the optical depth we need to find the form of the velocity dispersion function out to $z = 3 \sim 4$ where the galaxy population is significantly different from recent times (Bundy et al., 2005; Muzzin et al., 2013; van de Sande et al., 2014).

Several studies have investigated the evolution of the velocity dispersion function out to $z \sim 1.5$ (e.g., Chae, 2010; Bezanson et al., 2011, 2012, 2013). These works are consistent with no evolution, but have large uncertainties. Measurements of velocity dispersion beyond $z > 2$ are very difficult as the brightest emission lines fall within near-IR atmospheric absorption regions (Kriek et al., 2006; Belli et al., 2014a).

Therefore, we estimate the evolution of the velocity dispersion function at high redshift based on the evolution of the stellar mass function, a related quantity that has been well-measured at $z > 2$. We convert the stellar mass function into the velocity dispersion function by means of the well-known correlation between stellar velocity dispersion (σ) and stellar mass (M_{stell}) taken from Auger et al. (2010): $\log(\sigma[\mathrm{km\ s^{-1}}]) = p\overline{M} - 11p + q$, where $p = 0.24 \pm 0.02$, $q = 2.34 \pm 0.01$ and $\overline{M} = \log(M_{\mathrm{stell}}/M_{\odot})$. This relation was derived for massive lens galaxies with high velocity dispersions, which will be the strongest contribution to the optical depth as $\tau \sim \sigma^4$.

High-redshift galaxies are observed to have higher velocity dispersions at fixed mass than in the local universe (e.g., van de Sande et al., 2013; Belli et al., 2014b; Bezanson et al., 2015). Thus the stellar mass-velocity dispersion relation is expected to evolve with redshift. Following van de Sande et al. (2013) we expect evolution of the form $(\sigma/\sigma_0) \propto (1+z)^{\beta}$, where σ_0 is the expected velocity dispersion at $z \sim 0$. In Figure 3.1 we plot publicly available data from van der Wel et al. (2008); van Dokkum et al. (2009); Newman et al. (2010); Toft et al. (2012); Bezanson et al. (2013); van de Sande et al. (2013); Belli et al. (2014b,a) and fit a relation of this form for all galaxies with estimated stellar masses between $10.8 < \log(M_{\rm stell}/M_{\odot}) < 12.0$, and measured velocity dispersion $\sigma > 200$ km s^{-1} as this was the region where the Auger et al. (2010) relation was derived. We find $\beta = 0.20 \pm 0.07$. Our result is lower than the result from van de Sande et al. (2013) because we use the Auger et al. (2010) stellar mass-velocity dispersion relation for massive lens galaxies as σ_0, whereas van de Sande et al. (2013) compare to a dynamical mass-velocity dispersion relation. As demonstrated in van de Sande et al. (2013) $M_{\rm stell}/M_{\rm dyn}$ increases with redshift, so will reduce the evolution we find compared to that in van de Sande et al. (2013). If we consider the same galaxy sample and fit both our relation derived from stellar masses and the van de Sande et al. (2013) dynamical mass relation, and include the evolution in $M_{\rm stell}/M_{\rm dyn}$, our results are consistent. We note that because the optical depth depends on velocity dispersion to the fourth power, the form of the velocity dispersion function at $z > 2$ is the greatest source of uncertainty in the calculation of optical depths.

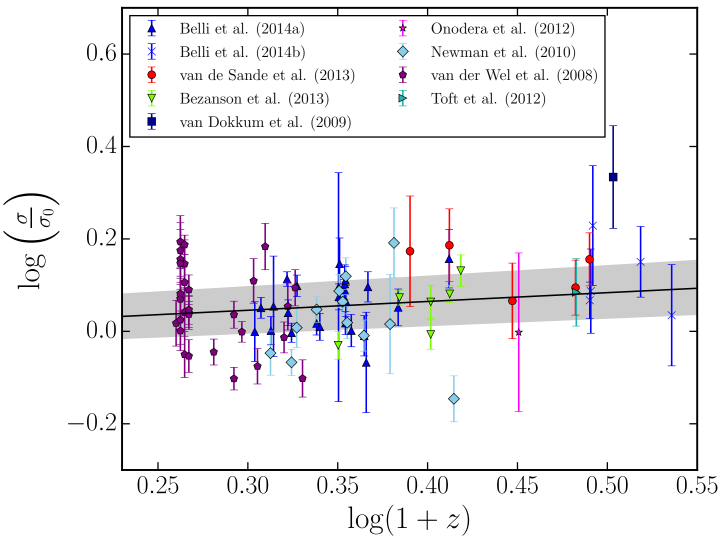

Figure 3.1: Redshift evolution of massive galaxy velocity dispersion, relative to the velocity dispersion estimated from inferred stellar masses via the Auger et al. (2010) relation. We find evolution of the form $(\sigma/\sigma_0) \propto (1+z)^{0.20\pm0.07}$, where σ_0 is the velocity dispersion estimated using the stellar mass-velocity dispersion relation from Auger et al. (2010). We plot the mean linear fit (black line) and the 1σ confidence region (gray shaded region).

The stellar mass function can be described by a Schechter function (e.g., Muzzin et al., 2013):

$$\Phi_S(\overline{M}) = (\ln 10)\ \Phi_S^*\ 10^{\left(\overline{M}-\overline{M}_S^*\right)(1+\alpha_S)}\ \exp\left[-10^{\overline{M}-\overline{M}_S^*}\right] \tag{3.11}$$

The characteristic stellar mass is given by $\overline{M}_S^* = \log\left(M_{\rm stell}^*/M_\odot\right)$, Φ_S^* is the characteristic density normalization, and α_S is the low-mass-end slope.

In order to model the redshift evolution of the stellar mass function, we use publicly available data on quiescent galaxies at $z \leq 4$ from the COSMOS/UltraVISTA Survey (Muzzin et al., 2013). They derive the best-fit single Schechter function parameters for the stellar mass function as a function of redshift. Their stellar mass function parameters for quiescent galaxies, allowing for evolution of α_S, are plotted as a function of redshift in Figure 3.2. We assumed the redshift evolution $X = X_0(1+z)^a$, where X represents the stellar mass function Schechter parameters and X_0 represents the values at $z = 0$.

We used a Bayesian MCMC linear fitting method to fit this functional form to the data, and plot the mean and one standard deviation confidence fits in Figure 3.2. There is significant evolution in Φ^*_M. However, there is also large uncertainty in the evolution of Φ^*_M due to the spread of the data. We ignore evolution in the low-mass-end slope, since the lensing effect is dominated by the most massive galaxies. We also ignore evolution in $\overline{M}^*_S$, for which the evolution appears non-negligible but it has little effect on Equation (3.11). The redshift-dependent velocity dispersion function obtained in this way becomes

$$\Phi(\sigma, z) = p^{-1} \frac{\Phi^*_S(z)}{\sigma(1+z)^\beta} \left(\frac{\sigma}{\sigma^*}\right)^{p^{-1}(1+\alpha_S)} \exp\left[-\left(\frac{\sigma}{\sigma^*}\right)^{p^{-1}}\right] \tag{3.12}$$

with $p = 0.24 \pm 0.02$, $\beta = 0.20 \pm 0.07$ (obtained from the evolution of velocity dispersion in Figure 3.1), $\Phi^*_S(z) = 3.75 \pm 2.99 \times 10^{-3}(1+z)^{-2.46\pm0.53}$ Mpc^{-3}, $\alpha_S = -0.54 \pm 0.32$ and $\sigma^* = 216 \pm 18$ km s^{-1}. This was derived using the stellar mass-velocity dispersion relation above (Auger et al., 2010), including the scatter in the relation. At $z = 0$ recent well-measured velocity dispersion functions (e.g., Sheth et al., 2003; Choi et al., 2007) are within the uncertainties of this redshift-evolving relation, showing that our inferred evolution is consistent with direct measurements where they overlap.

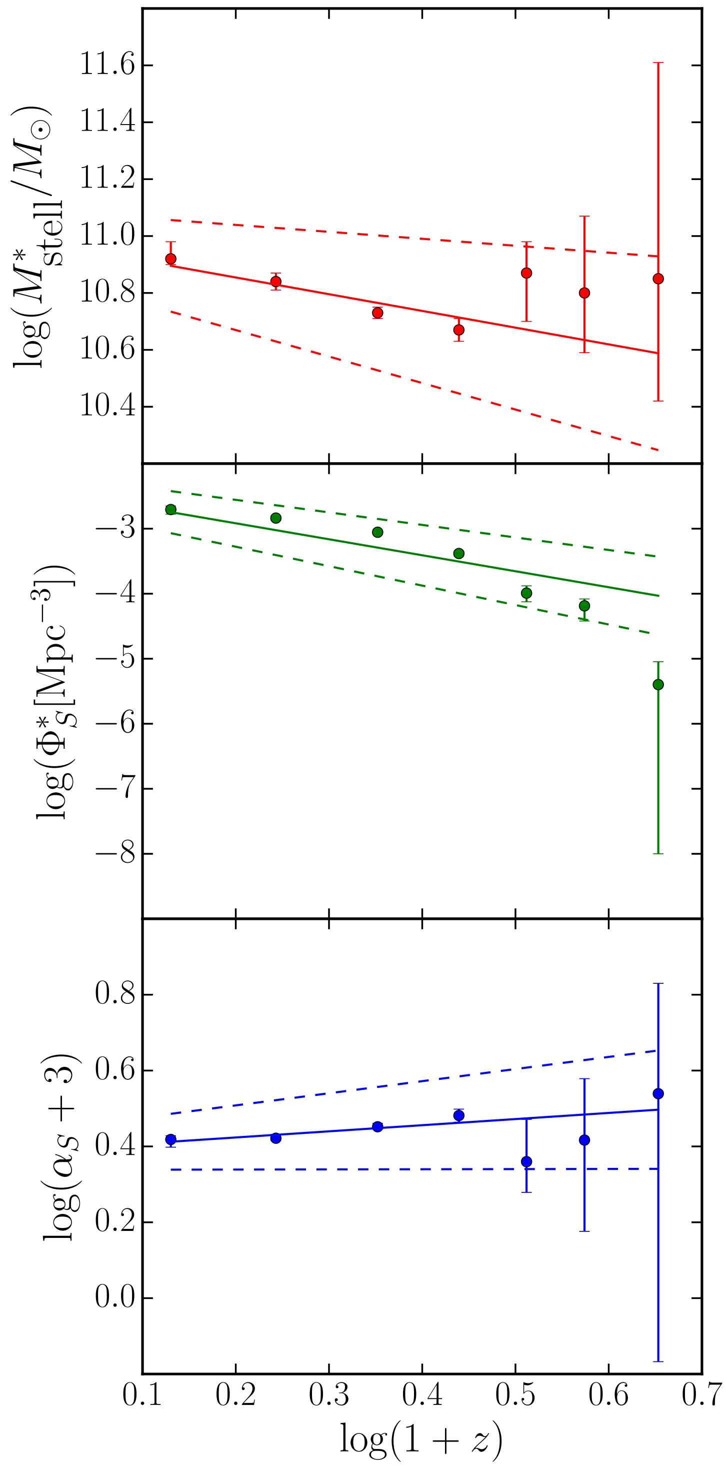

Figure 3.2: Redshift evolution of the best-fit single Schechter function parameters from Muzzin et al. (2013) for the stellar mass function of quiescent galaxies, allowing for evolution of α_S. Fits of the form $X_0(1+z)^a$ are plotted: the solid lines show the mean fit, dotted lines show the 1σ error on the data. Only $\Phi^\star_M$ shows significant evolution with redshift.

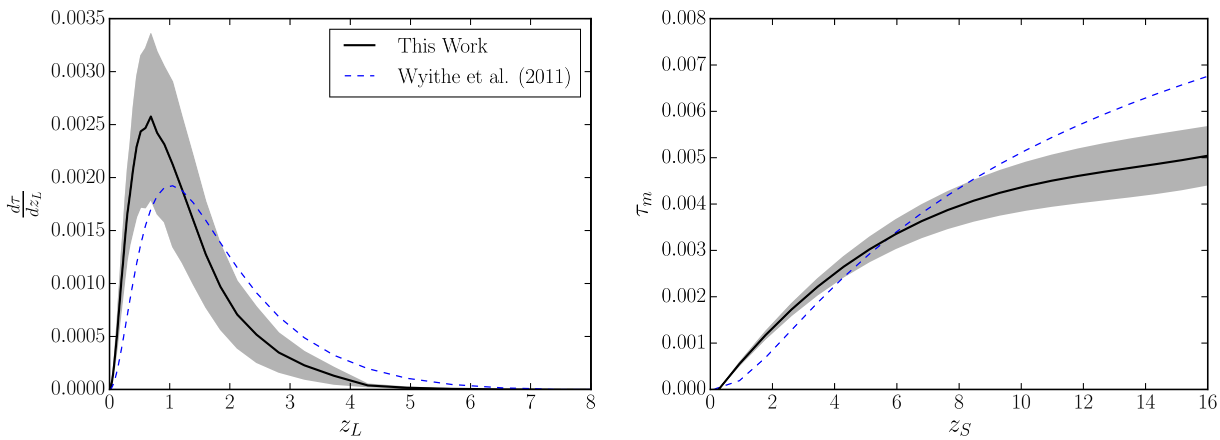

Figure 3.3: (Left) Contribution to the optical depth for a source at $z \sim 8$ to be multiply imaged as a function of the lens redshift, z_L, (solid black line) calculated using Equation (3.6), including the evolution of the deflector population with redshift (Section 3.4.1), for comparison we plot the contribution for a constant comoving density of lens galaxies (dashed blue line, Wyithe et al., 2011). **(Right)** Optical depth for multiple imaging as a function of source redshift, including evolution of the deflector population (solid black line). The gray shaded regions show the 1σ uncertainty bounds on the optical depth and its distribution, given the uncertainties in velocity dispersion and stellar mass evolution described in the text. The optical depth without redshift evolution of lens galaxies is also plotted for comparison (dashed blue line, Wyithe et al., 2011).

Using this redshift-dependent velocity dispersion function we compute the optical depth for strong lensing, and the distribution of the optical depth with lens redshift. In the left panel of Figure 3.3, now using the redshift evolving deflector population from Equation (3.6) and Equation (3.12), we see that the majority of the contribution to the optical depth is from lens galaxies at $z \lesssim 1.5$, which agrees with current observations of lensed high-redshift dropouts (Barone-Nugent et al., 2015; Schmidt et al., 2014a; Atek et al., 2015a). In the right panel of Figure 3.3 we plot the optical depth as a function of source redshift and find that including the redshift evolution of the deflector population reduces the optical depth at high redshift compared with the work in Wyithe et al. (2011) as expected by theoretical predictions (Barkana & Loeb, 1999), and it appears to start to flatten by $z_S \sim 10$.

Our estimated optical depth at $z < 8$ is in good agreement with values derived by an independent method by Barone-Nugent et al. (2015), and consistent with Wyithe et al. (2011) for $z \lesssim 8$. We note the optical depths presented in Barone-Nugent et al. (2015) are marginally higher than the results of this paper, but we can recover their optical depth using a steeper evolution of $\sigma(z)$. It is clear that the uncertainty in the evolution of velocity dispersion, which is the best indicator of the mass of lens galaxies, provides the largest uncertainty in determining the optical depth.

Finally, we compute the probability that high-redshift galaxies in a flux-limited sample have been multiply imaged. This is shown in Figure 3.4 as a function of limiting magnitude for each of the BoRG fields. As expected, the probability that a source in each field is multiply imaged, $F_{\rm mult}$ (Equation (3.9)) increases with the survey limiting magnitude, owing to the magnification bias. We estimate 3-15 % of observed sources brighter than $M^\star$ have been strongly lensed, this is consistent with the results of Barone-Nugent et al. (2015) who use an independent method to infer the lensed fraction.

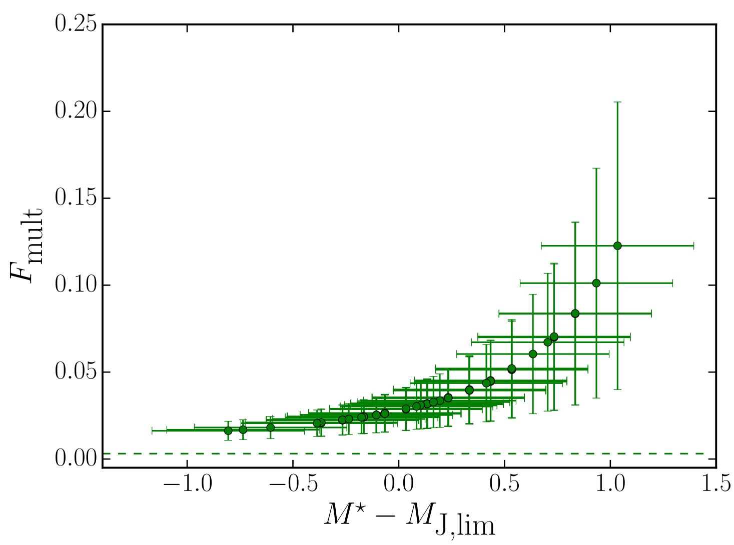

Figure 3.4: Multiply-imaged fraction (see Equation (3.9)) for $z \sim 8$ sources brighter than the J-band limiting magnitude in each of the BoRG fields, as a function of the UV characteristic magnitude, $M^\star$, including the evolution of the deflector population (Section 3.4.1). The probability of a high-redshift source being multiply imaged increases as the survey magnitude limit becomes brighter than $M^\star$. We expect very few intrinsically bright sources, so any bright source has a high likelihood of being significantly magnified according to the magnification bias. We have used the full MCMC chain for $M^\star$ from Schmidt et al. (2014b) and plot the mean value with errorbars of one standard deviation. The optical depth, the probability of multiple imaging without including the magnification bias factor, B (Section 3.3.4), is plotted as the green dashed line.

3.4.2 Identifying Significantly Magnified Sources

Whilst all the fields are subject to weak lensing, it is necessary to establish which of the individual sources experience multiple-imaging ($\mu > 2$), or are close enough to a deflector to experience an intermediate magnification ($1.4 < \mu < 2$). We expect strong lensing evens to be rare, but possible given the size of the BoRG survey. Among the BoRG sources, Barone-Nugent et al. (2015) presented a candidate strongly-lensed system in borg_0440-5244 (for naming conventions see Bradley et al., 2012). The candidate appears to be lensed by a foreground group with an Einstein radius of $1.49''$, corresponding to a velocity dispersion of ~ 300 km s^{-1}, producing a magnification of 3.7 ± 0.2 of the dropout. In this Section we describe a method to identify other potentially lensed sources in the catalogs and illustrate how to account for them systematically when estimating the LF.

For computational speed, we considered as potential deflectors only $z < 3$ objects within 18 arcseconds of the $z \sim 8$ dropouts in each field (the typical Einstein radius is of order 1-2 arcseconds for massive galaxies). The key quantity that we need to estimate the lensing strength is the velocity dispersion (Turner et al., 1984; Treu,Tommaso et al., 2010). Thus for every galaxy sufficiently close to a dropout, we estimate their velocity dispersions by comparing their photometry with that of samples of similar objects with spectroscopically-determined velocity dispersions. We selected galaxy samples with HST photometry in bands used in BoRG in order to estimate velocity dispersion based on our own photometry. As a comparison sample, we used data from Treu et al. (2005) and Belli et al. (2014b,a), as described in Section 3.2.2.

As described in Section 3.4.1, the velocity dispersion-stellar mass relation is believed to evolve weakly with redshift since $z \sim 2$ (e.g., van de Sande et al., 2013; Belli et al., 2014a; Bezanson et al., 2015), and galaxies will be intrinsically brighter at higher redshift due to younger stellar populations (e.g. Treu et al., 2005). We account for this by fitting an evolving Faber & Jackson (1976) relation to the comparison sample of the form $L \propto \sigma^4(1+z)^\beta$.

In practice, we bin the data in redshift, and fit a function of the form $\log \sigma = -0.1m + a \log(1+z) + b$ using a Bayesian MCMC estimation where σ is the velocity dispersion in km s^{-1}, m is apparent magnitude in a given band, z is galaxy redshift, and a and b are constants. We restrict our fit to galaxies with a measured velocity dispersion of at least 200 km s^{-1}, where samples are less affected by incompleteness and selection effects. We present the estimated parameters in Table 3.1 and fits to the data are shown in Figure 3.5.

Table 3.1: Correlation between velocity dispersion, redshift and apparent magnitude

Redshift	Band (m)	a	b
$z < 0.5$	F606W	2.26 ± 0.79	4.08 ± 0.12
$0.5 < z < 1.0$	F089M	0.93 ± 0.13	4.20 ± 0.03
$z > 1.0$	F160W	1.02 ± 0.15	4.12 ± 0.05

NOTE. – Fits of the form $\log \sigma = -0.1m + a \log(1 + z) + b$

The posterior probability distribution function of Einstein radii for each object are found using Equation (3.4), sampling over the full MCMC chain for the velocity dispersion. The redshifts of the objects were determined using the Bayesian Photometric Redshifts (BPZ) code, using a flat prior and the default parameters and templates (Benítez et al., 2004; Coe et al., 2006). All photometric redshifts for relevant foreground galaxies are well-fit by BPZ and have uncertainties in photometric redshift < 15%. The PDF for magnification, $p(\mu)$ is found by computing the magnification, μ (Equation (3.5)), at the position of the dropout given the distribution of Einstein radii found for each foreground object using the distribution for its velocity dispersion, $\sigma_{\rm inf}$ estimated from the fits in Table 3.1. The greatest source of error in this procedure is the magnitude-velocity dispersion-redshift relation: uncertainties in magnitude and redshift determination have small effects on the magnification PDFs in comparison to the uncertainty in velocity dispersion.

When the mean magnification produced by such a foreground object exceeds $\mu = 1.4$ we use the magnification PDF derived from the above procedure and treat the dropout as described in Section 3.6.2.2 in our calculations of the LF.

Using this method, we find one of the dropouts (borg_0436-5259_1233, presented in Bradley et al., 2012) has a magnification probability distribution consistent with strong lensing. This dropout is shown in the top left panel of Figure 3.6 and its estimated lensing properties are given in Table 3.2. The dropout appears to be magnified by a large galaxy at $z \sim 0.40$ with estimated velocity dispersion 294 ± 47 km s^{-1} (estimated from photometry via the empirical relation presented in Table 3.1). We estimate its magnification to be $\mu = 2.05 \pm 0.52$, the large uncertainty is due to the uncertainty in the relationship between apparent magnitude and velocity dispersion. If the dropout is indeed strongly lensed the counter image would be almost directly behind the center of the lens galaxy, and will be demagnified according to Equation (3.5), unfortunately making it impossible to detect. The dropout is very faint ($m_{\rm J} = 27.0 \pm 0.2$) and no significant elongation is detected in any of the observed bands but this dropout would be an excellent object for further investigation.

Three of the dropouts (borg_1301+0000_160, borg_1408+5503 and borg_2155-4411_341) experience mean magnification > 1.4. Postage stamps of these dropouts are shown in Figure 3.6 and their lensing properties are presented in Table 3.2. As described in Section 3.2.1 the fiducial BoRG contamination fraction is 42% (Bradley et al., 2012; Schmidt et al., 2014b) meaning that some of the sources presented here may be lower redshift interlopers (e.g., Hayes et al., 2012; Bouwens et al., 2014). Without further photometry and/or spectroscopy we cannot identify which of the sources are interlopers, but we note that the photometric redshift PDFs for these four sources (obtained from BPZ) all have strong peaks at $z \sim 8$, suggesting a higher probability than the average (58%) for these particular objects to be true $z \sim 8$ sources. Interestingly, borg_1301+0000_160 is the brightest dropout in the survey, with $m_J = 25.5 \pm 0.2$, and appears tangentially elongated in the J-band image (middle panel of Figure 3.6). This object is also a very interesting target for further imaging and spectroscopic follow-up.

We note that our method assigns a significantly lower velocity dispersion to the potential strong lens (borg_0440-5244_647) than the one estimated by Barone-Nugent et al. (2015) in their presentation of this object. They estimated the velocity dispersion of the deflector to be $\sigma \sim 300$ km s^{-1}, whereas our method estimates a mean velocity dispersion of $\sim 170 \pm 33$ km s^{-1}. This is likely to be because our method does not account for lensing by groups and clusters, while Barone-Nugent et al. (2015) suggest that this dropout is lensed by a group of at least two objects at $z \sim 1.8$, of which borg_0440-5244_647 is the largest. They estimated velocity dispersions of the deflector galaxies by using an abundance matching relation between mass and luminosity, derived from Cooray & Milosavljevic (2005), and measuring the angular size of the lensing objects. However, when using a redshift-dependent Faber & Jackson (1976) relation (Barone-Nugent et al., 2015) similar to ours (Table 3.1) they estimate the velocity dispersion of this single galaxy to be $\sim 180 \pm 46$ km s^{-1} (via private communication), which agrees with our result. Neglecting group-scale lensing is a potential limitation of our method, which may underestimate magnification in a few cases. However the impact on the overall estimation of the LF inference is negligible since the phenomenon is so rare.

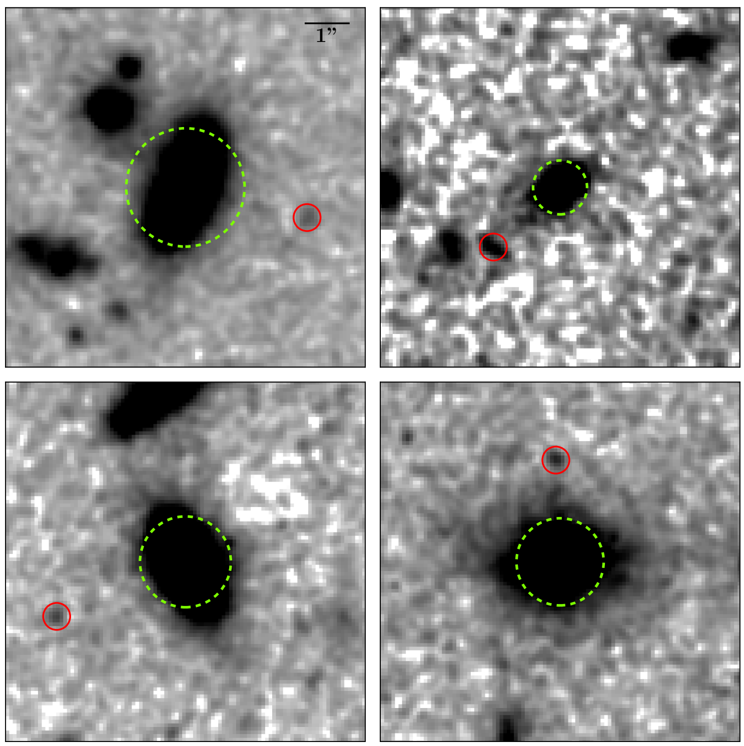

Figure 3.6: The four BoRG dropouts (from top left to bottom right: borg_0436-5259_1233, borg_1301+0000_160, borg_1408+5503 and borg_2155-4411_341) with significant magnification probabilities, shown in the F125W band with a Gaussian smoothing radius of 1 in 8″ boxes. The solid red lines outline the dropouts with a 0.3″ radius. The dashed green lines outline the potential foreground deflectors, with radius corresponding to the Einstein radius of an SIS deflector lensing a source at $z = 8$. The candidate strong lens system (borg_0436-5259_1233) is shown in the top left panel, and has an estimated magnification of $\mu = 2.05 \pm 0.52$. Interestingly, borg_1301+0000_160 (top right) is the brightest dropout in the BoRG survey. The parameters for all of these objects are given in Table 3.2.

Table 3.2: Strong and intermediate lensing parameters derived by estimating velocity dispersions of bright foreground galaxies close to $z \sim 8$ dropouts

Field	Dropout ID	J_{125} [a]	Foreground ID	z_f	Separation ($''$)	$\sigma_{\rm inf}$ (km s^{-1})	$\theta_{\rm ER}$ ($''$)	μ
borg_0436-5259	1233[b,c]	27.1 ± 0.2	1191	1.52 ± 0.03	2.79	294 ± 47	1.32 ± 0.40	2.05 ± 0.52
borg_1301+0000	160[d]	25.5 ± 0.2	144	1.14 ± 0.15	1.99	184 ± 31	0.60 ± 0.20	1.47 ± 0.30
borg_1408+5503	980[c]	27.0 ± 0.2	959	0.40 ± 0.06	3.11	193 ± 69	1.01 ± 0.70	1.54 ± 0.62
borg_2155-4411	341[c]	26.6 ± 0.2	244	0.74 ± 0.11	2.27	216 ± 22	0.97 ± 0.20	1.80 ± 0.33

NOTE. – [a] Total (AUTOMAG) apparent magnitude in the J-band of the dropout (Bradley et al., 2012). [b] Strongly-lensed candidate. [c] 5σ source. [d] 8σ source.

3.5 Weak Lensing

In this section we discuss the methods used to find the PDFs for magnification of a source at $z \sim 8$ by all intervening matter. We used the Pangloss code[2] developed by Collett et al. (2013) that generates lensing parameters for reconstructed lines-of-sight. We describe the production of magnification PDFs from simulation data from the Millennium Simulation (Springel et al., 2005) in Section 3.5.1 and in Section 3.5.2 we present the BoRG field weak magnification PDFs. Our PDFs agree well with other theoretical work at lower redshifts (Hilbert et al., 2007; Hilbert et al., 2009; Greene et al., 2013).

3.5.1 Estimating Magnification from Simulation Catalogs

The weak lensing reconstruction model developed by Collett et al. (2013) takes simulation halo catalogs and places halos in a three-dimensional grid, with each halo contributing convergence κ_i and shear γ_i along a line-of-sight to a source at a given redshift. Halos are modeled as truncated NFW profiles (Baltz et al., 2009):

$$\rho(r) = \frac{\rho_{\mathrm{NFW}}(r)}{1 + \left(\frac{r}{r_t}\right)^2} \tag{3.13}$$

where we used the truncation radius $r_t = 5r_{200}$, shown to be robust by Collett et al. (2013). Where r_{200} is the radius at which the mass density falls to 200 times the critical mass density of the universe. The convergence and shear derived from this profile are given in Baltz et al. (2009). Magnification due to all intervening deflectors along a line-of-sight is given by Equation (3.7).

We built PDFs for all lensing parameters by sampling over 10^3 of lines-of-sight. As described in Section 3.2.3 we used lightcones built from the Millennium Simulation (Henriques et al., 2012; Springel et al., 2005).

The simulated catalogs provide a list of halos with associated galaxies, but they do not include other dark structure, clumped in filaments and absent in voids. This missing matter

[2] `http://github.com/drphilmarshall/Pangloss`

will affect the overall density of the universe so it is necessary to take this into account when estimating κ and μ. We account for this by subtracting convergence from redshift slices so that the mean convergence along all lines-of-sight in the catalogs to a given redshift equals zero, and the mean magnification is unity, as they should be.

Following work by Suyu et al. (2010) and Greene et al. (2013), we compare lines-of-sight in the BoRG fields with simulation data based on relative density of objects. We define the overdensity parameter

$$\xi = \frac{n_i}{n_{\text{tot}}} \tag{3.14}$$

where n_i is the number of objects per unit area in each lightcone (or real field) and n_{tot} is the total number of objects divided by the total survey area. Given that the simulation catalogs are $\sim 500\times$ larger than the total BoRG survey area we expect them to give representative results.

We then calculate the number of objects per square arcsecond brighter than $m = 24$ in the J-band in each of the BoRG fields compared to the total number of objects above this flux limit in the whole survey. Similarly we calculate the overdensity of objects above the same limit in the simulated lightcones. Henriques et al. (2012) include mock photometry based on stellar population synthesis codes by Maraston (2005) which include J-band magnitudes. As shown in Figure 3.7, the distribution of overdensities for the observed data is within the range of that for simulated data. Finally, to generate magnification PDFs for a given BoRG field, we combine the magnifications from all simulation lines-of-sight which are within $\pm 2\%$ in overdensity of the observed value.

In Figure 3.8 we plot the magnification PDFs for a source at various redshifts over all lines-of-sight. As the source redshift increases, the peak of the distribution shifts to lower magnification, but the high-magnification tail becomes more important, such that the mean magnification over all lines-of-sight remains unity. We match results for $z < 6$ from Hilbert et al. (2007) well. It is clear that there is little change in the distribution between $z_S = 6$ and $z_S = 8$, as there are negligible numbers of large halos above $z > 5$.

In Figure 3.9 we plot the magnification PDFs for a variety of overdensities. The more overdense lines-of-sight produce a higher mean magnification, as expected, but also have a greater variance than the distributions for underdense lines-of-sight. This agrees well with the estimates at lower redshift by Greene et al. (2013).

3.5.2 BoRG Weak Lensing Magnification PDFs

The kernel density estimates (Rosenblatt, 1956; Parzen, 1962) fit to the magnification PDFs for all the BoRG fields are shown in Figure 3.10. As expected, the BoRG fields do not have significant over- or underdensities, but are rather typical of blank fields at $z \sim 8$, as shown in Figure 3.8.

There is significant motivation for the magnification PDFs to take a log-normal form. The 3D matter density distribution of the universe is well-described by a log-normal random field (Coles & Jones, 1991), and weak lensing probability distributions arise directly from the mass distribution. However, when accounting for the magnification bias in individual fields to infer the LF from the dropout sample (see Section 3.6) it was necessary to express the magnification distributions in a form that could easily convolve analytically with a Gaussian distribution (for more details see Appendix 3.9). For this we used a Bayesian MCMC approach to fit the distributions of magnification for each field as a linear sum of Gaussian functions.

3.6 Recomputing the LF

In this section we outline the method of estimating the $z \sim 8$ LF from the BoRG high-redshift candidates, taking the magnification bias into account.

Following Schmidt et al. (2014b), who did not account for the magnification bias when estimating the BoRG $z \sim 8$ LF, we use the Bayesian inference method devised by Kelly et al. (2008), which is described in Section 3.6.1 and in Appendix 3.9. In Section 3.6.2 we describe in more detail how we take into account the weak and intermediate lensing magnification.

3.6.1 Bayesian Estimation of the LF

As in Schmidt et al. (2014b), we assume that the intrinsic luminosity function is modeled by the Schechter function in Equation (3.3). In order to facilitate comparison with our previous work we use the sample of 38 BoRG Y-band dropouts and 59 additional fainter dropouts from the Hubble Ultra-Deep Field (HUDF) and Early Release Science (ERS) programs (Bouwens et al., 2011).

Bayesian statistics allows us to express the posterior probability that the LF is fit by a Schechter function with parameters $\theta = (\alpha, L^\star, \Psi^\star)$ given the observed luminosity $L_{\mathrm{J,obs}}$ of the dropouts in the J-band, and the non-detections in the V-band ($I_V = 0$), as the product of the prior on the Schechter parameters and the likelihood:

$$p(\theta \,|\, L_{\mathrm{J,obs}}, I_V = 0) \propto p(\theta) \times p(L_{\mathrm{J,obs}}, I_V = 0 \,|\, \theta) \tag{3.15}$$

This posterior probability can be expressed (see Appendix 3.9 for full details) as:

$$\begin{aligned} p(\theta \,|\, L_{\mathrm{J,obs}},\ I_{\mathrm{V}} = 0) \quad \propto \quad & p(\theta) \times C^{N_z}_{(1-f)n} \times C^{\frac{f}{1-f}N_z}_{fn} \\ \times \quad & \prod_l^{\mathcal{C}} \left[1 - \frac{A_l}{\overline{\mu}_l A_{\mathrm{sky}}}\, p(I = 1 \,|\, \theta) \right]^{\frac{N_z - (1-f_l)c_l}{1-f_l}} \\ \times \quad & \prod_i^n p(L_{\mathrm{J,obs},i} \,|\, \theta) \end{aligned} \tag{3.16}$$

Where we iterate over l fields with i $z \sim 8$ candidates. Here N_z is the number of high-z dropouts in the surveyed comoving cosmological volume, A_l is the area of the individual $\mathcal{C}$ fields in Schmidt et al. (2014b), which each contain c_l high redshift candidates ($n = \sum_l^{\mathcal{C}} c_l$). Each candidate has an assumed contamination fraction of f_l. We use a fiducial value for the contamination of 42% for the BoRG sample, the contamination fractions for the HUDF/ERS samples are included in the selection function, see Appendix 3.9, as described in Oesch et al. (2012); Bradley et al. (2012) and Schmidt et al. (2014b). Changing the contamination value in the range $f = 0 - 0.60$ effects the characteristic magnitude and the number density of the LF by less than their estimated 1σ uncertainties, and the change in the faint-end slope is comparable to its 1σ uncertainty (Bradley et al., 2012; Schmidt et al., 2014b). The Bayesian framework allows us to accurately estimate the LF parameters accounting for contamination. $A_{\rm sky}$ is the area of the full sky The C_b^a factors are binomial coefficients which are the fully correct method of modeling source counts.

We assume uniform priors on α, $\log_{10} L^\star$ and $\log_{10} N_z$. $p(I = 1 \,|\, \theta)$ is the probability distribution of an object making it into the dropout sample based on the photometric selection described in Schmidt et al. (2014b). $p(L_{\rm J,obs,\it i} \,|\, \theta)$ is the likelihood function for the observed J-band luminosity of the i'th object in the sample.

The last term includes marginalization over the magnification PDF:

$$p(L_{\rm J,obs} \,|\, \theta) = \int \int p(\mu)\, p(L_{\rm J,obs} \,|\, \mu L_{\rm J,true}) \times p(L_{\rm J,true} \,|\, \theta)\, dL_{\rm J,true}\, d\mu \tag{3.17}$$

In Appendix 3.9 we give the expanded expression of the posterior distribution from Equation (3.16) used when performing the LF parameter inference and describe the derivation and motivation for Equation (3.17). We refer to Appendix 3.9 and Schmidt et al. (2014b) for further details.

3.6.2 Including the Lensing Corrections

3.6.2.1 Analytic Form for Magnification PDFs

In order to make integration of Equation (3.17) computationally feasible we require a simple analytic form for $p(\mu)$ that will convolve simply with a Gaussian distribution (see Appendix 3.9). As described in Section 3.5.2, the weak lensing magnification PDF is well-fit by a log-normal distribution. However, this cannot be convolved analytically with a Gaussian.

Therefore, we fit the magnification PDFs from all regimes as a linear combination of Gaussian functions with different means and standard deviations. The weak lensing magnification PDFs (see Section 3.5.2) are well-fit by a combination of three Gaussian functions. The intermediate lensing PDFs (see Section 3.4.2) are also well-fit by a combination of three Gaussian functions.

3.6.2.2 Combining Lensing Regimes

All of the fields have a weak lensing magnification PDFs based on their overdensity (see Section 3.5), but we have also identified one strongly-lensed candidate and three dropouts close to large foreground galaxies that produce an intermediate magnification PDF (see Section 3.4.2).

To account for the magnification bias, we need to use the correct magnification PDF for each field. In the case when a strong or intermediate lens appears present, we split the field into two parts for the calculation of the posterior: one is a circle with radius 10 $\theta_{\rm ER}$ containing the dropout and the deflector, where we use the strong or intermediate lens magnification PDF. For the remainder of the field we use the weak lensing magnification PDF.

Whilst the total flux across the sky is conserved, locally over- or underdensities that produce magnification not only magnify fluxes, but also increases areas. Hence, the individual BoRG fields we observe have been magnified (or demagnified) from their true sizes. We account for this in the posterior probability Equation (3.16) by dividing the measured area of each field by the mean magnification in that field, $\overline{\mu}_l$ from the magnification PDFs. For weak lensing magnification PDFs $\langle \mu_l \rangle \sim 1$. For the intermediate lensing case $1.4 < \overline{\mu}_l < 2$ due to our selection process.

As magnification is most important for the bright-end of the LF, and negligible at the faint end, for simplicity and without loss of precision, we adopt $\mu = 1$ for the 59 fainter dropouts (Bouwens et al., 2011). Additionally, one of the BoRG fields (borg_1815_3244) is centered on the Galactic plane and is dominated by stars. We discard this field in our calculation of the LF.

3.7 Results

Using the framework described in Section 3.6 to account for the magnification bias we present our estimation of the $z \sim 8$ galaxy LF based on our sample of 97 $z \sim 8$ LBGs (described in Section 3.2). First, in Section 3.7.1 we compare our estimates of strong and intermediate lensing probabilities with the actual observations. Then, in Section 3.7.2 we carry out the inference of the $z \sim 8$ LF. Finally, in Section 3.7.3, we use our semi-analytical model of strong lensing optical depths described in Section 3.4 to predict the form of observed LFs at $z \geq 8$.

3.7.1 Strong and Intermediate Lensing Events in the BoRG Survey

The simple SIS strong lensing model described in Section 3.4.1 predicts the probability of $z \sim 8$ sources in the BoRG survey being multiply imaged to be $\sim 3-15\%$, increasing as the field limiting magnitude becomes brighter than $M^{\star}$. The majority of the BoRG fields have a multiple-image probability for high-redshift sources of $< 10\%$ (see Figure 3.4). We predict that 1-2 of the 38 BoRG Y-band dropouts may be strongly lensed.

One candidate strong lens system in BoRG was presented by Barone-Nugent et al. (2015), a rigorous search for strong lenses in all 71 BoRG fields as part of this work revealed one more candidate. Additionally, this search revealed three candidate intermediate lens systems, with $\mu > 1.4$. These candidates are presented in Figure 3.6 and Table 3.2. Whilst strong lensing creates larger magnification, the probability of encountering a strong lens along the line-of-sight is low: as shown in Figure 3.3 the optical depth is roughly $\tau \approx 0.31\%$ for a source at $z = 8$. The optical depth for intermediate lensing is much higher: for an object to experience intermediate lensing it must be within $3.5\theta_{\mathrm{ER}}$ of the foreground deflector, resulting in $\tau \approx 4\%$ for a source at $z = 8$. Thus, intermediate lensing offers an additional boost to the flux of high-redshift galaxies, and must be correctly accounted for in estimations of the LF.

3.7.2 Inference of the Intrinsic $z \sim 8$ LF

We estimate the $z \sim 8$ LF from the sample of 97 LBG described in Section 3.2, including the 38 $\mathrm{S/N_J} > 5$ objects from the BoRG survey, including the effects of magnification bias. We sample the posterior distribution function for the Schechter function parameters with an MCMC chain of 40 000 steps.

The results of the estimated LF are shown in Figure 3.11, and the correlations between the Schechter function parameters and their PDFs are shown in Figure 3.12. We plot the results of Schmidt et al. (2014b) for comparison in both figures. We see a small deviation from the uncorrected LF of ~ 0.15 mag at the limit of the brightest BoRG source, and there is negligible difference between the LFs at $M > -21$. The Schechter function parameters for the new LF are within the uncertainties of the estimation by Schmidt et al. (2014b), though we find a slightly fainter value of $M^\star$ and higher value of $\Psi^\star$ than Schmidt et al. (2014b). This is expected because of the slight deviation at the bright end of the LF, and there is a strong correlation between these parameters, as shown in Figure 3.12. It is clear that magnification bias is not a significant effect at this redshift and the luminosity range of the BoRG sources. This also demonstrates that although we predict $3 - 15\%$ of the BoRG sources are strongly lensed this does not affect the LF within the survey limits, as predicted in Section 3.3.4.

Our results are in good agreement with those of Fialkov & Loeb (2015) who use an independent semi-analytic method to show the effect of magnification bias is small below $M > -21.5$. Fialkov & Loeb (2015) predict that if the brightest observed galaxy has absolute magnitude $M_{\text{UV}} = -24.5$ - lying in the significantly distorted tail of the magnified LF (Wyithe et al. 2011) - there is a $\sim 13.3\%$ discrepancy in the normalization of a Schechter LF at $z \sim 8$ for sampled galaxies with $\mu_{\text{max}} = 2$ (i.e. only weak and intermediate lensing effects) compared to the intrinsic LF. Whilst this upper limit is several orders of magnitude brighter than currently observed, this demonstrates that it will be important to include the effects of magnification bias from weak and intermediate lensing in surveys that find extremely bright galaxies.

Table 3.3 summarizes the estimated Schechter function parameters for this LF in comparison with other recent LF estimates from the literature. We find that our fit parameters are in good agreement with the recent literature, demonstrating that magnification bias is not affecting current $z \sim 8$ LF observations. Note that our results have significantly smaller error bars than those of Finkelstein et al. (2015b), because their sample contains only 3 $z \sim 8$ galaxies brighter than $M = -21$, making their fit less well-constrained at the bright end.

Our results show that magnification bias does not affect current estimates of the LF

Table 3.3: Comparison of $z \sim 8$ Schechter LF parameters

Reference	$M^\star$	α	$\log_{10} \Psi^\star$ [Mpc^{-3}]
This work	$-19.85^{+0.30}_{-0.35}$	$-1.72^{+0.30}_{-0.29}$	$-3.00^{+0.23}_{-0.31}$
Finkelstein et al. (2015b)	$-20.89^{+0.74}_{-1.08}$	$-2.36^{+0.54}_{-0.40}$	$-4.14^{+0.65}_{-1.01}$
Bouwens et al. (2015b)	-20.63 ± 0.36	-2.02 ± 0.23	-3.68 ± 0.32
Schmidt et al. (2014b) 5σ	$-20.15^{+0.29}_{-0.38}$	$-1.87^{+0.26}_{-0.26}$	$-3.24^{+0.25}_{-0.34}$
Schmidt et al. (2014b) 8σ	$-20.40^{+0.39}_{-0.55}$	$-2.08^{+0.30}_{-0.29}$	$-3.51^{+0.36}_{-0.52}$
McLure et al. (2013)	$-20.12^{+0.37}_{-0.48}$	$-2.02^{+0.22}_{-0.23}$	$-3.35^{+0.28}_{-0.47}$
Schenker et al. (2013b)	$-20.44^{+0.47}_{-0.35}$	$-1.94^{+0.21}_{-0.24}$	$-3.50^{+0.35}_{-0.32}$

at $z \lesssim 8$ and therefore cannot explain the apparent flattening of the bright-end of the LF recently observed by Bowler et al. (2015, 2014) and Finkelstein et al. (2015b) at $z \sim 7-8$. Bowler et al. (2015, 2014) accounted for strong lensing of bright sources, but they still find a deviation of ~ 0.4 mag from a Schechter fit at $M = -22$. We predict a lensed fraction of $\sim 3-15\%$ for bright galaxies (Figure 3.4) from the BoRG survey which is essentially free of cosmic variance (Trenti & Stiavelli, 2008), so providing cosmic variance and contamination by lower redshift interlopers (Hayes et al., 2012; Bradley et al., 2012; Bouwens et al., 2014; Schmidt et al., 2014b) were correctly accounted for in the work of Bowler et al. (2015, 2014) and Finkelstein et al. (2015b), we expect the magnification bias to be negligible in the bright-end of these LFs. This lends credence to the interpretation that these observations may be the result of the changing intrinsic properties of galaxies at $z \gtrsim 7$, possibly due to changing dust fractions (Cai et al., 2014) and/or feedback processes (Somerville et al., 2012).

3.7.3 Predictions for $z > 8$ and Future Surveys

There is clear evolution in the LF for $z < 8$ (e.g. Bouwens et al., 2007; van der Burg et al., 2010; Bouwens et al., 2015b; Bowler et al., 2015; Finkelstein et al., 2015b), and this is expected to continue to higher redshifts. However, the processes which drive this evolution are not well-understood: the evolution is thought to follow hierarchical structure formation and the evolution of the halo mass function (Vale & Ostriker, 2004), but there are also important quenching processes that may reduce star formation in massive galaxies

(Schneider et al., 2006; Somerville et al., 2012), and changes in the amount of dust present in galaxies will affect the attenuation of flux. Thus there are a multitude of theoretical models for the evolution of the LF.

The gravitationally lensed LF (Equation (3.10)) exhibits a significant 'kick' in the bright-end tail for $M \lesssim -22$ at $z \sim 8$. This is just beyond the brightest BoRG objects, so it is unlikely that the BoRG survey observes the regime of magnification bias at the bright-end. This is in agreement with theoretical studies by Wyithe et al. (2011) and Fialkov & Loeb (2015). However, in upcoming wide-area surveys magnification bias presents a useful tool to test LF evolution models because it allows us to probe the bright end, where there are large theoretical uncertainties and the evolution is expected to be fast (Bowler et al., 2015).

In order to explore the range of possible scenarios, in Figure 3.13 we plot the predicted intrinsic (dashed lines) and observed (solid lines) LFs for a range of redshifts, comparing a variety of evolution models. We assume these models are the intrinsic LFs at a given redshift and used Equation (3.10) to estimate the observed LF. We plot the BoRG $z \sim 8$ LF (Schmidt et al., 2014b) for comparison. Additionally, we mark the comoving volumes and magnitude ranges accessible to future high-redshift surveys.

The top left panel shows the LF model from Bouwens et al. (2015b) which is an extrapolation from observations at $z < 10$. The top right panel shows the LF model from Finkelstein et al. (2015b) which is an extrapolation from observations at $4 < z < 8$. The bottom left panel shows the model developed by Muñoz (2012) which follows the evolution of the halo mass function, and includes dust attenuation. The bottom right panel is a model from Behroozi & Silk (2015) constructed from a comparison of the specific star formation rate to the specific halo mass accretion rate, and including dust models from Charlot & Fall (2000). The four models have significantly different behaviors at the bright end. While the Bouwens et al. (2015b) model has by construction a bright end that is very similar to that measured at lower redshifts, the Muñoz (2012) model has a very shallow bright end, and the Finkelstein et al. (2015b) and Behroozi & Silk (2015) models are in-between. As a result, the effects of magnification bias (which are stronger for the steeper LF) are very different: negligible in the Muñoz (2012) case and appreciable in the three other cases. However, the bright end of the Muñoz (2012) model is the easier one to test observationally, within reach of a James Webb Space Telescope medium depth, medium width survey (e.g. JWST MD Windhorst et al., 2006).

Except in the case of a very shallow bright end, we do not expect the magnification bias to be significant in our upcoming BoRG $z \sim 9, 10$ survey (HST Cycle 22, PI Trenti). In all cases, it is clear that surveys covering > 100 deg^2, e.g. Euclid and WFIRST, should find many bright $z > 8$ LBGs. We expect the observed high-redshift galaxy samples will be dominated by magnification bias in these surveys. We predict almost all $z \sim 8$ sources in Euclid will have been strongly lensed. The framework developed in this work will be crucial for determining the intrinsic luminosity of high-redshift sources found in such surveys.

Our results confirm the suggestion by Wyithe et al. (2011) that magnification bias will be important to probe the bright end of the LF at high redshift. However, we find that the magnitude of the effect is less pronounced than in that study, owing mostly to our accounting for the redshift evolution of the deflector population.

3.8 Summary and Conclusion

We have introduced a systematic way to account for the magnification bias in estimations of high-redshift LFs. The method involves estimating the probability density function for weak lensing magnification along a given line-of-sight by comparison with results from the reconstruction of simulated halo data, and by estimating the strong and intermediate lensing magnification PDF of dropouts due to massive deflector galaxies in close proximity to the dropout.

We applied this method to estimate the $z \sim 8$ LF from the 38 BoRG Y-band dropouts and 59 fainter dropouts from Bouwens et al. (2011). Our main results are summarized as follows:

(a) The probability of a BoRG $z \sim 8$ dropout being multiply imaged is $\sim 3 - 15\%$, increasing with limiting magnitude. This is consistent with finding two strongly-lensed dropouts in the BORG survey: the candidate system presented in Barone-Nugent et al. (2015), and the additional strongly-lensed candidate dropout in this paper. We also find three dropouts which may experience significant magnification without multiple imaging, consistent with our expectations.

(b) We extended the Bayesian formalism for the estimation of the LF parameters presented by Schmidt et al. (2014b) to account for the magnification bias. This involves marginalizing over the magnification PDFs for strong and weak lensing effects. The inferred Schechter function parameters are:

$$M^\star = -19.85^{+0.30}_{-0.35},$$

$$\alpha = -1.72^{+0.30}_{-0.29},$$

$$\log_{10} \Psi^\star[\mathrm{Mpc}^{-3}] = -3.00^{+0.23}_{-0.31},$$

These values do not differ significantly from estimates not accounting for the magnification bias.

(c) Thus magnification bias cannot be an explanation for the apparent flattening of the bright-end of the LF recently observed by Bowler et al. (2015, 2014) and Finkelstein et al. (2015b).

(d) The $z \sim 8$ LF appears significantly magnified for extremely bright galaxies ($M_{\mathrm{UV}} < -22$). Though current surveys have not observed such rare, luminous galaxies, future wide-field surveys will probe this region. For surveys > 100 deg^2, e.g. WFIRST, Euclid, we predict that samples of $z \gtrsim$ galaxies will be dominated by magnification bias.

(e) Magnification bias will be a useful tool to distinguish between high-redshift LF evolution models. In particular it could help determine whether the LF transitions from a Schechter form to a power-law form at high redshift, indicating significant changes in the astrophysical properties of those galaxies.

We thank Joey Muñoz for useful discussions and providing his LF evolution model; Peter Behroozi for providing his LF evolution model; Sirio Belli for providing photometry of the galaxies described in Belli et al. (2014b,a); and Stefan Hilbert for useful comments regarding the weak lensing simulations.

This work was supported by the HST BoRG grants GO-11700, 12572, and 12905. This paper is based on observations made with the NASA/ESA Hubble Space Telescope, obtained at the Space Telescope Science Institute.

This work made use of the freely available Pangloss code, written by Tom Collett and Phil Marshall. The Millennium Simulation databases used in this paper are publicly available through the German Astrophysical Virtual Observatory.

3.9 Appendix: Bayesian Framework for Estimating the luminosity function

We use Bayesian statistics to find the relationship between the prior probability of the $z \sim 8$ dropouts being galaxies with LF Schechter parameters $\theta = (\alpha,\ L^\star,\ \Psi^\star)$, and these parameters' posterior probability given the dropout candidates' detection threshold in the J-band, assuming their non-detection in the V-band. The posterior probability is given by:

$$p(\theta \,|\, L_{\mathrm{J,obs}}, I_V = 0) \propto p(\theta) \times p(L_{\mathrm{J,obs}}, I_V = 0 \,|\, \theta) \tag{3.18}$$

where the last term is the likelihood and $p(\theta)$ is the prior on the LF parameters. We will assume uniform priors on α and $\log_{10} L^\star$.

We can expand the expression for the posterior:

$$\begin{aligned} p(\theta \,|\, L_{\mathrm{J,obs}}, I_{\mathrm{V}} = 0) \;\; \propto \;\; & p(\theta)\, C^{N_z}_{n_z} \prod_l^{\mathcal{C}} \left[1 - A_l/A_{\mathrm{sky}}\, p(I = 1|\theta)\right]^{N_z - c_{l_z}} \times \prod_i^{n_z} p(L_{\mathrm{J,obs},i} \,|\, \theta) \\ & \times C^{N_c}_{n_c} \prod_l^{\mathcal{C}} \left[1 - A_l/A_{\mathrm{sky}}\; p(I = 1|\theta)\right]^{N_c - c_{l_c}} \times \prod_i^{n_c} p(L_{\mathrm{J,obs},i} \,|\, \theta) \end{aligned} \tag{3.19}$$

where the C^a_b terms are binomial coefficients which correctly model the distribution of source counts. N_z and N_c are the number of high-redshift sources given the intrinsic LF and the number of potential contaminants in the Universe respectively. We will assume a uniform prior on $\log_{10} N_z$. In the observed sample the number of high-redshift sources and contaminants are given by n_z and n_c. The total number of galaxies in the observed sample, n_t is given by their sum. We take the product over $\mathcal{C}$ individual observed fields where c_l represents the number of galaxies in the l'th field with n_t also given by the sum of c_l over all of the fields. The fraction of the sky covered by the l'th field is given by A_l/A_{sky}. The contamination fraction in each field, f_l is set at the fiducial value of 42% (Schmidt et al., 2014b; Bradley et al., 2012) for the BoRG sources, the contamination fraction for the fainter HUDF/ERS sources (Bouwens et al., 2011) is included in the selection function (see below).

The last term in Equation (3.19) is the likelihood for the i'th object in the sample. In Schmidt et al. (2014b) this was expressed as:

$$\begin{aligned} p(L_{\mathrm{J,obs}} \,|\, \theta) &= \int_0^\infty p(L_{\mathrm{J,obs}} \,|\, L_{\mathrm{J,true}})\, p(L_{\mathrm{J,true}} \,|\, \theta)\, dL_{\mathrm{J,true}} \\ &= \int_0^\infty \mathcal{N}(L_{\mathrm{J,obs}} \,|\, L_{\mathrm{J,true}},\, \delta L_{\mathrm{J,field}})\, \mathrm{gamma}(L_{\mathrm{J,true}} \,|\, \alpha, L^\star)\, dL_{\mathrm{J,true}} \end{aligned} \tag{3.20}$$

where we use $p(L\,|\,\theta) \propto \frac{\Psi(L,\theta)}{\Psi^\star}$ (see Equation (1) of Kelly et al. (2008)). The function $\mathrm{gamma}(L_{\mathrm{J,true}} \,|\, \alpha, L^\star)$ is related to the Schechter LF (Equation (3.3)) as $\mathrm{gamma}(L \,|\, \alpha, L^\star) = \frac{\Psi(L)}{\Psi^\star \Gamma(\alpha+1)}$.

$$\mathcal{N}'(L_{\mathrm{J,obs}} \,|\, L_{\mathrm{J,true}},\, \delta L_{\mathrm{J,field}}) = \frac{1}{\delta L_{\mathrm{J,field}}\sqrt{2\pi}} \exp\left[-\frac{(L_{\mathrm{J,obs}} - L_{\mathrm{J,true}})^2}{2\,\delta L_{\mathrm{J,field}}^2}\right] \tag{3.21}$$

represents the true luminosity inferred from the observations assuming a Gaussian measurement error with $\delta L_{\mathrm{J,field}}$ being the median photometric error in the J-band in the given field.

In order to include the effects of the magnification bias, we must integrate over the nuisance parameter $L_{\mathrm{J,mag}}$, which represents the luminosity of an object in the J-band, magnified above its true luminosity. Including this Equation (3.20) becomes:

$$p(L_{\mathrm{J,obs}} \,|\, \theta) = \int\int p(L_{\mathrm{J,obs}} \,|\, L_{\mathrm{J,mag}})\, p(L_{\mathrm{J,mag}} \,|\, L_{\mathrm{J,true}})\, p(L_{\mathrm{J,true}} \,|\, \theta)\, dL_{\mathrm{J,true}}\, dL_{\mathrm{J,mag}} \tag{3.22}$$

where $p(L_{\rm J,obs}\,|\,L_{\rm J,mag})$ is now the term with Gaussian measurement errors similar to Equation (3.21), given that we make observations of magnified luminosities:

$$\mathcal{N}(L_{\rm J,obs}\,|\,L_{\rm J,mag},\,\delta L_{\rm J,field}) = \frac{1}{\delta L_{\rm J,field}\sqrt{2\pi}}\exp\left[-\frac{(L_{\rm J,obs}-L_{\rm J,mag})^2}{2\,\delta L^2_{\rm J,field}}\right] \tag{3.23}$$

To find the probability that luminosity is magnified from its true luminosity, $p(L_{\rm J,mag}\,|\,L_{\rm J,true})$, we must integrate over the full magnification probability density:

$$p(L_{\rm J,mag}\,|\,L_{\rm J,true}) \;=\; \int p(L_{\rm J,mag}\,|\,\mu, L_{\rm J,true})\; p(\mu)\; d\mu \tag{3.24}$$

We can marginalize over $L_{\rm J,mag}$ in the first part of Equation (3.22):

$$\begin{aligned}
p(L_{\rm J,obs}\,|\,L_{\rm J,true}) \;&=\; \int p(L_{\rm J,obs}\,|\,L_{\rm J,mag})\; p(L_{\rm J,mag}\,|\,L_{\rm J,true})\; dL_{\rm J,mag} \\
&=\; \int\!\!\int p(L_{\rm J,mag}\,|\,\mu, L_{\rm J,true})\; p(\mu)\; p(L_{\rm J,obs}, L_{\rm J,mag},\,\delta L_{\rm J,field})\; d\mu\; dL_{\rm J,mag} \\
&=\; \int\!\!\int \delta(L_{\rm J,mag}-\mu L_{\rm J,true})\; p(\mu)\; \mathcal{N}(L_{\rm J,obs}\,|\,L_{\rm J,mag},\,\delta L_{\rm J,field})\; d\mu\; dL_{\rm J,mag} \\
&=\; \int p(\mu)\; \mathcal{N}(L_{\rm J,obs}\,|\,\mu L_{\rm J,true},\,\delta L_{\rm J,field})\; d\mu \\
&=\; \int p(\mu)\frac{1}{\delta L_{\rm J,field}\sqrt{2\pi}}\exp\left[-\frac{(L_{\rm J,obs}-\mu L_{\rm J,true})^2}{2\,\delta L^2_{\rm J,field}}\right]\; d\mu
\end{aligned} \tag{3.25}$$

Here we have used the Dirac delta function $\delta(L_{\rm J,mag}-\mu L_{\rm J,true})$ to map true luminosities to magnified luminosities. To make computation of Equation (3.19) feasible, we integrate Equation (3.25) analytically and want to remove any $L_{\rm J,mag}$ dependence we fit the magnification PDFs as a normalized linear combination of Gaussian terms with coefficients β_i centered on $\overline{\mu}_{\rm i,mag}$ with standard deviation $\sigma_{\rm i,mag}$:

$$p(\mu) = \sum_i^n \beta_i \frac{1}{\sigma_{\rm i,mag}\sqrt{2\pi}}\exp\left[-\frac{(\mu-\overline{\mu}_{\rm i,mag})^2}{2\,\sigma^2_{\rm i,mag}}\right] \tag{3.26}$$

Equation (3.25) can then be integrated analytically:

$$p(L_{\rm J,obs}\,|\,L_{\rm J,true}) = \sum_i^n \frac{\beta_i}{\sqrt{2\pi}}\frac{1}{\sqrt{\sigma^2_{\rm i,mag}L^2_{\rm J,true}+\delta L^2_{\rm J,field}}}\exp\left[-\frac{(L_{\rm J,obs}-\overline{\mu}_{\rm i,mag}L_{\rm J,true})^2}{2\,(\sigma^2_{\rm i,mag}L^2_{\rm J,true}+\delta L^2_{\rm J,field})}\right] \tag{3.27}$$

As solid angle is also magnified in gravitational lensing we must divide the measured field area A_l by the average magnification in each field $\overline{\mu}_{\rm l}$. If $\overline{\mu}_{\rm l} > 1$ the fields we observe appear larger than their true sizes.

We can therefore express Equation (3.19) as (see Schmidt et al., 2014b, for details):

$$
\begin{aligned}
& p(\theta \,|\, L_{\rm J,obs}, I_{\rm V} = 0) \propto \; p(\theta) \;\times\; C^{N_z}_{(1-f)n_t} C^{\frac{f}{1-f}N_z}_{fn_t} \\
& \times \prod_l^{\mathcal{C}} \left[1 - \frac{A_l}{\overline{\mu}_l A_{\rm sky}} \int_0^\infty \int_0^\infty dL_{{\rm J,true},l}\, dL_{{\rm J,obs},l}\, \mathcal{S}(L_{\rm J,obs,l})\, \mathcal{F}(L_{{\rm J,obs},l}, L_{{\rm J,true},l}) \right]^{\frac{N_z-(1-f_l)c_l}{1-f_l}} \\
& \times \prod_i^{n_t} \int_0^\infty \mathcal{F}(L_{{\rm J,obs},i}, L_{{\rm J,true},i})\, dL_{{\rm J,true},i} \qquad (3.28)
\end{aligned}
$$

Here we have defined $\mathcal{F}(L_{\rm J,obs}, L_{\rm J,true}) = p(L_{\rm J,obs} \,|\, L_{\rm J,true})\ {\rm gamma}(L_{\rm J,true} \,|\, \alpha, L^\star)$ and included the selection function $\mathcal{S}(L_{\rm J,obs})$. The selection function estimates the completeness of the source selection and has been obtain for each individual BoRG field as explained in Oesch et al. (2012); Bradley et al. (2012) and Schmidt et al. (2014b).

Thus, Equation (3.28) is the posterior probability distribution for a sample of n_t binomially distributed objects, assumed have an intrinsic Schechter LF of the form shown in Equation (3.3). The observed luminosity of each object is related to its true luminosity via a magnification PDF and an assumed Gaussian error distribution.

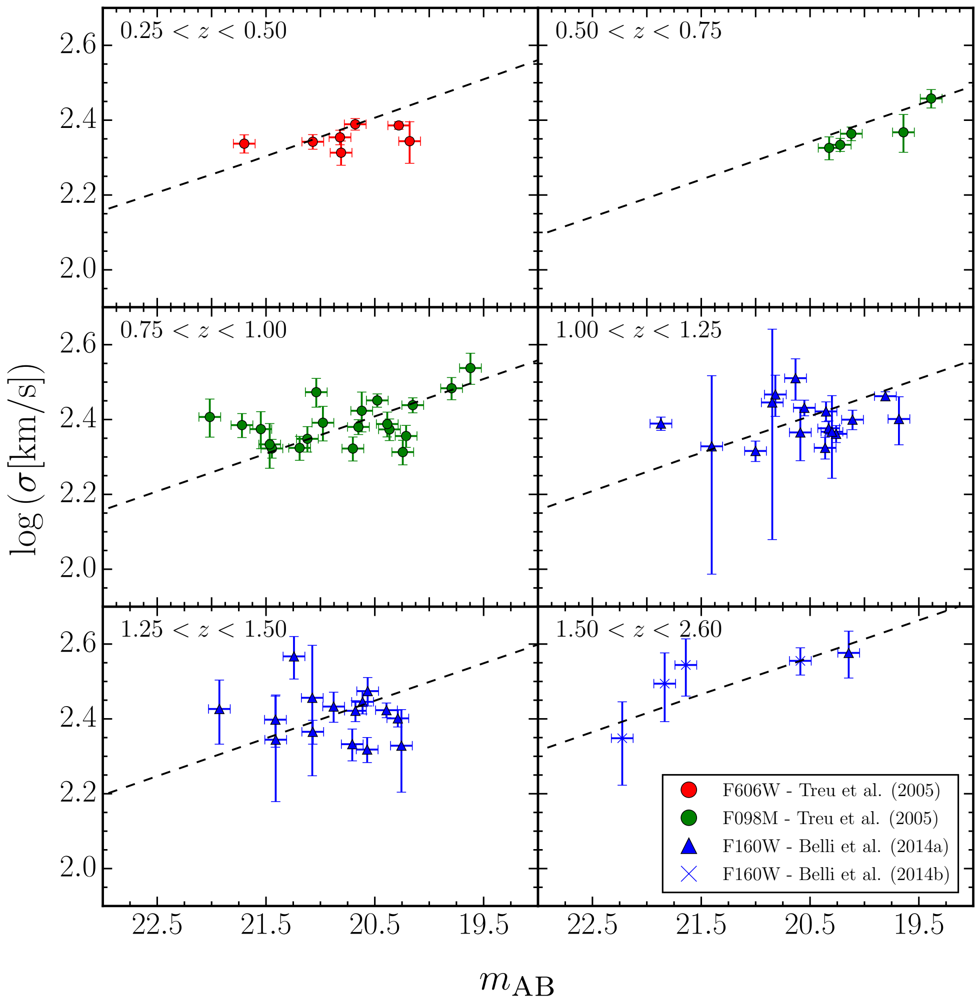

Figure 3.5: Evolving Faber-Jackson relation for massive galaxies with redshift. Data for $z < 1$ are from Treu et al. (2005) (red and green circles), data for $z > 1$ are from Belli et al. (2014b) (blue triangles) and Belli et al. (2014a) (blue crosses). Red points indicate apparent magnitude in the F606W band ($z < 0.5$), green points have magnitudes in the F098M band ($0.5 < z < 1$), and blue points are data with magnitudes in the F160W band ($z > 2$). Only galaxies with $\sigma > 200$ km s^{-1} were used in the fitting. The slope of the relation in velocity dispersion and magnitude is fixed at the Faber & Jackson (1976) result of $L \propto \sigma^4$. We fit the evolution with redshift, which changes the intercept of the line on the velocity dispersion axis. The uncertainty in magnitude is 0.1 mag which is a fiducial value given the fitting procedures. The black dashed lines shows the mean fit for the mean redshift of objects in each plotted bin. The fitting parameters are given in Table 3.1.

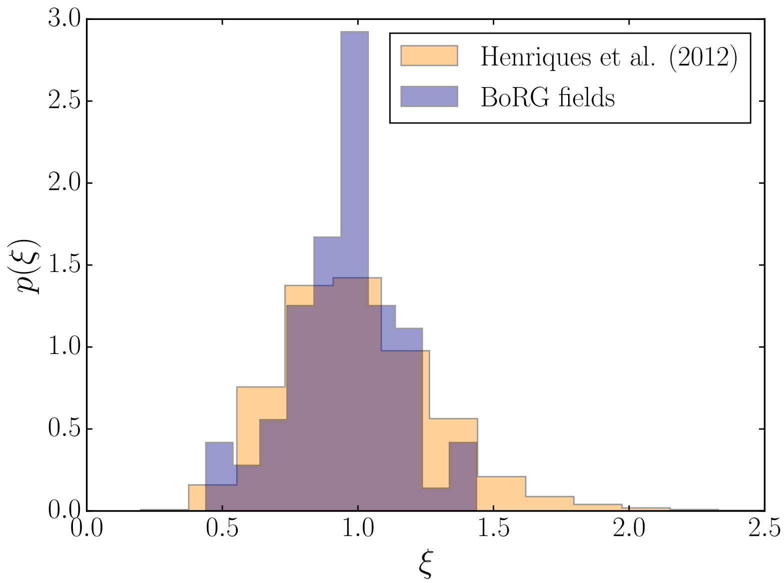

Figure 3.7: Comparison of the overdensity of lines-of-sight in the Millennium Simulation and the BoRG fields. $\xi = n_i/n_{\rm tot}$ where n_i is the number of objects per unit area above a certain flux limit in each lightcone (or real BoRG field) and $n_{\rm tot}$ is the total number of objects above the same flux limit divided by the total survey area. We use a flux limit of $m < 24$ in F125W (J-band).

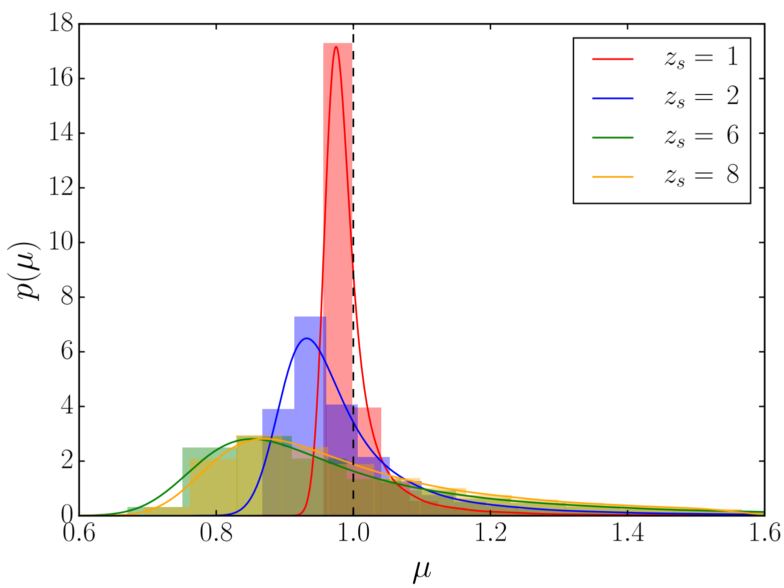

Figure 3.8: Probability distribution function for magnification for four values of source redshift. The dashed line marks the mean magnification of the universe. These results compare well with Hilbert et al. (2007). Due to the lack of significant mass between $z \sim 6$ and $z \sim 8$ there is little change in the distributions of magnification for sources at those redshifts, as the total convergence does not change much.

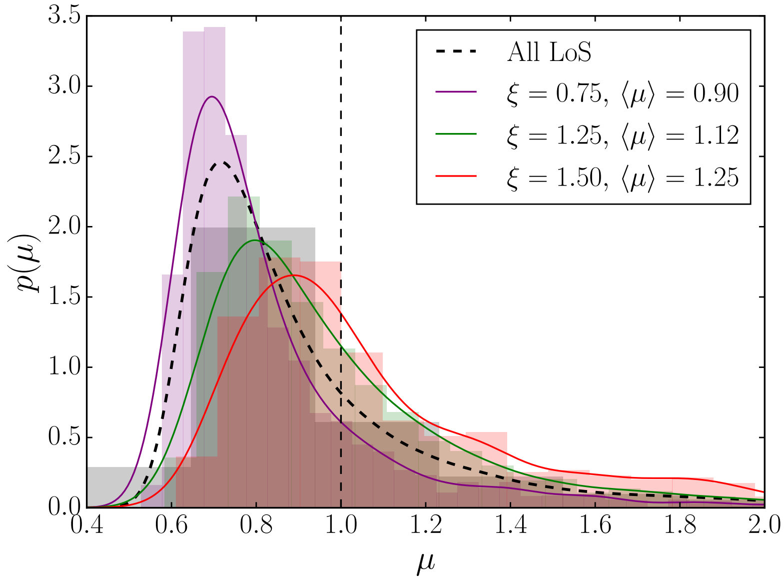

Figure 3.9: Probability distribution function for magnification for a range of values of overdensities for a source at $z = 8$. More overdense lines-of-sight are skewed towards higher magnification, with a broad distribution. More underdense lines-of-sight are skewed towards lower magnification, with a narrower distribution due to the deficit of intervening mass.

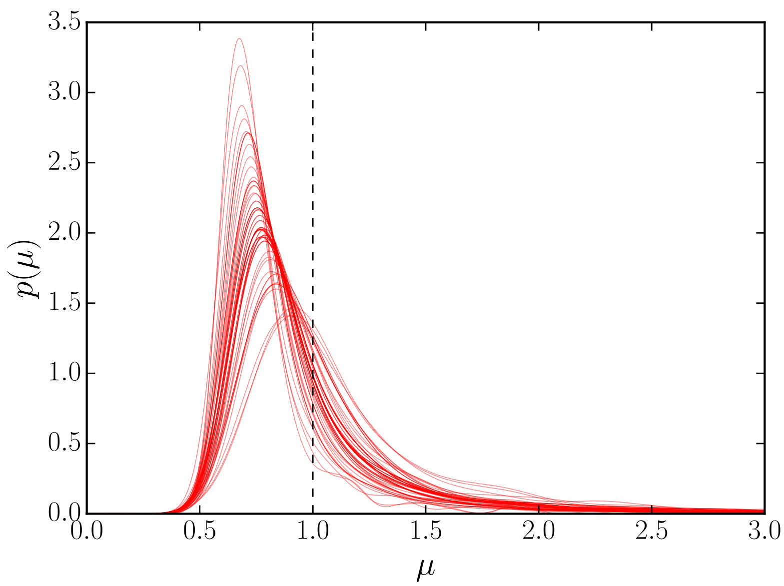

Figure 3.10: Probability distribution function for magnification for all of the BoRG fields, with a source at $z \sim 8$. The lines are kernel density estimations to the distributions. It is clear there is little range in overdensity for the BoRG fields.

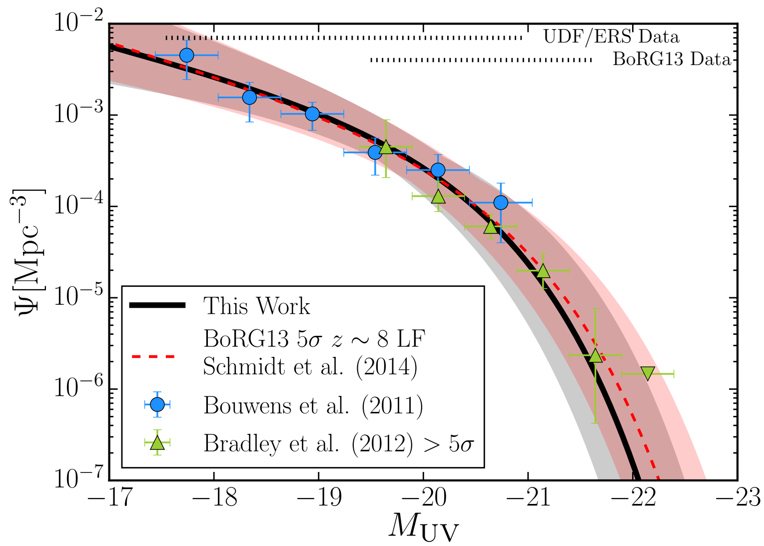

Figure 3.11: The intrinsic $z \sim 8$ LF, which is well-described by a Schechter (1976) function, including the magnification bias due to weak and intermediate lensing in all BoRG fields (solid black line). We plot the LF without the treatment of the magnification bias (Schmidt et al., 2014b) for comparison (dashed red line). The lines corresponds to the median values of the MCMC samples and the shaded regions correspond to the 68% confidence region of the samples. The LF estimated here is virtually indistinguishable from that of Schmidt et al. (2014b), demonstrating that magnification bias is not a significant effect at $z \sim 8$. The Schechter parameters for this LF are given in Table 3.3 along with literature values. The binned data from BoRG12 (Bradley et al., 2012) and the faint HUDF/ERS candidates (Bouwens et al., 2011) are also plotted as blue and green points respectively. The inverted green triangle denotes the brightest BoRG dropout. We note that the LF is estimated from the unbinned data.

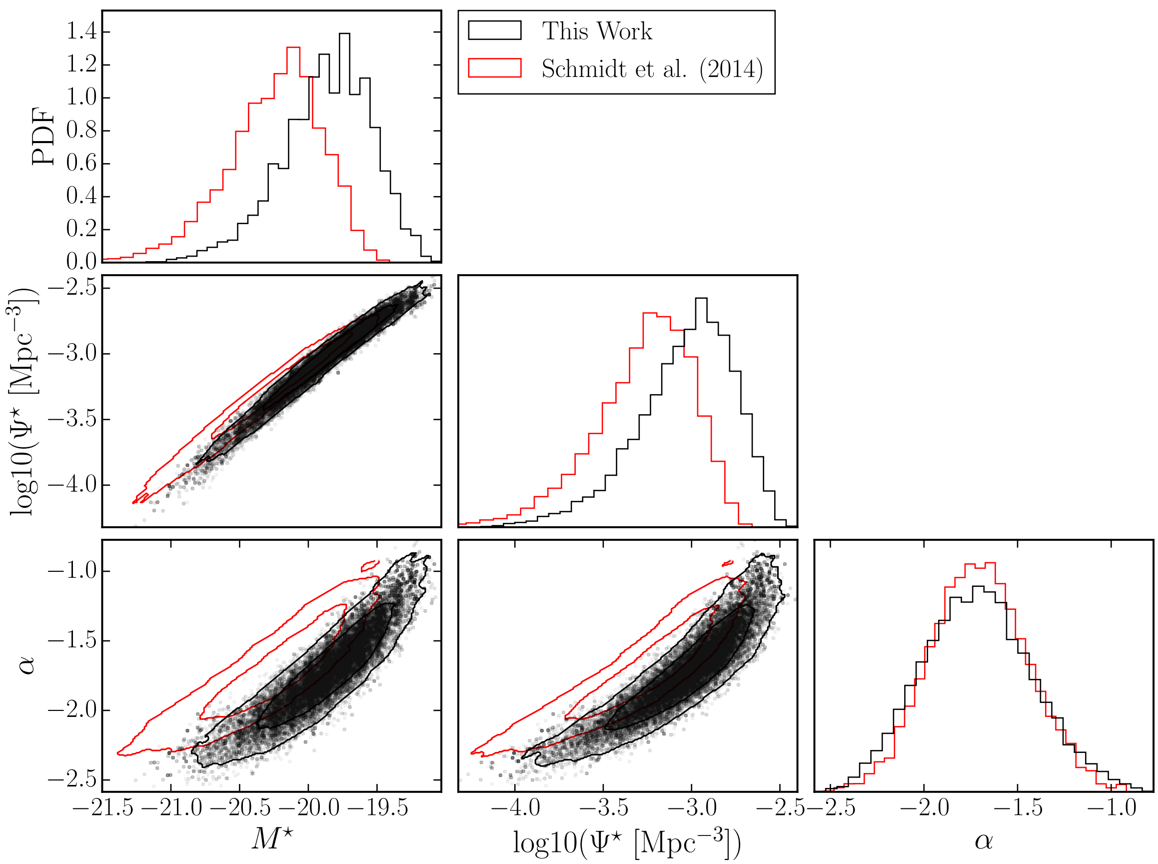

Figure 3.12: The correlations between the $z \sim 8$ LF Schechter function parameters (α, $M^{\star}$ and $\Psi^{\star}$) estimated from the BoRG dropouts including treatment of magnification bias (black), compared to the parameters obtained without the treatment of magnification bias (red, Schmidt et al., 2014b) with 1σ and 2σ confidence contours. There is clear correlation between all three parameters. The top panels show the marginalized PDFs for each parameter.

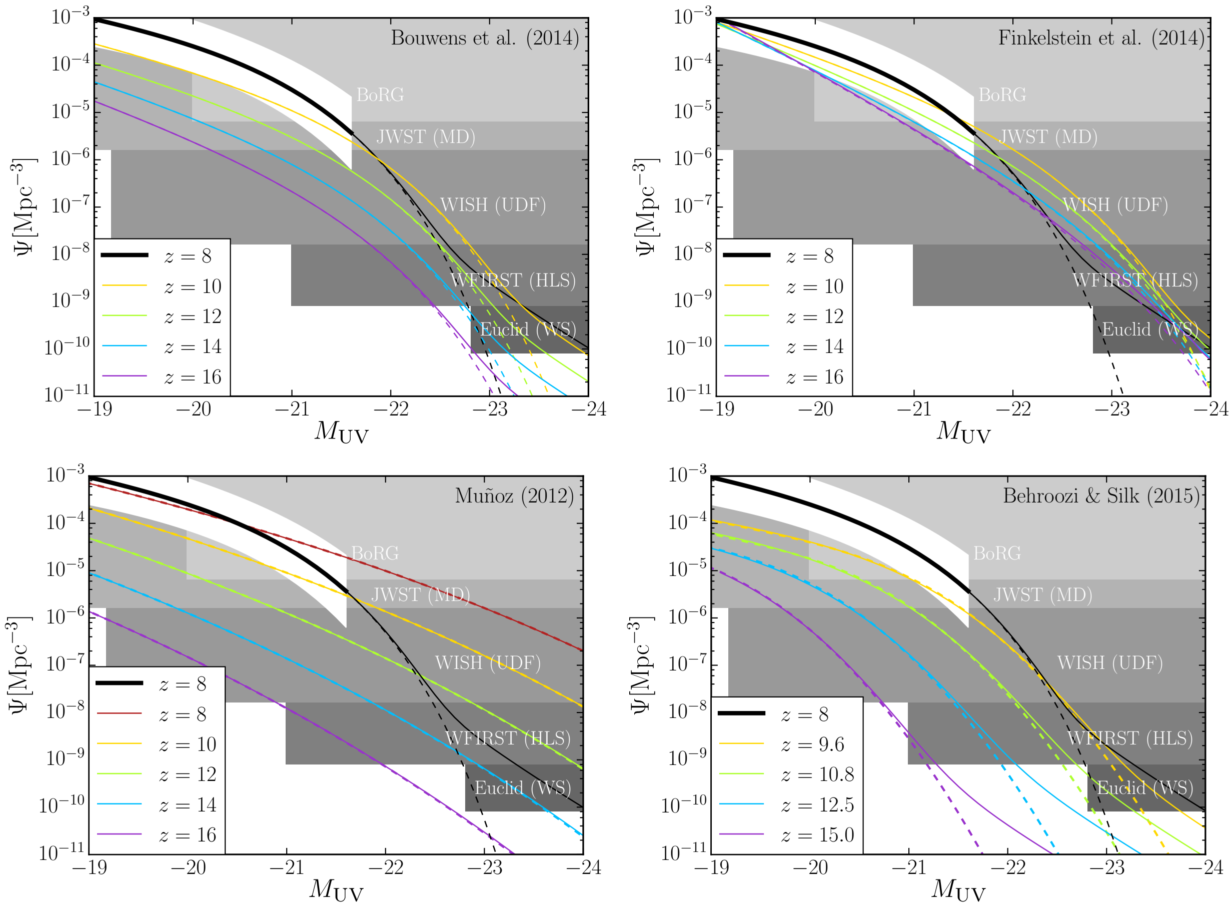

Figure 3.13: Predicted observed LFs for $z \geq 8$ redshifts. For $z = 8$ we use the Schechter LF from Schmidt et al. (2014b), plotted as a thick black line. The white band indicates the error on the Schechter function parameters, and the thin black line is the extrapolation of the LF beyond the observational limit. We show the regions of magnitude and volume observable by current and future surveys: the total BoRG survey including the $z \sim 8$ survey described in Section 3.2.1 and the upcoming BoRG $z \sim 9, 10$ survey (HST Cycle 22, PI: Trenti); the James Webb Telescope Medium Deep (JWST MD) (Windhorst et al., 2006); the Wide-Field Imaging Surveyor for High-Redshift Ultra-Deep Field (WISH UDF, http://wishmission.org/en/doc.html); the Wide-Field Infrared Survey Telescope High Latitude Survey (WFIRST HLS) (Spergel et al., 2013) and the Euclid Wide Survey (WS) (Laureijs et al., 2011). As explained in the text, BoRG does not survey enough area to observe the rarest bright sources which are most affected by magnification bias, but future wide-field surveys will be dominated by this effect. **(Top Left)** For $z > 8$ we use the LF model from Bouwens et al. (2015b) which is an extrapolation from $z \sim 10$. **(Top Right)** For $z > 8$ we use extrapolate the evolution of the Schechter function parameters over $4 < z < 8$ from Finkelstein et al. (2015b). **(Bottom Left)** For $z \geq 8$ we use the luminosity model from Muñoz (2012) which is based on the evolution of the halo mass function. These do not exhibit the sharp cut-off at the bright-end and are not affected by magnification bias. **(Bottom Right)** For $z > 8$ we use the LF evolution model from Behroozi & Silk (2015). The dashed lines indicate the intrinsic LFs, the solid lines are the observed LFs including the magnification bias calculated using Equation (3.10).

CHAPTER 4

The Universe is Reionizing at $z \sim 7$: Bayesian Inference of the IGM Neutral Fraction Using Lyα Emission from Galaxies

This paper was published as Mason, Treu, Dijkstra, Mesinger, Trenti, Pentericci, de Barros, & Vanzella (2018a), ApJ, 856, 2, and reproduced here with minor formatting changes.

We present a new flexible Bayesian framework for directly inferring the fraction of neutral hydrogen in the intergalactic medium (IGM) during the Epoch of Reionization (EoR, $z \sim 6-10$) from detections and non-detections of Lyman Alpha (Lyα) emission from Lyman Break galaxies (LBGs). Our framework combines sophisticated reionization simulations with empirical models of the interstellar medium (ISM) radiative transfer effects on Lyα. We assert that the Lyα line profile emerging from the ISM has an important impact on the resulting transmission of photons through the IGM, and that these line profiles depend on galaxy properties. We model this effect by considering the peak velocity offset of Lyα lines from host galaxies' systemic redshifts, which are empirically correlated with UV luminosity and redshift (or halo mass at fixed redshift). We use our framework on the sample of LBGs presented in Pentericci et al. (2014) and infer a global neutral fraction at $z \sim 7$ of $\overline{x}_{\rm HI} = 0.59^{+0.11}_{-0.15}$, consistent with other robust probes of the EoR and confirming reionization is on-going ~ 700 Myr after the Big Bang. We show that using the full distribution of Lyα equivalent width detections and upper limits from LBGs places tighter constraints on the evolving IGM than the standard Lyα emitter fraction, and that larger samples are within reach of deep spectroscopic surveys of gravitationally lensed fields and JWST NIRSpec.

4.1 Introduction

In the first billion years of the universe's history, intergalactic hydrogen atoms, formed at Recombination, were ionized (e.g., Robertson et al., 2015; Mesinger, 2016; Planck Collaboration et al., 2016b). This reionization of the intergalactic medium (IGM) was driven by the first sources of light: stars, and accretion disks around black holes, in galaxies. By understanding the process and timeline of reionization we can learn about the nature of these nascent populations of galaxies.

Ground-breaking observations within the last decade have provided significant information about this *Epoch of Reionization* (EoR, $z \sim 6-10$). With the largest near-IR instruments in space and on the ground we have now discovered large populations of galaxies at $z \gtrsim 6$ (e.g., McLure et al., 2010; Trenti et al., 2011; Bradley et al., 2012; Illingworth et al., 2013; Schenker et al., 2013b; Schmidt et al., 2014a; Yue et al., 2014; Bouwens et al., 2015b; Finkelstein et al., 2015b; Calvi et al., 2016). Young stars in these galaxies are likely the primary sources of reionizing photons (e.g., Lehnert & Bremer, 2003; Bouwens et al., 2003; Yan & Windhorst, 2004; Bunker et al., 2004; Finkelstein et al., 2012a; Robertson et al., 2013; Schmidt et al., 2014a), though a contribution from AGN cannot be excluded (Giallongo et al., 2015; Madau & Haardt, 2015; Onoue et al., 2017): we do not know if sufficient hard ionizing photons escape from galaxies as we do not fully understand the interactions between these early galaxies and their surrounding media.

Absorption features in quasar spectra suggest reionization was largely complete by $z \sim 6$ (<1 Gyr after the Big Bang, e.g., Fan et al., 2006; Schroeder et al., 2013; McGreer et al., 2015; Venemans et al., 2015), whilst the electron scattering optical depth to the CMB (Planck Collaboration et al., 2016a,b; Greig & Mesinger, 2017b) indicates significant reionization was occurring at $z \sim 7.8-8.8$. A robust constraint, albeit from a single sightline, on on-going reionization comes from the absorption spectrum of the $z=7.1$ quasar ULAS J1120+0641, where Greig et al. (2017) recently inferred a neutral fraction of $\overline{x}_{\text{HI}} = 0.40^{+0.21}_{-0.19}$.

To produce a timeline of reionization consistent with the evolution suggested by observations generally requires optimistic assumptions about the numbers of as-yet undetected ultra-faint galaxies (Shull et al., 2012; Robertson et al., 2013; Mason et al., 2015a) – which are likely the hosts of high redshift gamma-ray bursts (Kistler et al., 2009; Trenti et al., 2012a), and/or the production efficiency and escape fraction of hard ionizing photons (Bouwens et al., 2015a; Ma et al., 2015; Grazian et al., 2017; Vanzella et al., 2017). However, the timeline of reionization is not well-constrained, especially beyond $z \gtrsim 6$ where quasars become extremely rare (Fan et al., 2001; Manti et al., 2016).

Into the EoR, a powerful probe of the IGM is the Lyman alpha (Lyα, 1216Å) emission line from galaxies, which is strongly attenuated by neutral hydrogen (Haiman & Spaans, 1999; Malhotra & Rhoads, 2004; Santos, 2004; Verhamme et al., 2006; McQuinn et al., 2007a; Dijkstra, 2014). Observing Lyα at high redshift gives us key insights into both the IGM ionization state and galaxy properties, and, whilst quasars probably live in the densest regions of the early universe (Mesinger, 2010), observing galaxies enables us to trace reionization in cosmic volumes in a less biased way.

Dedicated spectroscopic follow-up of young star-forming galaxies at high redshift, identified as photometric dropouts (Lyman break galaxies, hereafter LBGs) combined with low redshift comparison samples (Hayes et al., 2013; Yang et al., 2016) show that the fraction of LBGs emitting Lyα increases with redshift (Stark et al., 2010; Curtis-Lake et al., 2012; Hayes et al., 2011; Cassata et al., 2015), likely because the dust fraction in galaxies decreases (e.g., Finkelstein et al., 2012b; Bouwens et al., 2014) which reduces the absorption of Lyα (Hayes et al., 2011). However, there is a potential smoking gun signature of reionization at $z > 6$: recent observations show a declining fraction of Lyα emitters in the LBG population with redshift (e.g. Fontana et al., 2010; Stark et al., 2010; Caruana et al., 2012; Treu et al., 2013; Caruana et al., 2014; Faisst et al., 2014; Tilvi et al., 2014; Schenker et al., 2014; Pentericci et al., 2014), as well as an evolving Lyα luminosity function (e.g., Ouchi et al., 2010; Zheng et al., 2017; Ota et al., 2017; Konno et al., 2017), suggesting an increasingly neutral, but inhomogeneous, IGM (Dijkstra et al., 2014; Mesinger et al., 2015).

Robust conversions from observations to the IGM state are challenging, however, and current constraints from Lyα emission measurements show some tension. The sudden drop in Lyα emission from LBGs suggests a high neutral fraction at $z \sim 7$, $\overline{x}_{\text{HI}} \gtrsim 0.5$ (Dijkstra et al., 2014; Choudhury et al., 2015; Mesinger et al., 2015), whereas measurements from clustering of Lyα emitters at $z = 6.6$ imply a lower neutral fraction ($\overline{x}_{\rm HI} \lesssim 0.5$, Ouchi et al., 2010; Sobacchi & Mesinger, 2015). These constraints are consistent within 1σ but the qualitative tension motivates a more thorough treatment of the properties of Lyα emitters during reionization. Given this, and that tight constraints on the reionization history can constrain properties of the sources of reionization (e.g., the minimum mass/luminosity of galaxies, and the escape fraction of ionizing photons, Bouwens et al., 2016a; Mitra et al., 2015; Greig & Mesinger, 2017a,b), we aim to develop a robust framework for inferring the ionization state of the IGM from observations Lyα from galaxies.

The conversion from the evolving transmission of Lyα emission from galaxies to a constraint on the IGM ionization state is non-trivial and involves physics from pc to Gpc scales. Multiple observations (e.g., Treu et al., 2013; Pentericci et al., 2014; Becker et al., 2015) and simulations (Furlanetto et al., 2006; McQuinn et al., 2007b) suggest reionization of the IGM is likely a 'patchy' process, with large ionized bubbles growing faster in overdense regions filled with star-forming galaxies. An accurate model of reionization must include realistic large-scale IGM structure (Trac et al., 2008; Iliev et al., 2014; Sobacchi & Mesinger, 2014).

Irrespective of reionization, as a highly resonant line, Lyα photons experience significant scattering within the interstellar medium (ISM) of their host galaxies, and absorption within the circumgalactic medium (CGM) which affects the visibility of emission (Verhamme et al., 2006, 2008; Dijkstra et al., 2007; Laursen et al., 2011). ISM effects on Lyα are likely to correlate with galaxy mass and star formation rate (SFR) via dust absorption, neutral hydrogen column density and covering fraction, and outflows (Erb et al., 2014; Erb, 2015; Oyarzún et al., 2016; Hayward & Hopkins, 2017; Yang et al., 2017).

UV faint galaxies ($M_{\rm UV} > M^* \sim -20$) tend to be the strongest Lyα emitters at all redshifts due to lower dust masses and neutral hydrogen column densities (Yang et al., 2016, 2017). However, a small sample of UV bright galaxies at $z > 7.5$ with strong Spitzer/IRAC excesses have recently been observed with Lyα (Finkelstein et al., 2013; Roberts-Borsani et al., 2016; Oesch et al., 2015; Zitrin et al., 2015b; Stark et al., 2017), at a redshift when the IGM is expected to be significantly neutral (Planck Collaboration et al., 2016b; Greig

& Mesinger, 2017b). Are these objects a new class of highly ionizing galaxies (Stark et al., 2017), emitting Lyα with very high EW so some flux is still observable even after attenuation in the IGM? Do they inhabit large ionized bubbles in the IGM at high redshift? How do different halo environments and ISM properties affect the impact on reionization on galaxies?

Dijkstra et al. (2011) first considered the effects of the ISM on Lyα photons during reionization, using shell models (e.g. Verhamme et al., 2006; Gronke et al., 2015a) to mimic the ISM radiative transfer, and showed ISM effects had a large impact on the transmission of Lyα photons through the reionizing IGM. As described above, the Lyα photons' journey through the ISM depends on galaxy properties. However, previous constraints on the evolving transmission of Lyα emission at $z \gtrsim 6$ have limited treatment of this effect: Dijkstra et al. (2011) and Mesinger et al. (2015) parametrically accounted for the ISM but assumed the LBG galaxy population is homogeneous; Jensen et al. (2013) obtained similar results combining cosmological hydro-simulations of reionization with a different sub-grid prescription for Lyα radiative transfer in the ISM; simpler models do not treat the ISM but consider two bins of UV bright and faint galaxies (e.g., Treu et al., 2012).

In this paper we introduce a flexible modeling framework to enable Bayesian inference of the IGM neutral fraction from detections and non-detections of Lyα from LBGs. Our framework includes realistic cosmological IGM simulations which contain the large-scale structure of the reionizing IGM. We generate 1000s of sightlines through these simulations to halos born from the same density field as the IGM, and populate these halos with simple, but realistic, ISM properties drawn from empirical models, which, for the first time in a reionization model, are linked to observable galaxy properties.

Our model asserts the impact of the ISM on the Lyα line profile is the most important galaxy property to consider when trying to make accurate inferences about reionization. In our model we include this effect via the peak velocity offset of the Lyα line profile from systemic (Δv), which correlates with galaxy mass (or UV magnitude at fixed redshift), for which there are a handful of measurements at $z \gtrsim 6$ (Pentericci et al., 2016; Bradač et al., 2017; Mainali et al., 2017; Stark et al., 2017). Galaxies with high Lyα velocity offsets have higher probabilities of transmitting Lyα photons through the IGM. This effect is robustly accounted for in our model as a nuisance parameter in our inference.

The paper is structured as follows: in Section 4.2 we explain the ISM, CGM, and IGM radiative transfer modeling components of our model; in Section 4.3 we describe our flexible Bayesian framework for inferring the neutral fraction $\overline{x}_{\rm HI}$; in Section 4.4 we give our results including key insights from the model, the inferred value of $\overline{x}_{\rm HI}$ from current observations and forecasts for spectroscopic surveys with the James Webb Space Telescope (JWST); we discuss our results in Section 4.5 and present a summary and conclusions in Section 4.6.

We use the Planck Collaboration et al. (2016a) cosmology where $(\Omega_\Lambda, \Omega_{\rm m}, \Omega_{\rm b}, n, \sigma_8, H_0) =$ (0.69, 0.31, 0.048, 0.97, 0.81, 68 km s^{-1} Mpc^{-1}), and all magnitudes are given in the AB system.

4.2 ISM, CGM, and IGM Radiative Transfer Modeling

Lyα photons are significantly affected by the neutral hydrogen they encounter within the ISM of their source galaxies, their local CGM, and the IGM through which they travel to our telescopes. To make constraints in the Epoch of Reionization we must model Lyα radiative transfer in all three media. Here we describe the combination of empirical formalisms and numerical simulations to model the effect of the ISM (Section 4.2.1) and the CGM and IGM (Section 4.2.2) on Lyα transmission.

4.2.1 ISM Lyα radiative transfer

Lyα photons are produced predominantly via recombination in H II regions around young stars and have a high cross-section for resonant scattering (for a detailed review see Dijkstra, 2014). As the ISM of individual galaxies contains a large amount of neutral hydrogen gas to escape the ISM Lyα photons must diffuse both spatially *and* spectrally (e.g., Shapley et al., 2003; McLinden et al., 2011; Chonis et al., 2013; Mostardi et al., 2013; Song et al., 2014). This produces the fiducial double-peaked Lyα lineshape, for which the red (blue) peak is enhanced for outflows (inflows) (Zheng & Miralda-Escude, 2002; Verhamme et al., 2006).

In this work, we model the Lyα lineshape *after transmission through the ISM* as a Gaussian, centered at a velocity offset Δv from the systemic redshift of the galaxy (due to scattering through the ISM, described in Section 4.2.1.1) with a velocity dispersion σ_α (due to scattering and thermal broadening in the ISM, described in Section 4.2.1.2). We refer to this lineshape as 'intrinsic', examples are shown as dotted black lines in Figure 4.1. As described below in Section 4.2.2 even after reionization residual neutral gas in the IGM and CGM will absorb all blue flux at $z \gtrsim 6$.

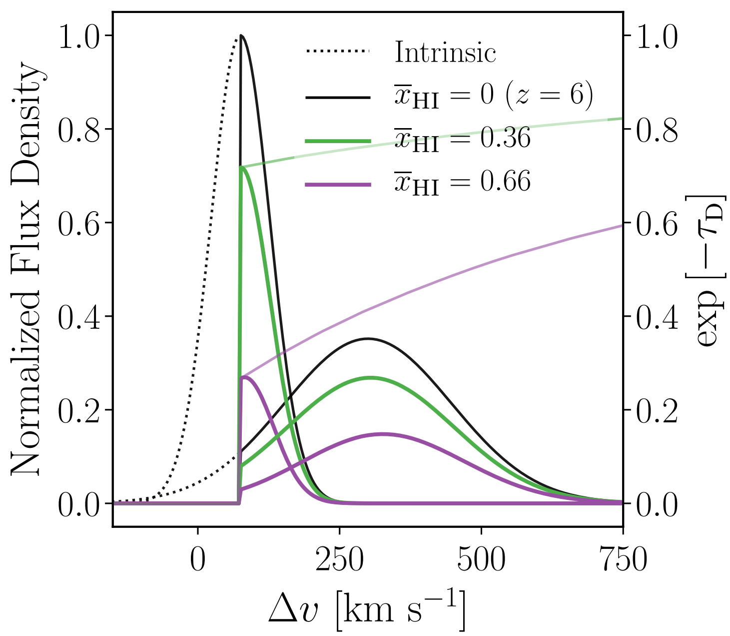

Figure 4.1: The effect of the IGM on simulated line profiles. We show two example intrinsic line profiles (black dotted lines), with peak velocity offsets of 75 and 300 km s^{-1}, with flux densities normalized to that of the line at 75 km s^{-1}. This is the line *after transmission through the ISM*. The solid black shows the lineshape in an ionized universe at $z \sim 6$ where *all flux bluer than the halo's circular velocity is resonantly absorbed* by neutral hydrogen in the local CGM/IGM (i.e. they experience only $\tau_{\rm HII}$). The colored lines show the emission lines after transmission through a reionizing IGM with damping wing optical depths $\tau_{\rm D}$, where the median IGM attenuation is also plotted (lighter line, corresponds to right axis). Lines emitted with high velocity offsets are less attenuated by the IGM: for the line with $\Delta v = 75$ km s^{-1} $\sim 70\%$ of the emitted flux is observed for $\overline{x}_{\rm HI} = 0.36$ (green), for the line with $\Delta v = 300$ km s^{-1} this fraction rises to $\sim 75\%$. For $\overline{x}_{\rm HI} = 0.66$ (purple) $\sim 30\%$ of the total flux is transmitted from the line with $\Delta v = 75$ km s^{-1} whilst $\sim 40\%$ is emitted for the line at $\Delta v = 300$ km s^{-1}.

4.2.1.1 Modeling Lyα velocity offsets

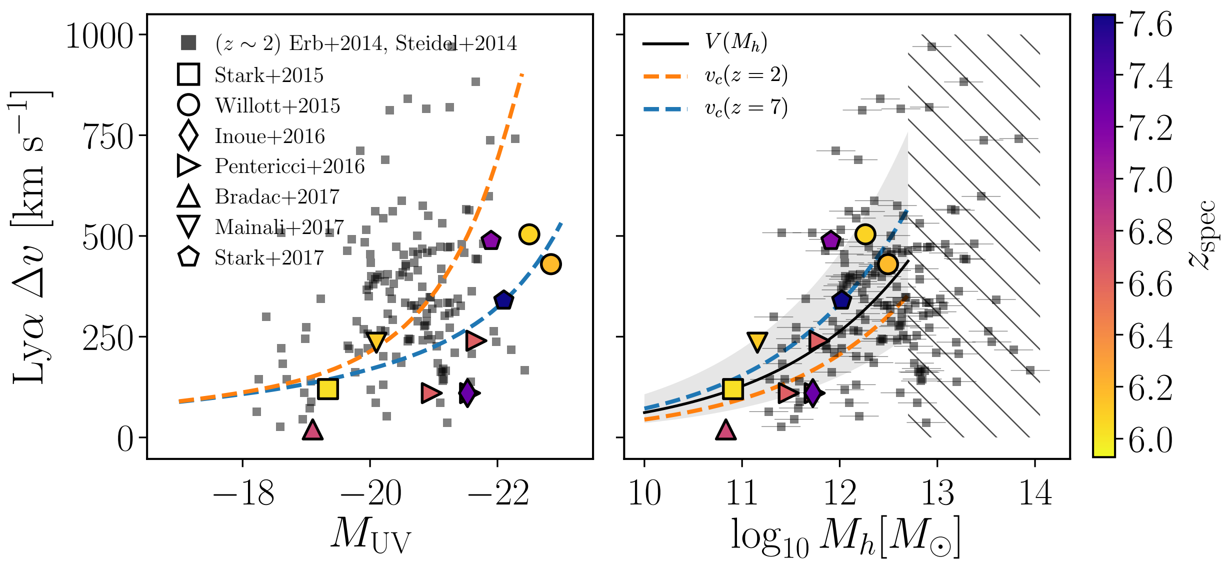

Figure 4.2: Lyα velocity offset as a function of UV absolute magnitude (left), halo mass (right, derived from the Mason et al. (2015a) UV magnitude - halo mass relation) for a collection of data from the literature (Erb et al., 2014; Steidel et al., 2014; Willott et al., 2015; Stark et al., 2015, 2017; Inoue et al., 2016; Mainali et al., 2017; Pentericci et al., 2016; Bradač et al., 2017). The gray squares show data from a $z \sim 2$ sample, whilst the colored points are at $z > 6$. We take the $z \sim 2$ distribution as complete and intrinsic and fit a log-normal distribution to the $\Delta v - M_h$ points as shown in Equation 4.1. The median $\Delta v - M_h$ fit is shown as a black solid line, and the gray shaded region shows the σ_v scatter. We add a 0.2 mag uncertainty to the UV magnitude measurements to account for scatter in the UV magnitude – halo mass relation and use the propagated uncertainties in halo mass in the $\Delta v - M_h$. The hashed region in the right panel indicates the galaxies with $M_{\rm UV} < -21$ which are discarded from fitting due to large uncertainties in assigning their halo masses. We plot the circular velocities, v_c of halos at $z \sim 2$ (dashed orange) and $z \sim 7$ (dashed blue) for comparison. The $\Delta v - M_h$ relation closely traces the circular velocities, suggesting galaxy mass is a key mediator of Lyα radiative transfer.

Numerous studies of star-forming galaxies at $z \lesssim 4$ have identified the column density of neutral hydrogen ($N_{\rm HI}$) within the ISM as a key mediator of Lyα radiative transfer. Lyα photons traveling through highly dense neutral ISM scatter more frequently and emerge with larger velocity offsets than galaxies with lower $N_{\rm HI}$ (Shibuya et al., 2014; Hashimoto et al., 2015; Yang et al., 2016, 2017; Guaita et al., 2017).

Low mass galaxies, especially at high redshifts, are less likely to contain significant fractions of neutral gas due to enhanced photoionization feedback. Additionally, strong star formation feedback may drive outflows and/or reduce the covering fraction of neutral gas in the ISM which can facilitate Lyα escape (Jones et al., 2013b; Trainor et al., 2015; Leethochawalit et al., 2016b).

Recently, a correlation has been suggested between UV magnitude and Lyα velocity offset (Schenker et al., 2013a; Erb et al., 2014; Song et al., 2014; Stark et al., 2015; Mainali et al., 2017; Stark et al., 2017), again indicating galaxy mass and/or SFR strongly affects Lyα escape. However, galaxies with the same UV magnitudes at different redshifts likely have very different masses because of increasing SFR at high redshift (e.g., Behroozi et al., 2013c; Barone-Nugent et al., 2014; Mason et al., 2015a; Finkelstein et al., 2015a; Harikane et al., 2016, 2017) so one should be cautious of comparing galaxies with the same UV magnitudes at different redshifts. We plot a compilation of $M_{\rm UV} - \Delta v$ measurements from the literature (Erb et al., 2014; Steidel et al., 2014; Bradač et al., 2017; Inoue et al., 2016; Mainali et al., 2017; Pentericci et al., 2016; Stark et al., 2015, 2017; Willott et al., 2015) in Figure 4.2 (left) where it is clear the high redshift galaxies have lower Δv at given $M_{\rm UV}$ compared to the low redshift galaxies, probably because they have lower mass.

To model the effect of the ISM on Lyα escape we assume the column density of neutral hydrogen within the ISM is determined by halo mass and is the most important quantity for understanding the emerging Lyα line profile. This is likely an over-simplification, e.g. 'shell' models take ~ 6 parameters to model Lyα lines (Verhamme et al., 2006, 2008; Gronke & Dijkstra, 2016), but is an efficient first-order approach. With this in mind, we assume a correlation between Δv and halo mass of the form $\Delta v \sim (M_h)^m$, where we determine m empirically from observations, as described below.

We take a sample of 158 $z \sim 2-3$ galaxies with both UV magnitudes and Lyα velocity offsets from Erb et al. (2014) and Steidel et al. (2014). The Steidel et al. (2014) sample (from the KBSS-MOSFIRE survey) is effectively complete at $M_{\rm UV} \lesssim -20$ where $\sim 90\%$ of their photometrically-selected LBGs have rest-frame optical emission lines detected in deep near-IR spectroscopy with *Keck*/MOSFIRE (McLean et al., 2012). The Erb et al. (2014) sample comprises 36 galaxies selected as Lyα emitters in narrow-band photometry with $-21 \lesssim M_{\rm UV} \lesssim -18$, all these objects had rest-frame optical lines detected in MOSFIRE observations. We note the Erb et al. (2014) sample does not include faint Lyα emitters ($W \lesssim 25$Å), which may have higher velocity offsets given observed anti-correlations between Lyα EW and Δv (Hashimoto et al., 2013; Shibuya et al., 2014; Erb et al., 2014). Whilst these samples are the largest available to measure a $M_{\rm UV} - \Delta v$ correlation, future rest-frame optical follow-up of large samples of galaxies with detected Lyα emission (e.g. from the HETDEX and MUSE-Wide spectroscopic surveys, Song et al., 2014; Herenz et al., 2017) will provide more complete information about the relationships between Lyα radiative transfer in the ISM and galaxy properties.

As described above, it is difficult to directly compare galaxies at fixed UV magnitude across cosmic time, so we map UV magnitudes to halo mass. To first order the depth of a halo's gravitational potential well is the dominant influence on galaxy properties independent of redshift (Behroozi et al., 2013a; Mason et al., 2015a; Moster et al., 2017). We assume no redshift evolution between halo mass and velocity offset. We convert UV magnitude to halo mass using the successful model derived by Mason et al. (2015a) which assumes the SFR is proportional to the halo mass assembly rate at a given halo mass and redshift, and is consistent with $M_{\rm UV} - M_h$ measurements from clustering at $z \sim 7$ (Barone-Nugent et al., 2014; Harikane et al., 2016, 2017). We add a 0.2 mag uncertainty to the UV magnitude measurements to account for scatter in the UV magnitude – halo mass relation (e.g., Finkelstein et al., 2015a) and use the propagated uncertainties in halo mass in the $\Delta v - M_h$.

In the right panel of Figure 4.2 we plot the literature Δv measurements as a function of the estimated halo masses. Due to the uncertainties in mapping from UV magnitude to halo mass for very bright galaxies at $z \lesssim 4$, which may be significantly more starbursty than average, we discard the $z \sim 2$ galaxies with $M_{\rm UV} < -21$ from further analysis. Likewise, we exclude from this inference the galaxies at $z \sim 7$ with $M_{\rm UV} < -22$, deferring their analysis to a later paper (Mason et al., 2018b).

When we transform to halo mass the high redshift literature points clearly lie within the low redshift data space. This suggests halo mass is a useful approximately redshift independent indicator of Lyα escape routes. We note gravitationally lensed objects at intermediate redshifts suggest these trends hold at low mass/luminosity (e.g., a lensed $M_{\rm UV} = -17$ galaxy at $z \sim 3$ was recently observed with a Lyα velocity offset of 51 km s^{-1}, Vanzella et al., 2016). Further studies, using NIRSpec on JWST, will be able to investigate these trends at high redshifts.

The distribution is well-described by a log-normal distribution with a peak which increases with increasing luminosity, and approximately constant variance:

$$p(\Delta v \,|\, M_h) = \frac{\exp\left[-\frac{(\log_{10}\Delta v - V(M_h))^2}{2\sigma_v^2}\right]}{\Delta v \ln 10 \sqrt{2\pi}\sigma_v} \tag{4.1}$$

where V is a linear relation corresponding to the most likely $\log_{10}(\Delta v)$ at a given halo mass:

$$V(M_h) = m \log_{10}\left(\frac{M_h}{1.55 \times 10^{12} M_\odot}\right) + c \tag{4.2}$$

To find the parameters m, c and σ_v we take Equation 4.1 as the likelihood function and perform a Bayesian inference on the $z \sim 2$ galaxies with $M_{\rm UV} > -21$, with uniform priors on the parameters. The inferred parameters are: $m = 0.32 \pm 0.07$, $c = 2.48 \pm 0.03$ and $\sigma_v = 0.24 \pm 0.02$. We show this relation on Figure 4.2.

We can obtain an approximate relation between velocity offset, UV magnitude and redshift by approximating the Mason et al. (2015a) UV magnitude - halo mass relation as broken linear: $\log_{10} M_h[M_\odot] \approx \gamma(M_{\rm UV} + 20.0 + 0.26z) + 11.75$, where $\gamma = -0.3$ for $M_{\rm UV} \geq -20.0 - 0.26z$, and $\gamma = -0.7$ otherwise. The mean velocity offset in km s^{-1} can then be approximated as:

$$\log_{10} \Delta v(M_{\rm UV}, z) \approx 0.32\gamma(M_{\rm UV} + 20.0 + 0.26z) + 2.34 \tag{4.3}$$

In this work we sample directly from the distribution in Equation 4.2 to calculate velocity offsets directly for simulated halos, including scatter.

In Figure 4.2 we also plot the circular velocity ($v_c = [10GM_hH(z)]^{1/3}$) at $z = 2$ and $z = 7$ for comparison with the observed data. The circular velocities are higher at low redshifts as halos are less dense and more extended, but there is a clear similarity in our derived trend $\Delta v \sim M_h^{0.32}$ and the circular velocity $v_c \sim M_h^{1/3}$. Investigating these trends with larger samples at low redshifts with dynamical mass measurements (e.g., Trainor et al., 2015; Erb et al., 2014) could determine to what extent Lyα radiative transfer depends on the gravitational potential of the halo.

4.2.1.2 Modeling Lyα line widths

The widths of Lyα lines are also likely dominated by radiative transfer effects which both shifts and broadens the line (Verhamme et al., 2006, 2008; Gronke et al., 2016). Lyα velocity dispersions are also observed to be systematically higher than in nebular emission lines which are not resonantly scattered (Trainor et al., 2015).

For simplicity we model the FWHM of the Lyα lines as equal to the velocity offset of the line, which accounts for the broadening of the lines through scattering and is a good approximation for the observed correlation between Lyα FWHM and velocity offset (Yang et al., 2016, 2017, Verhamme et al. submitted).

4.2.1.3 EW distribution in an ionized universe

The key observable of Lyα emission lines at high redshift is their equivalent width (EW or W), is a measure of the brightness of the emission line relative to the UV continuum. As Lyα photons from high redshift galaxies are attenuated by neutral gas in the intervening CGM and IGM we observed only a fraction, $\mathcal{T}_{\text{IGM}}$ (the Lyα *transmission fraction*) of the emitted EW, i.e. $W_{\text{obs}} = W_{\text{em}} \times \mathcal{T}_{\text{IGM}}$, where W_{em} is the emitted equivalent width without any damping due to reionization.

In this work we consider the differential evolution of Lyα equivalent widths between $z \sim 6$ and $z \sim 7$, and assume the distribution of equivalent widths changes *only* because of the increasing neutrality of the IGM due to reionization. This is likely a simplification, as trends at lower redshifts show increasing EW with redshift as dust decreases in galaxies (Hayes et al., 2011), but the time between $z \sim 6$ and $z \sim 7$ is short (< 200 Myr). If the underlying EW distribution does evolve significantly during that time it will likely be to increase the emitted EW (due to decreasing dust, Hayes et al., 2011), thus the reduction due to reionization would need to be greater to match the observed EW distribution at

$z \sim 7$ (Dijkstra et al., 2011). Papovich et al. (2011)suggests there may be an increase in gas reservoirs with increasing redshifts due to rapid accretion rates, which could also reduce the emission of strong Lyα.

Thus observed equivalent widths at $z \sim 7$ are $W_7 = W_6 \times \mathcal{T}_{\text{IGM},7}/\mathcal{T}_{\text{IGM},6}$, where $\mathcal{T}_{\text{IGM},z}$ is the transmission fraction of Lyα emission for a single object at redshift z. In Section 4.2.2 below we describe the calculation of transmission fractions along thousands of lines-of-sight using state-of-the-art cosmological reionization simulations.

A key input to the model then is the $z \sim 6$ distribution of EW as a function of galaxy properties. Lyα EWs for UV continuum-selected galaxies have an observed equivalent width distribution with a peak at zero and some tail to high EW - which is usually parameterized as an exponential function (Dijkstra & Wyithe, 2012), log-normal (Schenker et al., 2014) or truncated normal distribution plus a delta function (Treu et al., 2012). At $z \lesssim 2$, where large samples exist, including the local 'Green Peas', Lyα EW is observed to anti-correlate strongly with UV luminosity (Shapley et al., 2003; Stark et al., 2011; Hashimoto et al., 2013) SFR (Verhamme et al., 2008), H I covering fraction (Shibuya et al., 2014) and Lyα escape fraction (Yang et al., 2017), all indicating Lyα photons are significantly absorbed by neutral hydrogen gas and dust inside the ISM of massive, highly star-forming galaxies (e.g. Verhamme et al., 2008; Erb et al., 2014; Yang et al., 2017). At high redshift, the Lyα EW distribution is usually parameterized as a conditional probability of $p(W \,|\, M_{\text{UV}})$ (Treu et al., 2012; Dijkstra & Wyithe, 2012), though dependence on UV spectral slope β has also been considered (Schenker et al., 2014).

We take the $z \sim 6$ EW distribution from De Barros et al. (2017) and Pentericci et al. (2018, in preparation) from a Large Program with VLT/FORS2. This sample contains 127 objects, with UV magnitudes between $-22.5 \lesssim M_{\text{UV}} \lesssim -17.5$, of which 63% have Ly$\alpha$ detections. We parameterize it as an exponential distribution plus a delta function:

$$p_6(W \,|\, M_{\text{UV}}) = \frac{A(M_{\text{UV}})}{W_c(M_{\text{UV}})} e^{-\frac{W}{W_c(M_{\text{UV}})}} H(W) + [1 - A(M_{\text{UV}})]\, \delta(W) \tag{4.4}$$

A and W_c account for the fraction of non-emitters, and for the anti-correlation of EW with M_{UV}. $H(W)$ is the Heaviside step function and $\delta(W)$ is a Dirac delta function. A implicitly includes contamination by low redshift interlopers in the photometric selection (the interloper fraction is $\leq 29\%$ for this sample assuming all non-detections were low redshift contaminants, De Barros et al., 2017), i.e. we do not distinguish between non-emitters at $z \sim 6$ and low redshift contaminants when accounting for non-detections in fitting the parameters (see below). Within our framework this means we assume a similarly small total interloper and non-emitter fraction at $z \sim 7$. Recent work by Vulcani et al. (2017) supports this assumption: they found comparably low contamination fractions at $z \sim 6$ and $z \sim 7$ in an evaluation of photometric selections.

To find these parameters we divided the sample into three bins: $M_{\mathrm{UV}} \leq -21$; $-21 < M_{\mathrm{UV}} < -20$; and $M_{\mathrm{UV}} \geq -20$. We used Equation 4.4 as a likelihood ($p_6(W \,|\, A, W_c)$) and performed a Bayesian inference to infer A and W_c for each bin, similar to the methods of Oyarzún et al. (2017), using uniform priors with $0 < A < 1$ and $0 < W_c < 100$. In the inference we fully account for the the non-detections of Lyα (using $p_6(W < W_{\mathrm{lim}} \,|\, A, W_c)$ as the likelihood given an EW limit W_{lim}, in the same way as described in more detail in Section 4.3 below). The uncertainties and EW limits calculated by De Barros et al. (2017) are obtained using simulations which fully account for incompleteness and wavelength sensitivity. We note that in this framework the EW limits are a conservative minimum which could be measured over the entire wavelength range (see also Section 4.4.2), future work could incorporate the full wavelength-dependent line flux sensitivity. To allow these parameters to smoothly vary with magnitude between $-21 < M_{\mathrm{UV}} < -20$ we use a hyperbolic tangent function to connect our inferred parameters, without extrapolating beyond the range of the data. We find $A = 0.65 + 0.1 \tanh\left[3(M_{\mathrm{UV}} + 20.75)\right]$ and $W_c = 31 + 12 \tanh\left[4(M_{\mathrm{UV}} + 20.25)\right]$Å from fitting to the data. A and W_c vary smoothly with magnitude.

We choose this exponential parameterization of the data because is gives a good description of the data and is easy to treat analytically, and has previously been shown to be an excellent fit to Lyα EW PDFs (e.g., Oyarzún et al., 2017). We do not include uncertainties in these parameters and we note the parameterization of $p_6(W \,|\, M_{\mathrm{UV}})$ is fairly arbitrary but does not qualitatively affect Lyα modeling during the EoR (Treu et al., 2012; Gronke et al., 2015b). Indeed we get the same results, within the uncertainties, if we use the $p_6(W)$ truncated Gaussian distribution from Treu et al. (2012) based on the sample presented in Stark et al. (2011).

Example PDFs given by Equation 4.4 are plotted in Figure 4.3 for two values of $M_{\rm UV}$. We show both the intrinsic PDF and the distribution convolved with a 5Å typical measurement error which introduces at 'bump' around $W = 0$ where the underlying distribution is a delta function. We also show histograms of the EW observations of De Barros et al. (2017) and Pentericci et al. (2018, in preparation) in two bins corresponding to UV bright and faint LBGs. As shown by e.g., Verhamme et al. (2008); Stark et al. (2010) and Oyarzún et al. (2017), Lyα EW strongly depends on UV magnitude.

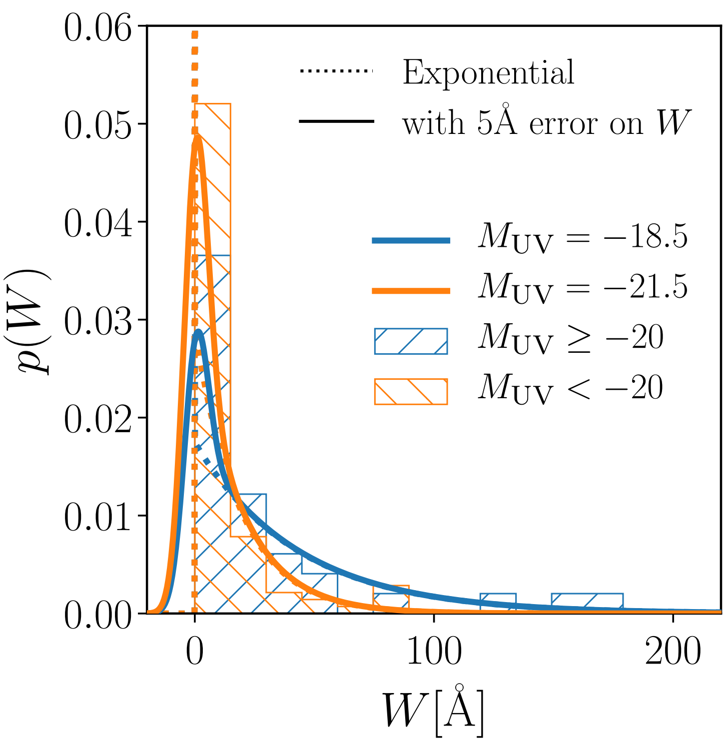

Figure 4.3: $z \sim 6$ Lyα equivalent width distributions for Lyman Break galaxies given by Equation 4.4. The dotted lines show the true distribution. For better comparison with the data, we show the PDFs convolved with a 5Å typical measurement error on W as solid lines. We plot the PDFs for two values of UV magnitude: $M_{\rm UV} = -18.5, -21.5$ (blue, orange) . UV faint objects tend to have higher EW and a higher duty cycle of Lyα emission, whereas UV bright galaxies are less likely to emit Lyα and have lower EWs. We also plot the observed EW from De Barros et al. (2017) and Pentericci et al. (2018, in preparation) in UV bright (orange) and UV faint (blue) bins. In these histograms we plot all upper limits at $EW = 0$, though note we fully account for upper limits in fitting the EW distribution and the reionization inferences (see Equation 4.11).

4.2.2 IGM and CGM Lyα Radiative Transfer

A Lyα emission line is significantly attenuated by the CGM and IGM as its photons redshift into resonance with abundant neutral hydrogen along the line-of-sight. Effectively, for a Lyα line at $z \gtrsim 6$, all photons emitted blue-ward of the Lyα resonance (1216Å) are absorbed by the IGM as even after reionization there is still is a fraction of neutral hydrogen within H II regions (Gunn & Peterson, 1965). Infalling overdense gas around halos can also increase the opacity of the IGM near the Lyα resonance and onto the red side of the Lyα line (Santos, 2004; Dijkstra et al., 2007; Laursen et al., 2011).

For simplicity we assume all Lyα photons emitted below the circular velocity of a halo are absorbed in the CGM, and all redder photons are transmitted (Dijkstra et al., 2011; Laursen et al., 2011). This treatment of the CGM may be crude but it enables us to investigate the relative difference between observations at $z \sim 6$ and $z \sim 7$ assuming any evidence of a difference is driven by reionization. Future work could incorporate more complex modeling of CGM absorption (e.g., Kakiichi & Dijkstra, 2017). Figure 4.1 show example model Lyα emission lines, where the dotted black lines correspond to the intrinsic line profile after transmission through the ISM and the black solid lines correspond to the lineshape after resonant absorption in the CGM/IGM which absorbs the flux blueward of v_circ.

During reionization, there is an additional opacity to Lyα caused by the presence of cosmic diffuse neutral hydrogen patches which attenuate the damping wing of the Lyα line cross-section (Miralda-Escude, 1998). The transmission of Lyα photons through the reionizing IGM is driven by the global fraction of neutral hydrogen, $\overline{x}_\mathrm{HI}(z)$.

Thus the total opacity to Lyα due to neutral hydrogen within the IGM is given by:

$$\tau_\mathrm{IGM}(z,v) = \tau_\mathrm{D}(z,v) + \tau_\mathrm{HII}(z,v) \tag{4.5}$$

where $\tau_\mathrm{D}(z,v)$ is the damping wing optical depth which is only present during the EoR, and $\tau_\mathrm{HII}(z,v)$ is the optical depth due to resonant absorption within the CGM of galaxies (infalling gas) and any neutral hydrogen within the local H II region of a galaxy. For simplicity, we assume $e^{-\tau_\mathrm{HII}} = H(v - v_\mathrm{circ})$ at both $z \sim 6$ and $z \sim 7$.

In this model, we assume the universe is fully ionized at $z \sim 6$, thus the damping wing opacity only becomes important at $z > 6$. This may not be exactly the case, but current constraints on $\overline{x}_{\text{HI}}$ at $z \sim 6$ suggest the neutral fraction is low ($\overline{x}_{\text{HI}} < 0.1$, McGreer et al., 2015) so the reionization effect on Lyα emission will be small.

To obtain the damping wing optical depths $\tau_{\text{D}}(z = 7, v)$ requires a model of the IGM topology during reionization. Whilst observation papers of Lyα emission with reionization inferences have used simple 'patchy' or 'smooth' IGM topologies (Treu et al., 2012, 2013; Pentericci et al., 2014; Tilvi et al., 2014), for this work, we consider realistic reionization topologies from state-of-the-art theoretical modeling. We obtain Lyα damping optical depths from the public Evolution of 21cm Structure (EoS) suite of reionization simulations described by Mesinger et al. (2015, 2016)[1].

Due to the strong clustering of the first galaxies spatial fluctuations in the IGM neutral fraction during reionization existed on scales of tens of Mpcs. Accurately modeling these fluctuations and the growth of ionized H II bubbles in the IGM requires cosmological simulations at least 100 Mpc in size (Trac & Gnedin, 2011; Mesinger et al., 2015). The EoS reionization simulations use 21CMFASTV2 (Sobacchi & Mesinger, 2014) where inhomogeneous recombinations and ionizations in the IGM are treated at a sub-grid level on a density field in a box with sides 1.6 Gpc with a resolution 1024^3. The simulations produce $\overline{x}_{\text{HI}}$ maps at different redshifts and superimpose them on the $z \sim 7$ halo field to produce cubes of the $z \sim 7$ IGM for a range of neutral fractions. For the bulk of reionization, this is analogous to changing the ionization efficiency at a fixed redshift (e.g., McQuinn et al., 2007b; Mesinger & Furlanetto, 2008b).

The timeline and topology of reionization is determined by the mass of galaxies which dominate reionization and the ionization efficiency, $\zeta \propto f_{\text{esc}} \times f_\star$, where f_{esc} is the fraction of ionizing photons which escape galaxies into the IGM, and $f_\star$ is the stellar mass fraction in galaxies. As both of these parameters are expected to scale with halo mass in complementary ways (i.e. low mass halos host galaxies with a low stellar mass fraction and high escape

[1] `http://homepage.sns.it/mesinger/EOS.html`

fraction, e.g., Kimm et al., 2017; Trebitsch et al., 2017), over the relevant range of halo masses which host galaxies which dominate reionization ($M_h \lesssim 10^{11} M_\odot$, e.g., Kimm et al., 2017), ζ is assumed to be constant in the EoS simulations. The simulations use a free parameter which sets the minimum mass of halos capable of hosting star formation, and then adjust ζ to produce a Thompson scattering optical depth to the CMB consistent with Planck Collaboration et al. (2016a).

We use the fiducial 'Faint Galaxies' run which corresponds the primary drivers of reionization being low mass star-forming galaxies with an atomic cooling threshold of $T_{\rm vir} \gtrsim 10^4$ K, with $\zeta = 20$, producing IGM morphologies characterized by small HII regions. Whilst the EoS simulations have another run, 'Bright Galaxies', where reionization is driven by more massive galaxies, producing larger HII regions, it has been shown that information about the reionization morphology is mostly smeared out when using galaxies spread in redshift ($\Delta z \gtrsim 0.1$ bin, e.g., Sobacchi & Mesinger, 2015, though with large spectroscopic samples, $\Delta z \sim 0.01$, the sensitivity does increase), as is the case for our sample (see Section 4.4.2), so we do not expect a significant change in our results if we were to use an alternative run. Indeed, Mason et al. (2018b) uses both simulation runs but shows that the transmission of Lyα from galaxies $M_h \sim 10^{10} - 10^{12}$ is relatively independent of the reionization morphology. Similarly, Greig et al. (2017) show QSO damping wing effects are not particularly sensitive to the reionization morphology.

Halos are located in the same density field as the IGM simulation. We ignore absorption from Damped Lyα Absorbers (DLAs) inside the cosmic H II regions (Bolton & Haehnelt, 2013) which has been shown to have a minor impact on the Lyα fraction when self-shielding is calculated more accurately (Mesinger et al., 2015). We refer the reader to (Mesinger et al., 2016) for more details of the simulation. For this work we focus on $z \sim 7$, where large samples of LBGs have spectroscopic follow-up (Pentericci et al., 2014; Schmidt et al., 2016), but it is easy to extend the work to any other redshift.

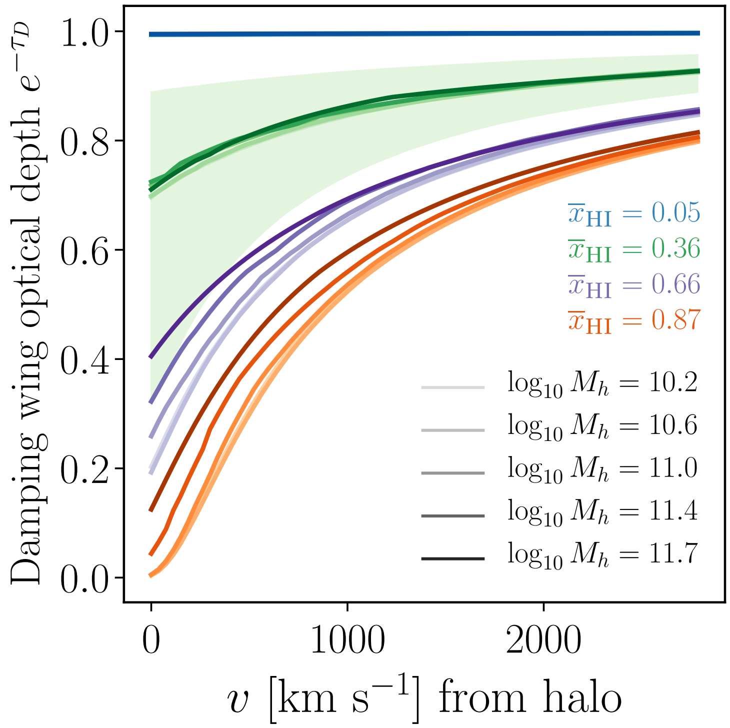

Figure 4.4: Median Lyα IGM damping wing optical depths due to cosmic H I patches during reionization as a function of velocity offset from the center of the source halos. We plot optical depths for 5 different mass halos (indicated by tone of the line - where darkest lines are the highest mass halos) and for 4 volume-averaged neutral fractions $\overline{x}_{\rm HI}$ (indicated by color). We plot the median optical depth for each halo from the 1000s of simulated sightlines. For $\overline{x}_{\rm HI} = 0.36$ we plot the 1σ confidence region for the optical depths from all the sightlines to the $\log_{10} M_h = 10.2$ halos as a shaded area, showing the large variation across sightlines.

We take 1000s of sightlines emanating from halos with masses $\sim 10^{10-12} M_\odot$ (comparable to typical $z \gtrsim 5$ halo masses for $-22 \lesssim M_{\rm UV} \lesssim -18$ galaxies, Barone-Nugent et al., 2014; Harikane et al., 2016, 2017) and compute the damping wing optical depth, $\tau_{\rm D}$, for Lyα emission as a function of velocity offset from the systemic redshift of the source halos in boxes with a range of global neutral fractions. Median values of $\exp[-\tau_{\rm D}]$ along ~ 50 (to the rarest high mass halos) to $\gtrsim 4000$ (to typical $10^{10.5} M_\odot$ halos) sightlines are plotted in Figure 4.4 for a range of halo masses and $\overline{x}_{\rm HI}$. The optical depths are smooth functions of velocity and clearly damp Lyα more effectively for higher $\overline{x}_{\rm HI}$. In general, higher mass halos have lower optical depths to Lyα as their large bias means they are more likely to live in the centers of large H II regions, relatively more distant from the cosmic H I patches which produce the damping wing absorption during the EoR.

For a given sightline, the final fraction of Lyα photons emitted by a galaxy in a halo with mass M_h which are transmitted through the IGM, $\mathcal{T}_{\rm IGM}$, is given by:

$$\mathcal{T}_{\rm IGM}(\overline{x}_{\rm HI}, M_h, \Delta v) = \int_0^\infty \mathrm{d}v \; J_\alpha(\Delta v, M_h, v) e^{-\tau_{\rm IGM}(\overline{x}_{\rm HI}, M_h, v)} \tag{4.6}$$

where Δv is the velocity offset of the Lyα line center from the systemic redshift of the source galaxy (which depends on the galaxy's ISM, as described in Section 4.2.1) and $J_\alpha(\Delta v, M_h, v)$ is the line profile of Lyα photons escaping from the galaxy as function of velocity v.

As any photons emitted bluer than the halo circular velocity will be resonantly absorbed by intervening neutral hydrogen (Gunn & Peterson, 1965; Dijkstra et al., 2007; Zheng et al., 2010; Laursen et al., 2011; Schroeder et al., 2013), J_α is described as:

$$J_\alpha(\Delta v, M_h, v) \propto \begin{cases} \frac{1}{\sqrt{2\pi}\sigma_\alpha} e^{-\frac{(v-\Delta v)^2}{2\sigma_\alpha^2}} & \text{if } v \geq v_{\rm circ}(M_h) \\ 0 & \text{otherwise} \end{cases} \tag{4.7}$$

If J_α is normalized $\mathcal{T}_{\rm IGM,6} = 1$, as we assume $\tau_{\rm D} = 0$ at $z \sim 6$. Compared to the intrinsic emitted line $\mathcal{T}_{\rm IGM,6}$ can be very low (Dijkstra et al., 2007; Zheng et al., 2010; Laursen et al., 2011). For ease of notation we refer to the differential transmission at $z \sim 7$, $\mathcal{T}_{\rm IGM,7}/\mathcal{T}_{\rm IGM,6}$, as $\mathcal{T}_{\rm IGM}$.

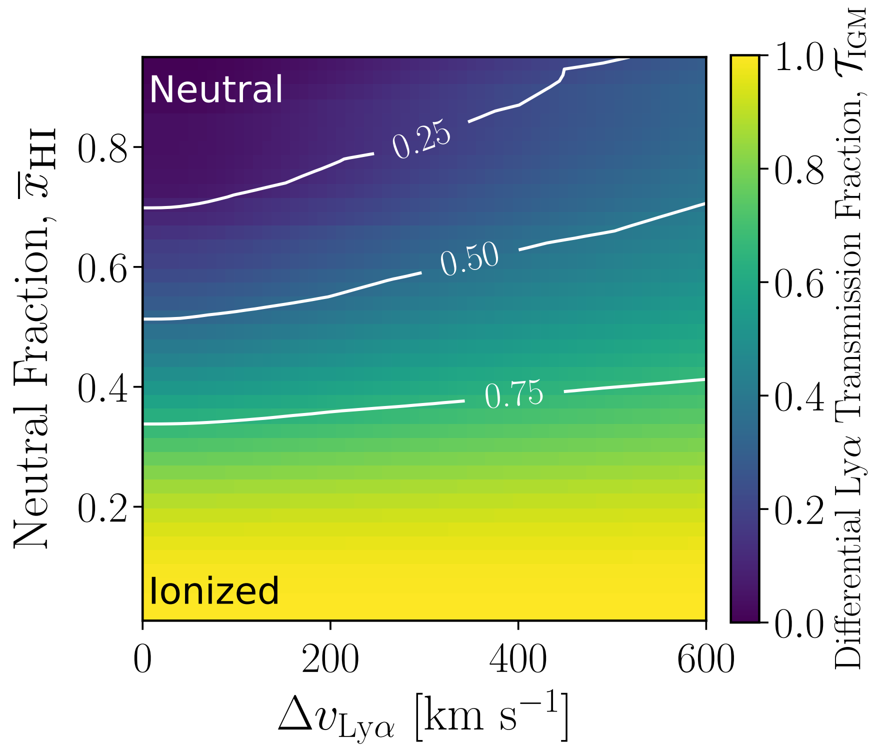

Figure 4.5: Median fraction of Lyα photons transmitted through the IGM, $\mathcal{T}_{\rm IGM}$, as a function of $\overline{x}_{\rm HI}$ and Δv computed with Equation 4.6 from $\sim$5000 sightlines to halos with mass $10^{10} M_\odot$, assuming $\mathcal{T}_{\rm IGM,6} = 1$. Contours show transmission fractions of 25%, 50% and 75%. In a predominantly neutral universe Lyα photons have higher probability of escape through predominately ionized IGM and if emitted at high velocity offsets from their originating galaxies.

Example intrinsic and transmitted emission lines are plotted in Figure 4.1. Sightline median values of $\mathcal{T}_{\rm IGM}(\overline{x}_{\rm HI}, \Delta v)$ at fixed halo mass are plotted in Figure 4.5. As expected, as the neutral fraction increases the transmission fraction of Lyα decreases smoothly. Whilst at low neutral fractions the velocity offset of Lyα has little impact, in a predominantly neutral universe, ($\overline{x}_{\rm HI} \gtrsim 0.6$) lines are more easily transmitted if they were emitted at high velocity offset.

In Figure 4.6 we plot probability distribution functions for $\mathcal{T}_{\rm IGM}$ for three different values of $M_{\rm UV}$, where we have transformed from halo mass to $M_{\rm UV}$ using the Mason et al. (2015a) LF model as above and drawn Δv values for halos using the distribution in Equation 4.2. The transmission distributions evolve smoothly with neutral fraction and UV magnitude. Transmission of Lyα evolves more slowly for the brightest galaxies, due to a combination of their increased velocity offsets and their locations in the most overdense regions, far from the cosmic H I regions which cause the damping wing absorption.

Galaxies in high mass halos ($M_h > 10^{12} M_\odot$, corresponding to approximately $M_{\rm UV} < -22$) require special attention. First, they are rare and lines of sights to such objects in the simulations are not well-sampled leading to large statistical errors. Second, the correlation between $M_{\rm UV}$ and M_h is particularly uncertain in this regime. Third, such bright galaxies have been observed to buck the trend in the declining Lyα emission fraction at $z \gtrsim 7$ at $z > 7.5$ (Curtis-Lake et al., 2012; Stark et al., 2017). For these reasons, they require special attention, especially because they are prime targets for detailed spectroscopic follow-up. Since they are intrinsically rare, they would contribute negligibly to the analysis presented in this paper. Thus, we leave their analysis for future work (Mason et al., 2018b) and exclude them from the sample considered here.

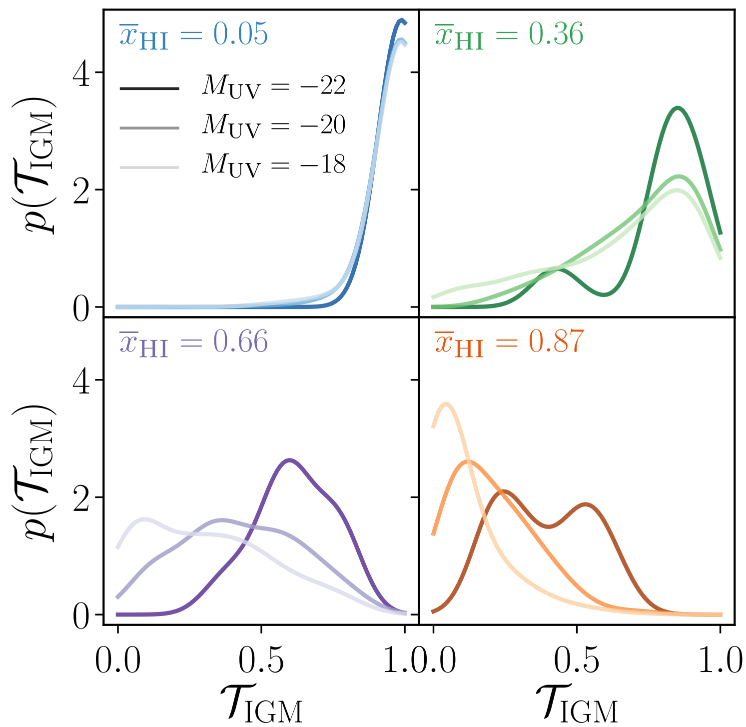

Figure 4.6: Distributions of differential Lyα transmission fractions $\mathcal{T}_{\rm IGM}$ at $z \sim 7$ for simulated galaxies of different UV luminosities (UV bright = darkest lines), for a range of IGM neutral fractions $\overline{x}_{\rm HI}$. As described in Section 4.2.2 this is the ratio of Lyα transmission at $z \sim 7$ to that at $z \sim 6$ where there is already significant absorption within the ionized IGM (Dijkstra et al., 2007; Zheng et al., 2010; Laursen et al., 2011). The transmission fractions evolve smoothly with the neutral fraction, though the evolution is more gradual for UV bright galaxies.

4.3 Bayesian Inference

Bayes' Theorem enables us to infer the posterior distribution of model parameters of interest, θ given our observed data Y from the likelihood of obtaining the data given our model and our prior information of the model parameters. The posterior probability of θ is written as:

$$p(\theta \,|\, Y) = \frac{p(Y \,|\, \theta)\, p(\theta)}{p(Y)} \tag{4.8}$$

where $p(Y \,|\, \theta)$ is the likelihood function, $p(\theta)$ is the prior, and $p(Y)$ is the Bayesian Evidence which normalizes the posterior.

We want to obtain the posterior distribution of the volume averaged fraction of neutral hydrogen, $\overline{x}_{\rm HI}$, a global IGM property, given the observed data: measurements of Lyα equivalent widths W and galaxy rest-frame UV absolute magnitudes $M_{\rm UV}$. As described in Section 4.2 we model both IGM and ISM effects on Lyα transmission and produce forward models of the observed Lyα equivalent widths for galaxies of a given UV magnitude.

Using Bayes' Theorem we can write the posterior probability for $\overline{x}_{\rm HI}$ inferred from one observation in the absence of noise as:

$$p(\overline{x}_{\rm HI}\,|\,W, M_{\rm UV}) \propto p(W\,|\,\overline{x}_{\rm HI}, M_{\rm UV})\, p(\overline{x}_{\rm HI}) \tag{4.9}$$

where $p(W\,|\,\overline{x}_{\rm HI}, M_{\rm UV})$ is the likelihood of observing a Lyα equivalent width given our forward model of the ISM and IGM, and $p(\overline{x}_{\rm HI})$ is the prior on the neutral fraction which we assume is uniform between 0 and 1.

Usually, the likelihood function is obtained from a model with an analytic form - e.g. a normal distribution, however, due to including simulated IGM cubes, our model is complex and does not have an analytic parameterization. We therefore generate the likelihood by sampling 10^6 realizations of galaxies in our model at a given $(\overline{x}_{\rm HI}, M_{\rm UV})$ and then perform a Kernel Density Estimation (Rosenblatt, 1956; Parzen, 1962) to fit a smooth probability density function to the sampled distribution. Examples of the likelihood function are shown in Figure 4.7. Generation of the likelihoods is described in more detail below in Section 4.3.1.

In reality, our observations will always have measurement uncertainties, and some observations can only place an upper limit on a measurement, given a noise level. When we include noise, our likelihood for measuring an equivalent width W_i with Gaussian noise level σ_i becomes:

$$p(W_i\,|\,\overline{x}_{\rm HI}, M_{\rm UV}) = \int_0^\infty \mathrm{d}W\, \frac{e^{-\frac{(W-W_i)^2}{2\sigma_i^2}}}{\sqrt{2\pi}\sigma_i} p(W\,|\,\overline{x}_{\rm HI}, M_{\rm UV}) \tag{4.10}$$

and the likelihood for upper limits, $W_i < \mathcal{W}$ is given by:

$$\begin{aligned} p(W_i < \mathcal{W}\,|\,\overline{x}_{\rm HI}, M_{\rm UV}) &= \int_{-\infty}^{\mathcal{W}} \mathrm{d}W\; p(W_i\,|\,\overline{x}_{\rm HI}, M_{\rm UV}) \\ &= \int_0^\infty \mathrm{d}W\, \frac{1}{2}\,\mathrm{erfc}\left(\frac{W-\mathcal{W}}{\sqrt{2}\sigma_i}\right) \times\; p(W\,|\,\overline{x}_{\rm HI}, M_{\rm UV}) \end{aligned} \tag{4.11}$$

where erfc(x) is the complementary error function for x.

In this work we consider samples with good redshift completeness (i.e. the probability of a Lyα line falling within the observable range is close to one, see Section 4.4.2). Thus, this inference framework does not include information about redshift in the likelihood, this is left for future work.

We can combine the inference from a set of independent observations (i.e. individual galaxies) by simply multiplying the posteriors:

$$p(\overline{x}_{\rm HI}\,|\,\{W, M_{\rm UV}\}) \propto \prod_{i}^{N_{\rm gals}} p(W_i\,|\,\overline{x}_{\rm HI}, M_{{\rm UV},i})\, p(\overline{x}_{\rm HI}) \tag{4.12}$$

4.3.1 Generating the likelihood

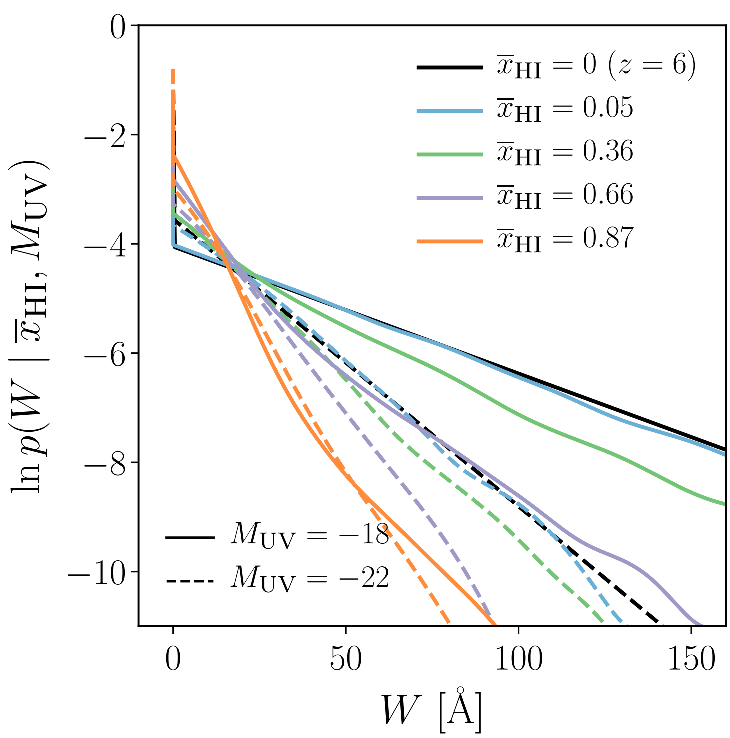

Figure 4.7: Simulated observed distribution of Lyα equivalent widths (the likelihoods for our model) for a range of neutral fractions (colors), for faint (solid line) and bright (dashed line) UV magnitudes. The intrinsic distributions (Equation 4.4) are shown as black lines. The EW distribution evolves significantly for the UV faint galaxies with increasing $\overline{x}_{\rm HI}$, whilst the distribution for UV bright galaxies evolves more slowly.

Our observed data are a set of Lyα equivalent widths (and limits) and absolute magnitudes from galaxies at a given redshift: $\{W, M_{\rm UV}\}$. Due to the complexity of the IGM topology, there is no simple analytic model to express the likelihood of obtaining these data given a neutral fraction $\overline{x}_{\rm HI}$. Thus we use our model to generate large samples of mock observations which provide a non-analytic likelihood.

We take IGM simulations with global neutral fractions $0.01 \leq \overline{x}_{\rm HI} \leq 0.95$ ($\Delta\overline{x}_{\rm HI} \sim 0.02$) and a population of halos with masses $10^{10} \lesssim M_h[M_\odot] \lesssim 10^{12}$ with $\Delta \log M_h \sim 0.1$. This mass range corresponds to UV magnitudes of $-16 \gtrsim M_{\rm UV} \gtrsim -22$ at $z \sim 7$ (Mason et al., 2015a). The likelihood is computed in the following way:

1. Obtain the Lyα damping wing optical depths (see Section 4.2.2) along thousands of different sightlines to individual halos in each simulation, to account for the inhomogeneous nature of reionization.

2. For a grid of UV magnitudes $-22 \leq M_{\rm UV} \leq -17$ we nearest-neighbor match the simulation halo masses with UV magnitudes at $z \sim 7$ given by the relation in Mason et al. (2015a) which is consistent with $M_{\rm UV} - M_h$ measurements from clustering at $z \sim 7$ (Barone-Nugent et al., 2014; Harikane et al., 2016, 2017). We do not add scatter to this matching, but note the halo mass step in the simulations (~ 0.13 dex) is not dissimilar to the scatter in the inferred $M_{\rm UV} - M_h$ relation for galaxies around $M_{\rm UV}^\star$ (e.g., 0.3 dex, Finkelstein et al., 2015a), so some $M_{\rm UV} - M_h$ scatter is included. Furthermore we note the optical depth scatter between sightlines for a given halo mass is far greater than the scatter between sightlines between halos of different masses (compare lines and shaded region in Figure 4.4), thus the $M_{\rm UV} - M_h$ scatter is sub-dominant.

3. Populate these model galaxies with Lyα line velocity offsets from the distribution $p(\Delta v \,|\, M_h)$ as described by Equation 4.2, including the scatter σ_v, and the Lyα equivalent widths for an ionized universe (we which assumed to be the same as at $z \sim 6$), $p_6(W_{\rm em} \,|\, M_{\rm UV})$ described in Section 4.2.1, creating 10^6 realizations of a galaxy in each halo.

4. We compute the differential Lyα transmission fraction, $\mathcal{T}_{\rm IGM}$ with Equation 4.6 along sightlines through the IGM to every model galaxy and the observed equivalent width,

where $W_{\rm obs} = \mathcal{T}_{\rm IGM} \times W_{\rm em}$.

5. The distributions of model observed $W_{\rm obs}$ at fixed $(\overline{x}_{\rm HI}, M_{\rm UV})$ are described by the form:

$$p(W \,|\, \overline{x}_{\rm HI}, M_{\rm UV}) = A(M_{\rm UV}) f(W, \overline{x}_{\rm HI}) H(W) + [1 - A(M_{\rm UV})]\, \delta(W) \tag{4.13}$$

where $f(W, \overline{x}_{\rm HI})$ describes the evolution of the equivalent width distribution as the neutral fraction evolves and is fitted with a Gaussian Kernel Density Estimator (Rosenblatt, 1956; Parzen, 1962), and $A(M_{\rm UV})$ denotes the fraction of non-emitters and contaminants as described in Equation 4.4 which does not change as the neutral fraction increases ($\mathcal{T}_{\rm IGM} \neq 0$ exactly).

These distributions $p(W \,|\, \overline{x}_{\rm HI}, M_{\rm UV})$ are the likelihoods for the observed data. Some examples are plotted in Figure 4.7. For increasing neutral fraction the EW distribution becomes steeper, as more Lyα is damped by cosmic neutral patches. The evolution of $p(W \,|\, \overline{x}_{\rm HI}, M_{\rm UV})$ is slower for more UV bright (more massive) galaxies because the transmission functions evolve more slowly with increasing neutral fraction (see Section 4.2.2 and Figure 4.6).

We chose to marginalize out Δv at this stage to ease computation by reducing a degree of freedom, but it is possible to produce the likelihood conditional on Δv: $p(W \,|\, \overline{x}_{\rm HI}, M_{\rm UV}, \Delta v)$. It is then possible to infer Δv for an individual observed galaxy, or, if Δv is already known, recover a narrower posterior on the neutral fraction.

4.4 Results

In this section we describe the key results and predictions from our model. In Section 4.4.1 we show our method can accurately recover the neutral fraction for simulated datasets. We perform inference on current data from Pentericci et al. (2014) in Section 4.4.2. In Section 4.4.3 we make predictions for future surveys with JWST.

4.4.1 Large samples of galaxies can accurately constrain the neutral fraction

To test our inference framework we perform simulated surveys of LBG follow-up. We draw a realistic sample of LBGs at $z \sim 7$ from the Mason et al. (2015a) UV luminosity function model (which is consistent with all observations, including new deep data from the Hubble Frontier Fields at $z \gtrsim 7$ e.g., Atek et al., 2015b; McLeod et al., 2016; Livermore et al., 2017; Bouwens et al., 2017a). We populate these galaxies with an EW given by our simulated $p(W \,|\, \overline{x}_{\rm HI}, M_{\rm UV})$ (see Section 4.3.1) for several test values of the neutral fraction.

We assume an apparent magnitude limit of $m_{\rm AB} = 28.5$, corresponding to $M_{\rm UV} \sim -18.5$ and a 5σ flux limit of 10^{-18} erg s^{-1} cm^{-2}. We draw samples of 100 and 1000 total galaxies, and perform the inference on the full samples including upper limits.

In Figure 4.8 we plot the resulting posterior distributions for $\overline{x}_{\rm HI}$. With large samples we can clearly recover the input neutral fraction well. With small samples the posterior distribution is broader as we sample less of the likelihood, but the posteriors still include the input value within 1σ.

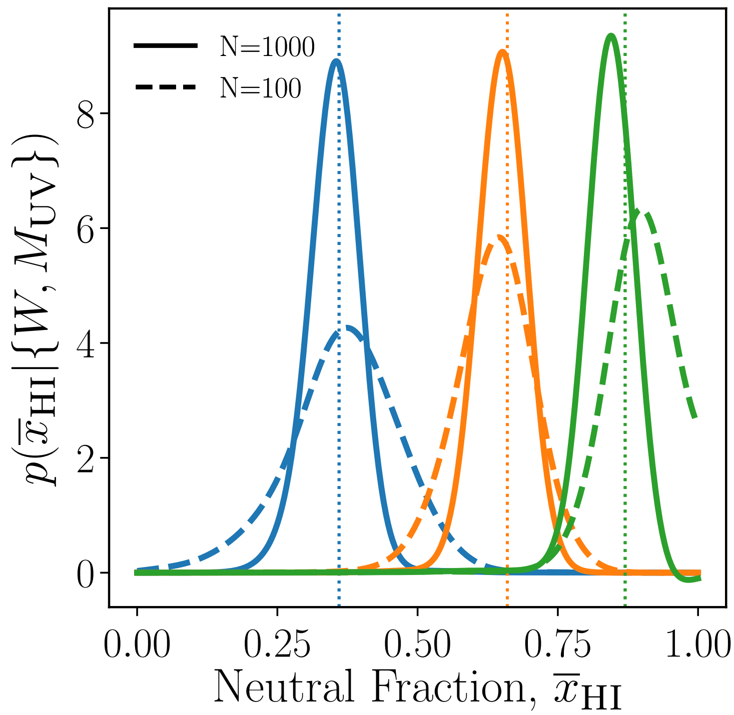

Figure 4.8: Posterior distributions for $\overline{x}_{\rm HI}$ from simulated samples of Lyα detections from 1000 (solid lines) and 100 (dashed lines) galaxies, for a simulation input value of $\overline{x}_{\rm HI} = [0.36, 0.66, 0.87]$ (blue, orange, green - the input value is shown by the vertical dotted line). With large samples input neutral fraction is recovered well. With smaller samples, the posterior is wider, but includes the true value within 1σ uncertainty.

4.4.2 Inference from current data

We use the inference framework described above to infer the neutral fraction from current observations. We take the largest published sample of LBGs at $z \sim 7$ with spectroscopic follow-up to-date, presented in Pentericci et al. (2014). These data comprise 68 galaxies spanning UV magnitudes $-22.75 \lesssim M_{\rm UV} \lesssim -17.8$ and include 10 intrinsically faint objects gravitationally lensed behind the Bullet Cluster (Bradač et al., 2012) as well as observations in deep HST legacy fields (Fontana et al., 2010; Vanzella et al., 2011; Ono et al., 2012; Schenker et al., 2012).

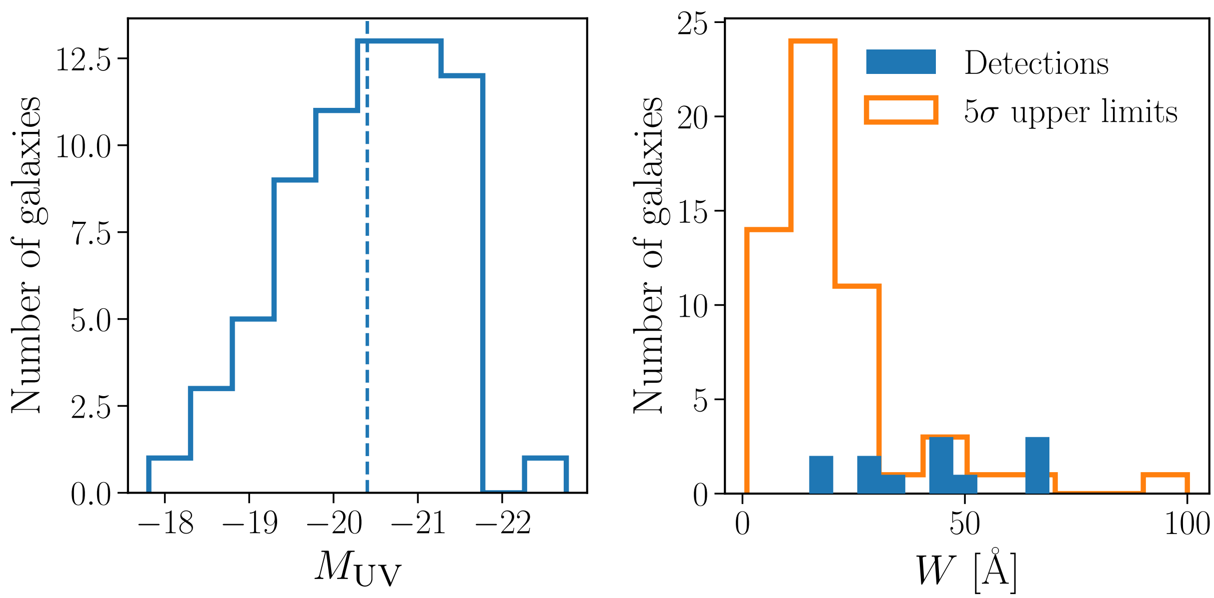

Figure 4.9: (Left) UV magnitude distributions for the $z \sim 7$ sample used for the inference. We plot the median UV magnitude of the sample as a dashed line ($M_{\rm UV} = -20.4$). (Right) EW distribution for the $z \sim 7$ sample used for the inference. We show both the Lyα EW measurements (filled blue) and 5σ upper limits for the non-detections (orange line)

In total, the sample comprises 8 independent lines-of-sight with field areas $\sim 50 - 100$ arcmin^2 each. The detections are spread over these fields. Pentericci et al. (2014) quantified the cosmic variance in this sample is very low ($\sim 6\%$ uncertainty in the optical depth to Lyα, see also Trenti & Stiavelli, 2008). Of the 68 LBGs 12 Lyα lines were spectroscopically confirmed. In Figure 4.9 we plot the UV magnitude and the EW distributions for this sample. As for the De Barros et al. (2017) $z \sim 6$ sample, the EW limits are obtained by inserting simulated lines of varying flux, FWHM, and redshift into raw data and then trying to recover them. A conservative minimum flux that could be measured over the entire wavelength range is used for the EW limit. Our framework utilizes the fact that the non-detections must be fainter than this conservative limit: fainter lines could be observed, e.g., in regions free of sky lines. Future work could include the wavelength-dependent line flux sensitivity in the likelihood for non-detections (Equation 4.11).

The majority of targets were z_{850}-dropouts selected primarily using a color criteria technique, described in detail in Grazian et al. (2012), to find targets with a high probability of having redshifts $6.5 \lesssim z \lesssim 7.5$. The median redshift for this selection function was $z = 6.9$ (see Figure 1 in Grazian et al., 2012). For literature targets not directly observed by the Pentericci et al. (2014) group, but included in the sample, they only included z-dropouts with colors consistent with the color selection criteria. As noted by Pentericci et al. (2014) the probability of galaxies being outside of the observable range for their setup ($z \sim 7.3$) is negligibly, except for the 10 objects in the Bullet Cluster (Bradač et al., 2012) where $\sim 48\%$ of objects could be above this redshift due to the broad J filter used for selection of that sample (Hall et al., 2012). To test the impact of these few objects potentially being at higher redshifts we ran the inference excluding the Bullet Cluster and found it does not significantly impact the results.

For each galaxy in this sample, we compute the likelihoods for obtaining the observed equivalent width or upper limit using Equations 4.10 and 4.11 for every value of the neutral fraction in our simulations. We exclude the brightest objects ($M_{\rm UV} < -22$, 1 object) due to the insufficient sampling of very massive halos in the simulations (see Section 4.2.2) and the uncertainty in their intrinsic EW evolution (Stark et al., 2017), but note this does not affect the inferred neutral fraction for our sample because the UV bright objects are so rare. We use an MCMC sampler (Foreman-Mackey et al., 2013) to infer the posterior distribution of $\overline{x}_{\rm HI}$ from these data, which is shown in Figure 4.10. We infer a neutral fraction of $\overline{x}_{\rm HI} = 0.59^{+0.11}_{-0.15}$ $(16 - 84\%)$.

This constraint is much tighter than previous measurements of the neutral fraction from Lyα observations (e.g., Pentericci et al., 2014; Mesinger et al., 2015) because we use the full distribution of equivalent widths, $p(W|M_{\rm UV})$ in our inference. Previous analyses used only the fraction of galaxies emitting Lyα with $W > 25$Å, $f_{{\rm Ly}\alpha}$, to constrain the neutral fraction. In Figure 4.10 we also plot the posterior distribution obtained if we had used only $f_{{\rm Ly}\alpha}$, i.e. the posterior is $p(\overline{x}_{\rm HI}|f_{{\rm Ly}\alpha})$, where we compare the simulation $f_{{\rm Ly}\alpha}(\overline{x}_{\rm HI})$ derived from Equation 4.13 with the fraction obtained in Pentericci et al. (2014): $f_{{\rm Ly}\alpha} = 0.29^{+0.20}_{-0.15}$ (for their faint sample, $20.25 < M_{\rm UV} < 18.75$). With just the Ly$\alpha$ fraction we infer a neutral fraction of $\overline{x}_{\rm HI} = 0.46 \pm 0.29$. Clearly, using the full distribution of EW enables us to constrain the neutral fraction much more accurately and, now large samples of LBGs with spectroscopic follow-up are available, should become the statistic of choice for Lyα reionization inferences.

Where does this constraint sit in our consensus picture of reionization? In Figure 4.11 we plot constraints derived from observations of: Lyα emission from galaxies (Mesinger et al., 2015); the clustering of Lyα emitting galaxies (Ouchi et al., 2010; Sobacchi & Mesinger, 2015); Lyα and Lyβ forest dark fraction (McGreer et al., 2015); QSO ULASJ1120+0641 damping wings (Greig & Mesinger, 2017b). We also plot the neutral hydrogen fraction as a function of redshift, using the Mason et al. (2015a) UV luminosity function model assuming galaxies are the source of ionizing photons and using two limiting magnitudes for the galaxy population: $M_{\rm UV} < -17$ (currently detectable galaxies) and $M_{\rm UV} < -12$ (ultra-faint undetected galaxies). The uncertainties in the Mason et al. (2015a) reionization histories comes from the range of possible reionization parameters (e.g., ionizing photon escape fraction, IGM clumping factor, number of ionizing photons per UV photon).

Our constraint is consistent within 1σ with the other constraints at $z \sim 7$, providing more strong evidence that reionization is on-going at $z \sim 7$. Our constraint lies $\Delta\overline{x}_{\rm HI} \sim 0.2$ higher than the constraint from the $z = 7.1$ QSO ULASJ1120+0641 damping wings (Greig et al., 2017), but is still consistent within the uncertainties.

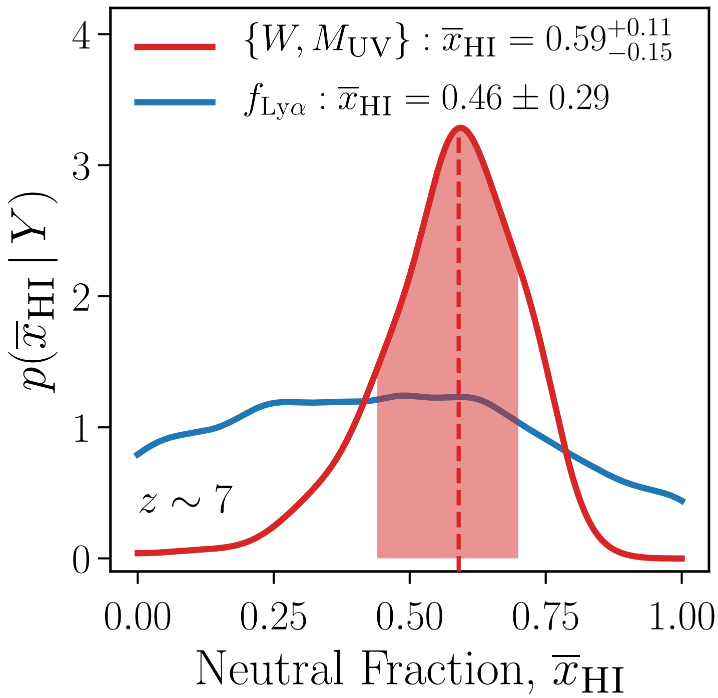

Figure 4.10: Posterior distribution for $\overline{x}_{\rm HI}$ from the dataset of 68 galaxies at $z \sim 7$ (including 12 with detected Lyα emission) from Pentericci et al. (2014). In red we plot the posterior distribution obtained from the full sample of $\{W, M_{\rm UV}\}$ measurements as described in Section 4.3, and infer a neutral fraction of $\overline{x}_{\rm HI} = 0.59^{+0.11}_{-0.15}$ $(16-84\%)$. The dashed line shows the median value, and shaded region shows the (16$^{\rm th}$ and 84$^{\rm th}$) percentile bounds. For comparison, in blue we plot the posterior for $\overline{x}_{\rm HI}$ obtained if we used only the fraction of galaxies emitting Lyα with $W > 25$Å, $f_{\rm Ly\alpha}$. In this case we infer $\overline{x}_{\rm HI} = 0.46 \pm 0.29$. Using the full distribution of EW provides much more information about the evolving IGM compared to $f_{\rm Ly\alpha}$ and allows for tighter constraints on the neutral fraction.

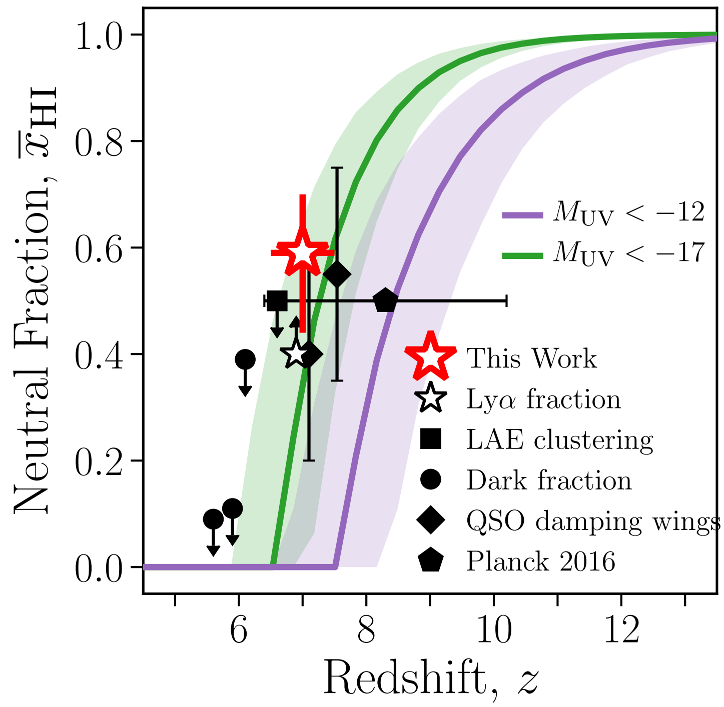

Figure 4.11: The fraction of neutral hydrogen as a function of redshift. Our new constraint is plotted as a red open star. We plot constraints derived from observations of: previous estimates from the fraction of LBGs emitting Lyα (open black star, Mesinger et al., 2015); the clustering of Lyα emitting galaxies (square, Ouchi et al., 2010; Sobacchi & Mesinger, 2015); Lyα and Lyβ forest dark fraction (circle, McGreer et al., 2015); and QSO damping wings (diamond, Greig & Mesinger, 2017b; Bañados et al., 2017). We offset the constraints at $z \sim 7$ (QSO ULASJ1120+0641 damping wing, Greig et al., 2017, Lyα fraction and our new constraint) by $\delta z = 0.1$ for clarity. We also plot the Planck Collaboration et al. (2016b) redshift range of instantaneous reionization (black hatched region). We show as shaded regions the reionization history from integrating the Mason et al. (2015a) UV luminosity function to two magnitude limits of $M_{\rm UV} = -17$ (green) and $M_{\rm UV} = -12$ (purple) and drawing from uniform distributions for the ionizing photon escape fraction $10-30\%$ and clumping factor $C = 1-6$, and log-normal distribution for the ionizing efficiency $\xi_{\rm ion}$ with mean 25.2 and standard deviation 0.15 dex. There are many uncertainties in obtaining the reionization history from luminosity functions so these should not be taken as real constraints on the neutral fraction, but given that galaxies fainter than $M_{\rm UV} = -17$ likely exist (e.g., Kistler et al., 2009; Weisz & Boylan-Kolchin, 2017; Livermore et al., 2017; Bouwens et al., 2017b) our result suggests high escape fractions may not be necessary for reionization.

4.4.3 Predictions for JWST

JWST will be uniquely equipped to observe Lyα and rest-frame optical emission lines into Cosmic Dawn, with extremely sensitive spectrometers NIRSpec and NIRISS covering $1-5\,\mu$m in a large field of view (Gardner et al., 2006; Stiavelli et al., 2007). This will enable direct measurement of the Lyα Δv and detailed studies of the ISM properties of galaxies during Reionization.

Using our inferred value of $\overline{x}_{\rm HI} = 0.59^{+0.11}_{-0.15}$ for the neutral fraction at $z \sim 7$ we predict the number of Lyα emitters detectable in one NIRSpec pointing ($\sim$ 9 sq arcmins) by drawing galaxies from the Mason et al. (2015a) UV luminosity function and populating them with EW given by our simulated $p(W \,|\, \overline{x}_{\rm HI}, M_{\rm UV})$. We transform Ly$\alpha$ equivalent width W to flux using the relation:

$$f(W, m, z) = W f_0 10^{-0.4 m_{\rm UV}} \frac{c}{\lambda_\alpha^2 (1+z)} \left(\frac{\lambda_{\rm UV}}{\lambda_\alpha}\right)^{-\beta-2} \tag{4.14}$$

where $f_0 = 3.631 \times 10^{-20}$ erg s^{-1} Hz^{-1} cm^{-2}, $m_{\rm UV}$ is the apparent magnitude of the UV continuum, c is the speed of light, λ_α is the rest-frame wavelength of Lyα, $\lambda_{\rm UV}$ is the rest-frame wavelength of the UV continuum (usually 1500Å), and β is the UV slope. For simplicity we assume $\beta = -2$, consistent with observations of $z \sim 7$ objects (e.g., Bouwens et al., 2012), though very UV faint galaxies likely have steeper slopes due to extremely low metallicities (Vanzella et al., 2016).

We plot the predicted number counts in Figure 4.12, where we assume a 5σ UV continuum flux limit of $m_{\rm AB} > 29$ ($M_{\rm UV} \sim -18$, corresponding to $\sim$ 1 hour integration in JWST NIRCam). We predict a 3 hour exposure in one pointing ($\sim$ 9 sq arcmins) with JWST NIRSpec will detect $\sim 6 \pm 3$ $z \sim 7$ Lyα lines with a 5σ flux limit of $\sim 3 \times 10^{-18}$ erg s^{-1} cm^{-2} (calculated using the JWST ETC), from a total of $\sim$ 80 LBG dropout detections. We also show the forecast for a cluster lensing survey (e.g., GLASS, Treu et al., 2015; Schmidt et al., 2016) assuming a simple uniform magnification factor of $\mu = 2$ due to gravitational lensing (i.e. $p(\mu) = \delta(\mu - 2)$). In this case, all fluxes are magnified by μ whilst the area decreases by $1/\mu$, and assuming the same flux limit as above we predict $\sim 10 \pm 2$ Lyα lines from a total of $\sim$ 90 LBG detections. The NIRSpec field-of-view is still small compared to large scale structure at $z \sim 7$ so wide area random pointing surveys will be essential to estimate the global $\overline{x}_{\rm HI}$.

We simulate a 10 pointing NIRSpec survey with F070LP/G140M ($R = 1000$), with 3 hour exposures in each field, by again sampling the Mason et al. (2015a) luminosity function in a larger area. We perform the inference on these mock JWST observations at $z \sim 7$, assuming $\overline{x}_{\rm HI} = 0.59$. This yields ~ 60 detections from ~ 800 LBGs. Again, we assume a 5σ flux limit of $> 3 \times 10^{-18}$ erg s^{-1} cm^{-2}. The posterior distribution obtained from the JWST mock observations is shown in Figure 4.13, with the posterior from the current observations (Section 4.4.2) shown for comparison. We obtain $\overline{x}_{\rm HI} = 0.60^{+0.02}_{-0.06}$, a $\sim 70\%$ reduction in uncertainty compared to the current sample. We note this is an average forecast, and a more realistic survey forecast would require sampling the simulation directly (e.g., Mesinger & Furlanetto, 2008a). We also caution our mock survey assumes 100% completeness, and maximized filling of NIRSpec slits, but, nevertheless, observations with NIRSpec will constrain the neutral fraction much more tightly than current observations.

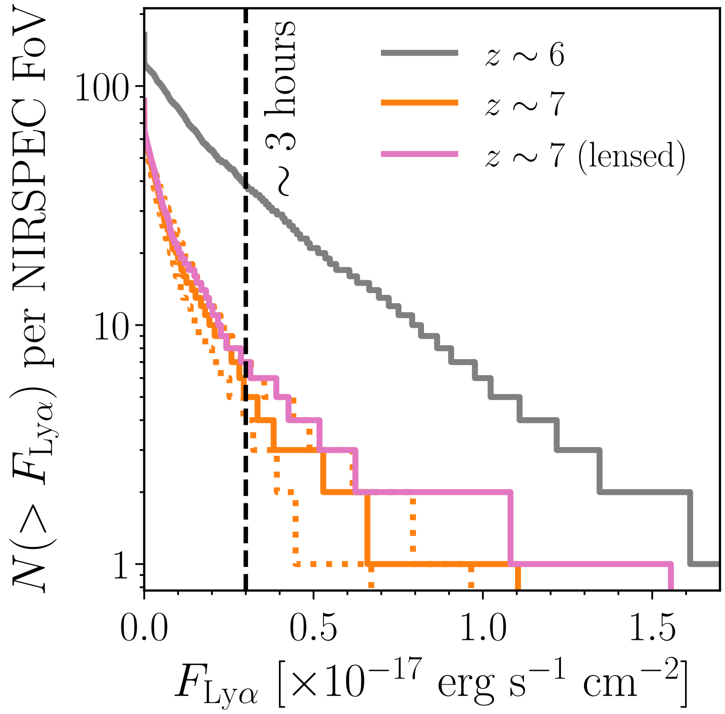

Figure 4.12: Predicted cumulative number counts of LAEs with JWST NIRSpec at $z \sim 6$ (gray), and $z \sim 7$ (orange) using our recovered neutral fraction $\overline{x}_{\mathrm{HI}} = 0.59^{+0.11}_{-0.15}$. Galaxies are drawn from the Mason et al. (2015a) UV luminosity function model and populated with equivalent widths via $p(W \mid M_{\mathrm{UV}}, \overline{x}_{\mathrm{HI}})$ - the likelihood described in Section 4.3.1. The number counts obtained within the $(16 - 84\%)$ regions on $\overline{x}_{\mathrm{HI}}$ are shown as dotted orange lines. We also show the cumulative number counts for a gravitationally lensed field where we assume a uniform magnification factor of $\mu = 2$ (pink line), which would reveal more emission lines. We obtain the Lyα fluxes using Equation 4.14. The dashed black line shows the flux limit for a ~ 3 hour exposure at $R = 1000$ with JWST NIRSpec F070LP/G140M at $1 - 1.5\mu$m calculated with the JWST ETC (`https://jwst.etc.stsci.edu`)

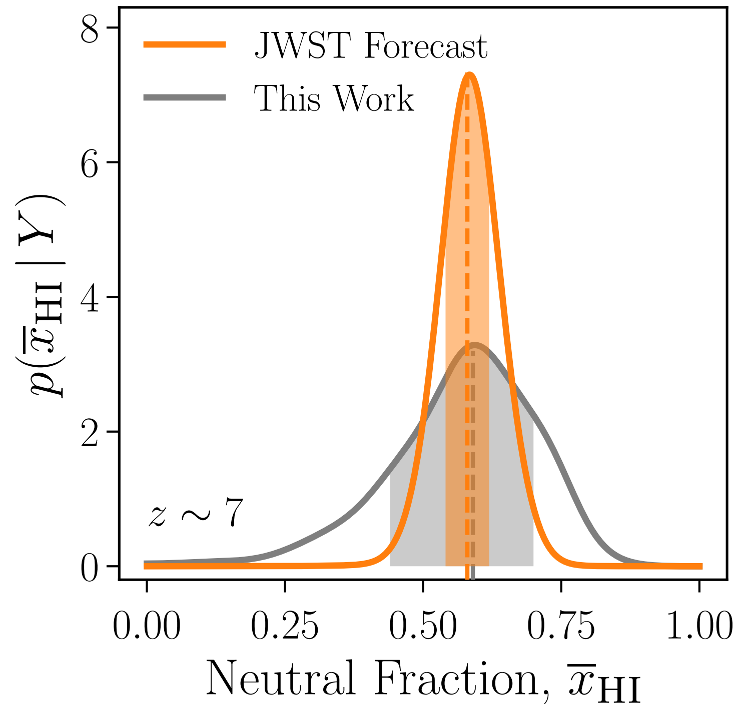

Figure 4.13: Posterior distribution of $\overline{x}_{\rm HI}$ for a simulated 10 pointing JWST NIRSpec survey (orange) which is able to tightly constrain the IGM neutral fraction compared to our inference on current observations (red - same as Figure 4.10). Dashed lines show the median of the distributions, the shaded regions show the $16-84\%$ regions. We take a 10 pointing JWST/NIRSpec mock survey at $z \sim 7$ which assumes $\overline{x}_{\rm HI} = 0.58$ as described in Section 4.4.3, and perform Bayesian inference, assuming a 5σ flux limit of $> 3 \times 10^{-18}$ erg s^{-1} cm^{-2}. We show the posterior distribution for $\overline{x}_{\rm HI}$ inferred from current data (as described in Section 4.4.2) for comparison. In this example JWST could reduce the uncertainty on the neutral fraction by $\sim 70\%$.

4.5 Discussion

In this section we discuss our result in the context of other probes of reionization (Section 4.5.1), and we discuss the implications of the mass-dependent Lyα velocity offset on the evolving Lyα fraction for average (Section 4.5.2) and UV bright (Section 4.5.3) galaxies.

4.5.1 The global reionization history

Robust constraints on the reionization history are challenging. Whilst quasars provide high S/N information about individual (but rare) lines of sight they are likely to be biased to overdense and more ionized regions (Barkana & Loeb, 2004; Mesinger, 2010; Decarli et al., 2017), and the number densities of bright quasars drop dramatically at $z > 6$ (Fan et al., 2001; Manti et al., 2016; Parsa et al., 2018). Constraining reionization with large samples of galaxies clearly avoids these problems; with the help of gravitational lensing in clusters, e.g. the Frontier Fields (Lotz et al., 2017), we know there are large populations of faint galaxies at $z > 6$ (Yue et al., 2014; Atek et al., 2015a; Livermore et al., 2017; Vanzella et al., 2017), and GRB host galaxy searches indicate far fainter galaxies must also exist (Kistler et al., 2009; Trenti et al., 2012a).

Lyα emission from galaxies has long been recognized as a probe of reionization (Haiman & Spaans, 1999; Malhotra & Rhoads, 2004; Santos, 2004; Verhamme et al., 2006; McQuinn et al., 2007a; Dijkstra, 2014), and the framework presented in this paper provide a direct constraint on the IGM neutral fraction from observations of Lyα emission from galaxies, incorporating both realistic galaxy properties and realistic IGM topologies for the first time.

Our constraint on the neutral fraction, $\overline{x}_{\rm HI} = 0.59^{+0.11}_{-0.15}$, is consistent with other robust probes of IGM neutrality at $z \sim 7$ (Mesinger et al., 2015; Greig et al., 2017) demonstrating the power of Lyα follow-up of LBGs to constrain the neutral fraction, and providing more strong evidence that the IGM is undergoing significant reionization at $z \sim 7$. Using the full distribution of observed $\{W, M_{\rm UV}\}$ as inputs to our inference provides much tighter constraints than using the standard 'Lyα fraction', as we demonstrated in Figure 4.10.

Our median value lies $\Delta\overline{x}_{\rm HI} \sim 0.2$ higher than that inferred by Greig et al. (2017) from the QSO ULASJ1120+0641 damping wings at $z = 7.1$, which was obtained using the same IGM simulations, though our posterior distribution is marginally skewed to lower values (see Figure 4.10). This offset is not significant given the uncertainties, and does not require us to invoke any additional evolution in galaxy properties. Within the next few years larger samples, as demonstrated in our mock survey with JWST described in Section 4.4.3, will greatly reduce the uncertainties in our constraints from Lyα detections and non-detections.

With large samples, it will be possible to measure the variations in $\overline{x}_{\rm HI}$ over the sky, and cross-correlate with other constraints from quasars and eventually 21cm observations

(Lidz et al., 2009; Vrbanec et al., 2016; Sobacchi et al., 2016; Mirocha et al., 2016; Mesinger et al., 2016; Greig & Mesinger, 2017a) to directly observe the inhomogeneous process of reionization. Furthermore, with tighter constraints on the timeline of reionization, it will be possible to better constrain the sources of ionizing photons: as the ionizing photon budget from galaxies depends on e.g., the minimum mass/luminosity of galaxies and the rate of ionizing photons per unit UV luminosity.

4.5.2 A sudden drop in Lyα emission – redshift evolution of Δv?

In our model, we include empirically calibrated relations for both the intrinsic dependence of Lyα EW on UV magnitude and ISM radiative transfer in galaxies of a given halo mass (UV magnitude at fixed redshift), which builds in a simple redshift evolution assuming galaxies of the same UV magnitude live in less massive halos at higher redshifts. In this framework, UV faint galaxies have intrinsically high EW than UV bright galaxies and lower Lyα velocity offsets.

These correlations are motivated by numerous observations of Lyα emission from galaxies at a range of redshifts, including very low redshift samples where detailed spatial and spectral observations are possible (Hayes et al., 2013; Yang et al., 2016). It is likely the density and distribution of neutral gas in the ISM plays a key role in the mediation of Lyα propagation through galaxies: an ISM with high column densities of neutral hydrogen, N_{HI}, scatters Lyα photons more significantly, spectrally and spatially (Verhamme et al., 2006; Zheng et al., 2010). Observations of $z < 4$ galaxies confirm high N_{HI} correlates with high Lyα velocity offset (Yang et al., 2016; Hashimoto et al., 2015; Henry et al., 2015), and more Lyα extended halos (Hayes et al., 2013; Guaita et al., 2017).

With increasing redshift, when galaxies were less massive (Lacey & Cole, 1993), Lyα should escape more easily with high EW: these galaxies will contain less dust (as ALMA and Plateau de Bure Interferometer (PdBI) results are suggesting, Walter et al., 2012; Ouchi et al., 2013; Ota et al., 2014; Schaerer et al., 2015; Maiolino et al., 2015; Capak et al., 2015; Bouwens et al., 2016b; Pentericci et al., 2016) and neutral gas than at low redshifts. Additionally, the covering fraction of neutral hydrogen may evolve with galaxy mass, star formation rate, stellar populations and/or redshift. Hard ionizing spectra from low metallicity stars (which may be significant at high redshifts, Mainali et al., 2017; Stark et al., 2015; Schmidt et al., 2017; Stark et al., 2017) can create more ionized holes through the ISM, reducing the covering fraction, an effect which is enhanced for low mass galaxies (Trebitsch et al., 2017). A low covering fraction would facilitate Lyα escape closer to the galaxy systemic velocity, and some observations have indicated a decreasing covering fraction with redshift (Leethochawalit et al., 2016b; Jones et al., 2013b).

All these factors, and the correlation of Δv with halo mass as shown in Figure 4.2, suggest velocity offsets should decrease with increasing redshift for galaxies at fixed UV magnitude. These low velocity offsets are correlated with reduced scattering within the ISM and thus a higher EW of Lyα. This should increase the visibility of Lyα *until* the IGM starts to become neutral and these low Δv lines are easily attenuated by nearby neutral hydrogen. As was noted by Mesinger et al. (2015) and Choudhury et al. (2015) this offers a simple explanation for evolving galaxy properties which may accelerate the decline in Lyα in UV faint galaxies.

4.5.3 Lyα from UV bright galaxies – redshifted away from resonance?

A high fraction of Lyα observed in some UV bright ($M_{\rm UV} < -21.5$) galaxies at $z > 6$ (Curtis-Lake et al., 2012; Stark et al., 2017, though c.f. Treu et al. (2013) for non-detections of Lyα in slightly fainter galaxies) is surprising for several reasons: the electron scattering optical depth from the Planck Collaboration et al. (2016b) favors a significant IGM neutral fraction at these redshifts, with instantaneous reionization occurring at $z = 7.8 - 8.8$; and the observed fraction of UV faint galaxies appears to steadily decrease at the same redshifts (Pentericci et al., 2014; Schenker et al., 2014). Why can we more easily see Lyα in some UV bright galaxies into the Epoch of Reionization?

The most UV bright galaxies at high redshift probably reside in halos with mass $\gtrsim 10^{11} M_\odot$, which may already have stable gaseous disks, as suggested by recent ALMA observations of two UV bright galaxies at $z \sim 6$ (Smit et al., 2018) and observations of stable rotation in low mass galaxies at $z \sim 1-2$ (Stott et al., 2016; Mason et al., 2017). Thus, it is likely Lyα photons traveling from these galaxies will experience significant radiative transfer effects with the ISM.

The enhanced Doppler shift of the emerging Lyα photons in UV bright galaxies provides some explanation for the high fraction of Lyα observations for these populations compared to UV faint galaxies at $z \sim 7$. As shown in Figures 4.6 and 4.7, we predict transmission of UV bright galaxies evolves more slowly with the evolving IGM compared to fainter objects, making them visible far into the epoch of reionization and thus prime targets for spectroscopic confirmation. Though note their underlying EW distribution is likely much steeper and has a higher peak of non-emitters than for UV faint galaxies. When Lyα is emitted from UV bright objects it is likely to have low EW as the photons are so dispersed spatially and spectrally.

However, this effect is also highly correlated to the large scale environment in which these galaxies reside; assessing the relative contributions of evolving galaxy properties and environment to this apparent increase in the Lyα fraction is explored by Mason et al. (2018b). The high Lyα transmission of UV bright galaxies make them ideal targets for spectroscopic follow-up to understand the star formation processes occurring in the early universe.

4.6 Summary and Conclusions

We have developed a flexible Bayesian inference framework to infer the IGM neutral fraction during reionization by forward-modeling the observed equivalent width distribution of Lyα emission from LBGs. Our model incorporates sightlines through realistic IGM simulations to model galaxies with realistic ISM properties.

Our main conclusions are as follows:

(i) The Lyα line profile emerging from the ISM has a huge impact on the probability of transmission through the IGM (Dijkstra et al., 2011), and is related to the properties of the source galaxy. This must be systematically accounted for in reionization inference.

(ii) We introduce a simple empirical relation between the halo mass of a galaxy (or UV luminosity at fixed redshift) and its Lyα line peak velocity offset, where the most massive galaxies have the largest velocity offsets likely due to increased $N_{\rm HI}$ in the ISM, higher halo circular velocities and/or the presence of star-formation induced outflows.

(iii) This relation predicts that with increasing redshift, Lyα velocity offsets will decrease for galaxies at fixed UV luminosity, making Lyα lines more susceptible to absorption in the IGM. This effect would accelerate the decline in Lyα emission compared to other reionization probes and be a factor in explaining the sudden drop of Lyα emission observed at $z > 6$.

(iv) We conduct a Bayesian inference from current observations at $z \sim 7$ from Pentericci et al. (2014) and infer the first direct constraint on the neutral fraction from Lyα transmission of $\overline{x}_{\rm HI} = 0.59^{+0.11}_{-0.15}$, which is consistent with other robust probes of the neutral fraction and confirms reionization is on-going at $z \sim 7$.

(v) Using the full distribution of Lyα equivalent width measurements enables us to provide much tighter constraints on the neutral fraction compared to the standard 'Lyα fraction', $P(W > 25\text{Å})$, used in previous analyses.

(vi) We make predictions for spectroscopic surveys with JWST and find a ~ 30 hour LBG follow-up survey with JWST/NIRSpec could reduce the uncertainty in $\overline{x}_{\rm HI}$ by $\sim 70\%$.

Future near-IR spectrographs in space, such as JWST NIRSpec and NIRISS, will be able to observe both Lyα and rest-frame optical lines for galaxies to $z \lesssim 12$ and to measure SFRs and Lyα velocity offsets for these objects, enabling us to further understand the interactions between star-forming regions, the ISM, and the reionizing IGM. It will soon be possible to apply our framework to large samples, free of cosmic variance, to get accurate universal constraints on the evolution of the neutral fraction.

The authors thank Dawn Erb and Dan Stark for providing their observational data. We thank Simon Birrer, Fred Davies, Max Gronke, Joe Hennawi and Crystal Martin for useful discussions.

C.M. acknowledges support by NASA Headquarters through the NASA Earth and Space Science Fellowship Program Grant NNX16AO85H. A.M. acknowledges support from the European Research Council (ERC) under the European Unions Horizon 2020 research and innovation program (grant agreement No 638809 AIDA). This research was partially supported by the Australian Research Council through awards FT130101593 and CE170100013. This work was supported by the HST BoRG grants GO-12572, 12905, and 13767, and the HST GLASS grant GO-13459

This work made use of the following open source software: IPython (Pérez & Granger, 2007), matplotlib (Hunter, 2007), NumPy (Van Der Walt et al., 2011), SciPy (Oliphant, 2007), Astropy (Robitaille et al., 2013) and EMCEE (Foreman-Mackey et al., 2013).

CHAPTER 5

Beacons into the Cosmic Dark Ages: Boosted transmission of Lyα from UV bright galaxies at $z \gtrsim 7$

This paper was Mason, Treu, de Barros, Dijkstra, Fontana, Mesinger, Pentericci, Trenti, & Vanzella (published as 2018b, ApJL, 857, 11) and reproduced here with minor formatting changes.

ecent detections of Lyman alpha (Lyα) emission from $z > 7.5$ galaxies were somewhat unexpected given a dearth of previous non-detections in this era when the intergalactic medium (IGM) is still highly neutral. But these detections were from UV bright galaxies, which preferentially live in overdensities which reionize early, and have significantly Doppler-shifted Lyα line profiles emerging from their interstellar media (ISM), making them less affected by the global IGM state. Using a combination of reionization simulations and empirical ISM models we show, as a result of these two effects, UV bright galaxiesin overdensities have $> 2\times$ higher transmission through the $z \sim 7$ IGM than typical field galaxies, and this boosted transmission is enhanced as the neutral fraction increases. The boosted transmission is not sufficient to explain the observed high Lyα fraction of $M_{\text{UV}} \lesssim -22$ galaxies (Stark et al., 2017), suggesting Lyα emitted by these galaxies must be stronger than expected due to enhanced production and/or selection effects. Despite the bias of UV bright galaxies to reside in overdensities we show Lyα observations of such galaxies can accurately measure the global neutral hydrogen fraction, particularly when Lyα from UV faint galaxies is extinguished, making them ideal candidates for spectroscopic follow-up into the cosmic Dark Ages.

5.1 Introduction

Reionization of hydrogen in the universe's first billion years was driven by the first sources of light. Accurately measuring the timeline of reionization, i.e. average neutral hydrogen fraction ($\overline{x}_{\rm HI}$) as a function of redshift, enables us to infer properties of these sources. Lyα emission from galaxies has long been touted as a tracer of $\overline{x}_{\rm HI}$ during reionization: Lyα photons are absorbed by neutral hydrogen (e.g., Dijkstra, 2014).

The rapidly declining fraction of Lyman-break galaxies (LBGs) emitting Lyα at $z > 6$ (e.g., Fontana et al., 2010; Stark et al., 2010; Treu et al., 2013; Schenker et al., 2014; Pentericci et al., 2014; Mason et al., 2018a) and strong damping wing absorption of $z \sim 7$ quasar spectra (Greig et al., 2017; Bañados et al., 2017) suggest the universe is significantly neutral at $z \gtrsim 7$. Recent detections of Lyα from galaxies at $z > 7.5$ (Roberts-Borsani et al., 2016; Zitrin et al., 2015b; Oesch et al., 2015; Stark et al., 2017) are therefore surprising. Furthermore, these detections come from $M_{\rm UV} \lesssim -22$ galaxies ($\gtrsim 2.5L^*$). At lower redshifts UV bright galaxies are least likely to have strong Lyα (e.g. Stark et al., 2010). Why can we see Lyα from these galaxies?

Reionization is likely highly inhomogeneous – overdense regions reionize more rapidly as they are filled with many ionizing sources (e.g., McQuinn et al., 2007b). The brightest galaxies likely reside in overdensities (e.g., Trenti et al., 2012b; Barone-Nugent et al., 2014; Castellano et al., 2016). How easily are Lyα photons from such galaxies in overdensities transmitted through the IGM, compared to field galaxies? How does the ISM radiative transfer of Lyα affect its IGM transmission? (Figure 5.1) Can these biased galaxies still measure $\overline{x}_{\rm HI}$?

Here we combine cosmological reionization simulations with empirical models of galaxy properties to understand the transmission of Lyα from UV bright galaxies. We describe our combination of simulations and empirical models in Section 5.2. In Section 5.3 we present our results on the evolving transmission of Lyα emission from galaxies in massive halos, the interpretation of the observed 'Lyα fraction', and the efficacy of UV bright galaxies as probes of $\overline{x}_{\rm HI}$. We discuss our results in Section 5.4 and summarize in Section 5.5.

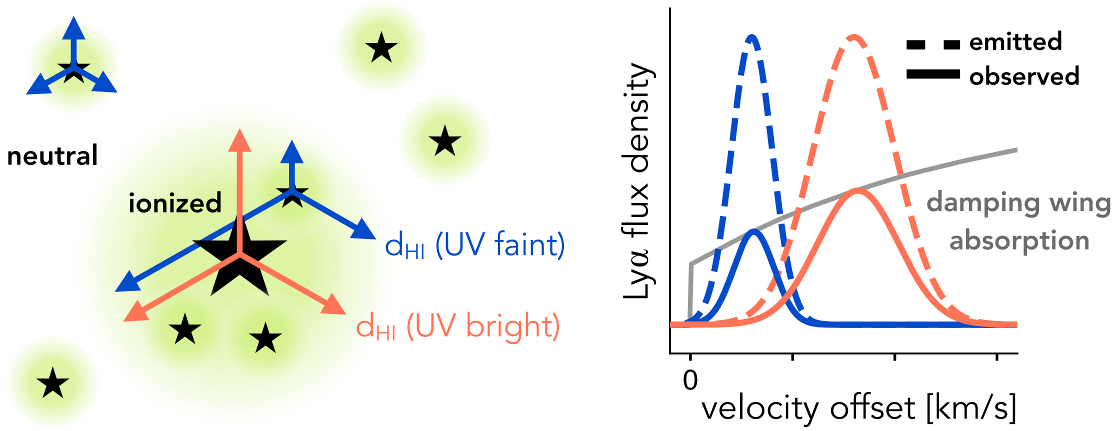

Figure 5.1: Left: UV bright galaxies (large stars) preferentially live in overdensities, which reionize early (green regions). Lyα damping wing optical depths are dominated by the distance to the first neutral patch (white regions) photons encounter, d_{HI}, thus UV bright galaxies have higher average Lyα transmission than UV faint galaxies (small stars) as they live further from neutral patches. The sightline-to-sightline scatter of Lyα transmissions for UV bright galaxies is lower due to lower scatter in d_{HI} (orange arrows for UV bright galaxies, blue arrows for UV faint galaxies). **Right:** Gas and dust resonantly scatter and absorb Lyα photons inside galaxies. Lyα emitted (dashed lines) by UV bright galaxies (orange) is usually more Doppler-shifted than Lyα from UV faint galaxies (blue), as they contain more gas and dust. Damping wing absorption during reionization attenuates Lyα smoothly with wavelength/velocity offset (gray line – example shown is $\overline{x}_{\mathrm{HI}} = 0.66$), so Ly$\alpha$ transmitted (solid lines) through the IGM depends on galaxy properties.

We use the Planck Collaboration et al. (2016a) cosmology. All magnitudes are in the AB system.

5.2 Method

To model the transmission of Lyα photons from galaxies through the reionizing IGM we combine the public Evolution of Structure simulations (EoS[1], Mesinger et al., 2016) with empirical models of galaxy properties. We follow the method of Mason et al. (2018a) (hereafter M18) and refer the reader there for more details. We describe our methods briefly below.

The EoS simulations treat inhomogeneous recombinations and ionizations at a sub-grid

[1] http://homepage.sns.it/mesinger/EOS.html

level on a density field in a 1024^3 box with sides 1.6 Gpc. The simulations have two runs to bracket the potential reionization parameter space: FAINT GALAXIES, where ionization sources are primarily low mass galaxies, producing reionization morphologies characterized by small HII patches; and BRIGHT GALAXIES, where reionization is dominated by more massive galaxies, producing larger HII patches. We use the fiducial FAINT GALAXIES, but show in Section 5.3.1 our results do not significantly depend on the choice of simulation run.

We populate dark matter halos in the simulations with physically motivated galaxy properties: UV luminosities from the Mason et al. (2015a) model; and emitted Lyα rest-frame equivalent widths (EW) and Lyα line velocity offsets from source galaxies' systemic redshifts, Δv. We use the empirical model presented by M18 where Δv is correlated with halo mass to encompass the complex ISM radiative transfer. Massive halos have higher Δv, likely due to increased scattering in their denser ISM (Figure 5.1, right panel). We model lines as Gaussians, centered at Δv, with $FWHM = \Delta v$ (for $\Delta v < 20$ km s^{-1} we set $FWHM = 20$ km s^{-1}, comparable to the maximum expected thermal broadening). We assume the observed $z \sim 6$ Lyα EW distribution, $p(EW_{\mathrm{Ly}\alpha})$, is equivalent to the emitted $z \sim 7$ $p(EW_{\mathrm{Ly}\alpha}^{\mathrm{emit}})$ (i.e. the change observed between these redshifts is due to reionization only) and use a $p(EW_{\mathrm{Ly}\alpha}|M_{\mathrm{UV}})$ fit to the $z \sim 6$ sample presented by De Barros et al. (2017) (the fit is described by M18, and accounts for Lyα non-detections).

A key quantity we compute is the differential *transmission fraction* of Lyα photons through the IGM: $\mathcal{T}_{\mathrm{IGM}}(\overline{x}_{\mathrm{HI}}) = EW(\overline{x}_{\mathrm{HI}})/EW(\overline{x}_{\mathrm{HI}} = 0)$. We calculate $\mathcal{T}_{\mathrm{IGM}}$ by modeling the emitted Lyα lineshape and attenuating it with the damping wing absorption optical depth (τ_{IGM}) from cosmic neutral hydrogen patches along the line of sight in the simulations:

$$\mathcal{T}_{\mathrm{IGM}}(\overline{x}_{\mathrm{HI}}, M_h, \Delta v) = \int_0^\infty \mathrm{d}v \; J_\alpha(\Delta v, M_h, v) e^{-\tau_{\mathrm{IGM}}(\overline{x}_{\mathrm{HI}}, M_h, v)} \tag{5.1}$$

where $J_\alpha(\Delta v, M_h, v)$ is the normalized Lyα lineshape emitted from galaxies. We model circumgalactic medium (CGM) absorption by truncating the lineprofiles at the halo circular velocity. As we are only interested in the differential evolution of EW this is valid assuming the only significant change in the optical depth to Lyα between $z \sim 6$ and $z \sim 7$ is due to reionization. We discuss the impact of an evolving CGM in Section 5.4.

We calculate $\mathcal{T}_{\text{IGM}}$ for millions of realizations of model galaxies along thousands of sightlines in 40 $z = 7$ IGM simulation cubes with average neutral fractions $0 \leq \overline{x}_{\text{HI}} \leq 0.95$ ($\Delta\overline{x}_{\text{HI}} \sim 0.02$) to generate $p(\mathcal{T}_{\text{IGM}}|\overline{x}_{\text{HI}}, M_h)$ and forward-model the observed $p(EW_{\text{Ly}\alpha})$.

5.3 Results

Here we describe the key results of our study: Lyα from UV bright galaxies in massive halos can have high transmission through the IGM, even in a highly neutral universe (Section 5.3.1); our model is consistent with the observed evolution of the Lyα fraction, except for extremely bright galaxies ($M_{\text{UV}} \lesssim -22$) which must have higher than expected emitted Lyα EWs (Section 5.3.2); and UV bright galaxies can measure $\overline{x}_{\text{HI}}$ if their emitted Lyα EW distribution is known (Section 5.3.3).

5.3.1 Boosted transmission of Lyα from massive halos

To explore the differences between the most biased galaxies and the bulk of the high redshift galaxy population we examine $p(\mathcal{T}_{\text{IGM}})$ in two halo mass bins: $10^{11.5} \leq M_h \leq 10^{12} M_\odot$ (57 sightlines in the EoS simulations, hosting $M_{\text{UV}} \lesssim -21$ galaxies) and $10^{10} \leq M_h \leq 10^{11}$ ($\sim 10^4$ sightlines, $M_{\text{UV}} \gtrsim -19.5$ galaxies, comparable to the faintest $z > 6$ LBGs with detected Lyα, e.g. Huang et al., 2016b; Hoag et al., 2017).

Figure 5.2 shows $p(\mathcal{T}_{\text{IGM}}|\overline{x}_{\text{HI}}, M_h)$, using three models for Lyα velocity offsets: (1) drawn from the M18 $p(\Delta v|M_h)$ model: low mass halos have median $\Delta v \sim 90$ km s^{-1}, high mass halos have median $\Delta v \sim 220$ km s^{-1}. (2) $\Delta v = 200$ km s^{-1}, often the fiducial value used in reionization Lyα modeling (e.g., Dijkstra et al., 2011; Mesinger et al., 2015). (3) $\Delta v = 50$ km s^{-1}.

Irrespective of emitted line properties, galaxies in massive halos have higher $\mathcal{T}_{\text{IGM}}$, as they preferentially live in overdensities which reionize early (e.g., McQuinn et al., 2007b), so their Lyα photons are redshifted into the flattest part of the damping wing (Figure 5.1) by the time they reach cosmic neutral patches. Mass-dependent velocity offsets enhance this effect:

Lyα from low mass halos is more easily attenuated as they have low Δv, whereas $\mathcal{T}_{\text{IGM}}$ from massive halos is boosted.

The scatter in $\mathcal{T}_{\text{IGM}}$ is lower for massive halos: the smaller scatter in distance from source galaxies to the first neutral patch (Figure 5.1) reduces the sightline-to-sightline variation in optical depths. This makes galaxies in massive halos accurate probes of $\overline{x}_{\text{HI}}$. The effect is most pronounced for $0.3 \lesssim \overline{x}_{\text{HI}} \lesssim 0.6$, when neutral patches are narrower and more widely separated (Mesinger & Furlanetto, 2008a). As noted by Mesinger & Furlanetto (2008a) (though in the context of quasars), if halo masses can be estimated for galaxies the accuracy in $\overline{x}_{\text{HI}}$ increases.

The top panel of Figure 5.3 investigates contributions to $\mathcal{T}_{\text{IGM}}$. We compare $\mathcal{T}_{\text{IGM}}$ from galaxies in low and high mass halos, with fixed low or high Δv, to galaxies in low mass halos with low Δv. Massive halos always have high $\mathcal{T}_{\text{IGM}}$, as they reside in larger ionized bubbles, indicating halo mass is the dominant cause of high transmission. When Lyα is emitted at high Δv $\mathcal{T}_{\text{IGM}}$ is significantly boosted for massive halos. In the very early stages of reionization $\mathcal{T}_{\text{IGM}}$ is boosted for low mass halos with high Δv compared to low Δv, massive halos, likely because ionized bubbles around massive halos are still small.

The lower panel of Figure 5.3 shows a realistic estimate of the boosting, using mass-dependent Δv (comparing the top panels of Figure 5.2). For $\overline{x}_{\text{HI}} > 0.6$ $\mathcal{T}_{\text{IGM}}$ for massive halos are $> 2\times$ higher than for low mass halos, rising to a factor ~ 10 for $\overline{x}_{\text{HI}} > 0.9$. We compare the transmission ratio for the two EoS simulations: Faint Galaxies and Bright Galaxies (Section 5.2). The transmission boost is comparable; this effect is relatively independent of the timeline and morphology of reionization. We use these realistic $\mathcal{T}_{\text{IGM}}$ for UV bright galaxies in the next sections.

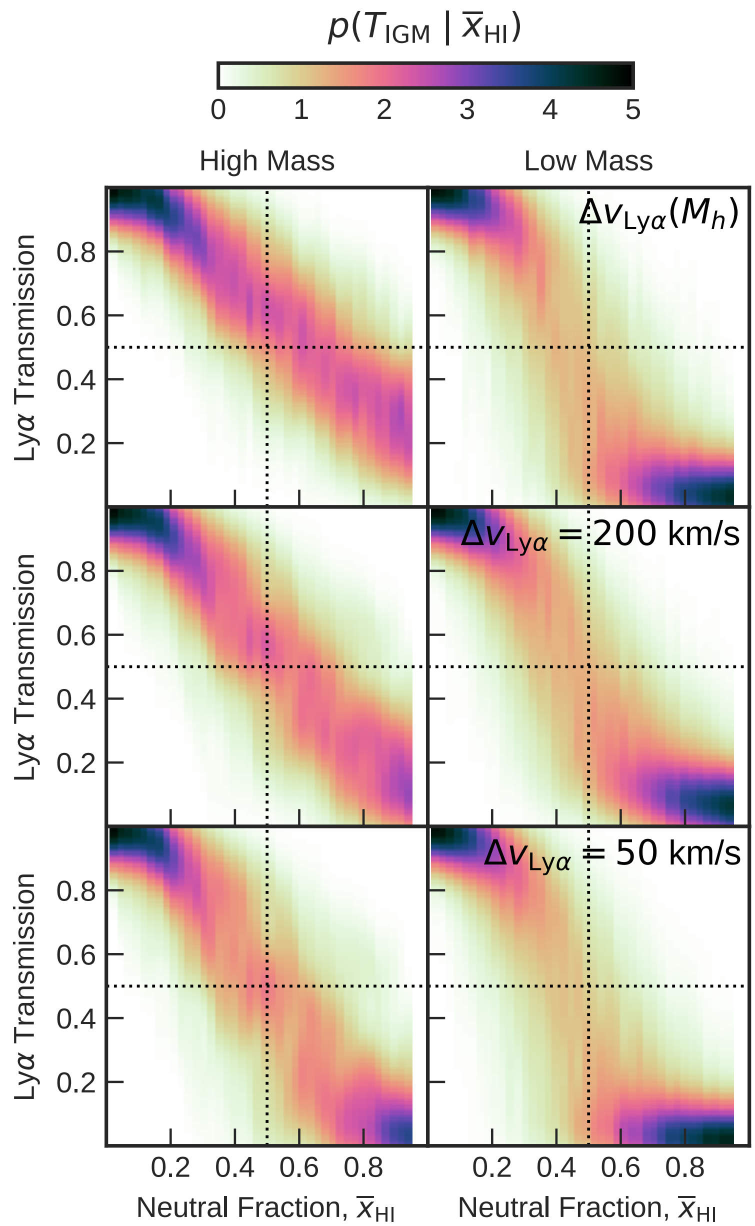

Figure 5.2: Lyα transmission fraction distributions, $p(\mathcal{T}_{\rm IGM})$ at a given $\overline{x}_{\rm HI}$. Highest density/darkest regions correspond to most likely values of $\mathcal{T}_{\rm IGM}$ at each $\overline{x}_{\rm HI}$. We show $p(\mathcal{T}_{\rm IGM})$ in two mass bins ($10^{11.5} \leq M_h \leq 10^{12} M_\odot$, left; $10^{10} \leq M_h \leq 10^{11} M_\odot$, right). We use three models for emitted Lyα lines: (upper panels) the mass-dependent model presented by M18, with high mass halos having higher Δv; (middle) $\Delta v = 200$ km s^{-1}; (lower) $\Delta v = 50$ km s^{-1}. With mass-dependent velocity offsets $\mathcal{T}_{\rm IGM}$ is boosted for high mass halos.

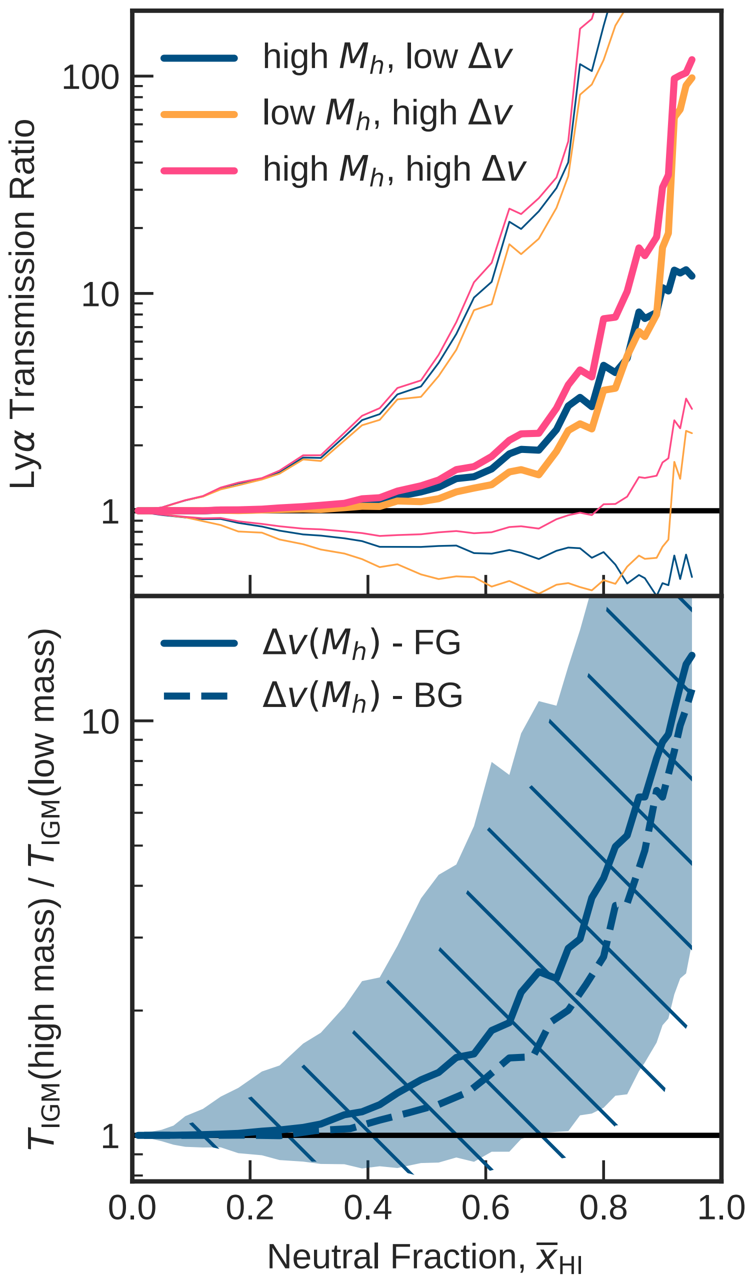

Figure 5.3: Upper: Ratio of $\mathcal{T}_{\rm IGM}$ comparing galaxies in low mass halos with $\Delta v = 50$ km s^{-1} with galaxies in: high mass halos, $\Delta v = 50$ km s^{-1} (blue); low mass halos, $\Delta v = 200$ km s^{-1} (orange); high mass halos, $\Delta v = 200$ km s^{-1} (pink). We use $p(\mathcal{T}_{\rm IGM})$ and mass bins from Figure 5.2. We plot median ratios as solid thick lines and $16-84\%$ range (due to sightline-to-sightline variations) as thin solid lines. The biggest boost is for galaxies in massive halos with high Δv. **Lower:** Ratio of $\mathcal{T}_{\rm IGM}$ for galaxies in low and high mass bins, assuming mass-dependent Δv. We show the ratio derived using the two EoS simulation runs: the fiducial Faint Galaxies (median - solid line, $16-84\%$ - shaded region); Bright Galaxies (median - dashed line, $16-84\%$ - hashed region). $\mathcal{T}_{\rm IGM}$ boosting in massive halos is relatively insensitive to simulation choice.

5.3.2 Evolving Lyα fraction for UV bright galaxies

An increasing fraction of Lyα emitters (EW > 25Å) is observed in the LBG population over $2 \lesssim z \lesssim 6$ (e.g., Stark et al., 2010; Cassata et al., 2015), likely due to decreasing dust in galaxies (Hayes et al., 2011). A drop in the Lyα fraction at $z > 6$ is usually attributed to absorption by an increasingly neutral IGM during reionization (see Dijkstra, 2014, for a recent review).

Figure 5.4 (right panel) shows the $4 \leq z \leq 8$ Lyα fraction for UV bright galaxies. At $z < 6$ the observations are consistent, but at $z \geq 6$ the Lyα fraction measured for samples with $M_\text{UV} \lesssim -21.5$ (Curtis-Lake et al., 2012; Stark et al., 2017) is significantly higher than for those at lower luminosities. Much of this discrepancy may be due to selection effects: using only the z_{850}-band for LBG selection the Curtis-Lake et al. (2012) sample could be biased towards strong Lyα emission (De Barros et al., 2017), and the Stark et al. (2017) sample was selected via red Spitzer/IRAC [3.6]-[4.5] colors (Roberts-Borsani et al., 2016) making them likely strong [OIII]+Hβ emitters, requiring hard radiation fields and young stellar populations, which increase Lyα production and escape (Finkelstein et al., 2013; Zitrin et al., 2015b). Using our model we test how the boosted $\mathcal{T}_\text{IGM}$ for galaxies in massive halos (Section 5.3.1) contributes to their Lyα emitter fraction.

We plot the evolution allowed by the M18 $z \sim 7$ neutral fraction estimate ($\overline{x}_\text{HI} = 0.59^{+0.11}_{-0.15}$) for galaxies in massive halos, using the maximum transmission demonstrated in Figure 5.2 (top left panel). We forward-model $p(EW^\text{obs}_{\text{Ly}\alpha})$ by convolving $p(\mathcal{T}_\text{IGM})$ with the UV magnitude-dependent $p(EW^\text{emit}_{\text{Ly}\alpha})$ described in Section 5.2. $p(EW^\text{emit}_{\text{Ly}\alpha})$ is a major uncertainty so we use a range of distributions: Low-EW, Mid-EW and High-EW, corresponding to the measured $z \sim 6$ distributions for LBGs with $M_\text{UV} \sim \{-21, -20.5, -20\}$, which bracket the EW variation in the De Barros et al. (2017) sample (Figure 5.4, left panel). Based on $z \leq 6$ observations we expect UV bright galaxies to have Low-EW or Mid-EW distributions.

The observed evolution of the Lyα fraction for $M_\text{UV} > -21.5$ samples is consistent with negligible evolution in $p(EW^\text{emit}_{\text{Ly}\alpha})$. The High-EW distribution is required to be consistent with the Stark et al. (2017) Lyα fraction error region, which is unexpected given UV bright galaxies at lower redshifts tend to have low Lyα EWs (e.g., Stark et al., 2010).

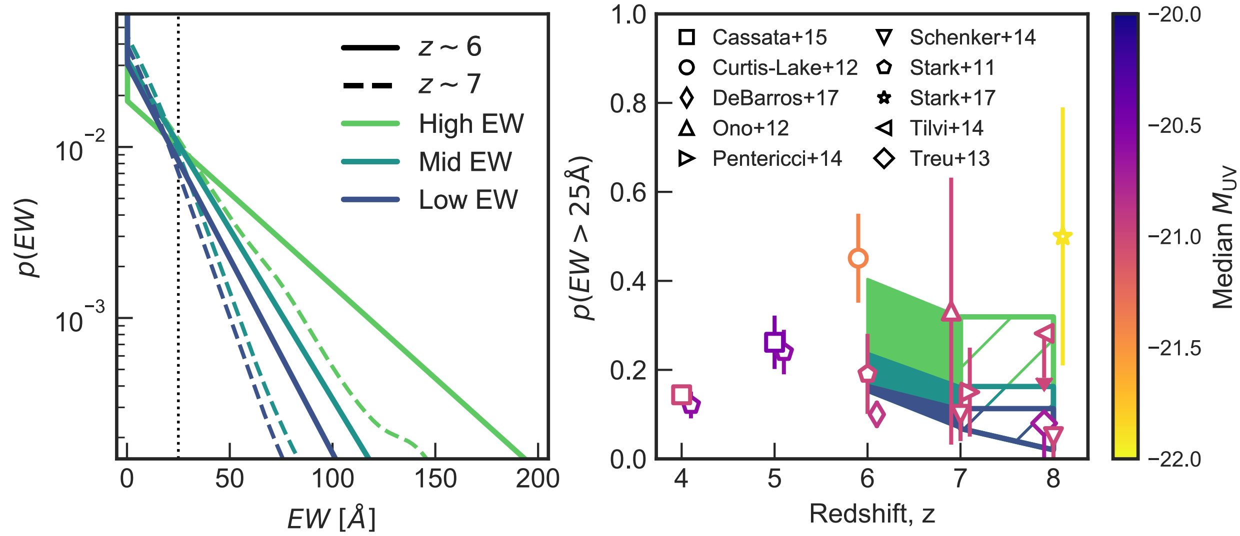

Figure 5.4: Redshift evolution of $p(EW_{\mathrm{Ly}\alpha})$ for galaxies in massive halos, for three model $p(EW_{\mathrm{Ly}\alpha})$ (Low, Mid and High). **Left:** Each $p(EW_{\mathrm{Ly}\alpha})$ model at $z \sim 6$ (solid, fit from De Barros et al., 2017) and $z \sim 7$ (dashed, assuming the inferred median $\overline{x}_{\mathrm{HI}} = 0.59$ by M18). **Right:** The fraction of LBGs showing Lyα $EW > 25$Å (dotted black line in left panel). We plot observations of UV bright samples (indicated by point shape, Stark et al., 2011; Curtis-Lake et al., 2012; Ono et al., 2012; Treu et al., 2013; Tilvi et al., 2014; Pentericci et al., 2014; Schenker et al., 2014; Cassata et al., 2015; Stark et al., 2017; De Barros et al., 2017), with the samples' median M_{UV} indicated by color. Shaded regions show the range of evolution allowed by the M18 $\overline{x}_{\mathrm{HI}}$ constraints ($16-84\%$ range), for a given model $p(EW_{\mathrm{Ly}\alpha})$. Hashed regions indicate the allowed evolution to $z = 8$ assuming $\overline{x}_{\mathrm{HI}}$ does not increase.

5.3.3 UV bright galaxies as probes of reionization

To test the efficacy of UV bright galaxies as probes of reionization we perform a Bayesian inference to obtain the posterior distribution of the neutral fraction given simulated observations of galaxies with Lyα EW and M_{UV} measurements: $p(\overline{x}_{\mathrm{HI}} \mid \{EW_{\mathrm{Ly}\alpha}, M_{\mathrm{UV}}\})$. Using Bayes' theorem this posterior is proportional to $\prod_i p(EW_{\mathrm{Ly}\alpha,i} \mid \overline{x}_{\mathrm{HI}}, M_{\mathrm{UV}A,i}) \times p(\overline{x}_{\mathrm{HI}})$, assuming the observations are independent.

We follow the method described by M18 and generate the likelihood of observing a given EW: $p(EW_{\mathrm{Ly}\alpha} \mid \overline{x}_{\mathrm{HI}}, M_{\mathrm{UV}})$, by convolving the high halo mass $p(\mathcal{T}_{\mathrm{IGM}})$, described in Section 5.3.1, with a distribution of emitted EWs. For this work we consider $M_{\mathrm{UV}} = -22$

galaxies. By assigning galaxies to a range of halo masses we include some scatter in $M_h - M_{UV}$ (e.g., Finkelstein et al., 2015a). To generate mock observations we draw EW values from a likelihood for a given $\overline{x}_{HI}$, convolve with a 5Å uncertainty and treat galaxies with EW < 15Å as non-detections (which are robustly accounted for in the inference). We perform the inference using these mock observations.

Figure 5.5 shows the posteriors obtained using a simulated sample of 100 UV bright galaxies for a grid of input $\overline{x}_{HI}$ values. The inferred posteriors are consistent with the input values over the entire range within the $16 - 84\%$ region, showing UV bright galaxies can be accurate tracers of the average IGM state. We note our posteriors are broad ($\Delta\overline{x}_{HI} \sim 0.4$) compared to those obtained using fainter galaxies (c.f. $\Delta\overline{x}_{HI} \sim 0.25$ in M18). This uncertainty is driven by the shape of $p(EW_{\mathrm{Ly}\alpha})$, which declines with increasing EW. Reionization further kills the high EW tail of the distribution, making high EW objects rare.

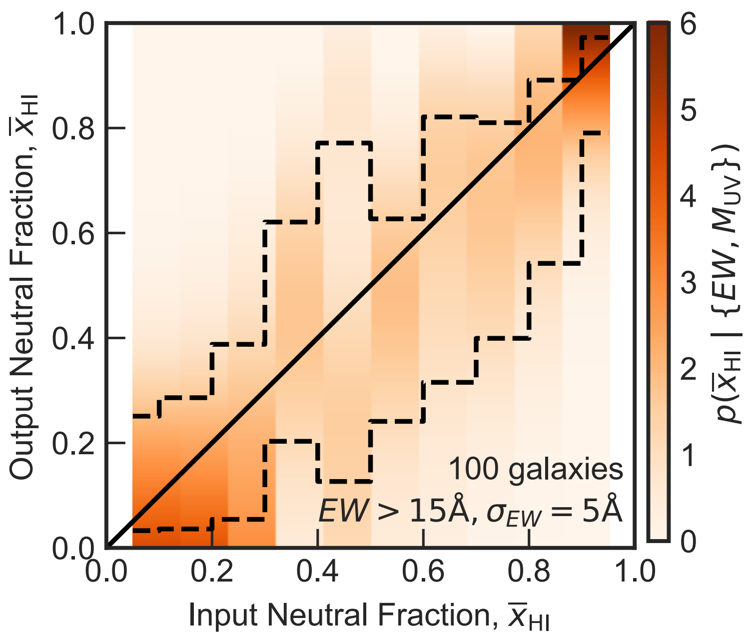

Figure 5.5: Posterior distributions for $\overline{x}_{HI}$ for a grid of input $\overline{x}_{HI}$ using simulated samples of 100 $M_{UV} = -22$ galaxies. Each vertical strip is a posterior for input $\overline{x}_{HI}$, darkest colors show the highest probabilities. The one-to-one relation between input and output $\overline{x}_{HI}$ is shown as a solid black line. We plot the $16 - 84\%$ range for each posterior (within dashed lines). The posteriors are consistent with the input $\overline{x}_{HI}$ within this range.

5.4 Discussion

We have shown UV bright galaxies in high mass halos can be precise probes of reionization and are increasingly valuable in reionization's early stages when Lyα in UV faint galaxies, emitted close to systemic velocity, is overwhelmingly absorbed in the IGM. However, there are two limitations to using such galaxies to probe reionization: (1) they are rare; (2) they emit less Lyα due to absorption in their dense ISM. Below we discuss prospects for overcoming these limitations.

Wide-area photometric surveys such as the Brightest of Reionizing Galaxies survey (BoRG, Trenti et al., 2011), UltraVISTA and UDS (e.g., Bowler et al., 2015) and GOLDRUSH (Ono et al., 2017) have discovered ~ 100 $z \gtrsim 7$ $M_{\rm UV} \lesssim -21$ LBGs in ~ 100 deg^2. Future wide-area surveys with e.g., *WFIRST* (Spergel et al., 2013) and *Euclid* (Laureijs et al., 2011) will likely increase this by a factor $\gtrsim 100$ in $> 15,000$ deg^2. These sources will be ideal candidates for spectroscopic follow-up to measure the Lyα EW distribution needed to infer the neutral fraction.

Do UV bright galaxies emit less Lyα? Whilst most $z \lesssim 6$ observations indicate they do (e.g., Verhamme et al., 2008; Stark et al., 2010), our results suggest the $z \sim 8$ galaxies presented by Stark et al. (2017) must have high intrinsic Lyα EW. Recent observations of a $M_{\rm UV} \sim -22$ galaxy after reionization at $z \sim 4$ detected Lyα emission with low Δv and Lyman continuum radiation (Vanzella et al., 2018), suggesting significantly ionized pathways through the ISM and/or CGM from such galaxies. If these galaxies are efficient producers of ionizing radiation, they may also increase their local ionization field to boost Lyα transmission through the CGM/IGM.

A holistic understanding of Lyα emission as a function of redshift and galaxy properties is therefore crucial to improve the use of Lyα as a cosmological tool. These measurements are becoming increasingly feasible with multi-wavelength observations of LBGs, and time should be invested in establishing Lyα emission properties over a wide redshift and galaxy mass/UV magnitude range, both in wide areas, and in deep lensed fields with *HST* (e.g., Treu et al., 2015; Schmidt et al., 2016) and in the near future with *JWST* (Treu et al., 2017).

Better measurements of these properties will enable us to disentangle IGM, CGM and ISM effects.

5.5 Summary and Conclusions

We have investigated the IGM transmission of Lyα from UV bright galaxies during the Epoch of Reionization by combining reionization simulations and empirical relations for galaxy and Lyα properties. Our main conclusions are:

(i) Lyα emitted by UV bright galaxies in massive halos has a higher mean and lower dispersion in IGM transmission than Lyα from typical field galaxies in low mass halos. This is primarily due to massive halos predominantly residing in overdensities which reionize early, and boosted by their higher Lyα velocity offsets, reducing damping wing absorption by cosmic neutral hydrogen.

(ii) This boosted transmission is not sufficient to explain the observed evolution of the $6 \lesssim z \lesssim 8$ Lyα fraction for extremely UV bright galaxies (Stark et al., 2017), suggesting these objects have higher emitted Lyα EW than expected.

(iii) With sufficient numbers, the observed Lyα EW distribution of UV bright galaxies can place tight constraints on the IGM neutral fraction during reionization, and may be the only way to probe the IGM at $z > 7$ when quasars are exceedingly rare and Lyα from most UV faint galaxies is extinguished.

More comprehensive measurements of the Lyα EW distribution as a function of redshift and galaxy properties are necessary to understand the evolving visibility of Lyα emission and to disentangle the effects of the ISM and IGM during reionization. Current and upcoming spectroscopic observations have the ability to this and increase the efficacy of Lyα as a cosmological tool.

We thank Dan Stark and Crystal Martin for useful discussions. CM acknowledges support through the NASA Earth and Space Science Fellowship Program Grant NNX16AO85H. AM acknowledges European Research Council support under the European Union's Horizon 2020 research and innovation program (grant No 638809 - AIDA). MT acknowledges support by the Australian Research Council (awards FT130101593 and CE170100013). This work was supported by *HST* BoRG grants GO-12572, 12905, 13767 and 15212, and *HST* GLASS grant GO-13459.

Software: IPython (Pérez & Granger, 2007), matplotlib (Hunter, 2007), NumPy (Van Der Walt et al., 2011), and EMCEE (Foreman-Mackey et al., 2013).

CHAPTER 6

First Results from the KMOS Lens-Amplified Spectroscopic Survey (KLASS): Kinematics of Lensed Galaxies at Cosmic Noon

This paper was published as Mason, Treu, Fontana, Jones, Morishita, Amorin, Bradac, Finney, Henry, Hoag, Huang, Schmidt, Trenti, & Vulcani (2017), ApJ, 838, 14, and reproduced here with minor formatting changes.

We present the first results of the KMOS Lens-Amplified Spectroscopic Survey (KLASS), a new ESO Very Large Telescope (VLT) large program, doing multi-object integral field spectroscopy of galaxies gravitationally lensed behind seven galaxy clusters selected from the *HST* Grism Lens-Amplified Survey from Space (GLASS). Using the power of the cluster magnification we are able to reveal the kinematic structure of 25 galaxies at $0.7 \lesssim z \lesssim 2.3$, in four cluster fields, with stellar masses $7.8 \lesssim \log(M_\star/M_\odot) \lesssim 10.5$. This sample includes 5 sources at $z > 1$ with lower stellar masses than in any previous kinematic IFU surveys. Our sample displays a diversity in kinematic structure over this mass and redshift range. The majority of our kinematically resolved sample is rotationally supported, but with a lower ratio of rotational velocity to velocity dispersion than in the local universe, indicating the fraction of dynamically hot disks changes with cosmic time. We find no galaxies with stellar mass $< 3 \times 10^9 M_\odot$ in our sample display regular ordered rotation. Using the enhanced spatial resolution from lensing, we resolve a lower number of dispersion dominated systems compared to field surveys, competitive with findings from surveys using adaptive optics. We find that the KMOS IFUs recover emission line flux from *HST* grism-selected objects more faithfully than slit spectrographs. With artificial slits we estimate slit spectrographs miss on

average 60% of the total flux of emission lines, which decreases rapidly if the emission line is spatially offset from the continuum.

6.1 Introduction

With the advent of integral field spectroscopy, which obtain spectra in spatial pixels, it is finally possible to achieve a three-dimensional view of galaxies. Spatially resolved spectroscopy allows us to observe large star-forming regions themselves and make inferences about the physical conditions within galaxies.

The redshift range $1 \lesssim z \lesssim 3$ was the most active time in the universe's history, covering the peak of the cosmic star formation history (Madau & Dickinson, 2014) when more than half of the stellar mass in the universe was built up (Ilbert et al., 2013; Muzzin et al., 2013). Photometric surveys have revealed that star formation rates (SFRs) and SFR surface densities in this period are systematically higher than in the local universe (e.g., Madau et al., 1996; Hopkins & Beacom, 2006; Willott et al., 2015; Shibuya et al., 2015). Many galaxies at this epoch appear morphologically disordered (e.g. Mortlock et al., 2013; Lee et al., 2013; Shapley et al., 2001), a far cry from the clear morphological bimodality in the galaxy population in the local universe, between rotating disks and dispersion dominated elliptical galaxies. How this bimodality arises and what processes change galaxies from disks to ellipticals are still open questions (Conselice, 2014; Bundy et al., 2005). Merger interactions are expected to play a role in shaping galaxies (Nipoti et al., 2003; Bundy et al., 2005; Puech et al., 2012), but observing such dynamical processes via the 'snapshots' available to astronomers is challenging.

Using integral field spectroscopy we can ask questions about how galaxies' morphologies and kinematics are related to their past and ongoing star formation. A key question is whether the increase in SFRs is purely driven by an increase in density and smooth gas accretion rates at higher redshifts (e.g., Mason et al., 2015a; Tacchella et al., 2013) producing steady in-situ star formation (Bundy et al., 2007; Conselice, 2014), or more stochastic processes for gas infall such as major mergers (Somerville et al., 2001; Cole et al., 2000).

Additionally, changing physical conditions at high redshift may alter the nature and efficiency of star formation: e.g. decreased AGN activity, lower metallicities, or other evolving feedback processes (Hayward & Hopkins, 2017; Cullen et al., 2016).

The first generations of integral fields surveys using single integral field unit (IFU) instruments, e.g. SINFONI/SINS (Forster Schreiber et al., 2006; Genzel et al., 2011), SINFONI/AMAZE-LSD (Gnerucci et al., 2011) and IMAGES/FLAMES-GIRAFFE (Flores et al., 2006) have primarily targeted star forming galaxies with stellar masses $\gtrsim 10^{10} M_{\odot}$. Most surveys found samples of $z \sim 1-3$ galaxies which were roughly equally separated into 3 kinematic classifications: rotation dominated systems, dispersion dominated systems, and merging/morphological unstable systems. A key result was that the rotation dominated systems had systematically higher velocity dispersions than local disks (Epinat et al., 2010; Bershady et al., 2010), suggesting that high redshifts disks are highly turbulent. In addition, the highest mass objects were rotating disks at high redshift, in contrast to the local universe where most objects with stellar mass over $10^{10} M_{\odot}$ are dispersion dominated ellipticals. Similar trends are seen with slit spectrographs (e.g. Price et al., 2016).

The K-band Multi-Object Spectrometer (KMOS, Sharples et al., 2013) on the European Southern Observatories Very Large Telescope (ESO/VLT) is the first multi-object near-IR IFU instrument and capable of producing large samples of kinematically resolved galaxies. Recent surveys using KMOS, KMOS^{3D} (Wisnioski et al., 2015) and KROSS (Stott et al., 2016), find the majority of Hα-selected galaxies at $z \sim 1-2$ are highly turbulent gas rich disks. However, these and previous kinematic surveys have probed only the high mass end of the galaxy mass function ($\gtrsim 10^{9} M_{\odot}$) and thus there is no clear picture of the kinematic evolution of low mass galaxies.

Seeing-limited IFU observations have been shown to misclassify objects: at low spatial resolution beam smearing can both smooth out irregular rotation curves so that kinematically irregular galaxies look like rotators (Leethochawalit et al., 2016b), or produce large velocity dispersions in kinematic maps of compact galaxies, so that rotators look like dispersion dominated systems (Newman et al., 2012). Adaptive optics (AO) on the single-object IFU instruments Keck/OSIRIS and VLT/SINFONI have enabled high spatial resolution spectroscopy of a handful of $z \sim 1-3$ galaxies (Newman et al., 2012), including objects which are gravitationally lensed, with stellar masses as low as $6.3 \times 10^8 M_\odot$ (Jones et al., 2010; Livermore et al., 2015; Leethochawalit et al., 2016b). The surveys using AO find a lower fraction of dispersion dominated systems: high spatial resolution is needed to clearly distinguish rotationally supported galaxies from mergers and pressure supported systems.

Whilst IFU surveys at $z \gtrsim 1$ have produced interesting results, there are clear limitations: there is a need for large samples of galaxies, spanning a broad range in stellar mass, and with higher spatial resolution than provided by natural seeing. Gravitational lensing provides a unique tool to study the internal motions of galaxies with lower stellar masses than in the field, and at higher spatial resolution than natural seeing. By targeting cluster lens fields with a multi-object IFU instrument such as KMOS we can efficiently produce a large sample of lensed high redshift star forming galaxies for the first time.

The KMOS Lens-Amplified Spectroscopic Survey (KLASS) was designed to efficiently survey lensed low mass high redshift galaxies in order to answer questions about how galaxies' star formation histories are related to their kinematics. KLASS is an ESO/VLT large program (PI: A. Fontana), targeting gravitationally lensed galaxies behind seven massive clusters from the Grism Lens Amplified Survey from Space (GLASS, PI: T. Treu, Treu et al., 2015; Schmidt et al., 2014b).

In this paper we present a kinematic study of 32 lensed galaxies at cosmic noon ($1 \lesssim z \lesssim 3$) with stellar masses $7.8 \lesssim \log(M_\star/M_\odot) \lesssim 10.5$. We resolve kinematic structure with a high signal-to-noise ratio (S/N > 5) in 25/32 galaxies.

By combining the magnifying power of gravitational lensing (median magnification factor of ~ 2 for the objects presented here) and the multi-object capabilities of KMOS, KLASS efficiently surveys galaxies at better spatial resolution than natural seeing and with stellar mass up to an order of magnitude smaller than previous studies. 5 of the galaxies with resolved kinematics at $z > 1$ in our sample have stellar masses below $6.3 \times 10^8 M_\odot$, lower than any object previously observed with an IFU.

Our sample reveals a large diversity in the star forming galaxy population at cosmic noon, with a range in inferred kinematic structure and galaxy properties at every redshift.

This paper is structured as follows: in Section 6.2 we introduce the GLASS and KLASS surveys; in Section 6.3 we describe the KLASS sample selection, observations and data reduction in Section 6.4 we present the analysis and key results of our data, which are discussed in Section 6.5. We summarize our findings in Section 6.6.

We use a Planck Collaboration et al. (2016a) cosmology and all magnitudes are in the AB system.

6.2 The KMOS Lens-Amplified Spectroscopic Survey

KLASS is an ongoing ESO VLT KMOS Large Program targeting the fields of seven massive galaxy clusters, including the four Hubble Frontier Fields visible from the Southern Hemisphere. A comprehensive description of the survey and data will be presented in Mason et al. (in prep). Here, we provide a brief overview.

KLASS is a ground-based follow-up program for the Grism Lens Amplified Survey from Space[1] (GLASS, Treu et al., 2015; Schmidt et al., 2014b), a large Hubble Space Telescope (*HST*) program which has obtained grism spectroscopy of the fields of ten massive galaxy clusters, including the Hubble Frontier Fields (HFF, Lotz et al., 2017) and 8 of the CLASH clusters (Postman et al., 2012b). Near infra-red spectra were obtained with the Wide Field Camera 3 (WFC3) grisms G102 and G141, covering the wavelength range $0.8 - 1.6\mu$m with spectral resolution $R \sim 150$. Full details of the GLASS survey are described in Treu et al. (2015) and Schmidt et al. (2014b).

High spectral resolution follow-up is needed confirm the purity and completeness of the grism spectra, to measure lines that were unresolved in *HST*, and to obtain velocity information which the low resolution grisms cannot provide.

The key science drivers of KLASS are:

1. To probe the internal kinematics of galaxies at $z \sim 1{-}3$, with superior spatial resolution

[1] http://glass.astro.ucla.edu

to comparable surveys in blank fields. The kinematic data will be combined with metallicity gradients from the *HST* data to enable the study of metallicity gradients as a diagnostic of gas inflows and outflows (Jones et al., 2013a, 2015; Wang et al., 2016)

2. To confirm $z \gtrsim 7$ Lyα emission from the GLASS sample, enabling us to constrain the timeline and topology of reionization (Schmidt et al., 2016; Treu et al., 2013, 2012).

The former science driver is the main focus of this paper; the latter will be discussed in a future paper.

In this paper we present the first results for 32 targets, with $\sim 10-50\%$ of the planned exposure times, from four of the clusters: MACJS0416.1-2403 (hereafter MACS0416); MACSJ1149.6+2223 (MACS1149); MACSJ2129.4-0741 (MACS2129) and RXJ1347.5-1145 (RXJ1347). When complete, KLASS will have approximately 60 targets at $z \sim 1-3$ with all seven clusters. We are targeting ~ 70 candidate galaxies at $z > 7$ which will be described in future work after the full integrations are complete. Final integration times of targets are expected to be $10-15$ hours.

6.3 Observations and Data

In this section we describe the KMOS observations of the sample presented in this paper.

6.3.1 Target selection

Targets at 'cosmic noon' ($1 \lesssim z \lesssim 3$) were selected from the *HST* GLASS spectroscopic sample, with at least one bright nebular emission line (Hα, [O III] or [O II]) in the KMOS YJ range, away from bright OH sky lines. *HST* grism spectra for all of the targets presented in this paper are available in the public GLASS data release [2]. The selection by line flux means our sample is comprised of star forming galaxies, which would not necessarily be the case for mass-selected samples.

[2] https://archive.stsci.edu/prepds/glass/

6.3.2 Observations and data reduction

Observations presented in this paper were carried out in service mode in Periods 95 − 97, from July 2015 to April 2016. The KMOS YJ band is used for the entire program, covering $1 - 1.35\mu$m, with spectral resolution $R \sim 3400$, as required to resolve kinematics in our sample. Observations are executed in 1 hour observing blocks (each comprising a total 1800s on science objects and 900s on sky). Pixel dither shifts were included between science frames. A star is observed in 1 IFU in every observing block to monitor the point spread function (PSF) and the accuracy of dither offsets. All exposures had seeing $\leq 0\farcs8$ with median seeing $\sim 0\farcs6$. This corresponds to a spatial resolution of $\sim 5/\sqrt{\mu}$ kpc at $z \sim 1$, where μ is the gravitational lensing magnification of an object.

The total integration times of individual objects are listed in Table 6.1. The integration times are comparable to those of KROSS (2.5 hours per source, Stott et al., 2016) and generally lower than KMOS^{3D} (2-20 hours per source, Wisnioski et al., 2015). Though we note that the targets should all have 10 hour integrations when KLASS is complete.

All data were reduced using the ESO KMOS pipeline (Davies et al., 2013) including an optimized sky subtraction routine from Davies (2007). We also apply a correction for readout channel level offsets, a known problem with the KMOS detectors. Individual data cube frames are combined by sigma clipping and using spatial shifts determined by the position of the star observed in the same IFU in each frame. A full description of the reduction procedure will be given by Mason et al. (in prep).

6.4 Analysis and Results

In this section we present the key analyses and findings of our investigation. We find KMOS measures emission flux consistent with the *HST* grisms. After deriving galaxy properties from SED fitting and kinematic modeling, and correcting for lensing effects, we classify our sample in 5 kinematic categories. We find the majority are rotation supported and investigate correlations between kinematic properties and star formation parameters.

6.4.1 Comparison of *HST* grism and ground-based flux measurements

HST grism surveys such as GLASS and the Faint Infrared Grism Survey (FIGS, PI: Malhotra, Tilvi et al., 2016) are providing high spatial resolution near-IR spectroscopy, free from atmospheric attenuation. However, emission lines discovered in the *HST* grisms and followed up from the ground have shown some tension in line flux measurements: both for intermediate redshift nebular emission lines (Masters et al., 2014) and Lyα emission at $z \gtrsim 7$, with Keck/MOSFIRE measuring up to $\sim 5\times$ lower flux than the *HST* G102 grism for Lyα (Tilvi et al., 2016, Hoag et al. in prep).

Ensuring consistent flux measurements from space and ground-based spectroscopy is important to calibrate instruments, and for making physical inferences from data. Accurate flux measurements of Lyα emission are vital for making inferences about the epoch of reionization (Treu et al., 2012, 2013), which is a key science driver of KLASS and GLASS. Thus we want to investigate how fluxes measured with KMOS compare with those from the *HST* grisms.

In Figure 6.1 we compare flux measured by the *HST* grisms G102 and G141 and flux measured by KMOS YJ, for emission lines of objects $1 \lesssim z \lesssim 3$. We find good agreement between line fluxes measured in KMOS and those from the *HST* grisms in GLASS, in contrast to results from slit spectrographs (Masters et al., 2014; Tilvi et al., 2016; Huang et al., 2016a; Schmidt et al., 2016, Hoag et al. in prep), suggesting that slit losses can be a serious systematic problem, especially for faint objects, which seems to be avoided by the wide field of IFUs such as KMOS. Keck/DEIMOS and MOSFIRE are traditionally the instrument of choice for following-up faint high redshift targets, but our results show that IFU instruments such as KMOS are necessary to collect the true emission line flux from an object, especially if the emission is likely to be more extended than, and/or offset, from the UV continuum observed with *HST* - as is often the case for highly resonant lines such as Lyα (Wisotzki et al., 2016; Tilvi et al., 2016), and the offset can be enhanced by lensing (Smit et al., 2017).

To quantify the effect of slit losses and emission lines offset from the continuum we placed artificial slits on the KMOS data cubes. We used a slit width of $0\farcs8 = 4$ pixels, comparable to the slit width of the MOSFIRE/MOSDEF kinematic survey ($0\farcs7$, Price et al., 2016). We placed slits at the peak of the emission line and then at increasing radial offsets from the peak. We measure the flux in the slits aligned at random orientations and take the mean value from all slit orientations at each offset distance.

In Figure 6.2 we plot the ratio between flux measured in the slit and the total emission line flux in the KMOS cube as a function of spatial offset. When the spatial offset is $0''$ we recover the slit loss due to slit size. For our sample, $\sim 15-90\%$ of the total flux is measured when using a slit placed on the center of the emission line, with mean value $61 \pm 1\%$. There is a large scatter in recovered line ratios, due to spatial extent and varying morphologies, this produces ratios comparable to those seen by Masters et al. (2014). However, if the slit is offset from the spatial center of the emission line, the recovered flux decreases significantly: for a spatial offset of $1\farcs1$ the mean recovered flux ratio is only $\sim 20\%$. This flux loss due to spatial offset may explain the tension found for the Lyα measurements.

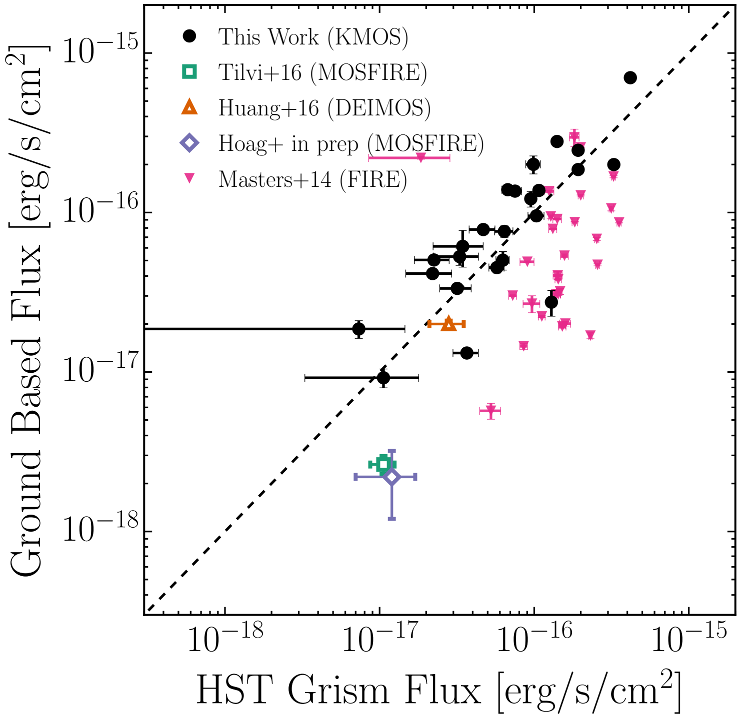

Figure 6.1: Line flux of nebular emission lines from multiple objects in the KLASS first results sample (black points), measured both from the *HST* grism in GLASS and from KMOS as described in this paper. We compare the KMOS data with recent results using slit spectrographs, which also have *HST* grism spectra (Masters et al., 2014; Tilvi et al., 2016; Huang et al., 2016a, Hoag et al. in prep). Nebular emission line measurements are shown as filled shapes, and Lyα line measurements are shown as empty shapes.

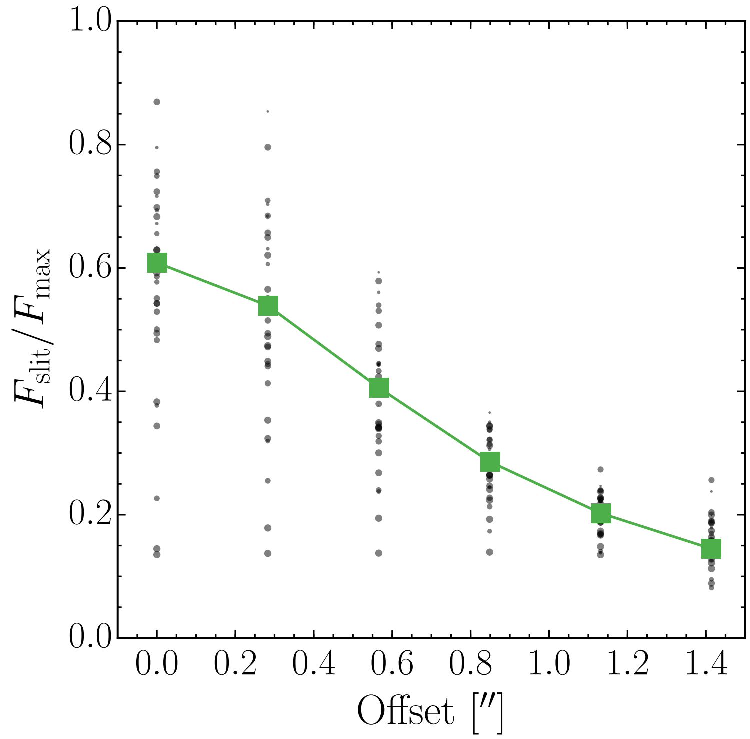

Figure 6.2: Fraction of emission flux measured by artificial slits with width 0.″8 compared to the total flux in a KMOS data cube as a function of slit spatial offset from the emission line center. Gray points are the mean measurement from artificial slits for all emission lines presented in this paper, with size representing the spatial extent of the emission line determined from a S/N map. The green points show the mean of the flux ratio for all lines at each spatial offset value. As well as regular slit losses, if the slit is not centered on an emission line a significant proportion of the total flux will be missed.

6.4.2 Photometric properties and gravitational lens modeling

The stellar masses are obtained from the spectral energy distributions (SEDs) of the galaxies in the HFF photometric catalogs (MACS0416 and MACS1149, Morishita et al., 2017), and the CLASH photometric catalog (MACS2129 and RXJ1347, Postman et al., 2012b). The SEDs are fit using the Fitting and Assessment of Synthetic Templates (FAST) code (Kriek et al., 2009) using the Bruzual & Charlot (2003) stellar populations with an exponential declining star formation history (SFH) and a Chabrier (2003) initial mass function (IMF). Reddening for the stellar continua, $A_{\mathrm{V,SED}}$ are obtained for a Calzetti et al. (2000) dust extinction law.

Table 6.1: Observed and derived galaxy properties

Cluster	ID[a]	R.A.	Dec.	$z_{\rm KMOS}$	Kinematic Line	Integration Time (hrs)	Magnification μ^b	$\log_{10} M_\star$ $[M_\odot]^c$	σ_0 [km/s]	$V_{\rm max}$ [km/s]	Kinematic Class[d]
MACS0416	94	64.0331	−24.0563	1.37	[O III]	4.75	$1.89^{+0.02}_{-0.01}$	9.88 ± 0.13	< 38	31 ± 9	3
MACS0416	372	64.0352	−24.0710	1.99	[O II]	4.75	$2.37^{+0.01}_{-0.02}$	10.20 ± 0.10	43 ± 28	–	5
MACS0416	394	64.0366	−24.0673	0.94	Hα	4.75	$18.47^{+0.96}_{-3.03}$	9.22 ± 0.12	12 ± 15	133 ± 22	2[e]
MACS0416	430	64.0536	−24.0660	2.10	[O II]	4.75	$2.92^{+0.05}_{-0.05}$	$9.17^{+0.12}_{-0.18}$	< 30	–	5
MACS0416	706	64.0514	−24.0713	1.35	[O III]	4.75	$2.11^{+0.03}_{-0.03}$	8.31 ± 0.11	< 36	24 ± 7	3
MACS0416	863	64.0169	−24.0742	1.63	[O III]	4.75	$2.98^{+0.12}_{-0.11}$	$8.84^{+0.27}_{-0.81}$	38 ± 6	191 ± 43	2[e]
MACS0416	880	64.0310	−24.0790	1.64	[O III]	4.75	$2.22^{+0.14}_{-0.13}$	9.73 ± 0.11	< 34	62 ± 5	4
MACS0416	955	64.0419	−24.0758	1.99	[O II]	4.75	$3.21^{+0.07}_{-0.04}$	9.77 ± 0.10	31 ± 23	–	5
MACS1149	593	177.4069	22.4075	1.48	[O III]	2.25	$2.34^{+0.02}_{-0.01}$	9.27 ± 0.10	8 ± 3	142 ± 9	1
MACS1149	683	177.3972	22.4062	1.68	[O III]	2.25	$9.90^{+0.33}_{-0.40}$	7.75 ± 0.10	< 25	30 ± 6	4
MACS1149	691	177.3824	22.4058	0.98	Hα	2.25	$2.00^{+0.11}_{-0.07}$	$9.30^{+0.12}_{-0.17}$	24 ± 11	27 ± 14	4
MACS1149	862	177.4034	22.4024	1.49	[O III]	2.25	$3.90^{+0.04}_{-0.04}$	9.66 ± 0.10	< 34	–	5
MACS1149	1237	177.3846	22.3967	0.70	Hα	2.25	$1.36^{+0.01}_{-0.00}$	8.64 ± 0.12	15 ± 36	27 ± 13	4
MACS1149	1501	177.3970	22.3960	1.49	[O III]	2.25	$12.42^{+1.28}_{-1.43}$	9.44 ± 0.11	15 ± 7	227 ± 32	2

NOTE. – [a] IDs match the GLASS IDs in the public data release, v001 available at `https://archive.stsci.edu/prepds/glass/`.

[b] Magnification estimate from cluster mass maps as described in Section 6.4.2.

[c] Stellar masses obtained from SED fitting (Section 6.4.2) have been corrected for magnification.

[d] Kinematic class described in Section 6.4.3. [e] Modeled with 2D velocity map model rather than GalPaK^{3D}. [f] Probable mergers.

Table 6.2: *Cont.*

Cluster	ID[a]	R.A.	Dec.	z_{KMOS}	Kinematic Line	Integration Time (hrs)	Magnification μ^b	$\log_{10} M_\star$ $[M_\odot]^c$	σ_0 [km/s]	$V_{\max}$ [km/s]	Kinematic Class[d]
MACS1149	1625	177.3900	22.3895	0.96	Hα	2.25	$1.80^{+0.02}_{-0.02}$	10.54 ± 0.12	123 ± 5	139 ± 11	4^f
MACS1149	1644	177.3944	22.3892	0.96	Hα	2.25	$1.79^{+0.03}_{-0.02}$	$10.35^{+0.12}_{-0.18}$	200 ± 12	108 ± 24	3
MACS1149	1757	177.4085	22.3868	1.25	[O III]	2.25	$3.83^{+0.13}_{-0.11}$	$8.39^{+0.12}_{-0.18}$	5 ± 29	16 ± 28	2^e
MACS1149	1931	177.4034	22.3816	1.41	[O III]	2.25	$2.05^{+0.03}_{-0.03}$	10.22 ± 0.10	44 ± 4	137 ± 13	2
MACS2129	37	322.3627	−7.7099	2.29	[O II]	1	$1.58^{+0.07}_{-0.06}$	$10.13^{+0.11}_{-0.15}$	94 ± 7	–	5
MACS2129	49	322.3528	−7.7101	1.88	[O II]	1	$1.38^{+0.01}_{-0.02}$	$9.80^{+0.14}_{-0.20}$	109 ± 45	–	5
MACS2129	329	322.3634	−7.7032	1.65	[O III]	1	$1.67^{+0.06}_{-0.05}$	$9.74^{+0.12}_{-0.17}$	11 ± 6	132 ± 23	2
MACS2129	1437	322.3508	−7.6819	1.36	[O III]	1	$1.66^{+0.02}_{-0.02}$	9.52 ± 0.10	38 ± 18	100 ± 50	2
MACS2129	1566	322.3724	−7.6792	1.48	[O III]	1	$1.56^{+0.07}_{-0.05}$	9.56 ± 0.12	101 ± 18	–	5
MACS2129	1739	322.3605	−7.6745	1.49	[O III]	1	$1.41^{+0.02}_{-0.02}$	9.32 ± 0.10	60 ± 6	52 ± 9	4^f
RXJ1347	188	206.8861	−11.7338	0.93	Hα	3	$2.42^{+0.04}_{-0.04}$	10.10 ± 0.10	6 ± 1	87 ± 12	2
RXJ1347	287	206.8910	−11.7474	1.01	[O III]	3	$2.34^{+0.08}_{-0.07}$	9.58 ± 0.11	39 ± 1	46 ± 6	2
RXJ1347	450	206.8757	−11.7645	0.85	Hα	3	$1.92^{+0.03}_{-0.03}$	10.12 ± 0.10	37 ± 54	145 ± 50	2^e
RXJ1347	472	206.8719	−11.7610	0.91	Hα	3	$2.78^{+0.10}_{-0.07}$	$9.44^{+0.15}_{-0.23}$	42 ± 3	108 ± 8	1
RXJ1347	795	206.8882	−11.7613	0.62	Hα	3	$1.51^{+0.02}_{-0.03}$	10.33 ± 0.10	45 ± 2	198 ± 8	2
RXJ1347	1230	206.8960	−11.7537	1.77	[O III]	3	$40.56^{+32.59}_{-12.83}$	$8.76^{+0.21}_{-0.40}$	62 ± 19	172 ± 49	2^e
RXJ1347	1261	206.9002	−11.7476	0.61	Hα	3	$1.76^{+0.02}_{-0.03}$	10.47 ± 0.10	12 ± 6	217 ± 17	1
RXJ1347	1419	206.9022	−11.7443	1.14	[O III]	3	$8.98^{+0.80}_{-0.60}$	9.30 ± 0.11	45 ± 2	25 ± 8	2

NOTE. – Same as Table 6.1

In Figure 6.3 we show the demagnified stellar mass distribution of objects in our sample, compared with the KMOS^{3D} and KROSS samples. While we have a smaller sample than those surveys, we cover a broader mass range and have larger proportion of low stellar mass objects. $\sim 63\%$ of our sample is comprised of objects with stellar mass below the KMOS^{3D} mass limit of $\sim 6 \times 10^9 M_\odot$. KROSS does contain objects with comparable stellar masses to KLASS, but in lower proportions: $\sim 5\%$ of the KROSS sample contains galaxies with stellar mass below $10^9 M_\odot$, compared to $\sim 19\%$ in KLASS. KLASS is the first IFU survey to resolve kinematics in objects with stellar mass below $\sim 6.3 \times 10^8 M_\odot$ at $z > 1$: 5 objects in our sample fall below this mass limit.

The lensing effects on each source due to the gravitational potential of the foreground cluster were obtained using the SWUnited cluster mass models (Juárez et al., 2010; Bradač et al., 2009). For the clusters which are part of the HFF we use the publicly available lens models[3] (Hoag et al., 2016), for MACS2129 we use the model described in Huang et al. (2016a), and the modeling for RXJ1347 will be presented in Finney et al. in prep. Lensing parameters were obtained at the position of each targets from the 2D maps of κ, the dimensionless mass surface density of the lensing system, or *convergence*, and $\gamma = \gamma_1 + i\gamma_2$ the *shear* which measures the distortion of images (e.g., Meylan et al., 2006; Keeton et al., 2005). Stellar masses and SFRs obtained from SED fitting and emission line flux measurements will be affected by gravitationally lensing, as fluxes are magnified. In the following sections we will refer to the magnification-corrected stellar masses and SFRs. Additionally, gravitational lensing distorts the images and kinematic maps, and removes symmetries in the velocity maps (De Burgh-Day et al., 2015).

In this first exploration of the sample, we chose not to do a full lensing reconstruction of the objects back to the source plane. The majority of the sources in this paper are not significantly lensed, with magnifications $\mu \sim 1.4 - 2.5$, and have small shears $|\gamma| \lesssim 0.1$, so the effect of lensing is small on the kinematic maps.

However, gravitational lensing will distort the axis ratios of objects derive from photom-

[3] `https://archive.stsci.edu/prepds/frontier/lensmodels/`

etry, which are needed for deriving effective radii and inclination angles, so when using these values we scale by the extra distortion induced by lensing. Following Keeton (2001), we derive the source plane axis ratio from the observed image plane axis ratio, $(b/a)_{\rm im}$ as:

$$\left(\frac{b}{a}\right)_{\rm s} = \frac{1}{q_L}\left(\frac{b}{a}\right)_{\rm im}, \tag{6.1}$$

$$\text{where } q_L = \frac{1-\kappa+|\gamma|}{1-\kappa-|\gamma|} \tag{6.2}$$

is the inverse of the axis ratio produced by lensing.

The source plane axis ratio is equal to $\cos i$ where i is the intrinsic inclination angle of a thin disk. We note that the axis ratio depends on the position angle of the source from the center of the lensing potential. We assume an average source position angle of 90° to derive this equation. The source plane effective radius is approximated as $r_{e,s} = (1-\kappa-|\gamma|)r_{e,\rm im}$. For the majority of sources presented here, the shear effects produce $< 40\%$ changes in effective radii and axis ratios. In the cases where objects have $\mu \gtrsim 4$ lensing effects on kinematics may be stronger, so we clearly mark these outliers on figures which follow.

KLASS is complemented by additional VLT follow-up of gravitationally lensed multiple images in the Frontier Fields clusters MACS0416 (with VIMOS and MUSE, Grillo et al., 2015; Caminha et al., 2016) and MACS1149 (with MUSE, Grillo et al., 2016). There is excellent agreement in spectroscopic redshifts for overlapping objects in KLASS and these studies. MACS0416_372 and MACS0416_955 are multiple images of the same galaxy (Grillo et al., 2015; Caminha et al., 2016). The derived intrinsic velocity dispersions (see Section 6.4.3) for these images from our data are consistent with being the same source (see Table 6.1), however, their stellar masses differ by 0.43 dex. We note that stellar population parameters which are independent of magnification (age and specific SFR) derived from the SEDs of these objects are consistent, so this discrepancy is likely due to systematics in the magnification map we used. Thus this is a good example of the complexities of cluster mass modeling and the need for many spectroscopically confirmed multiple images. MACS0416_394 is also a multiple image, which may be overlapping with an image of the same system (Caminha et al., 2016), we thus neglect it when fitting any trends to our data. MACS1149_1501 and MACS1149_862 are multiple images of the SN Refsdal host galaxy (Kelly et al., 2015; Treu et al., 2016; Grillo et al., 2016).

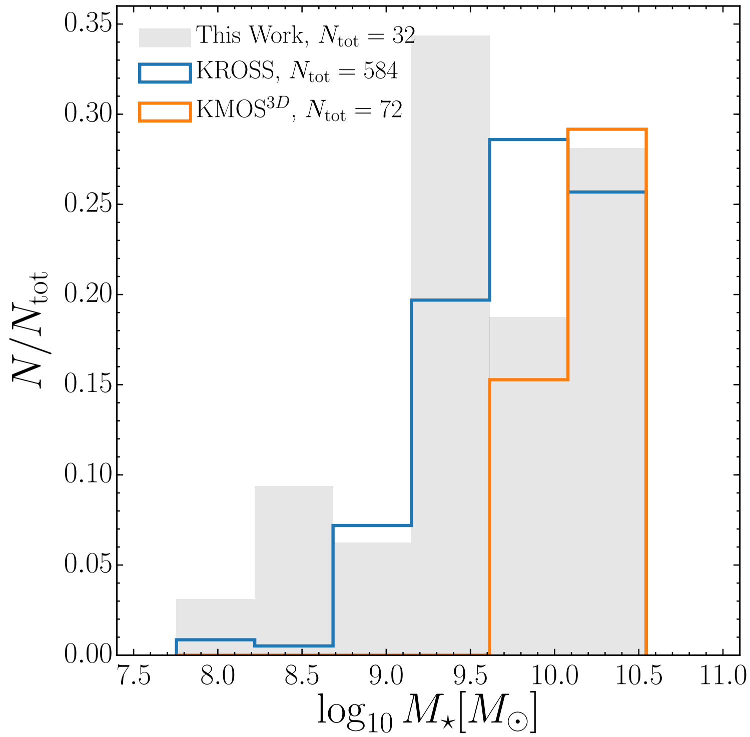

Figure 6.3: Histograms showing the normalized stellar mass distributions of our sample compared to those of KROSS (Stott et al., 2016, $z \sim 1$) and KMOS^{3D} (Wisnioski et al., 2015, $z \sim 1$ and $z \sim 2$). A high proportion of the KLASS sample ($\sim 19\%$) contains galaxies with stellar mass below $10^9 M_\odot$, compared to $\sim 5\%$ in KROSS, and no objects in KMOS^{3D}. While KROSS contains objects at $z \sim 1$ with comparable stellar masses to KLASS, KLASS is the first survey to resolve kinematics in galaxies with stellar mass below $\sim 6 \times 10^8 M_\odot$ at $z > 1$.

6.4.3 Kinematics

We derive kinematic properties of the galaxies by fitting the strongest available emission line: Hα at $z < 1$, the [O III] doublet at $1 \leq z < 1.8$, and the [O II] doublet at $z \geq 1.8$.

To measure integrated properties, we sum the flux in spaxels within a spatial aperture derived from the whitelight image of the full cube, which is then expanded to optimize the signal-to-noise ratio in the line. This results in a custom-extracted 1D spectrum for each galaxy. We then fit the emission lines as a Gaussian (two Gaussians for the doublets), plus a linear continuum component. The fits are weighted by the inverse variance spectrum derived from the sky emission lines and the bad pixel mask. To measure the total velocity dispersion in the ionized gas we subtract the instrumental broadening (FWHM $\sim 4\mathring{A}$) in quadrature and to correct for beam smearing due to the PSF we subtract the radial velocity gradient linearly (Stott et al., 2016):

$$\sigma_0^2 = \left(\sigma_{\rm obs} - \frac{\Delta V}{\Delta R_{\rm PSF}}\right)^2 - \sigma_{\rm instr}^2 \tag{6.3}$$

where $\sigma_{\rm obs}$ is the observed velocity dispersion measured from the 1D emission line fitting, $\Delta V/\Delta R_{\rm PSF}$ is the velocity gradient measured within the PSF radius, and $\sigma_{\rm instr}$ is the instrumental broadening measured from sky lines in the data. If no clear velocity gradient is measured we subtract 23.3 km/s, the median beam smearing value for the sample. We note that beam smearing is highly dependent on the flux profile of the individual galaxy compared to the size of the PSF, so this median value may not be suitable in all cases, but it provides a reduction of an appropriate order.

Kinematic maps are produced by fitting Gaussian profiles to the flux in individual spaxels over a 50Å range around the linecenter derived from the integrated emission line profile. We require a S/N > 5 for a successful fit. Following Livermore et al. (2015); Stott et al. (2016) we initially aim to fit the emission line in 1 spaxel ($0\farcs2 \times 0\farcs2$), but expand the fitting region to encompass neighboring spaxels in $0\farcs4 \times 0\farcs4$ and $0\farcs6 \times 0\farcs6$ apertures if the S/N criterion is not satisfied. We then reject any spaxels where the errors on the derived flux, central wavelength or line dispersion are $> 50\%$ of the measured values. The velocity and velocity dispersion maps are produced as the 1st and 2nd moments of the line profiles. The high S/N 2D flux and kinematic maps for our sample are presented in Appendix 6.7. We are able to produce kinematic maps for 25/32 galaxies.

To derive kinematic properties we use the kinematic fitting code GalPaK^{3D} (Bouché et al., 2015) which was designed for IFU instruments and fits disk models to 3D data cubes themselves (see also Teodoro & Fraternali, 2015; Di Teodoro et al., 2016, for an alternative 3D fitting tool). GalPaK^{3D} has been shown to work well with VLT/Multi Unit Spectroscopic Explorer (MUSE) data (Bacon et al., 2014b; Contini et al., 2016). This is the first time it has been used on KMOS data. We refer the reader to Bouché et al. (2015) for a full description of the fitting procedure, and we outline only the key points here.

Using GalPaK^{3D} we produce a three-dimensional galaxy model with an exponential radial flux profile and Gaussian disk luminosity thickness with scale height h_z. The velocity profile is modeled as an arctangent function (Courteau, 1997):

$$V(r) = V_{\max} \sin i \frac{2}{\pi} \arctan\left(\frac{r}{r_t}\right) \tag{6.4}$$

where r is the distance along the major axis of the galaxy in the plane of the sky, $V_{\max}$ is the asymptotic velocity in the plane of the disk, i is the inclination of the disk, and r_t is the turnover radius.

The total line-of-sight velocity dispersion, $\sigma_{\rm tot}$ has three components: (1) the local isotropic velocity dispersion, σ_d, due to the self-gravity of the disk, which is given by $\sigma_d(r) = h_z V(r)/r$ for a compact thick disk; (2) a mixing term due to the mixing of velocities along the line of sight in a disk with non-zero thickness; and (3) the intrinsic velocity dispersion, σ_0, which we assume to be isotropic and spatially constant, which measures the dynamical 'hotness' of the disk. The terms are added in quadrature:

$$\sigma^2_{\rm tot}(r) = \sigma_d(r)^2 + \sigma^2_m + \sigma^2_0 \tag{6.5}$$

By construction, $\sigma_{\rm tot}$ is radially symmetric. It is therefore likely that the galaxies best fit by GalPaK^{3D} have the most regular symmetric velocity dispersion maps. However, the observed total velocity dispersion maps of many galaxies in our sample, plotted in Figures 6.8-6.12, are not symmetric. This asymmetry may be due to clumpy star formation and/or slow mixing of turbulence in the disk (Genzel et al., 2011; Glazebrook, 2013).

The model is convolved with a 3D kernel comprised of the instrumental line spread function (LSF) of KMOS measured from sky lines and the median PSF of the data derived from observing faint stars (see Section 6.3.1). This 3D convolved model is then compared with the data itself. We use the Bayesian MCMC fitting method described in Bouché et al. (2015) to fit the 3D model to the data cubes in the vicinity of the emission line. We fix the x, y centroid of the emission line to the center of the YJ continuum and fit for 9 free parameters: λ_c the central wavelength of the emission line; $f_{\rm tot}$ the total flux in the emission line; $r_{1/2}$, the half-light radius of the disk; the inclination i of the disk and the position angle (PA) in the plane of the sky; the velocity profile turnover radius r_t; the asymptotic velocity $V_{\rm max}$; a systemic velocity offset $V_{\rm sys}$; and the intrinsic velocity dispersion σ_0. As inclination, r_t and $V_{\rm max}$ are degenerate in an arctangent model, if a source is not highly distorted by lensing magnification ($\mu < 4$) we additionally constrain the inclination using a uniform prior over $i_{\rm HST} \pm 20°$, where $i_{\rm HST}$ is obtained from the axis ratio of sources in the HST photometry (Section 6.4.2) using GALFIT (Peng et al., 2010) and assuming a thin disk.

Using a Bayesian method enables us to treat the uncertainties on all parameters simulatenously and robustly. We require the acceptance rate of useful iterations of the MCMC walk to be between $30 - 50\%$, the reduced$-\chi^2$ of the model velocity map to be < 15, and the RMS difference between the observed and model velocity maps to be $< 0.4 V_{\rm max} \sin i$ for fit to be accepted. 11 objects are fit by GalPaK^{3D}.

Some objects display clear velocity gradients in the 2D kinematic maps (Figures 6.8-6.12) but GalPaK^{3D} fits them poorly. For these objects we fit the 2D velocity map using Equation 6.4, rather than the full 3D fitting. We fit the 2D maps using a Bayesian model to fit for: the inclination i of the disk and the position angle (PA) in the plane of the sky; the velocity profile turnover radius r_t; the asymptotic velocity $V_{\rm max}$; and a systemic velocity $V_{\rm sys}$. We use the EMCEE MCMC sampler (Foreman-Mackey et al., 2013) and the same prior on inclination as described above. This 2D method produced kinematic parameters consistent with those from GalPaK^{3D} for the same objects. We accept 5 objects for which GalPaK^{3D} failed as well-fit by the 2D model, with the reduced$-\chi^2$ of the fit < 15, and the RMS difference between the observed and model velocity maps to be $< 0.4 V_{\rm max} \sin i$.

Of these 5 objects which were fit only by the 2D model, 2 are significantly magnified, with $\mu > 15$ (MACS0416_394 and RXJ1347_1230). As GalPaK^{3D} attempts to fit a model to the light profile of the galaxy, it is expected that GalPaK^{3D} will fail for highly magnified objects which are distorted. As lensing doesn't change the observed velocities (De Burgh-Day et al., 2015; Jones et al., 2010) it is still possible to fit a simple kinematic model to these objects, but due to the large uncertainties in measuring inclination deriving source plane parameters is challenging (see Section 6.4.2 for more discussion), so these objects are neglected in our further analyses. The other 3 objects (MACS0416_863, MACS1149_1757 and RXJ1347_450) are compact, with $r_{1/2} < r_{\rm PSF} \sim 0\farcs3$, so were unlikely to be well-fit by GalPaK^{3D}, which requires $r_{1/2} \gtrsim 1.5 r_{\rm PSF}$.

To transform to the source plane, we correct the inclination and radii fit by GalPaK^{3D} or the 2D method using Equation 6.1, and then calculate a source plane $V_{\rm max}$ using the corrected inclination.

For the remaining objects which were not well-fit by either GalPaK^{3D} or the 2D velocity map model we construct $V_{\rm max,obs} = (v_{\rm max} - v_{\rm min})/2$ from the 2D velocity maps as an approximate measure of the rotational velocity of these objects, which are unlikely to be regularly rotating. This measure of $V_{\rm max}$ is likely to underestimate an asymptotic velocity as we do not measure velocity with high S/N in the outer regions of many galaxies. Thus we rescale velocities measured in this way, assuming arctangent rotation curves (Equation 6.4):

$$V_{\rm max} = \frac{V_{\rm max,obs}}{\sin i} \frac{\pi}{2} \frac{1}{\arctan\left(R/\bar{r}_t\right)} \tag{6.6}$$

where i is the source plane inclination determined from photometry (Section 6.4.2) and corrected for lensing via Equation 6.1), R is a measure of the observed radial extent of the galaxy in KMOS ($R = \sqrt{(N_{\rm px}/\pi)}$, where $N_{\rm px}$ is the number of spaxels in the 2D velocity map) and $\bar{r}_t = 1.24$ is the median turnover radius of the sample fit by GalPaK^{3D} and the 2D method described above. This results in a median rescaling factor for the velocities of these objects of 1.25.

These 3 measures of maximum velocity (from GalPaK^{3D}, the 2D fit, and the rescaled velocity map) produce consistent velocities for the 11 galaxies which were well-fit by GalPaK^{3D}, it is reasonable to use 'last-resort' methods to estimate the velocity of rotating disks. We use velocities derived from GalPaK^{3D} and the 2D fit to investigate trends for objects which are likely rotating disks. The objects which were not fit by either GalPaK^{3D} or the 2D method do not have clear velocity gradients are unlikely to be rotating disks, here $V_{\rm max}$ gives us an approximate measure of gas kinematics in the galaxies.

Following the fitting we classify the galaxies into 5 kinematic categories:

1. Regular rotators: rotation dominated systems with $V_{\max}/\sigma_0 > 1$ and well-fit by GalPaK^{3D} with the reduced$-\chi^2$ of the model velocity map < 3 and the RMS difference between the observed and model velocity maps $< 0.15 V_{\max} \sin i$. These comprise 3/25 of the resolved systems.

2. Irregular rotators: systems with clear velocity gradients fit either by GalPaK^{3D} or the 2D method with reduced$-\chi^2$ of the fit < 15 and the RMS difference between the observed and model velocity maps $< 0.4 V_{\max} \sin i$, and $V_{\max}/\sigma_0 > 1$. These comprise 13/25 resolved systems.

3. Dispersion dominated: systems with $V_{\max}/\sigma_0 < 1$. These comprise 3/25 resolved systems.

4. Mergers/unknown: systems with merging signatures evident in *HST* images and/or kinematic maps, and systems with irregular kinematic maps where no clear velocity gradients are evident. These comprise 6/25 resolved systems, of which 2 appear to be mergers.

5. Unresolved: there are 7/32 total systems with unresolved kinematic maps. The majority of these systems are compact or in MACS2129, which had the shortest integration time. We measure the velocity dispersion of the these objects from their 1D spectra obtained in S/N optimized spatial apertures.

Table 6.1 shows the sources presented in this paper and their derived kinematics properties. Observed kinematic maps for the sample are shown in Appendix 6.7 in Figures 6.8-6.12. We plot the *HST* RGB images obtained from CLASH or HFF photometry, the whitelight image from KMOS YJ, the 2D emission line used for kinematic modeling, the velocity maps and velocity dispersion maps.

Rotation curves are produced by plotting 1D cuts in the velocity maps, along the major kinematic axis of the galaxy as determined by the Bayesian fitting, either from GalPaK^{3D}

or the 2D fitting. Rotation curves for the regular and irregular rotators (kinematic classes 1 and 2) are presented in Appendix 6.8.

The introduction of 2 classes of rotators was motivated by the 3 objects for which GalPaK^{3D} produced excellent fits, with the cut (reduced$-\chi^2$ of the model velocity map < 3 and the RMS difference between the observed and model velocity maps $< 0.15 V_{\rm max} \sin i$ for class 1) arising from a natural clustering in the fit statistics for the rotating objects. The class 1 objects have symmetric rotation curves (Figure 6.13) aligned with their photometric axes and velocity dispersion maps which appear to peak at the center of their light profiles (Figures 6.8, with the exception of MASC1149_593). The second 'irregularly rotating' group of galaxies display more asymmetries in their velocity and velocity dispersion maps (e.g. RXJ1347_287 and RXJ1347_188), and several have clumps in the HST photometry which may indicate intense star forming regions or minor mergers (e.g. MACS1149_1757, RXJ1347_1419 and RXJ1347_795).

6.4.4 Star formation drivers

To investigate the relationships between the high SFR observed at $z \gtrsim 1$ (e.g., Madau & Dickinson, 2014; Whitaker et al., 2014) we look for correlations between SFRs and the kinematic properties of our sample, and any evolution with redshift.

To derive SFRs we use the KMOS measured magnification-corrected line flux of Hα ($z < 1$), Hβ ($1 \leq z < 1.8$) or [O II] ($z \geq 1.8$). We convert line flux to SFR using relations from Kennicutt (1998) and divide SFRs by a factor of 1.7 to convert from a Salpeter (1954) to Chabrier (2003) initial mass function (IMF). We assume a Case B recombination extinction-corrected Balmer decrement of 2.86 for all Hβ measurements.

To correct for extinction we use the stellar reddening factors calculated from the SED fitting and additional empirical calibrations to convert continuum extinction to nebular emission line extinction. Objects MACS1149_593 and MACS1149_683 have nebular extinction values derived from GLASS data by Wang et al. (2016). For the remaining sources, we use the calibration from Wuyts et al. (2013) where $A_{\rm V,gas} = A_{\rm V,SED}(1.9 - 0.15 A_{\rm V,SED})$. We use the Cardelli et al. (1989) reddening curve with $R_V = 3.1$.

In Figure 6.4 we plot the galaxy stellar masses derived from photometry (Section 6.4.2) versus their SFRs derived from the KMOS line fluxes. We see that our galaxies are scattered around the star forming main sequence in their mean redshift bins. Our sample is too small to draw firm conclusions, but reflects a large diversity in the lives and dynamics of star forming galaxies at cosmic noon.

In Figure 6.5 we plot correlations between $V_{\rm max}/\sigma_0$, σ_0, stellar mass and specific SFR. We see that the majority of our systems have $V_{\rm max}/\sigma_0 > 1$ indicating most of these systems are rotationally supported. 16/25 resolved systems are rotationally supported (kinematic classes 1 and 2), with 5 additional objects with $V_{\rm max}/\sigma_0 > 1$, consistent with the 83% of systems in KROSS (Stott et al., 2016) at $z \sim 1$, and 93% of systems at $z \sim 1$ and 73% of systems at $z \sim 2$ in KMOS^{3D} (Wisnioski et al., 2015).

Of the 5 objects have $V_{\rm max}/\sigma_0 < 1$, we consider only 3 to be dispersion dominated. RXJ1347_1419 has a clear rotation curve so is classed as an irregular rotator (Figure 6.14), but is magnified by $\mu \sim 9$ so there are large uncertainties in deriving the source plane maximum velocity. MACS2129_1739 has multiple components (Figure 6.12) and a velocity gradient, suggesting this is a merger system.

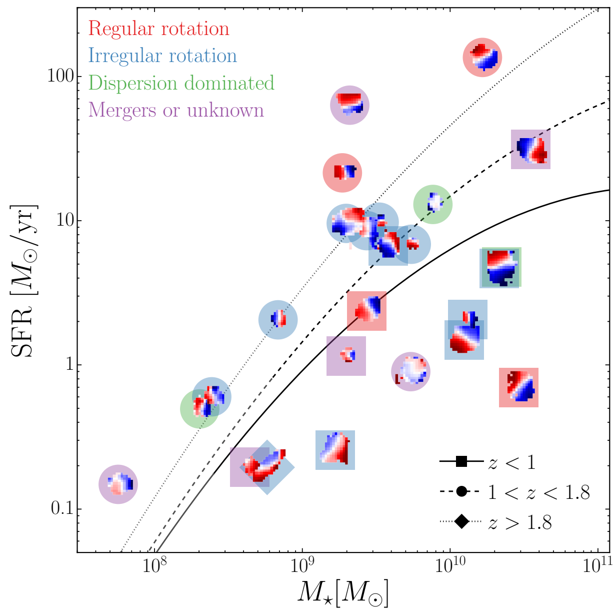

Figure 6.4: The velocity maps for galaxies in our sample with resolved kinematics, plotted at the galaxy's position on the SFR$-M_\star$ plane. We plot the empirical SFR models from Whitaker et al. (2014) at a range of redshifts (indicated by linestyle) to compare with KLASS. The shapes around the velocity maps indicate the redshift bin of the object: $z < 1$ (square), $1 \leq z < 1.8$ (circle) or $z \geq 1.8$ (diamond), and the colors indicate the kinematic class as described in Section 6.4.3. Our sample shows a large scatter around the star forming main sequence.

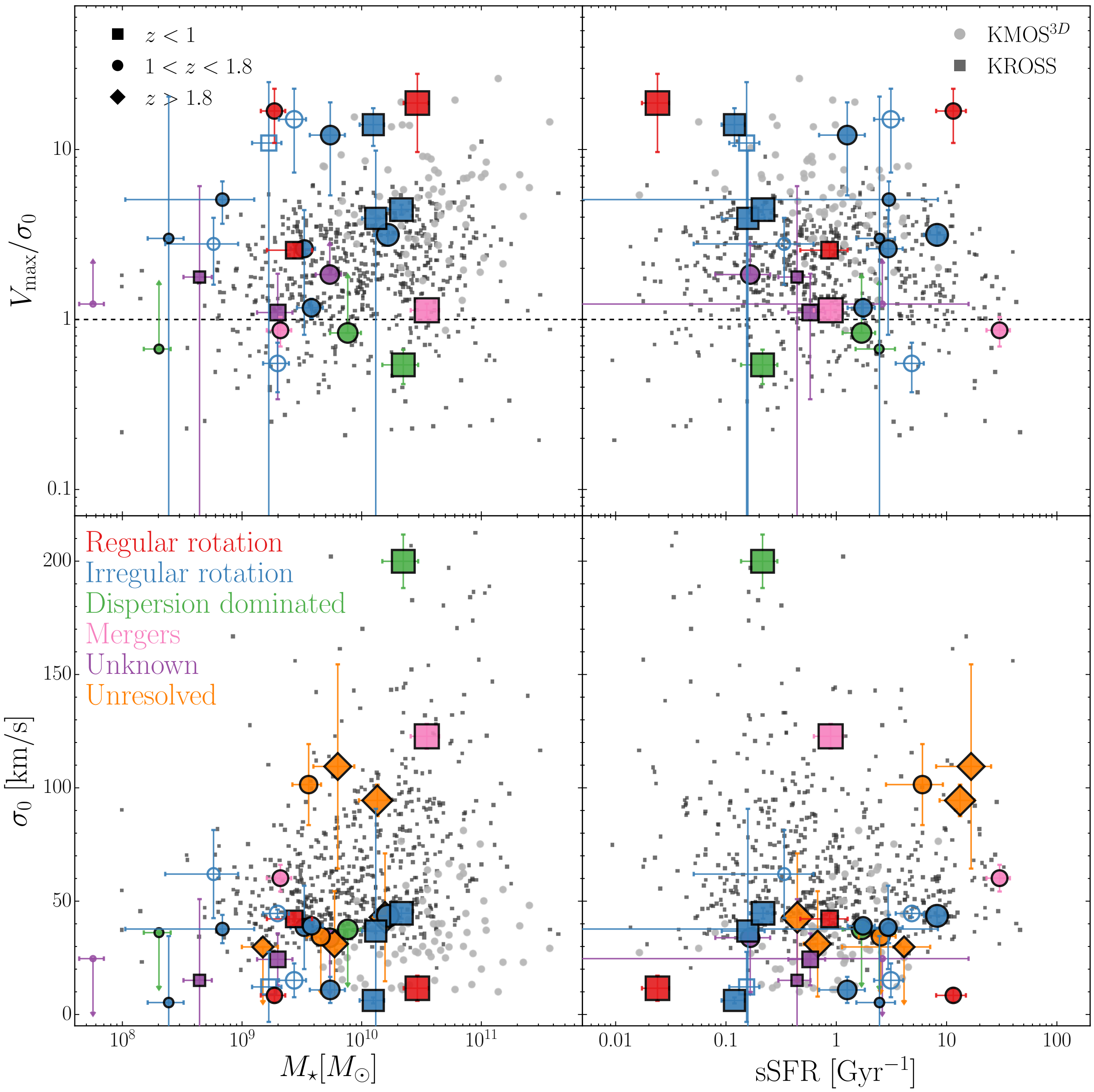

Figure 6.5: Velocity dispersion and $V_{\max}/\sigma_0$ as a function of stellar mass and sSFR for our sample. The marker styles indicate the redshift bins of the survey, the colors indicate the kinematic classification and the marker size indicates stellar mass. Open markers indicate the magnification of the object is large ($\mu > 4$) so intrinsic velocity measurements are more uncertain. We note that the majority of systems at $z > 2$ which are unresolved are in the the cluster MACS2129 which had the shortest integration time. We plot points from KROSS (Stott et al., 2016) and KMOS^{3D} (Wisnioski et al., 2015) for comparison. We measure σ_0 in a similar way to KROSS (Section 6.4.3), whereas KMOS^{3D} measuring σ_0 from the outer regions of 2D velocity dispersion maps. Stott et al. (2016) notes KROSS σ_0 obtained in this way are a factor ~ 2 higher than those from KMOS^{3D}.

6.4.5 Kinematic trends

KLASS shows a large diversity in the kinematics of star forming galaxies with mass and redshift. Regular rotating disks exist with stellar mass $> 3 \times 10^9 M_\odot$, with other irregular rotationally supported systems existing at a wider range of mass (upper left panel, Figure 6.5). The merging and irregular systems have sSFR $> 0.1\mathrm{Gyr}^{-1}$ (right panels, Figure 6.5), suggesting that their disturbed gas dynamics may be enhancing the SFRs in some of these objects compared to kinematically ordered systems. Our sample shows higher sSFRs at higher redshift (lower right panel, Figure 6.5), irrespective of kinematic class, consistent with the expectation of a higher mass accretion rate and densities at high redshifts (Tacchella et al., 2013; Mason et al., 2015a).

With the power of lensing, we can access the low mass galaxies that are missing from other surveys. Our sample includes 5 galaxies with stellar mass below $6.3 \times 10^8 M_\odot$, lower than any previous IFU targets at $z > 1$. In Figure 6.5 we can see that all the galaxies below $3 \times 10^9 M_\odot$ have complex kinematics: no regular rotators exist below this limit. These systems at $z > 1$ all have sSFR $> 1\mathrm{Gyr}^{-1}$. We discuss the low mass galaxies in Section 6.5.2.

The dispersion dominated systems exist at both low and high mass, and a decade apart in sSFR. These are clearly very different systems (see kinematic maps in Figure 6.10) and are discussed further in Section 6.5.3.

The mean $V_{\max}/\sigma_0$ for the regular rotator sample is 12.7 ± 2.4 - similar to the values in the local universe ($5 - 20$, e.g. Epinat et al., 2010), whilst for the irregularly rotator sample the mean value is lower at 5.5 ± 0.5, suggesting these objects are dynamically hotter. This justifies the splitting of the rotation dominated sample into 2 sub-samples.

In Figure 6.6 we plot $V_{\max}/\sigma_0$ for the rotation dominated galaxies in our sample, and σ_0 for all galaxies, as as function of redshift, to explore evolution in these parameters. We exclude 5 highly magnified galaxies ($\mu > 4$) and any galaxies for which we only have limits on these parameters. We also compare our data with results from other IFU surveys over the redshift range $0 \lesssim z \lesssim 3.5$. Comparing the data in redshift bins across all surveys, our data qualitatively support a trend of decreasing $V_{\max}/\sigma_0$ with redshift (Wisnioski et al., 2015;

Glazebrook, 2013), suggesting that disk galaxies are dynamically 'hotter' at high redshift.

To quantify any evolution in our sample we fit a simple model of the form $f \sim (M_\star/10^{10}M_\odot)^\alpha(1+z)^\beta$ using a Bayesian fitting procedure using the EMCEE sampler (Foreman-Mackey et al., 2013). We include dependence on mass because our sample spans a wide range in stellar mass which is correlated with velocity and, to some extent, velocity dispersion (e.g. Phillips, 1993; Kassin et al., 2007). For $V_{\rm max}/\sigma_0$, $\alpha = 0.29 \pm 0.05$ and $\beta = -0.08 \pm 0.37$, suggesting a very marginal decline with increasing redshift, but no redshift evolution is also consistent with the data. There is a stronger dependence on stellar mass, which is expected because the highest stellar mass objects are predominantly regular rotating disks, as discussed above. For σ_0, $\alpha = 0.42 \pm 0.02$ and $\beta = 1.09 \pm 0.12$, indicating an increase in σ_0 with both increasing stellar mass and redshift for our sample. An increase in σ_0 with redshift is also seen in other work (Wisnioski et al., 2015) and could be due to high densities and high rates of gas inflow at high redshift driving up velocity dispersion in a disk.

We investigate the importance of rotational velocity in supporting the sample in Figure 6.7. We plot the stellar mass Tully-Fisher relation between $M_\star$ and $V_{\rm max}$. We plot only the galaxies classified as rotating (classes 1 and 2) and exclude 4 high magnification objects due to the uncertainties in deriving source plane velocities. For comparison, we plot best-fit relations from the literature at similar redshifts (Conselice et al., 2005; Miller et al., 2011; Tiley et al., 2016) and a $z \sim 0$ relation from a compilation of data (Pizagno et al., 2007; Rhee, 2004; Reyes et al., 2011) produced by Tiley et al. (2016). We see that the regularly rotating systems are closest to the fiducial Tully-Fisher relation, whilst the irregularly rotating systems are mostly scattered below the relation. Whilst this is a very small sample, it is consistent with the conclusions of Tiley et al. (2016), which also found a large number of their rotating sample offset below the $z \sim 0$ relation, but present a 'disky' sub-sample (similar to our regular rotators) which lies closer to the $z \sim 0$ relation. Most previous studies on the Tully-Fisher relation at $z \sim 1$ (see also Di Teodoro et al., 2016) have preselected galaxies with disk morphologies, and thus are likely to miss objects such as those in our irregularly rotating sample which may not look like disks in photometric surveys but have velocity gradients.

We fit a linear relation ($\log_{10} M_\star = m \log_{10}(V/V^*) + c$, where V^* is the median velocity in the sample) with intrinsic scatter σ, using a Bayesian technique with EMCEE (Foreman-Mackey et al., 2013), to the total sample of 16 objects and to the 3 regular rotators only. For the total sample: $\log_{10} V^* = 2.13$, $m = 1.03^{+0.52}_{-0.39}$, $c = 9.85^{+0.14}_{-0.15}$ and $\sigma = 0.43^{+0.15}_{-0.10}$. For the regular rotators only: $\log_{10} V^* = 2.14$, $m = 4.66^{+1.62}_{-1.38}$, $c = 9.56^{+0.19}_{-0.17}$ and $\sigma = 0.05^{+0.59}_{-0.05}$. The regular rotator sample best-fit relation is consistent with the plotted literature relations, but with large uncertainty due to the small sample size. The full sample is consistent with Tiley et al. (2016) and suggests an additional source of support other than rotational velocity in the irregularly rotating galaxies.

Higher velocity dispersion may provide increased pressure support in disks, to investigate this we attempt to fit a similar relation between stellar mass and $S_{0.5} = \sqrt{V_{\rm max}^2/2 + \sigma_0^2}$ as introduced by Kassin et al. (2007) to the sample in Figure 6.7. Kassin et al. (2007) found reduced intrinsic scatter when including velocity dispersion. For the total sample our best-fit relation is $\log_{10} S^*_{0.5} = 1.99$, $m = 1.19^{+0.65}_{-0.47}$, $c = 9.82^{+0.14}_{-0.15}$ and $\sigma = 0.42^{+0.15}_{-0.10}$. There is no significant decrease in intrinsic scatter between the pure velocity and $S_{0.5}$ Tully-Fisher relations for our sample. Thus it is unclear that intrinsic velocity dispersion provides significant pressure support to the systems presented here.

We urge caution before over-interpreting these plots which are influenced strongly by the selection sample and other potential biases of our small sample, including uncertainties in the magnification models. It is clear that there is much observational work to be done to build large representative samples to further investigate redshift trends of kinematic properties.

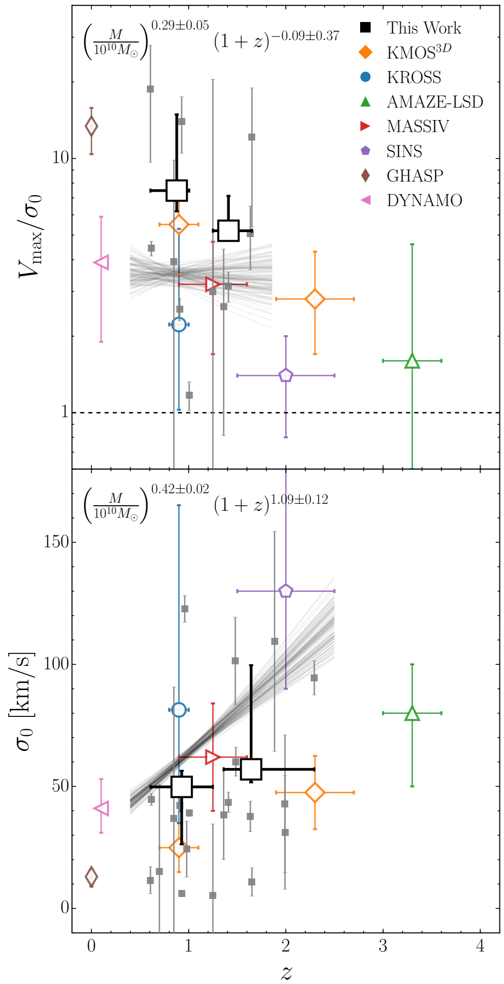

Figure 6.6: $V_{\rm max}/\sigma_0$ as a function of redshift for the galaxies classified as regular rotators and irregular rotators in our sample (Section 6.4.3), and intrinsic velocity dispersion as a function of redshift for all galaxies in our sample. We exclude highly magnified galaxies ($\mu > 4$) and galaxies for which we have only limits on these parameters. We plot the individual data as gray squares with 1 standard deviation error bars, and our data in two redshift bins as black squares (the squares are positioned at the mean value within the redshift bin, the vertical bars show the 50% range and the horizontal bars show the full redshift range of the bin. For comparison we plot the mean, 50% value range (vertical bars) and redshift range (horizontal range) of rotation dominated galaxies in other IFU surveys: KMOS^{3D} (orange diamonds, Wisnioski et al., 2015); KROSS (blue circles, Stott et al., 2016); AMAZE-LSD (green triangles, Gnerucci et al., 2011); MASSIV (red right triangles, Vergani et al., 2012); SINS (purple pentagons, Förster Schreiber et al., 2009); GHASP (brown triangles, Epinat et al., 2008a,b); and DYNAMO (pink left triangle, Green et al., 2013). We show draws from the MCMC samples for the redshift and mass dependent fit to our data as the gray lines (described in Section 6.4.4) and give the fitted exponents for redshift and stellar mass evolution. The trend in $V_{\rm max}/\sigma_0$ is dominated by stellar mass for our sample and an increase of velocity dispersion with increasing redshift is found for our sample.

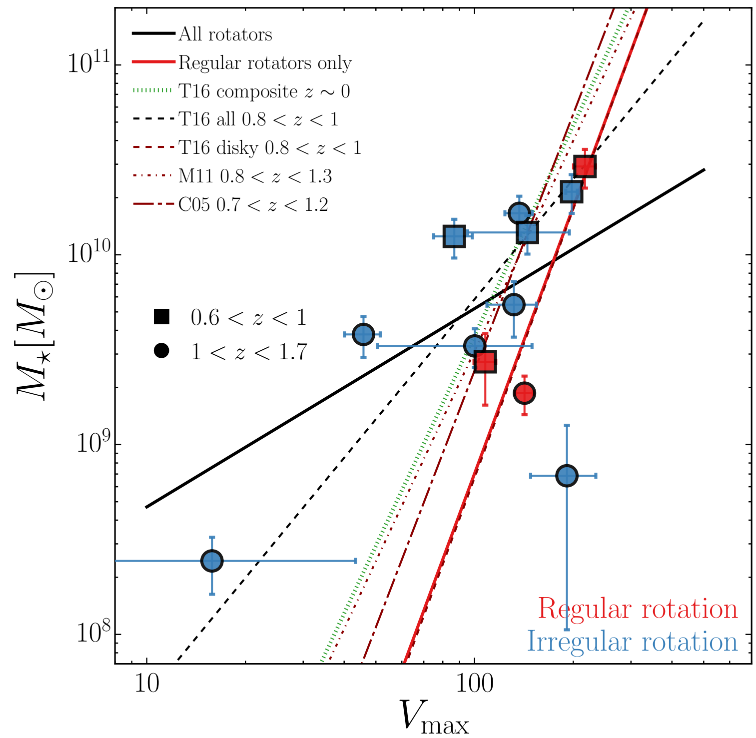

Figure 6.7: Stellar mass Tully-Fisher relation with $V_{\rm max}$ for rotating galaxies in our sample (kinematic classes 1 and 2). As before, the colors indicate the kinematic classification. Objects with magnification $\mu > 4$ are excluded. For comparison we plot stellar mass Tully-Fisher relations from the literature over a similar redshift range (red Conselice et al., 2005; Miller et al., 2011; Tiley et al., 2016) and a $z \sim 0$ relation (green dotted) from a compilation of data (Pizagno et al., 2007; Rhee, 2004; Reyes et al., 2011) produced by Tiley et al. (2016). From Tiley et al. (2016) we show the fits to their full rotator sample (dashed black) and their 'disky' sample (dashed red) which is similar to our regular rotator sample. The best-fit relation to our full sample of rotators (solid black) is shallower than that of the regular rotators (solid red) and other relations from the literature. Our best-fit to the regular rotators is consistent with those from the literature.

6.5 Discussion

6.5.1 What is the dynamical nature of galaxies at $z \gtrsim 1$?

Integral fields surveys (Forster Schreiber et al., 2006; Genzel et al., 2011; Gnerucci et al., 2011; Flores et al., 2006) of $z \sim 1 - 3$ galaxies have found rotation dominated systems, dispersion dominated systems, and merging/irregular systems, in roughly equal proportions. High redshifts disks were expected to be highly turbulent as rotation dominated systems had systematically higher velocity dispersions than local disks (Epinat et al., 2010; Bershady et al., 2010). This is in contrast to the local universe where most objects with stellar mass over $10^{10}M_{\odot}$ are dispersion dominated ellipticals, the highest mass objects at $z \gtrsim 1$ were rotating disks.

Our sample shows a large diversity in the kinematic nature of galaxies at $z \gtrsim 1$. The higher spatial resolution of KLASS compared to field surveys, due to the boost from lensing, has enabled us to clearly resolve rotating objects in our sample. The majority of our sample is rotation supported (16/25), but we find justification to define two rotation supported sub-samples: (1) regular rotators (3 objects) which are kinematically regular, with mean $V_{\max}/\sigma_0 = 12.7 \pm 2.4$, similar to values for local disks (Epinat et al., 2010), and (2) irregular rotators with more disturbed kinematics and lower mean $V_{\max}/\sigma_0 = 5.5 \pm 0.5$, suggesting dynamically hotter disks. This small fraction of galaxies exhibiting regular rotation was also seen recently in Leethochawalit et al. (2016a) using AO observations of lensed galaxies. Galaxies at high redshift are likely ongoing morphological and kinematic changes before settling into the bimodality we see in the local universe.

6.5.2 Revealing the kinematics of low mass galaxies

Gravitational lensing gives us access to the low mass galaxies missing from other surveys: KLASS has resolved kinematics in 5 galaxies at $z > 1$ with stellar mass below $6.3 \times 10^8 M_{\odot}$, lower than any previously studied.

From the kinematic maps (Figures 6.8-6.12) and Figure 6.5 we see that none of these low mass galaxies are regularly rotating: 2 are irregular rotators (MACS1149_1757 and RXJ1347_1230), 1 is dispersion dominated (MACS0416_706), and 2 have unknown/merging kinematic structure (MACS1149_683 and MACS1149_1237). In Figure 6.5 (right panels) we show that these systems also have sSFR $> 1\mathrm{Gyr}^{-1}$. Our data suggest the turbulent nature of star formation in low mass galaxies effects the kinematics of the whole galaxy: these low mass galaxies are all kinematically disturbed and rapidly star forming.

6.5.3 What are dispersion dominated galaxies?

High redshift dispersion dominated systems were first seen by Erb et al. (2006). This population has been observed at stellar mass ranges $\sim 1-5\times10^{10}M_\odot$ (the majority of high mass objects are observed with dominant rotation), and the number density of the population increases with redshift (Law et al., 2007, 2009; Vergani et al., 2012; Newman et al., 2012). The formation and evolution history of these objects is a relative mystery: perhaps formed by the collapse of a single molecular cloud; will they grow to large elliptical galaxies at low redshift, via mergers, or will they fade to remain relatively low mass?

High spatial resolution is needed to clearly distinguish rotationally supported galaxies from mergers and pressure supported systems. AO on Keck/OSIRIS and VLT/SINFONI have enabled high spatial resolution spectroscopy ($0''.2 \sim 1.7$ kpc at $z \sim 1$) of a handful of $z \sim 1-3$ galaxies, including objects which are gravitationally lensed and an order of magnitude lower in stellar mass than unlensed objects (Jones et al., 2010; Livermore et al., 2015). These studies indicated that high fractions of rotating galaxies would be misclassified as dispersion dominated at seeing-limited resolution. This was confirmed with AO followed of SINS galaxies: Newman et al. (2012) found the fraction of dispersion dominated systems in their sample dropped from 41% to $6-9\%$ when these galaxies were observed with AO. Additionally, surveys with AO (Gnerucci et al., 2011) and lensing (Leethochawalit et al., 2016a) have also shown that galaxies classified as rotators in seeing limited conditions have irregular velocity maps when observed with higher spatial resolution.

It is likely that the population of rotation dominated systems may be overestimated by low-resolution spectroscopy: most of these objects are compact with little resolved velocity information and highly affected by beam smearing which systematically increases velocity dispersion within the PSF. In our sample, which has median spatial resolution of $0''.4 \sim 3.3$ kpc at $z \sim 1$ after accounting for magnification, we find an upper limit of 3/25 dispersion dominated galaxies. This is consistent with the values of $6-9\%$ from AO surveys (Newman et al., 2012; Jones et al., 2010; Livermore et al., 2015) and lower than the fraction in KMOS^{3D} and KROSS ($\sim 17\%$ at $z \sim 1-2$): lensing is able to resolve kinematics on a comparable scale to AO.

The three dispersion dominated galaxies in our sample are extremely different from each other - one is very low mass (MACS0416_706, $\log M_\star = 8.31$), one is intermediate mass (MACS0416_94, $\log M_\star = 9.88$) and the other high mass (MACS1149_1644, $\log M_\star = 10.48$). The velocity dispersion of MACS1149_1644 is the highest in the sample (200 ± 12 km/s) and much more like dispersion dominated systems in previous work. This object has a low sSFR $\sim 0.2\mathrm{Gyr}^{-1}$ and could be a galaxy falling off the main sequence of star formation. MACS0416_94 has a low measured velocity dispersion (< 38 km/s after correcting for instrumental resolution and beam smearing) and relatively high sSFR $\sim 2\mathrm{Gyr}^{-1}$. MACS0416_706 is a compact low mass galaxy at $z = 1.35$ also with a very low measured velocity dispersion of < 36 km/s, and high sSFR $\sim 3\mathrm{Gyr}^{-1}$ and may represent a new class of low mass compact dispersion dominated objects, forming an elliptical structure in situ, which are undetected in surveys lacking the increase in depth and resolution that gravitational lensing provides in KLASS.

6.6 Conclusions

We have presented the first results from KLASS, showcasing KMOS IFU spectroscopy of 32 gravitationally lensed galaxies at cosmic noon. Our key findings are:

1. Emission line flux measured with KMOS is consistent with measurements of the same emission lines in the *HST* G102 and G141 grisms. This is in contrast to recent follow-up of *HST* grism-selected objects with slit-based spectrographs. Using simulated slits we find that slits recover only $\sim 60\%$ of the flux compared to KMOS, and this fraction declines rapidly if the emission line is offset from the center of the slit.

2. In 25 of the 32 galaxies presented here we obtain high S/N kinematic maps, which show a diversity in kinematic structure. The majority of unresolved galaxies are in the field with the shortest integration time. The majority of our sample with resolved kinematics have $V_{\mathrm{max}}/\sigma_0 > 1$ suggesting they are rotation dominated.

3. 3/25 of the resolved galaxies are classified as regularly ordered rotators with mean $V_{\max}/\sigma_0 = 12.7 \pm 2.4$, similar to local disks, but existing only at stellar masses $> 3 \times 10^9 M_\odot$.

4. 13/25 of the resolved galaxies are classified as irregularly rotating systems. The mean $V_{\max}/\sigma_0 = 5.5 \pm 0.5$ for these systems is lower than most disks in the local universe, indicating these are relatively turbulent 'hot' disks. Trends in $V_{\max}/\sigma_0$ are dominated by stellar mass.

5. With the power of lensing, we have resolved kinematics in galaxies with stellar masses below $> 3 \times 10^9 M_\odot$, none of which are regularly rotating and which have high sSFRs, indicating ongoing kinematic and morphological changes. 5 galaxies in our sample have stellar mass below $6.3 \times 10^8 M_\odot$, the lowest stellar mass objects at $z > 1$ ever observed with resolved kinematics.

6. We find a lower fraction of dispersion dominated systems compared to comparable surveys in blank fields. This is likely because the enhanced spatial resolution from lensing allows us to resolve velocity gradients in more compact systems consistent with results from surveys using AO.

Using the power of cluster lensing we have been able to efficiently resolve kinematics in objects at lower stellar masses than comparable multi-object IFU surveys, and at higher spatial resolution. We have seen a diversity in kinematic features for our sample, but find that only the highest mass objects form regular rotating disks at $z \gtrsim 1$, whilst lower mass galaxies are irregularly rotating or likely to be involved in mergers.

When the full survey is complete KLASS will provide kinematics of $\sim$ 60 galaxies at cosmic noon. Benefiting from 10 hour final integration times we expect be able to resolve velocity gradients at the edges of the objects and produce rotation curves to large radii for our wide range of stellar mass.

This paper is based on observations made with ESO Telescopes at the La Silla Paranal Observatory under programme IDs 095.A-0258 and 196.A-0778. The authors thank the ESO

KMOS team for carrying out our observations and answering our questions about the design and reduction of this Large Program. We thank Trevor Mendel for his code to correct the detector read-out bias and for insights into KMOS data reduction.

This work was supported by the *HST* GLASS grant GO-13459. C.M. acknowledges support by NASA Headquarters through the NASA Earth and Space Science Fellowship Program Grant 16-ASTRO16F-0002. T.T. acknowledges support by the Packard Foundation through a Packard Fellowship. T.J. acknowledges support provided by NASA through Program HST-HF2-51359 through a grant from the Space Telescope Science Institute, which is operated by the Association of Universities for Research in Astronomy, Inc., under NASA contract NAS 5-26555. T.M. acknowledges support from the Japan Society for the Promotion of Science (JSPS) through JSPS research fellowships for Young Scientists. B.V. acknowledges the support from an Australian Research Council Discovery Early Career Researcher Award (PD0028506).

This research made use of the following open-source packages for Python and we thank the developers of these: Astropy (Robitaille et al., 2013), SciPy libraries (Oliphant, 2007, including numpy and matplotlib) and PyFITS which is a product of the Space Telescope Science Institute, which is operated by AURA for NASA.

6.7 Appendix: Kinematic Maps

The resolved high S/N kinematics maps for our sample are shown in Figures 6.8-6.12. The procedure for producing the maps is described in Section 6.4.3.

We also show the *HST* RGB images for each galaxy. For MACS0416 and MACS1149 RGB images are produced using the HFF data (Lotz et al., 2017) in *HST* Wide Field Camera 3 (WFC3) filters F606W, F125W and F160W. For MACS2129 and RXJ1347 we use F606W, F125W and F160W data from CLASH (Postman et al., 2012b).

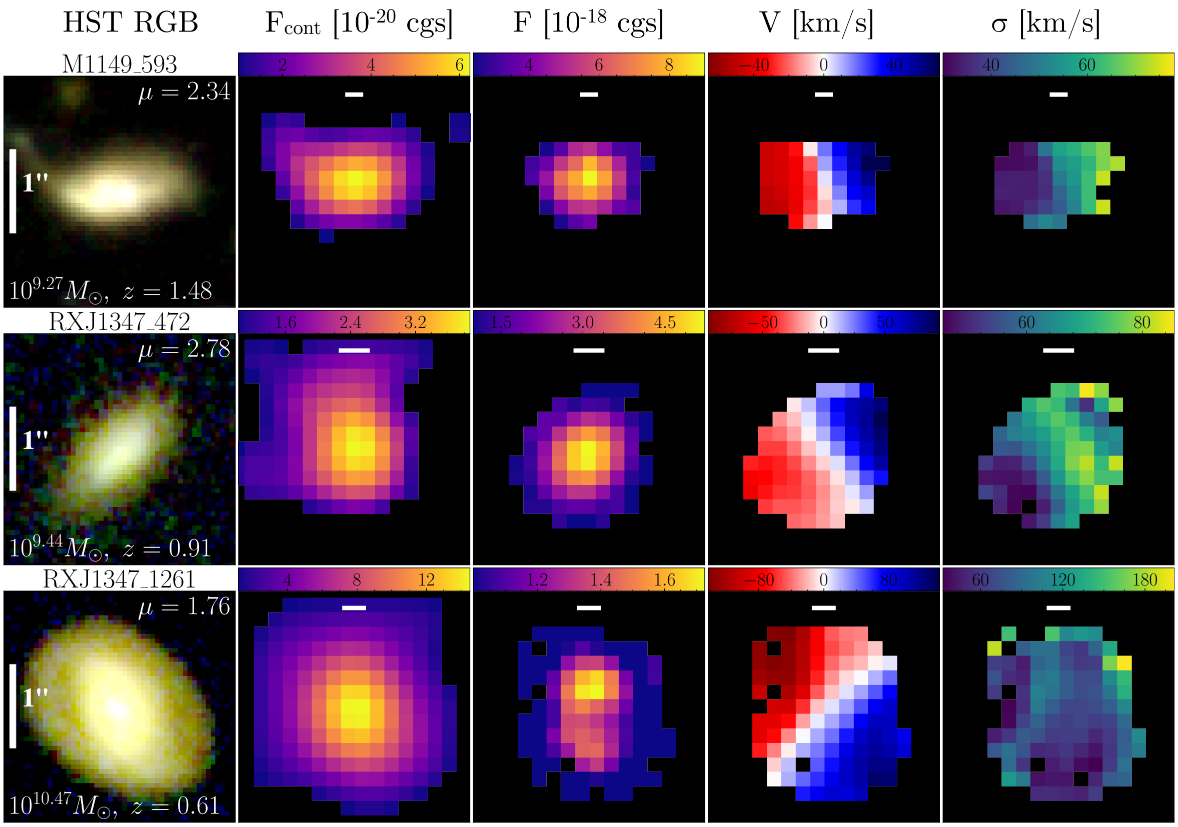

Figure 6.8: The *HST* RGB composite images, KMOS YJ continuum flux, 2D emission line spectra and velocity maps for the *regular rotators* class 1 of galaxies in KLASS, ordered by stellar mass. All maps are on the same spatial scale. The vertical white bar indicates 1″ in the image plane and the horizontal white bar indicates 1 kpc in the source plane (or 100 pc if indicated in cases of high magnification).

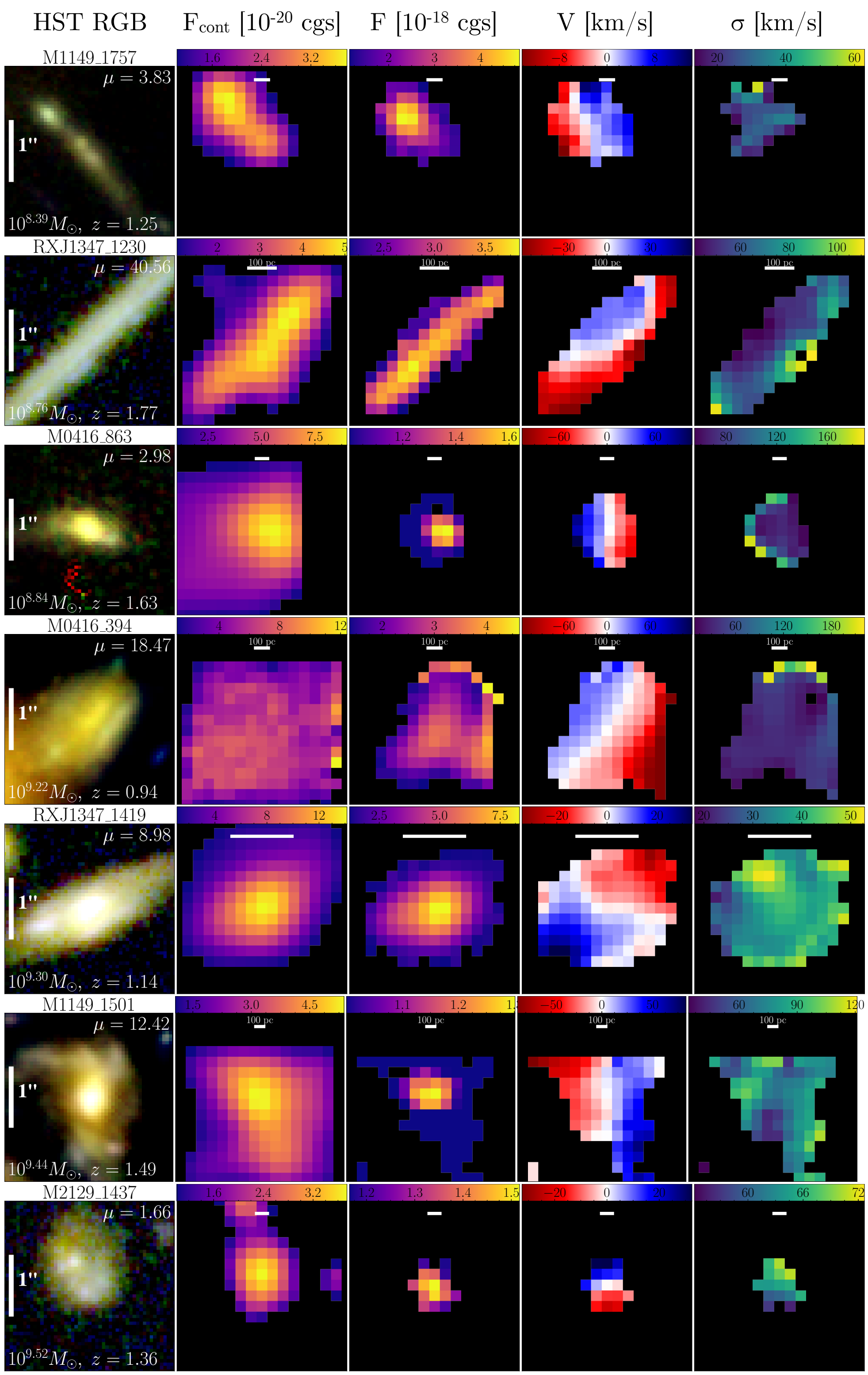

Figure 6.9: The *HST* RGB composite images, KMOS YJ continuum flux, 2D emission line spectra and velocity maps for the *irregular rotators* class 2 of galaxies in KLASS, ordered by stellar mass. All scales and labels are the same as in the above figures.

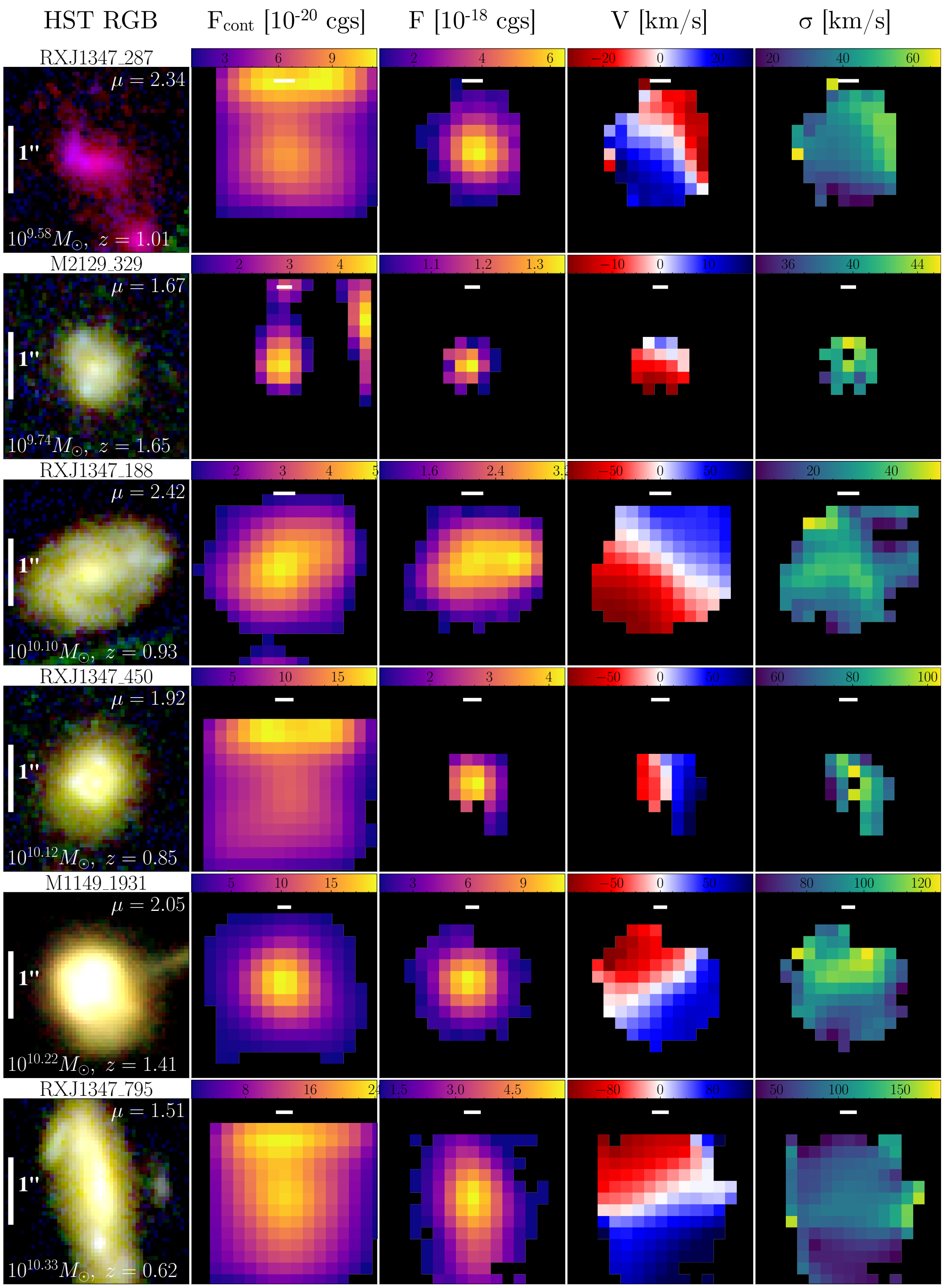

Figure 6.10: *(cont.)*

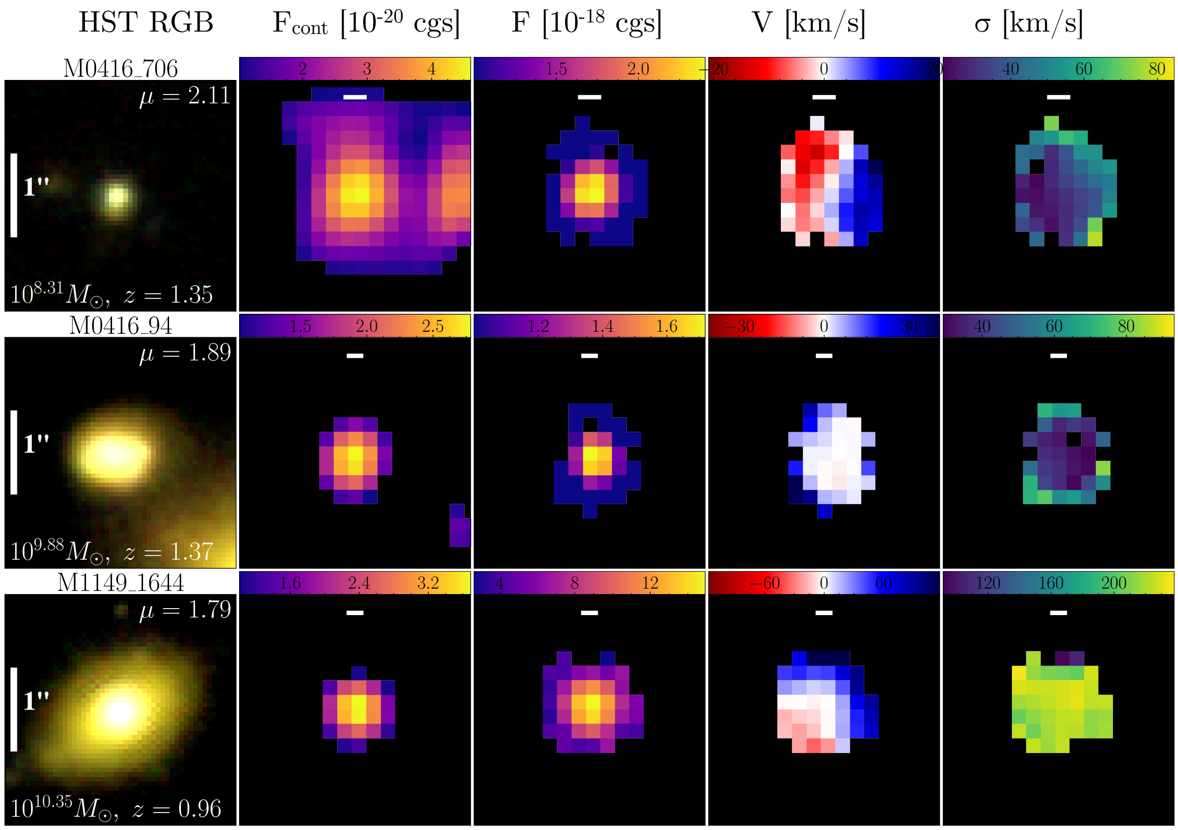

Figure 6.11: The *HST* RGB composite images, KMOS YJ continuum flux, 2D emission line spectra and velocity maps for the *dispersion dominated* class 3 of galaxies in KLASS, ordered by stellar mass. All scales and labels are the same as in the above figures.

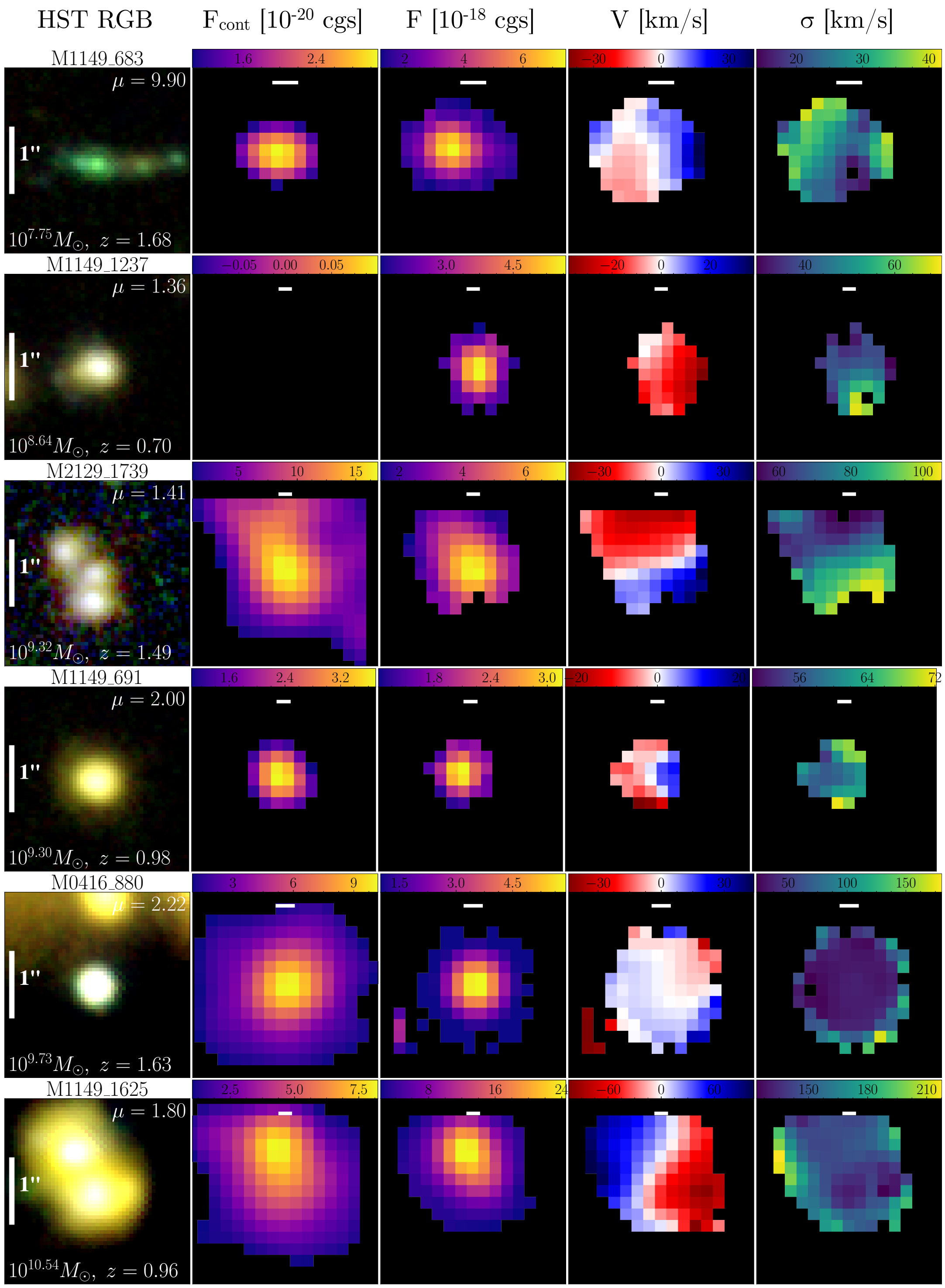

Figure 6.12: The *HST* RGB composite images, KMOS YJ continuum flux, 2D emission line spectra and velocity maps for the *mergers and unknown* class 4 of galaxies in KLASS, ordered by stellar mass. All scales and labels are the same as in the above figures.

6.8 Appendix: Rotation Curves

Rotation curves for rotating disks in our sample are presented in Figure 6.13-6.14 below. Rotation curves are obtained using the procedure outlined in Section 6.4.3.

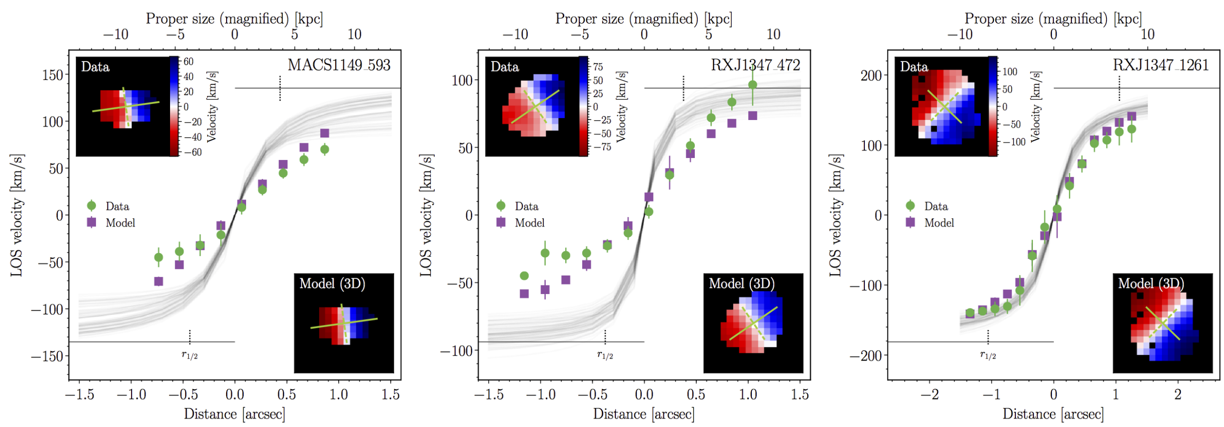

Figure 6.13: Rotation curves for the *regular rotators* class 1 of galaxies in KLASS. We plot the 2D measured velocity maps and convolved model velocity maps from 3D fitting to the data cube via GalPaK^{3D}. We plot the rotation curve extracted from a one pixel slit along the kinematic major axis as indicated by the green solid lines on the maps. We plot points from the measured map (green circles) and model map (purple squares, convolved with the 3D PSF and LSF kernel - see Section 6.4.3) and 100 sample line of sight model rotation curves drawn from the MCMC chain (gray lines). Solid horizontal black lines show the best-fit observed line-of-sight $V_{\max}$. Dotted black vertical lines show the inferred best-fit half-light radii from GalPaK^{3D} or from GALFIT to the HST images in the 2D kinematic fits if they are not strongly lensed. Rotation curves are measured beyond $r_{1/2}$ for the majority of objects.

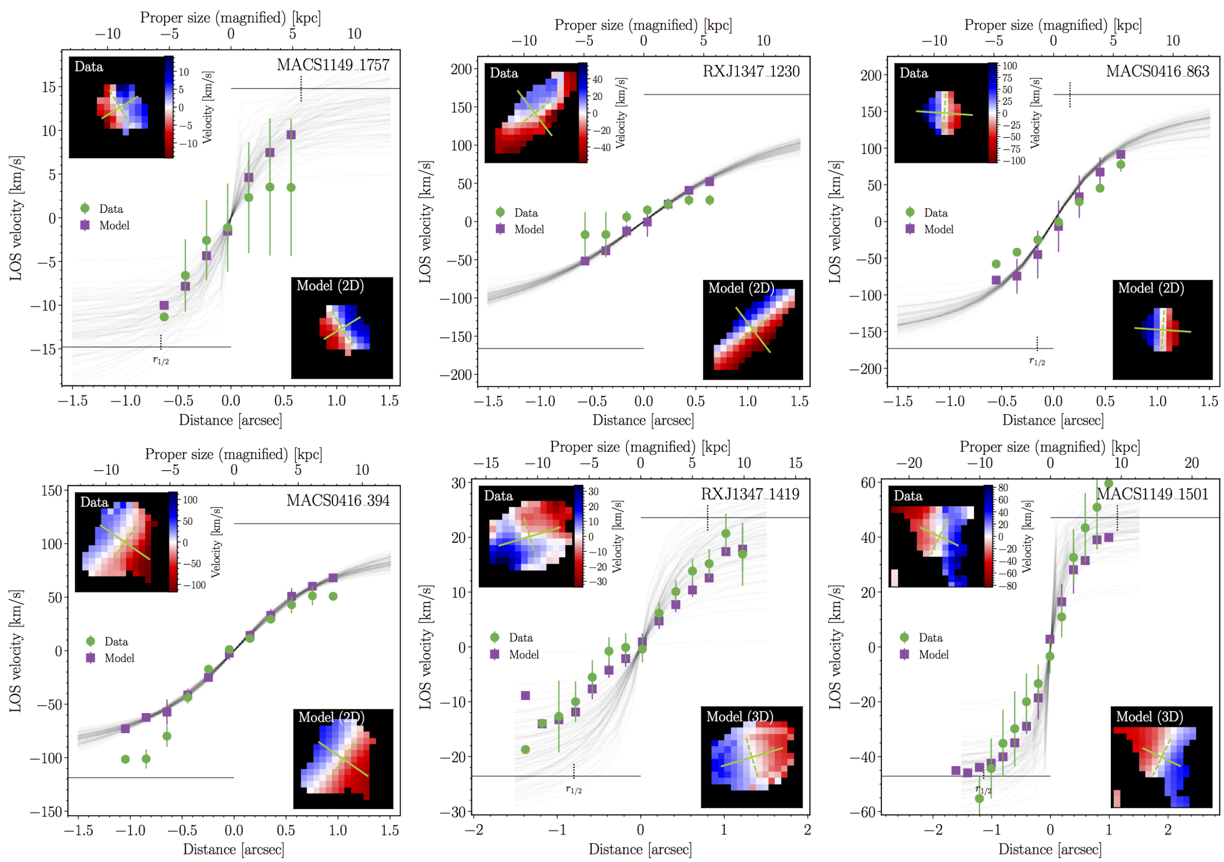

Figure 6.14: Rotation curves for the *irregular rotators* class 2 of galaxies in KLASS, plotted in the same way as Figure 6.13. Models are either 3D (from GalPaK^{3D}) or the 2D method described in Section 6.4.3.

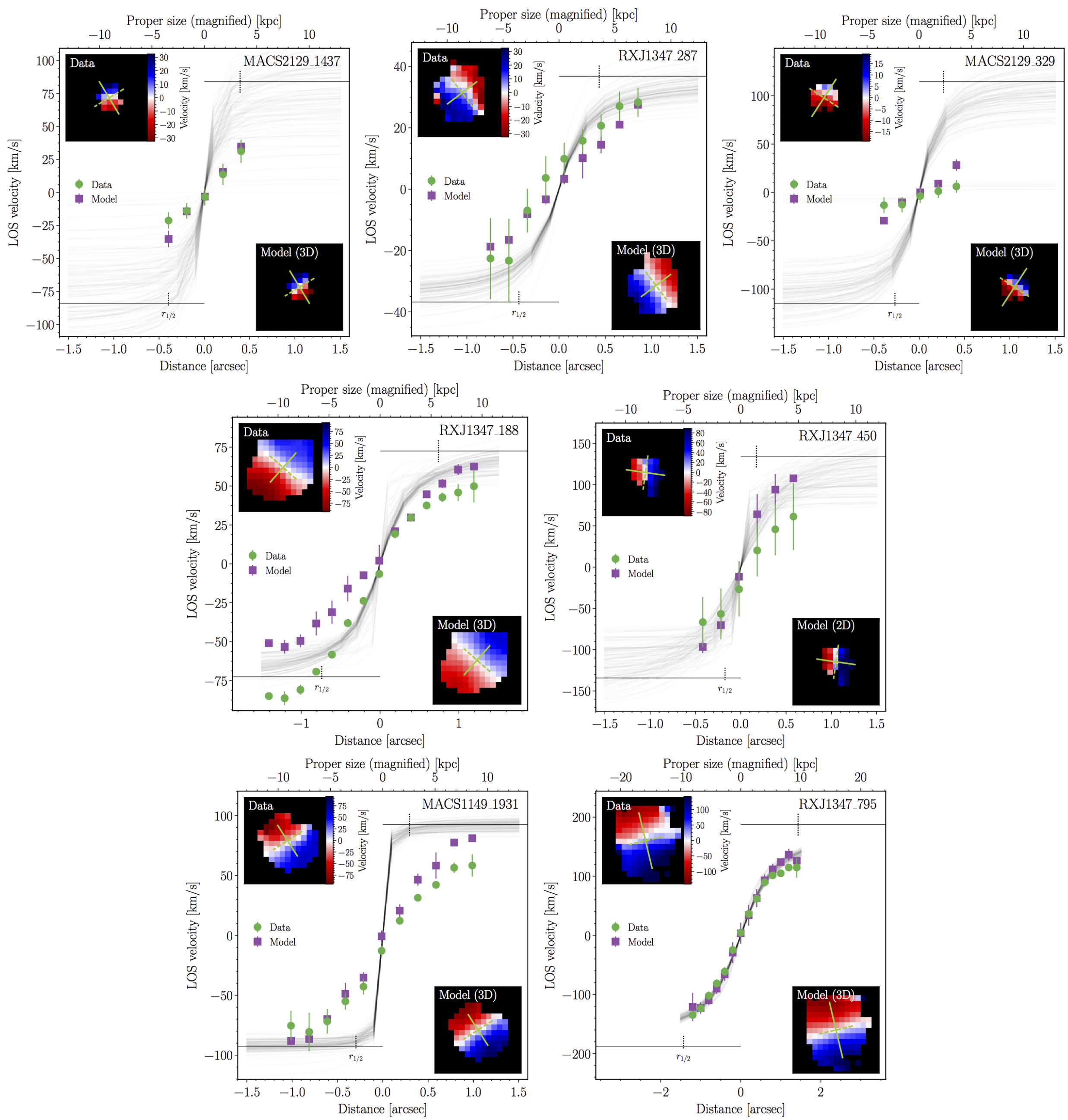

Figure 6.15: *(cont.)*

CHAPTER 7

Inferences on the Timeline of Reionization at $z \sim 8$ From the KMOS Lens-Amplified Spectroscopic Survey

This paper will be submitted as Mason, Fontana, Treu, Schmidt, Hoag, Abramson, Amorin, Guaita, Jones, Henry, Malkan, Pentericci, Trenti & Vanzella.

Detections and non-detections of Lyman alpha (Lyα) emission from $z > 6$ galaxies (< 1 Gyr after the Big Bang) can be used to measure the timeline of cosmic reionization. Of key interest to measuring reionization's mid-stages, but also increasing observational challenge, are observations at $z > 7$, where Lyα redshifts to near infra-red wavelengths. Here we present a search for $z > 7.2$ Lyα emission in 53 intrinsically faint Lyman Break Galaxy candidates, gravitationally lensed by massive galaxy clusters, in the KMOS Lens-Amplified Spectroscopic Survey (KLASS). With integration times of $\sim 7-10$ hours, we detect no Lyα emission with S/N > 5 in our sample. The median 5σ flux limit for our observations is 2.4×10^{-18} erg s^{-1} cm^{-2}. We define a photometrically selected sub-sample of 29 targets at $z = 7.9 \pm 0.6$, with a median 5σ Lyα EW limit of 31 Å. We perform a Bayesian inference of the average intergalactic medium (IGM) neutral hydrogen fraction using their spectra. Our inference accounts for the wavelength sensitivity and incomplete redshift coverage of our observations, and the photometric redshift probability distribution of each target. These observations, combined samples from the literature, enable us to place a lower limit on the average IGM neutral hydrogen fraction of > 0.80 (68%), > 0.57 (95%) at $z \sim 8$, providing further evidence of rapid reionization at $z \sim 6-8$. We show that this is consistent with reionization history models extending the galaxy luminosity function to $M_{\rm UV} \lesssim -12$, with low ionizing photon escape fractions, $f_{\rm esc} \lesssim 15\%$.

7.1 Introduction

The reionization of intergalactic hydrogen in the universe's first billion years is likely linked to the formation of the first stars and galaxies: considered to be the primary producers of hydrogen-ionizing photons (e.g., Lehnert & Bremer, 2003; Bouwens et al., 2003; Yan & Windhorst, 2004; Bunker et al., 2004; Shull et al., 2012). Accurately measuring the timeline of reionization enables us to constrain properties of these first sources (e.g., Robertson et al., 2013, 2015; Greig & Mesinger, 2017a).

Measurements of the reionization timeline are challenging, however, due to the rarity of bright quasars at $z > 6$ (Fan et al., 2001; Manti et al., 2016; Parsa et al., 2018), which have provided strong constraints on the end stages of reionization (e.g., McGreer et al., 2015; Fan et al., 2006; Greig & Mesinger, 2017b; Bañados et al., 2017). In the coming decade 21 cm observations are expected to provide information about the $z > 6$ IGM and the nature of the first galaxies (e.g., Liu & Parsons, 2016; Mirocha et al., 2016), but progress in the current era has been driven by observations of Lyα (rest-frame 1216 Å) emission in galaxies, using near infra-red (NIR) spectroscopy.

Lyα is a highly resonant line, and strongly scattered by intervening neutral hydrogen as it travels to our telescopes. Whilst young star-forming galaxies, selected with a Lyman Break (Lyman Break Galaxies – LBGs) show Lyα emission in abundance up to $z \sim 6$ (e.g., Stark et al., 2011; Hayes et al., 2011; Curtis-Lake et al., 2012; Cassata et al., 2015; De Barros et al., 2017), at higher redshifts the fraction of galaxies detected with Lyα emission, and the scale length of the Lyα rest-frame equivalent width (EW) distribution, decreases rapidly (e.g., Fontana et al., 2010; Pentericci et al., 2011; Caruana et al., 2012; Treu et al., 2012, 2013; Ono et al., 2012; Pentericci et al., 2014; Schenker et al., 2014; Tilvi et al., 2014; Faisst et al., 2014; Jung et al., 2018). This rapid decline of detected Lyα emission is most plausibly due to absorption in an increasingly neutral IGM (Dijkstra et al., 2011; Dijkstra, 2014; Mesinger et al., 2015).

Large spectroscopic surveys of LBG candidates are being assembled out to $z \sim 7$ (L. Pentericci et al. in prep), but exploring the earliest stages of reionization requires us to observe Lyα at even higher redshifts. Only a handful of Lyα emitters have been confirmed at $z \gtrsim 7.5$ (Zitrin et al., 2015b; Oesch et al., 2015; Roberts-Borsani et al., 2016; Stark et al., 2017; Hoag et al., 2017), where the dominance of sky emission in the NIR makes observations of faint sources even more challenging. Additionally, because Lyα emission can be spatially extended and/or offset from the UV continuum emission (Wisotzki et al., 2016; Leclercq et al., 2017), it is likely that slit-based spectroscopy is not capturing the full Lyα flux. Hence, the observed decline in Lyα emission at $z > 6$ could be partially due to redshift-dependent slit-losses as well as reionization.

In this paper we present a search for $z \gtrsim 7.2$ Lyα emission in NIR spectroscopy of 53 intrinsically faint LBG candidates ($M_{\rm UV} \gtrsim -20$), gravitationally lensed behind 6 massive galaxy clusters, including 4 of the Frontier Fields (Lotz et al., 2017), selected from the Grism Lens-Amplified Survey from Space (hereafter GLASS, Schmidt et al., 2014b; Treu et al., 2015). We also observe C IV emission in 3 images of a previously confirmed multiply-imaged $z = 6.11$ galaxy (Boone et al., 2013; Balestra et al., 2013; Monna et al., 2014).

The observations presented in this work were carried out with the ESO Very Large Telescope (*VLT*) K-band Multi Object Spectrometer (hereafter KMOS, Sharples et al., 2013). This work presents the first results of $z > 3.8$ observations with KMOS. KMOS is an integral field unit (IFU) instrument, and we demonstrate here that our observations are more complete to spatially extended and/or offset Lyα emission than traditional slit spectrographs.

We use our new deep spectroscopic observations to infer the IGM neutral hydrogen fraction ($\overline{x}_{\rm HI}$) at $z \sim 8$. Mason et al. (2018a, hereafter M18a) presented a flexible Bayesian framework to directly infer $\overline{x}_{\rm HI}$ from detections and non-detections of Lyα emission from LBGs. The framework combines realistic inhomogeneous reionization simulations and models of galaxy properties. That work measured $\overline{x}_{\rm HI} = 0.59^{+0.11}_{-0.15}$ ($16-84\%$ confidence intervals) at $z \sim 7$. Building on Treu et al. (2012) and M18 we extent that framework to us the full spectra obtained in our observations for the Bayesian inference, accounting for the incomplete wavelength coverage and spectral variation of the noise. Our framework uses the photometric redshift probability distribution of each object to robustly account for uncertainties in redshift determination.

The paper is structured as follows: Section 7.2 describes our KMOS observations and the target selection from the GLASS parent sample; Section 7.3 describes the search for Lyα emission in our KMOS data cubes, and the purity and completeness of our survey; and Section 7.4 describes the Bayesian inference of the neutral fraction and presents our limit on $\overline{x}_{\rm HI}$ at $z \sim 8$. We discuss our findings in Section 7.5, including an assessment of the performance of KMOS for background-limited observations using our deep observations, and summarise in Section 7.6.

We use the Planck Collaboration et al. (2016a) cosmology where $(\Omega_\Lambda, \Omega_{\rm m}, \Omega_{\rm b}, n, \sigma_8, H_0) =$ (0.69, 0.31, 0.048, 0.97, 0.81, 68 km s^{-1} Mpc^{-1}). All magnitudes are given in the AB system.

7.2 Observations

7.2.1 The KMOS Lens-Amplified Spectroscopic Survey

KLASS is an ESO VLT KMOS Large Program (196.A-0778, PI: A. Fontana) which targeted the fields of six massive galaxy clusters: Abell 2744 (hereafter A2744); MACS J0416.1-2403 (M0416); MACS J1149.6+2223 (M1149); MACS J2129.4-0741 (M2129); RXC J1347.5-1145 (RXJ1347); and RXC J2248.7-4431 (RXJ2248, aka Abell S1063). A2744, M0416, M1149 and RXJ2248 are all Frontier Fields (hereafter HFF, Lotz et al., 2017). Observations were carried out in Service Mode during Periods $96-99$ (October 2015 - October 2017).

KMOS is a multi-object IFU spectrograph, with 24 movable IFUs, split between 3 different spectrographs (Sharples et al., 2013). Each IFU is $2''.8 \times 2''.8$ field of view, with pixel size $0''.2 \times 0''.2$, and 2048 pixels along the wavelength axis[1].

The key science drivers of KLASS are:

1. To probe the internal kinematics of galaxies at $z \sim 1-3$, with superior spatial resolution compared to surveys in blank fields (Mason et al., 2017).

[1]We use the following definitions for describing 3D spectra in this paper. Pixel: 2D spatial pixel (size $0''.2 \times 0''.2$). Spaxel: the 1D spectrum in a single spatial pixel (spanning the spectral range $\sim 1-1.35\,\mu$m, in 2048 spectral pixels). Voxel: 3D pixel in the data cube with both spatial and spectral indices.

2. To investigate $z \gtrsim 7$ Lyα emission from the GLASS sample, independently of the HST spectroscopic observations, providing validation and cross-calibration of the results and enabling us to constrain the timeline and topology of reionization (Treu et al., 2012, 2013; Schmidt et al., 2016; Mason et al., 2018a).

Mason et al. (2017) addressed the first science driver by presenting spatially resolved kinematics in 4 of the 6 KLASS clusters from our early data, including five of the lowest mass galaxies with IFU kinematics at $z > 1$, and provided evidence of mass-dependent disk settling at high redshift (Simons et al., 2017). The KLASS kinematic data were combined with metallicity gradients from the *HST* GLASS data to enable the study of metallicity gradients as a diagnostic of gas inflows and outflows (Wang et al., 2016).

This paper addresses the second science driver by presenting our $z > 7$ candidate targets with complete exposures. We use the YJ observing band, giving us access to Lyα emission at $z \sim 7.2 - 10.1$.

The choice of an IFU instrument for high-redshift Lyα observations was motivated by indications that ground-based slit-spectroscopy measures lower Lyα flux than *HST* slit-less grism spectroscopy (Tilvi et al., 2016; Huang et al., 2016a; Hoag et al., 2017), which, as well as reionization, could contribute to the observed decline in Lyα emission at $z > 6$. Lyα emission can be spatially extended and/or offset from the UV continuum emission (Wisotzki et al., 2016; Leclercq et al., 2017), so it is likely that slit-based spectrographs do not capture the full Lyα flux.

By using IFUs our observations should be more complete to spatially extended and/or offset Lyα than traditional slit spectrographs. Mason et al. (2017) showed that only $\sim 60\%$ of emission line flux was contained in $\sim 0\farcs7$ simulated slits (a typical slit-width used for Lyα observations Hoag et al., 2017) on KMOS spectra, whereas the full flux is captured within the $2\farcs8 \times 2\farcs8$ KMOS field of view. Thus we expect most Lyα flux to be captured within the KMOS IFUs. The $2\farcs8$ wide IFUs cover ~ 14 proper kpc at $z \sim 8$, while the UV effective radii of galaxies at these redshifts is only $\lesssim 1$ proper kpc (Shibuya et al., 2015). We demonstrate in Section 7.3.3 that our KMOS observations have good completeness for spatially extended

Table 7.1: KLASS cluster targets

Cluster	Run ID	DIT [s]	NDITs*	Exposure [hrs]	Number of targets	
					Category 1	Category 2
A2744†,‡	A	900	25	6.25	3	7
M0416‡	B	900	43	10.75	2	5
M1149‡	C	900	40	10.00	2	6
M2129	E	450	85	10.625	3	7
RXJ1347	D	450	88	11.00	3	8
RXJ2248◇	F	300	93	7.75	1	6

NOTE. – * The number of Detector Integration Times (DITs) used in this analysis: we discarded DITs if the seeing was $> 0\farcs8$ as measured by stars observed in each DIT. The total exposure time = DIT × NDITs. † We had to discard our initial 4 hours of observations of A2744 due to irreparable flexure issues due to rotating the instrument between science and sky DITs. All subsequent observations were performed with no rotation of the instrument between science and sky DITs. ‡ Target selection in these clusters was primarily done from preliminary versions of the ASTRODEEP catalogues (Castellano et al., 2016; Merlin et al., 2016; Di Criscienzo et al., 2017), which did not include Spitzer/IRAC photometry. ◇ Due to a high proper motion reference star, some of the observations of RXJ2248 were taken at a slight offset from the required target centre, reducing the total exposure at that position. RXJ2248 also included 3 $z = 6.11$ targets (Appendix 7.7).

and/or offset Lyα emission.

7.2.2 Target selection

KLASS targets were selected from the GLASS survey[2] (Schmidt et al., 2014b; Treu et al., 2015), a large Hubble Space Telescope (*HST*) slit-less grism spectroscopy program. GLASS obtained spectroscopy of the fields of 10 massive galaxy clusters, including the HFF and 8

[2] http://glass.astro.ucla.edu

CLASH clusters (Postman et al., 2012a). The Wide Field Camera 3 (WFC3) grisms G102 and G141 were used to cover the wavelength range $0.8 - 1.6\,\mu$m with spectral resolution $R \sim 150$. We refer the reader to Schmidt et al. (2014b) and Treu et al. (2015) for full details of GLASS.

KLASS observations aimed to provide the high spectral resolution necessary to measure the purity and completeness of the grism spectra, to measure lines that were unresolved in *HST*, and to obtain velocity information for $z \sim 1$ targets which the low resolution grisms cannot provide. In combination with additional GLASS follow-up observations at Keck (Huang et al., 2016a; Hoag et al., 2017, A. Hoag et al. in preparation) we will address the purity and completeness of the HST grisms in a future work. In this work we present our high-redshift candidate targets and our inferences about reionization obtained from the KLASS data.

Two categories of high-redshift candidate KLASS targets were selected from the GLASS data:

1. Category 1: 14 objects with marginal (S/N ~ 3) candidate Lyα emission in the *HST* grisms, identified by visual inspection of the GLASS data, which fall within the KMOS YJ spectral coverage ($\sim 1 - 1.35\,\mu$m). 4 candidates were selected from a list of candidates in a preliminary census of GLASS data by Schmidt et al. (2016). The remaining candidates were selected in a similar method to the procedure followed by Schmidt et al. (2016).

2. Category 2: 39 LBG candidates selected with $z_{\text{phot}} > 7.2$, from an ensemble of photometric catalogues described by Schmidt et al. (2016). This includes two LBGs which were spectroscopically confirmed via sub-mm emission lines after our survey began: A2744_YD4 (A2744_2248 in this paper), at $z = 8.38$ (Laporte et al., 2017, discussed in Section 7.4.2 and 7.4.3) and M1149_JD1, at $z = 9.11$ (Hashimoto et al., 2018, discussed in Section 7.5.2).

An additional three targets were multiple images of the $z = 6.11$ system in RXJ2248

(Boone et al., 2013; Balestra et al., 2013; Monna et al., 2014) where we targeted C IV λ1548,1551 emission. This object is discussed in Appendix 7.7.

We ranked objects in order of the number of inspectors who reported a candidate emission line for our Category 1 targets, and then by the number of independent photometric catalogues the target appeared in (for both categories). Our observations were planned prior to the release of the full HFF datasets, so the photometric catalogues we used to select candidates did not contain the full photometry now available. In particular, deep Spitzer/IRAC data did not exist, which can be useful for distinguishing between high-redshift star forming galaxies and $z \sim 1 - 2$ passive galaxies. Nor were sophisticated intra-cluster light (ICL) removal techniques developed at that point (e.g., Merlin et al., 2016; Morishita et al., 2017; Livermore et al., 2017).

Thus our LBG selection was heterogeneous. We expect some faint candidates may have been spurious in the initial photometry and may not appear in the final deep catalogues. Additionally we expect that with the inclusion of Spitzer/IRAC photometry some of the objects originally selected to be $z > 7$ may be low redshift contaminants. In our reionization analysis we use catalogues built using the final HFF datasets to define a selection function for a photometrically-selected sample for our inference (described in Section 7.4.2). We demonstrate that this KLASS sub-sample is not a biased sample of the final parent catalogues in Appendix 7.8.

The GLASS median 1σ flux limit is $0.5 \times 10^{-18}\,\mathrm{erg\,s^{-1}\,cm^{-2}}$ (Schmidt et al., 2016), and we tried to be as inclusive as possible when assigning candidates to the KMOS IFUs from the GLASS parent catalogue. Most of the candidates were only 3σ significance in GLASS data and we hoped our deep KMOS observations would provide confirmation of those tentative targets.

However, as we describe below in Section 7.3.4, the median 1σ flux limit in KLASS is almost equivalent to the GLASS limit (and for our ground-based observations, at least 50% of the wavelength range is dominated by sky emission), so we are unable to confirm or rule out the GLASS candidates. In planning our observations we likely overestimated the sensitivity of KMOS YJ using the online exposure time calculator, especially at the blue end of the detectors. We discuss this in more detail in Section 7.5.4.

53 $z_{\rm phot} > 7.2$ candidate targets across the 6 clusters were assigned to 51 KMOS IFUs (two IFUs contained two nearby candidates). The cluster list and number of high-redshift candidate targets per cluster is shown in Table 7.1.

7.2.3 KLASS observing strategy and reduction

KLASS observations were carried out with KMOS YJ ($\sim 1 - 1.35\,\mu$m). The spectral resolution $R \sim 3400$ is sufficient to distinguish Lyα from potential low redshift contaminants with the [O II] $\lambda 3726, 3729$ emission doublet at $z \sim 2$.

Observations were carried out in service mode and executed in one hour observing blocks with repeating ABA science-sky-science integration units (detector integration times – DITs). Each observing block comprised 1800 s of science integration, and 900 s on sky. Pixel dither shifts were included between science frames. A star was observed in 1 IFU in every observing block to monitor the point spread function (PSF) and the accuracy of dither offsets. The PSF was well-described by a circular Gaussian and the median seeing of our observations was FWHM $\sim 0\farcs6$.

In each cluster, the 3 top priority targets were observed for 1.5$\times$ the average exposure time by assigning 2 IFUs per target and nodding between them during A and B modes.

7.2.4 Reduction

Data were reduced using the ESO KMOS pipeline v.1.4.3 (Davies et al., 2013). We apply a correction for known readout channel level offsets before running the pipeline. We run the pipeline including optimised sky subtraction routines `sky_tweak` (Davies, 2007) and `sky_scale`.

To improve the sky subtraction in the pipeline-reduced 'A-B' cubes we produced master sky residual spectra by median combining all IFUs on each spectrograph into a 1D master sky residual spectrum for each DIT, excluding cubes containing $z \lesssim 2$ targets with bright emission lines and/or continua. We then subtract these 1D sky residual spectra from the 'A-B' cubes on the same spectrograph for each DIT, rescaling the 1D spectra in each spaxel so that the resulting 1D spectrum in each spaxel is minimised.

Similar techniques to improve sky subtraction are described by Stott et al. (2016). This method worked best for our survey design. We note that this method performed better than in-IFU sky residual subtraction (i.e. subtracting a median sky residual spectrum produced from 'empty' spaxels in each IFU) as it preserved emission line flux in the modestly sized KMOS IFUs.

Cube frames from each DIT are combined via sigma clipping, using spatial shifts determined by the position of the star observed in the same IFU in each DIT, to produce flux and noise cubes. For this work we used only frames with seeing $\leq 0''.8$ (as measured by the star observed in our science frames). The median seeing was $\sim 0''.6$. DIT length, observing pattern and total integration times used for this paper are listed in Table 7.1. We note that due to the failure of one of the KMOS arms, no star was observed in the A2744 observations. We used a bright $z \sim 1$ target to estimate the dither offsets for this cluster.

For pure Gaussian noise, the pixel distribution of S/N should be normally distributed. We tested this by selecting non-central regions of cubes containing high-redshift candidate targets (i.e. where we expect very little source flux) and found the pixel distribution of S/N to have standard deviation > 1, suggesting the noise is underestimated by the pipeline.

We therefore apply a rescaling to the noise of the combined cubes. We create an average 1D noise spectrum in a single spaxel for each cluster by taking the root-mean-square (RMS) at every wavelength of every spaxel from the cubes containing high-redshift candidate targets. Since the cubes are predominantly noise, taking the RMS of the flux at each wavelength across multiple cubes should give the appropriate noise. We find this RMS spectrum is $\sim 1.2\times$ higher than the pipeline average 1D noise spectrum (taking the average of the noise cubes across the same set of high-redshift targets). We rescale the pipeline noise in every cube by this ratio of the cluster RMS noise spectrum to the cluster average noise spectrum.

Finally, we rescale the noise in each cube by a constant value so that the S/N distribution of all pixels has standard deviation 1 (clipping pixels within 99.9% to remove spurious peaks). We find the S/N distribution is well-described by a Gaussian distribution, with non-Gaussian tails only beyond the $\gtrsim 7\sigma$ confidence regions, due to bad sky subtraction residuals.

7.3 Emission Line Search, Purity and Completeness

In this section we describe our search for Lyα emission in our KMOS observations. We give our algorithm for line detection in Section 7.3.1, and calculate the purity and completeness of our observations in Sections 7.3.2 and 7.3.3. Given that we detect no convincing Lyα emission lines in our sample we present our flux and EW upper limits in Section 7.3.4.

7.3.1 Emission line detection technique

To search for emission lines in the KMOS cubes, to robustly determine the completeness and purity of our survey, and determine the flux limits of our observations, we used the following algorithm to flag potential lines:

1. Create a circular aperture with $r = 2\sigma_{\text{PSF}} \sim 0''.5 \sim 2.5$ pixels, which will capture 86% of the total flux for spatially unresolved emission line at the centre of the aperture.

2. Sum the flux, and take the RMS of the noise of all spaxels in the aperture to create 1D data and noise spectra.

3. Rescale the 1D noise spectrum so the S/N in all pixels (excluding the 0.1% most extreme S/N values) is Normal.

4. Scan through in wavelength and flag a detection if 3 adjacent wavelength pixels have $S/N > 3$. This corresponds to a $S/N \gtrsim 5$ detection of the integrated line flux.

5. Iterate over 25 apertures centred within 3 pixels ($0''.6$) of the IFU centre, i.e. $x = [-3, -1.5, 0, 1.5, 3]$, $y = [-3, -1.5, 0, 1.5, 3]$ where $(x, y) = (0, 0)$ is the IFU centre.

Our search covers $\sim 25 \times 2000 = 50,000$ potential emission line positions in each cube. As our detection threshold is 5σ we would expect a false positive rate of 6×10^{-7}, i.e. ~ 0.03 false detections per cube for Gaussian noise. As discussed in Section 7.2.4 the S/N has small non-Gaussian tails due to sky subtraction residuals so we expect a slightly higher false detection rate than this.

7.3.2 Candidate emission lines and sample purity

We ran the detection algorithm described in Section 7.3.1 on the 54 cubes containing our high-redshift candidate targets (including the 3 cubes containing the $z = 6.11$ images). 9 unique candidate lines were flagged (combining candidates at the same wavelength identified in different apertures). Each of these candidate lines was then visually inspected to determine whether it was a true emission line or a spurious noise peak. For our inspections we use both 1D spectra extracted in the detection apertures as well as 2D collapsed images of the candidate line obtained by summing cube voxels in the wavelength direction. The 2D images are helpful for determining plausible spatially compact emission from the uniform emission produced by sky residuals.

Our algorithm correctly identifies the C IVλ1551 emission at 11023.7 Å in the brightest image of the multiply-imaged $z = 6.11$ system, demonstrating the depth of our KMOS observations and the fidelity of our algorithm. Another detection is flagged in this object at 13358.6 Å but the emission appears diffuse and the wavelength is not consistent with other expected UV emission lines so we deem this spurious. We describe this object in more detail in Appendix 7.7.

Of the remaining 7 lines flagged, 6 are deemed to be spurious detections as they are at the spectral edges of the detector, or immediately adjacent to strong skylines and appear to have P-Cygni profiles, indicating extreme sky subtraction failures. Whilst it could be possible to add a cut to e.g. downweight flagged lines adjacent to skylines, given the relatively low spectral resolution of our observation ($R \sim 2700$) we were wary that many true emission lines could be overlapping with skylines, thus visual inspection was necessary. This clearly demonstrated in our detection of C IV emission where both doublet components overlap with sky lines (see Figure 7.9).

The remaining candidate emission line at 12683.7 Å is spatially offset from the $z > 7$ LBG candidate in the cube. We determine the detected emission to be associated with a nearby ($\sim 1.1''$) galaxy with $z_{\mathrm{phot}} = 4.2$, which has bright continuum emission in the GLASS data. The candidate line appears in a particularly bad spectral region of telluric absorption, and we determine the detection to be due to inadequate continuum subtraction of the $z \sim 4$ source.

In our reductions we subtract a sky residual spectrum to minimise the flux in each spaxel of the high-redshift candidate cubes (Section 7.2.4). During that process most of the continuum emission from the $z \sim 4$ object was poorly subtracted by scaling the sky residual spectrum to high values. Some residual flux is left, which correlates with the positions of sky residuals. We note that the LBG candidate targeted in this IFU is not present in the final deep photometric catalogues and is excluded from our reionization (it was likely a spurious detection in the original shallow photometry, Section 7.4.2). We remove this cube from further analysis.

Thus we determine our algorithm has detected 1 real emission line, and 7 spurious detections (excluding the $z \sim 4$ continuum object described above), allowing us to define the purity of our spectral sample:

$$P = 1 - \frac{N_{\mathrm{spurious}}}{N_{\mathrm{pos}}} \tag{7.1}$$

where $N_{\mathrm{spurious}} = 17$ is the total number of spurious flags (8 unique false detections which were sometimes flagged in multiple apertures) and $N_{\mathrm{pos}} = 101763 \times 25$ is the number of possible emission line positions in the 53 useful cubes, removing wavelength pixels not covered by certain detectors, in 25 apertures. We measure $P = 1 - 7 \times 10^{-6}$. Our spurious detection rate is $\sim 10\times$ higher than that expected for 5σ fluctuations in the noise, which was expected due to the non-Gaussian tail in our S/N distribution due to sky subtraction residuals. To verify that the S/N distribution is symmetrical we also ran the detection algorithm to look for negative peaks (S/N $\lesssim -5$) which should occur at the same rate. We found 12 flagged negative S/N detections, comparable to our 7 flagged spurious detections with positive S/N.

We ran the algorithm on our Category 1 sources with a lower S/N threshold: S/N > 2.5 per wavelength pixel, corresponding to $S/N \gtrsim 4$ in the integrated line. We found no convincing detections with this lower threshold and are thus unable to confirm any of the candidate GLASS emission lines. However, as we show in Section 7.3.4 below, our final KLASS flux limits are comparable to the original GLASS flux limit. Given that most of the GLASS Lyα candidates were of low significance in the GLASS *HST* data the comparable flux limits in the KMOS data make it more difficult than we anticipated to verify those candidate lines.

In Section 7.4.2 below we list the Lyα flux and EW limits for our most likely $z_{\rm phot}$ LBGs candidates. We discuss our limits on other UV lines in Section 7.5.3.

7.3.3 Completeness

To evaluate the completeness of our emission line search we carry out comprehensive Monte Carlo simulations: inserting simulated lines into cubes with varied total flux, spectral $\mathrm{FWHM}_{\rm spec}$, spatial position, spatial extent $\mathrm{FWHM}_{\rm spat}$, and wavelength, and testing whether they are detected by our detection algorithm (Section 7.3.1). Traditionally, these types of simulations are carried out by inserting simulated lines into real raw data and then running through the full reduction pipeline (Fontana et al., 2010; Pentericci et al., 2014; De Barros et al., 2017), however, due to the complexity of the KMOS pipeline which constructs 3D cubes from 2D frames we instead create simulated cubes and add Gaussian noise drawn from an average noise cube for each cluster, mimicking completeness simulations traditionally done in imaging.

We create simulated flux cubes with a 3D Gaussian emission line with varied properties and add noise to each voxel drawn from a Gaussian distribution with mean zero and standard deviation $\sigma_{x,y,\lambda}$ for each cluster. The $\sigma_{x,y,\lambda}$ cubes are constructed by taking the RMS at every voxel of all the final sky-subtracted cubes which do not contain bright $z \lesssim 2$ sources (~ 10 cubes per cluster). As each 'empty' cube is expected to be pure noise, taking the RMS at

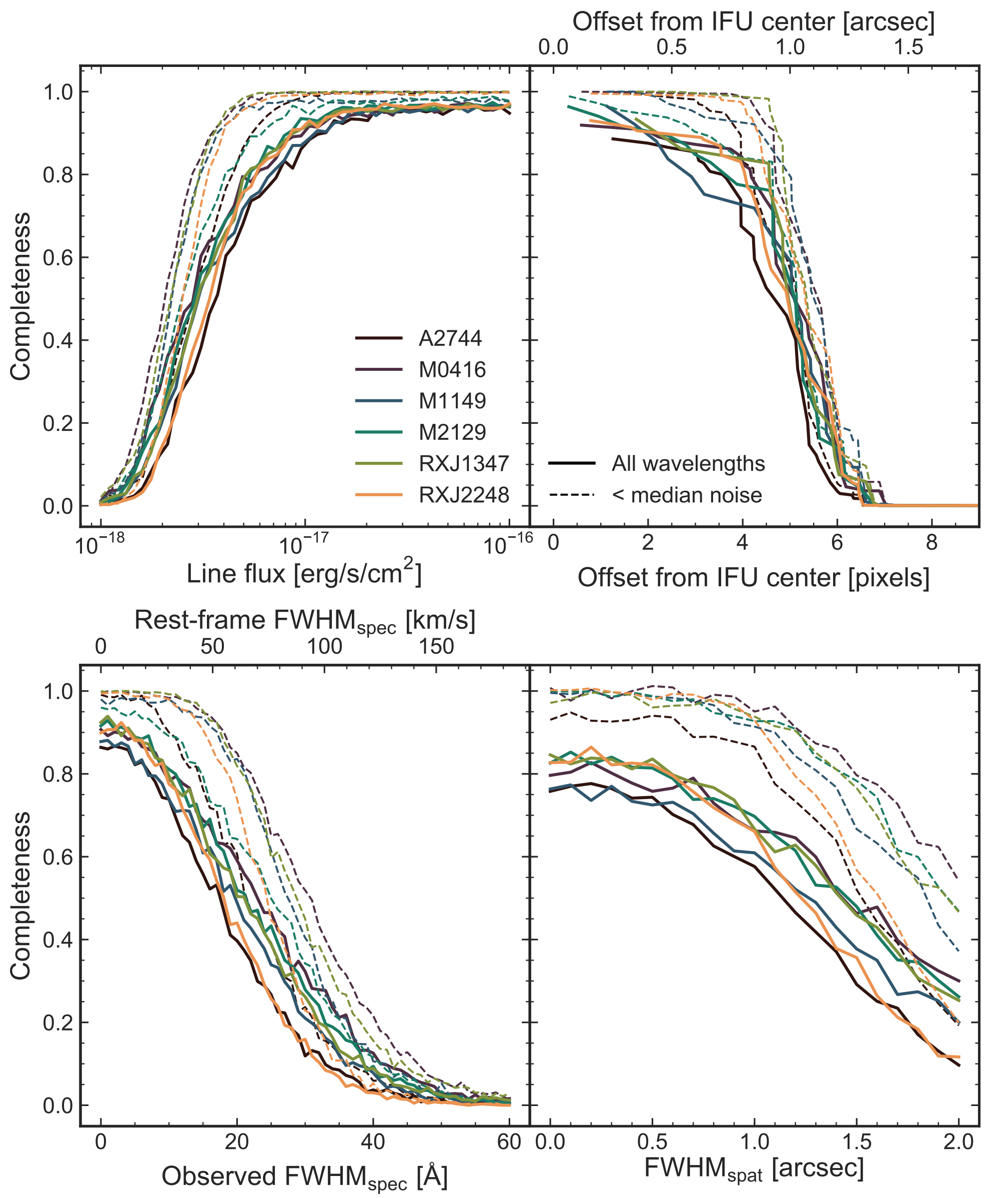

Figure 7.1: Completeness as a function of line flux (**top left**), spatial offset from IFU centre (**top right**), spectral linewidth (**lower left**) and spatial extent (**lower right**). Each colour corresponds to a separate cluster target. Dashed lines show the completeness across the entire wavelength range, solid lines show the completeness in wavelength regions where the noise level is below the median. Rest-frame FWHM$_{\rm spec}$ velocities were calculated assuming $z = 8$. Spatial extent, FWHM$_{\rm spat}$ is the extent of the source (excluding the PSF). In each plot the parameter of interest and wavelength are varied, while the other parameters are held constant. The fiducial parameters are: line flux $= 1 \times 10^{-17}$ erg s^{-1} cm^{-2}, observed FWHM$_{\rm spec} = 4$ Å (i.e. unresolved), line centred at the IFU centre, and FWHM$_{\rm spat} = 0''$ (i.e. unresolved point source).

each voxel across the cubes should give an estimate of the noise per voxel, $\sigma_{x,y,\lambda}$.

We calculate completeness as a function of flux, spatial offset from the IFU centre, spectral linewidth and spatial extent. For each simulation we vary the parameter of interest and wavelength, and fix the other three parameters. Our fiducial values for the parameters: are line flux $= 1 \times 10^{-17}\,\mathrm{erg\ s^{-1}\ cm^{-2}}$, observed line $\mathrm{FWHM_{spec}} = 4\,\mathrm{\AA}$ (the spectral resolution, i.e. unresolved lines), line centred at the IFU centre, with source spatial extent $\mathrm{FWHM_{spat}} = 0''$ (i.e. unresolved point source, the emission will have observed spatial extent with $\mathrm{FWHM_{spat,tot}} = \sqrt{\mathrm{FWHM_{PSF}^2} + \mathrm{FWHM_{spat}^2}}$). We draw 1000 realizations of an emission line with noise at every tested value of a parameter. The resulting completeness is the fraction of these simulated lines detected by our detection algorithm.

Our fiducial simulations assume Lyα emission will be spatially unresolved. These assumptions are reasonable for the intrinsically UV faint LBGs we are observing (Schmidt et al., 2016; Marchi et al., 2017). Typical slit spectrograph observations of Lyα emission centre slits on the UV continuum and use slit-widths $\sim 0\farcs7$, thus in KLASS we are more complete to Lyα emission that may be spatially extended and/or offset from the UV continuum.

Figure 7.1 shows the results of our completeness simulations for all clusters. We reach 80% completeness over the full wavelength range for lines $\gtrsim 5.7 \times 10^{-18}\,\mathrm{erg\ s^{-1}\ cm^{-2}}$, centred within $< 0\farcs8$ of the IFU centre and with emitted rest-frame line $\mathrm{FWHM_{spec}} \lesssim 27\,\mathrm{km\ s^{-1}}$, assuming $z = 8$ to calculate rest-frame $\mathrm{FWHM_{spec}}$ (median over all clusters). For wavelength ranges where the noise level is below the median across the whole spectrum, we reach 80% completeness for lines $\gtrsim 3.2 \times 10^{-18}\,\mathrm{erg\ s^{-1}\ cm^{-2}}$, centred with $< 0\farcs9$ of the IFU centre and with emitted rest-frame line $\mathrm{FWHM_{spec}} \lesssim 60\,\mathrm{km\ s^{-1}}$. The completeness is fairly flat for Lyα spatial extent $\lesssim 0\farcs6$ (total extent $\lesssim 0\farcs8$) demonstrating our good completeness for spatially extended Lyα emission, with the normalisation of the completeness as a function of $\mathrm{FWHM_{spat}}$ scaling with the completeness at a given total line flux.

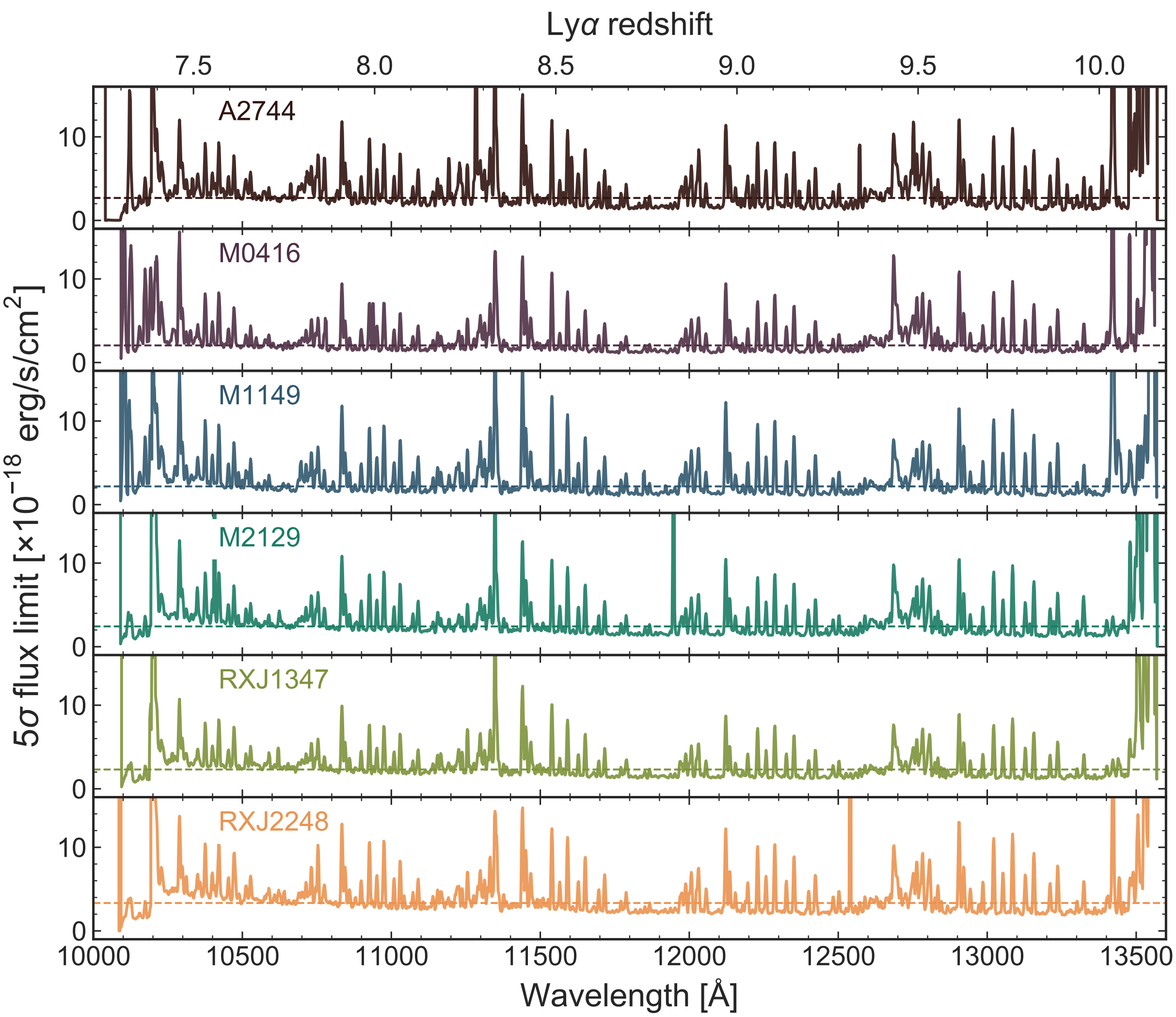

Figure 7.2: Average 5σ flux limits for each cluster as a function of wavelength, assuming emission lines are spatially unresolved. We use the 1D RMS noise spectrum for each cluster as described in Section 7.3.4 to obtain the flux limits. Each line corresponds to a different cluster target. The dashed horizontal lines mark the median flux limit for each cluster. The GLASS 5σ flux limit is 2.5×10^{-18} erg s^{-1} cm^{-2} (Schmidt et al., 2016).

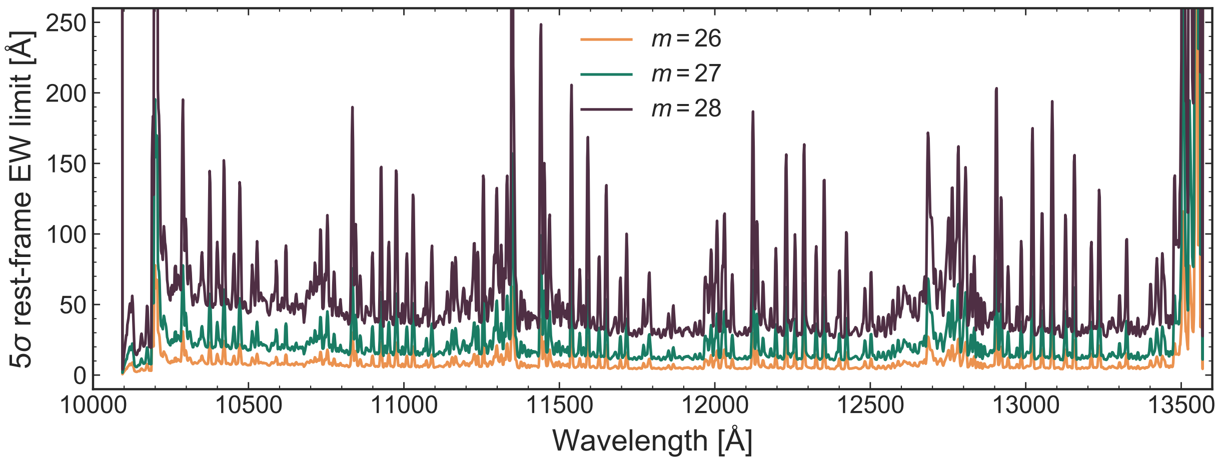

Figure 7.3: 5σ rest-frame Lyα EW limits in RXJ1347 as a function of wavelength, for 3 values of UV apparent magnitude m, assuming emission lines are spatially unresolved. We use the 5σ flux limit for RXJ1347 shown in Figure 7.2 and divide by the continuum flux and $(1 + z_{\mathrm{Ly}\alpha})$ at each wavelength to obtain the EW limit.

7.3.4 Flux and equivalent width limits

To calculate average flux limits for each cluster we take the average 3D noise spectrum for each cluster, $\sigma_{x,y,\lambda}$ (created by taking the RMS at every voxel across the ~ 10 IFUs observing high redshift candidates in each cluster). We then create a 1D noise spectrum by summing the average noise at each wavelength pixel in a circular aperture with radius $r = 2\sigma_{\mathrm{PSF}}$ (where we use our median seeing $\mathrm{FWHM}_{\mathrm{PSF}} = 0.''6$). At each wavelength pixel, i the flux limit in erg s^{-1} cm^{-2} is given by:

$$f_{\mathrm{lim},i} = 3 \times \frac{1}{1 - e^{-\frac{r^2}{2\sigma_{\mathrm{PSF}}^2}}} \sqrt{\sigma_{i-1}^2 + \sigma_i^2 + \sigma_{i+1}^2} \times \Delta\lambda \tag{7.2}$$

Here we are summing over the 3 noise wavelength pixels and use a threshold $S/N = 3$ from our detection algorithm in Section 7.3.1, which results in an integrated signal-to-noise ratio of $S/N \approx 5$. The term in the denominator accounts for the fact that the apertures only capture a fraction of the flux. For $r = 2\sigma_{\mathrm{PSF}}$ this results in a rescaling of 1.16. The spectral pixel width of KMOS YJ is $\Delta\lambda = 1.75\,\text{Å}$. The above calculation assumes the emission is spatially and spectrally unresolved by KMOS, which is reasonable given the expectation that Lyα emission from UV faint galaxies is likely to be more spatially compact and have lower linewidth than Lyα from UV bright galaxies (e.g., Schmidt et al., 2016; Marchi et al., 2017)

The 5σ flux limits for all clusters are shown in Figure 7.2. The median flux limit is 2.4×10^{-18} erg s^{-1} cm^{-2}, and the range of medians for each cluster is $2.0 - 3.3 \times 10^{-18}$ erg s^{-1} cm^{-2}. This is very comparable to the GLASS 5σ line flux limit (2.5×10^{-18} erg s^{-1} cm^{-2}, Schmidt et al., 2016).

Rest-frame Lyα equivalent widths are $W = (1+z)^{-1} f(\lambda)/f_\mathrm{cont}$, where $z = \lambda/\lambda_\alpha - 1$ (with $\lambda_\alpha = 1216\,\text{Å}$), and we define the continuum flux:

$$f_\mathrm{cont}(m, z) = f_0 10^{-0.4m} \frac{c}{\lambda_\alpha^2 (1+z)^2} \left(\frac{\lambda_\mathrm{UV}}{\lambda_\alpha} \right)^{-\beta-2} \tag{7.3}$$

where $f_0 = 3.631 \times 10^{-20}$ erg s^{-1} Hz^{-1} cm^{-2}, m is the apparent magnitude of the UV continuum, c is the speed of light, λ_UV is the rest-frame wavelength of the UV continuum (usually 1500 Å), and β is the UV slope. We assume $\beta = -2$, consistent with $z \sim 7$ observations (e.g., Bouwens et al., 2012). We use the magnitude measured in *HST* WFC3/F160W for the apparent magnitude (`automag`). Example EW limits for objects with a given apparent magnitude, using the RXJ1347 average flux limit, are plotted in Figure 7.3.

7.4 Reionization inference

In this section we describe the extension to the M18 Bayesian inference framework to include the full spectra, robustly including the uncertainties in redshift via the photometric redshift distribution (Section 7.4.1). Using the observations described above we now define a clear selection function for a photometrically-selected sample of LBGs within our survey (Section 7.4.2), and perform the inference of the IGM neutral fraction using these data (Section 7.4.3).

7.4.1 Bayesian inference framework

To use our observations to make inferences about the neutral hydrogen fraction at $z \sim 8$ we use the method described by M18. This forward-models the observed rest-frame Lyα EW distribution as a function of the neutral fraction and galaxy UV magnitude, $p(W \,|\, \overline{x}_\mathrm{HI}, M_\mathrm{UV})$, using a combination of reionization simulations with realistic inhomogeneous IGM structure

(Mesinger, 2016), and empirical and semi-analytic models of galaxy properties.

The models assume the observed $z \sim 6$ Lyα EW distribution is the 'emitted' distribution (i.e. the distribution without IGM attenuation due to reionization) and use that to forward-model the observed distribution, including the impact of Lyα velocity offsets. Here, as in M18, we use the recent comprehensive $z \sim 6$ Lyα EW observations from De Barros et al. (2017). We use the public Evolution of 21cm Structure (EoS) suite of reionization simulations described by Mesinger et al. (2015); Mesinger (2016)[3] to generate Lyα optical depths along millions of sightlines in simulated IGM cubes for a grid of volume-averaged $\overline{x}_{\rm HI}$ values. As the size of ionised regions during reionization is expected to be nearly independent of redshift at fixed $\overline{x}_{\rm HI}$ (as there is little difference in the matter power spectrum from $z \sim 7-11$, McQuinn et al., 2007a), we use the same $z \sim 7$ cubes as used by M18 rather than generating new $z \sim 8$ cubes.

We refer the reader to M18 for more details of the forward-modelling approach. Here we describe the modifications we have made to our Bayesian inference to make use of the spectral coverage and sensitivity of our observations. We account for the incomplete redshift coverage and for the gravitational lensing magnification of the objects by the foreground clusters. We also marginalise over the photometric redshift distribution for each galaxy to robustly account for uncertainties and degeneracies in redshift determination.

We want to obtain the posterior distribution for the neutral fraction: $p(\overline{x}_{\rm HI} \,|\, \{W\}, m, \mu)$ for each galaxy, where $\{W\}$ is the EW as a function of wavelength, m is the observed apparent UV magnitude, and μ is the magnification. A full derivation of the posterior is shown in Appendix 7.9, and we summarise it here.

We assume emission lines are spectrally unresolved, such that an emission line is observed in a single spectral pixel d and the rest of the spectrum is pure noise. Thus, the likelihood of observing a 1D EW spectrum $\{W\} = W(\lambda_i)$ for an individual galaxy (where i is the wavelength pixel index), given our model where the true EW is drawn from the conditional

[3] http://homepage.sns.it/mesinger/EOS.html

probability distribution $p(W\,|\,\overline{x}_{\text{HI}}, m, \mu, z_d)$ is:

$$p(\{W\}\,|\,\overline{x}_{\text{HI}}, m, \mu, z_d) = \prod_{i \neq d} \frac{1}{\sqrt{2\pi}\sigma_i} e^{-\frac{W_i^2}{2\sigma_i^2}} \times \int dW \, \frac{1}{\sqrt{2\pi}\sigma_d} e^{\frac{1}{2}\left(\frac{W_d - W}{\sigma_d}\right)^2} p(W\,|\,\overline{x}_{\text{HI}}, m, \mu, z_d = 8) \tag{7.4}$$

where σ_i is the uncertainty in EW at wavelength pixel i, d is the wavelength pixel index of the emission line, and $z_d = \lambda_d/\lambda_\alpha - 1$, with $\lambda_\alpha = 1216\,$Å. $p(W\,|\,\overline{x}_{\text{HI}}, m, \mu, z_d = 8)$ is the probability distribution for the observed rest-frame EW as a function of the neutral fraction, and galaxy properties – UV apparent magnitude, magnification, and redshift. This PDF is obtained by convolving the $p(W\,|\,\overline{x}_{\text{HI}}, M_{\text{UV}})$ model outputs from M18 with the probability distribution for each galaxy's absolute UV magnitude, including errors on m and μ (Equation 7.11).

Given our relatively small sample size, we choose to restrict our inference to $z \sim 8$, thus for ease of computation we evaluate $p(W\,|\,\overline{x}_{\text{HI}}, m, \mu, z_d)$ at $z_d = 8$, this has a negligible impact on the final likelihood. We keep z_d free in the rest of the inference. This product of likelihoods over the wavelength range of the spectrum accounts for the wavelength sensitivity of our observations, i.e. high noise regions are weighted lower than low noise regions.

We also note that EW is independent of magnification. Therefore, our inferences should be quite robust to magnification, which enters only through the dependency on M_{UV} of the assumed intrinsic EW distribution.

Using Bayes' theorem, the posterior distribution for $\overline{x}_{\text{HI}}$ and z_d is:

$$p(\overline{x}_{\text{HI}}, z_d\,|\,\{W\}, m, \mu) \propto p(\{W\}\,|\,\overline{x}_{\text{HI}}, m, \mu, z_d) \times p(z_d)\, p(\overline{x}_{\text{HI}}) \tag{7.5}$$

We use a uniform prior on $\overline{x}_{\text{HI}}$ between 0 and 1, $p(\overline{x}_{\text{HI}})$, and use the photometric redshift distribution for the prior $p(z_d)$. As we are only interested in the posterior probability of $\overline{x}_{\text{HI}}$ we can marginalise over z_d for each galaxy. To account for the incomplete wavelength coverage, we use the fact that if the object has Lyα outside of the KMOS wavelength range (covering $[z_{\min} = 7.2,\, z_{\max} = 10.1]$) we would measure a non-detection in our data. Thus the posterior for $\overline{x}_{\rm HI}$ from one galaxy is:

$$\begin{aligned} p(\overline{x}_{\rm HI}\,|\,\{W\}, m, \mu) \propto & \int_{z_{\rm min}}^{z_{\rm max}} dz_d \; p(\{W\}\,|\,\overline{x}_{\rm HI}, m, \mu, z_d) p(z_d) \\ & + \prod_i \frac{1}{\sqrt{2\pi}\sigma_i} e^{-\frac{W_i^2}{2\sigma_i^2}} \left(1 - \int_{z_{\rm min}}^{z_{\rm max}} dz_d \; p(z_d)\right) \end{aligned} \tag{7.6}$$

We assume all galaxies observed are independent, so that the final posterior is the product of the normalised posteriors (Equation 7.6) for each object.

Using the photometric redshift distributions as a prior on the redshift allows us to incorporate the probability of each galaxy truly being at high redshift (rather than a low redshift contaminant) in a statistically rigorous way. In combining the posteriors in Equation 7.6 for each galaxy, the photometric redshift distribution weights the individual posteriors based on the probability of the source being within our redshift range. LBGs usually have degeneracies in their photometry which make it difficult to determine whether they are high redshift star-forming galaxies or mature $z \sim 1-2$ galaxies. Thus with our method we are able to obtain reionization inferences from sources even when the photometric redshift distribution has multiple and/or broad peaks.

Whilst here we have carried out the inference at $z \sim 8$ only, with larger samples, it will be possible to measure $\overline{x}_{\rm HI}(z)$ directly, for example by parametrising its evolution with redshift and inferring the values of its redshift-dependent parameters, or in an Markov Chain Monte Carlo exploration of IGM simulations to also infer relevant astrophysical parameters (Greig & Mesinger, 2015; Greig & Mesinger, 2017a).

7.4.2 Defining a selection function for a photometric sample

To make accurate inferences for reionization it is important to have uniform and well-understood target selection functions for the sources we use. At the time of target selection for KLASS not all deep HFF data were available, nor were sophisticated ICL removal techniques developed (e.g., Merlin et al., 2016; Morishita et al., 2017; Livermore et al., 2017). This led to heterogeneous target selections. However, for this analysis we now use the most up-to-date photometry available to create a sub-sample for analysis with a homogeneous

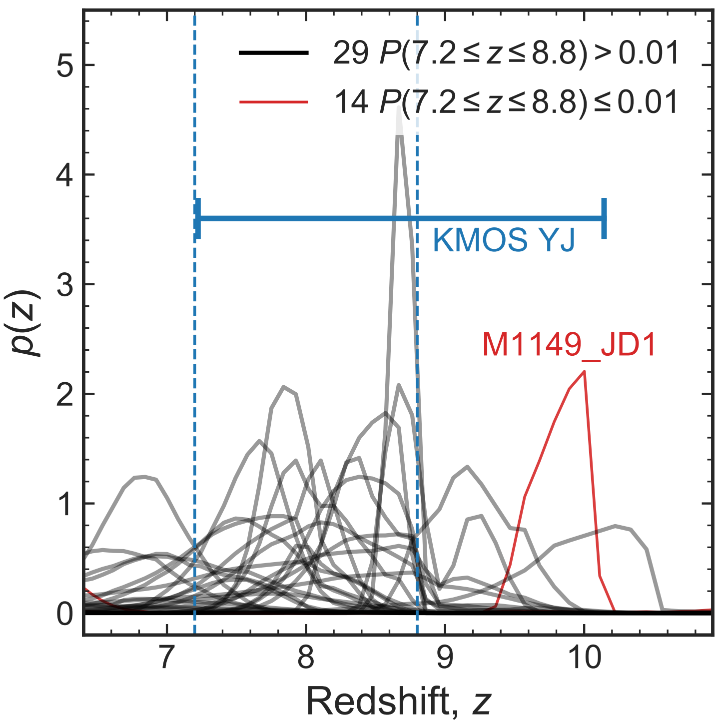

Figure 7.4: Photometric redshift distributions centred on the KMOS observable range. We show the KMOS YJ range for Lyα with the solid blue horizontal line. Black lines show the $p(z_{\rm phot})$ for the 29 sources which have $> 1\%$ probability of $7.2 \leq z_{\rm phot} \leq 8.8$ (marked by blue dashed vertical lines) which we use for the inference. 14 sources have $P(7.2 \leq z_{\rm phot} \leq 8.8) < 0.01$, including the galaxy M1149_JD1, recently spectroscopically confirmed at $z = 9.11$ with ALMA by Hashimoto et al. (2018). In our photometric catalogue this galaxy is correctly found to be outside of our redshift range of interest (shown here as the red curve with $z_{\rm phot} > 9$), so we do not use it for our reionization analysis but discuss it in Section 7.5.2. Note – the remaining 13 objects have photometric redshift distributions outside of the range plotted here.

Table 7.2: KLASS targets with $P(7.2 \leq z_{\rm phot} \leq 8.8)$ solutions

Object ID*	R.A. [deg]	Dec. [deg]	m_{160}	μ	$M^{\dagger}_{\rm UV}$	$P(7.2 \leq z_{\rm phot} \leq 8.8)^{\diamond}$	$f^{\ddagger}_{\rm lim} \times 10^{-18}$ [erg s^{-1} cm^{-2}]	$EW^{\ddagger,\star}_{\rm Ly\alpha}$ [Å]
A2744_2036	3.596087	−30.385836	26.95 ± 0.07	$2.4^{+7.4}_{-0.5}$	-19.27 ± 0.89	0.97	< 6.6	< 53
A2744_2346	3.606460	−30.380995	26.78 ± 0.06	$1.6^{+0.8}_{-0.5}$	-19.89 ± 0.41	1.00	< 5.6	< 38
A2744_2345	3.606572	−30.380932	26.49 ± 0.06	$1.6^{+0.8}_{-0.5}$	-20.19 ± 0.41	0.99	< 5.6	< 29
A2744_2261	3.603996	−30.382309	27.29 ± 0.10	$1.7^{+1.1}_{-0.5}$	-19.34 ± 0.47	0.79	< 5.7	< 62
A2744_2503	3.588979	−30.378668	27.27 ± 0.12	$2.2^{+0.9}_{-0.7}$	-19.04 ± 0.39	0.36	< 6.0	< 65
A2744_2257	3.598123	−30.382393	28.62 ± 0.18	$1.9^{+0.8}_{-0.4}$	-17.87 ± 0.36	0.54	< 5.7	< 208
A2744_20236	3.572523	−30.413267	28.61 ± 0.24	$1.8^{+1.0}_{-0.5}$	-17.94 ± 0.48	0.42	< 5.0	< 178
A2744_1040	3.592505	−30.401482	27.52 ± 0.15	$14.2^{+11.2}_{-6.3}$	-16.79 ± 0.65	0.04	< 5.1	< 68
A2744_2248**	3.603863	−30.382261	26.57 ± 0.07	$1.7^{+1.1}_{-0.5}$	-20.06 ± 0.47	0.96	< 5.7	< 32
M0416_99	64.039162	−24.093182	26.28 ± 0.05	$1.5^{+0.5}_{-0.3}$	-20.49 ± 0.30	0.78	< 1.8	< 7
M0416_286	64.037567	−24.088116	28.20 ± 0.17	$1.9^{+0.3}_{-0.5}$	-18.29 ± 0.31	0.66	< 1.9	< 46
M0416_743	64.048058	−24.081427	26.56 ± 0.06	$1.7^{+0.3}_{-0.2}$	-20.07 ± 0.19	0.07	< 1.6	< 9
M0416_1956	64.060333	−24.064962	28.16 ± 0.16	$1.9^{+0.2}_{-0.6}$	-18.33 ± 0.28	0.91	< 1.6	< 37
M0416_1997	64.049583	−24.064596	27.56 ± 0.17	$6.3^{+39.3}_{-1.5}$	-17.64 ± 1.23	0.90	< 1.5	< 21
M0416_22746	64.046509	−24.061630	27.77 ± 0.23	$8.1^{+4.3}_{-3.0}$	-17.15 ± 0.53	0.62	< 1.5	< 25

NOTE. – * IDs for A2744, M0416 and M1149 match the ASTRODEEP catalogue IDs (Merlin et al., 2016; Di Criscienzo et al., 2017). † These listed intrinsic magnitudes are calculated using $z = 8$ and the listed magnifications and errors. ◇ This is the photometric redshift from EAzY integrated between $z = 7.2$ and $z = 8.8$, i.e. the total probability of the object to have. ‡ Flux and EW limits are 5σ. ⋆ All EW are rest-frame. We stress that the EW limits only hold if the Lyα is actually in the KMOS range, which has probability given by $P(7.2 \leq z_{\rm phot} \leq 8.8)$. ** This object was spectroscopically confirmed by Laporte et al. (2017) at $z = 8.38$.

Table 7.3: *Cont.*

Object ID*	R.A. [deg]	Dec. [deg]	m_{160}	μ	$M_{\rm UV}^{\dagger}$	$P(7.2 \leq z_{\rm phot} \leq 8.8)^{\diamond}$	$f_{\rm lim}^{\ddagger} \times 10^{-18}$ [erg s^{-1} cm^{-2}]	$EW_{\rm Ly\alpha}^{\ddagger,\star}$ [Å]
M1149_23695	177.382996	22.412041	28.11 ± 0.14	$3.6^{+0.7}_{-2.1}$	-17.69 ± 0.58	0.77	< 2.3	< 52
M1149_3343	177.392715	22.384718	28.64 ± 0.28	$1.7^{+0.4}_{-0.5}$	-17.96 ± 0.42	0.04	< 2.8	< 105
M1149_1428	177.412216	22.394894	28.34 ± 0.17	$7.5^{+0.9}_{-2.8}$	-16.67 ± 0.36	0.25	< 1.7	< 46
M1149_945	177.412079	22.389055	27.92 ± 0.13	$9.2^{+14.4}_{-3.2}$	-16.87 ± 0.76	0.16	< 1.7	< 33
M2129_2633	322.345232	−7.671373	25.65 ± 0.12	$1.6^{+0.1}_{-0.1}$	-21.06 ± 0.13	0.20	< 1.8	< 4
M2129_2661	322.350848	−7.675239	26.38 ± 0.17	$1.7^{+0.0}_{-0.0}$	-20.25 ± 0.17	0.07	< 1.8	< 8
M2129_1556	322.344535	−7.688473	27.53 ± 0.26	$4.2^{+0.2}_{-0.2}$	-18.11 ± 0.27	0.01	< 1.8	< 24
RXJ1347_1831	206.896270	−11.742338	26.30 ± 0.26	$9.2^{+0.4}_{-0.4}$	-18.49 ± 0.26	0.06	< 1.7	< 7
RXJ1347_656	206.891246	−11.752607	26.43 ± 0.24	$20.4^{+1.6}_{-1.2}$	-17.49 ± 0.25	0.72	< 1.9	< 9
RXJ1347_101	206.880973	−11.769816	25.16 ± 0.15	$43.9^{+10.2}_{-5.4}$	-17.92 ± 0.26	0.20	< 1.9	< 3
RXJ1347_1368	206.893076	−11.760230	27.92 ± 0.43	$16.6^{+1.1}_{-1.1}$	-16.22 ± 0.43	0.34	< 1.6	< 31
RXJ1347_1280	206.896921	−11.763833	27.28 ± 0.28	$4.8^{+0.7}_{-0.5}$	-18.22 ± 0.31	0.03	< 1.5	< 15
RXJ2248_1006	342.208379	−44.537520	25.83 ± 0.17	$1.6^{+0.4}_{-0.4}$	-20.88 ± 0.32	0.92	< 2.4	< 7
RXJ2248_2086	342.179829	−44.525664	26.88 ± 0.13	$41.0^{+72.3}_{-25.5}$	-16.28 ± 1.09	0.48	< 2.0	< 14

NOTE. – Same as Table 7.3.

selection function. We demonstrate in Appendix 7.8 that this sub-sample is not a biased selection from the final parent catalogues.

Deep, multi-band *HST*, Spitzer-IRAC and HAWK-I photometry is now available for all our targets through the CLASH and HFF programs (Postman et al., 2012a; Lotz et al., 2017). For A2744, M0416 and M1149 we used the ASTRODEEP photometric catalogue which removed foreground intra-cluster light (Castellano et al., 2016; Merlin et al., 2016; Di Criscienzo et al., 2017). For M2129, RXJ1347 and RXJ2248 we created our own catalogues based on the ASTRODEEP methodology. Of the 56 high-redshift candidate targets we assigned to KMOS IFUs, 46 have matches in these final deep catalogues (including the 3 images of a $z = 6.11$ multiply-imaged system in RXJ2248).

To determine why 10 targets had no match in the final photometric catalogues we examined our target selection catalogues. We used preliminary versions of the ASTRODEEP catalogues for A2744, M0416 and M1149 in our initial selection, so all the objects targeted in A2744 and M0416 have matches in the final catalogues. 3 targets do not appear in the final M1149 catalogue, these objects were never in the preliminary ASTRODEEP catalogue but were selected from alternative preliminary HFF catalogues. 3 targets from M2129, 3 targets from RXJ1347 and 1 target from RXJ2248 have no matches in the final catalogues, which was expected as they were selected from an ensemble of preliminary photometric catalogues with shallower photometry, and narrower wavelength coverage compared to our final catalogues. 3 of the unmatched objects were Category 1 targets. These missing targets were likely faint in the initial photometry and so turn out to be spurious in deep photometry.

Photometric redshift distributions were obtained from the final catalogues with the EAzY code (Brammer et al., 2008). We perform the EAzY fit to the entire photometric dataset, and obtain photometric redshift posteriors without the magnitude prior (which weights bright objects to lower redshifts based on observations of field galaxies and may be inappropriate for our lensed sources). As described in Section 7.4.1 our inference framework uses the full photometric redshift distribution thus we can robustly use all objects with non-zero probability of being in our redshift range of interest for our inferences.

Taking the 43 high redshift KMOS targets matched in the catalogues (excluding the three images of the $z = 6.11$ galaxy described in Appendix 7.7) we then use the photometric redshift distributions to select objects which could be in the KMOS YJ range ($7.2 < z_{\rm phot} < 10.1$). We calculate $P(7.2 < z_{\rm phot} < 10.1) = \int_{7.2}^{10.1} p(z_{\rm phot}) dz_{\rm phot}$ using the normalised EAzY photometric redshift distribution for each object to find the total probability of the object being within that redshift range. We select 30 objects with $P(7.2 < z_{\rm phot} < 10.1) > 0.01$ (though the majority have a much higher probability of being in that redshift range). The photometric redshift distributions of these objects within the KMOS YJ range are plotted in Figure 7.4.

We examined the final deep photometry of the 13 objects which dropped out of the KMOS YJ range in this selection, which include 6 Category 1 targets. As expected, the selection of these objects shifts to lower redshifts now the full photometry is available. The majority of them have detections in the bluest bands which would negate a $z > 7$ Lyman Break, and several are clearly $z \sim 1$ passive galaxies when the IRAC bands are included.

Due to the relatively small sample size, we choose to perform our inference at $z \sim 8$, so we select only objects with some probability to have $7.2 < z_{\rm phot} < 8.8$. We calculate $P(7.2 < z_{\rm phot} < 8.8) = \int_{7.2}^{8.8} p(z_{\rm phot}) dz_{\rm phot}$. We select 29 objects with $> 1\%$ probability of being within this redshift range (21 have $> 10\%$ probability, and 13 $> 60\%$ probability). One object has $z_{\rm phot} > 9$ and is excluded from our inference. This is M1149_JD1, recently spectroscopically confirmed at $z = 9.11$ by Hashimoto et al. (2018). As this galaxy's photometric redshift distribution clearly puts it at $z > 9$ we do not include it in our $z \sim 8$ reionization inferences. Its $p(z_{\rm phot})$ can be seen in Figure 7.4 (red line) and we discuss our observations of it in Section 7.5.2.

Our inference uses the full $p(z_{\rm phot})$ distribution, to robustly account for any probability of an object being a lower redshift contaminant. The median and standard deviation of best-fit photometric redshifts over this range for the sub-sample of 29 objects is $z_{\rm phot} = 7.9 \pm 0.6$. These objects and their observed properties, including $P(7.2 < z_{\rm phot} < 8.8)$ are listed in Table 7.2. We demonstrate that this sub-sample is not a biased sample of the final photometric catalogues in Appendix 7.8.

We also cross-checked our Table 7.2 with publicly available spectroscopic catalogues from ground-based follow-up at optical wavelengths for clusters A2744 (Mahler et al., 2018), M0416 (Balestra et al., 2016; Caminha et al., 2017), M1149 (Grillo et al., 2016), M2129 (Monna et al., 2017) and RXJ2248 (Karman et al., 2015, 2016). We found no matches in those catalogues for any of the objects in Table 7.2. Non-detections of these objects in optical spectroscopy lends credence to their selection as $z > 7$ candidates.

One object has been spectroscopically confirmed at $7.2 < z < 8.8$ by another group. A2744_2248 (a.k.a. A2744_YD4) was confirmed at $z = 8.38$ via [[O III]]88μm emission in ALMA, and a tentative Lyα emission line was also reported with line flux $(1.82 \pm 0.64) \times 10^{-18}\,\mathrm{erg\,s^{-1}\,cm^{-2}}$ and $EW = 10.7 \pm 2.7$ (Laporte et al., 2017), which is well below our limit for that object. As discussed in Section 7.4.3 we do treat the object as a detection in our inference but it has a negligible impact on our inferred limits on the neutral fraction.

We obtain magnification estimates for each object using the publicly available HFF lens models[4]. We take the best-fit magnifications from the most recent versions of all available lens models for each object, drop the highest and lowest magnifications to produce an approximate 1σ range of estimated magnifications, $\{\mu\}$. We list the median magnification from this sub-sample, and the upper and lower bounds in Table 7.2. For the inference, we assume magnifications are log-normally distributed with mean given by the median $\log_{10}\{\mu\}$ and standard deviation given by half the range of $\log_{10}\{\mu\}$, which is a reasonable fit to the distribution of magnifications from the models. For M2129 and RXJ1347, the only non-HFF clusters, we use the magnification distribution from the Bradač group lens models (Huang et al., 2016a, A. Hoag et al., in prep) and obtain mean and standard deviation log magnifications. As discussed in Section 7.4.1 by using the EW in our inference, which is independent of magnification (as opposed to flux), our results are quite robust to magnification uncertainties.

We calculate flux and Lyα EW limits for individual objects as in Section 7.3.4, using Equations 7.2 and 7.3. The median intrinsic UV absolute magnitude (i.e., corrected for

[4] `https://archive.stsci.edu/prepds/frontier/lensmodels/`

magnification) of the sample is $M_{\rm UV} = -18.2$. The median observed flux 5σ upper limit in this sub-sample is $< 1.9 \times 10^{-18}$ erg s^{-1} cm^{-2}, and the median rest-frame Lyα EW 5σ upper limit is < 31 Å.

7.4.3 Inference on the IGM neutral fraction

We use 1D EW spectra and uncertainties as a function of wavelength for the 29 objects described above to infer the IGM neutral fraction at $z \sim 8$ using Equation 7.6 to calculate the posterior distribution of $\overline{x}_{\rm HI}$.

We obtain the EW using the cubes for each object, extracting flux and noise in a circular aperture with $r = 2\sigma_{psf}$, and apply a rescaling to both to account for the incomplete recovery of flux in the aperture, and a constant rescaling to the noise spectrum to ensure the S/N distribution of pixels in each spectrum is a Normal distribution. We then convert the flux and noise measurements to EW at every wavelength using $W = (1+z)^{-1} f(\lambda)/f_{\rm cont}$.

In Figure 7.5 we plot the posterior distribution for $\overline{x}_{\rm HI}$ obtained using our observations of the 29 $z \sim 8$ KLASS targets, as well as Keck/MOSFIRE observations of 8 $z \sim 8$ LBGs from the Brightest of Reionizing Galaxies survey (BoRG, Trenti et al., 2011; Bradley et al., 2012; Schmidt et al., 2014a) described by Treu et al. (2013). Using the BoRG sample allows us to cover a broader range in intrinsic magnitudes spanning opposite ends of the galaxy UV luminosity function: the IGM attenuation of Lyα from UV bright and UV faint galaxies is expected to be different due to differing Lyα escape paths through their interstellar and circumgalactic media (e.g., Stark et al., 2010, 2017; Mason et al., 2018b).

These two sets of independent observations, both indicate a predominantly neutral IGM at $z \sim 8$. The BoRG data alone produce a lower limit of $\overline{x}_{\rm HI} > 0.51$ (68%) and for the KLASS data alone $\overline{x}_{\rm HI} > 0.76$ (68%). Lower limits from the combined dataset are $\overline{x}_{\rm HI} > 0.80$ (68%) and $\overline{x}_{\rm HI} > 0.57$ (95%).

The BoRG spectra were less sensitive than our KMOS data: the median 5σ Lyα EW limit for the BoRG sample is 39 Å, compared to 31 Å for the KLASS sample. Our new KLASS same demonstrates that increased flux sensitivity, as well as the higher number of sources for the inference, produce tighter constraints on the IGM neutral fraction. In particular, by exploiting gravitational lensing, the KLASS sample sets much lower limits Lyα EW for instrically UV faint galaxies (which produce the strongest constraints on reionization's mid-stages, M18) than is possible in blank fields.

To test whether the inclusion of objects with candidate Lyα emission in GLASS data biased our sample, we tested the inference with and without including the Category 1 targets. We found no significant difference in the posteriors. We also tested the inference with and without including the $z = 8.38$ marginal detection of Lyα in object A2744_2248 by Laporte et al. (2017) (with spectroscopic confirmation from [O III] emission in ALMA observations). We use the EW reported by Laporte et al. (2017) $W = 10.7 \pm 2.7$ Å, which is well below our 5σ limit for that object (< 32 Å). Despite the potential detection, the posterior distribution for this single object strongly favours a mostly neutral IGM due to its very low EW and low significance. We did our inference using both our KMOS spectra and the Laporte et al. (2017) measurement for this object and found it to have a negligible impact on our final posterior (changing the inferred limit by only $\Delta\overline{x}_{\rm HI} \sim 0.01$). Our quoted posterior limits do include the object as a detection.

7.5 Discussion

We discuss our new lower limit on the neutral fraction and the implications for the timeline of reionization in Section 7.5.1, and show it favours reionization driven by UV faint galaxies with a low ionizing photon escape fraction. In Section 7.5.2 we discuss the recent tentative detection of Lyα at $z = 9.11$ by (Hashimoto et al., 2018) and show it is not inconsistent with our results. In Section 7.5.3 we discuss our EW limits on NV and CIV emission. Finally, in Section 7.5.4 we present a comparison of the KMOS ETC and our achieved S/N for background-limited observations.

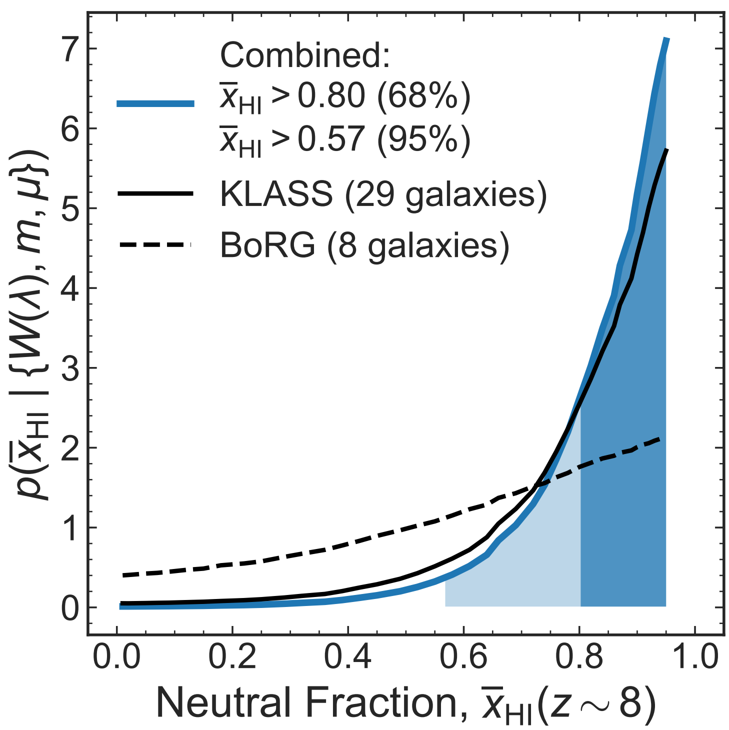

Figure 7.5: Posterior probability distribution for the IGM neutral fraction $\overline{x}_{\rm HI}$ at $z \sim 8$ obtained using Equation 7.6 and the EW spectra from the KLASS sample described in Section 7.4.2 (black solid line), and the BoRG sample described by Treu et al. (2013) (black dashed line). The blue line and shaded regions show the posterior from the combined datasets, and its 68% and 95% confidence regions (the darkest region is the 68% confidence range). Note – the EoS simulations end at $\overline{x}_{\rm HI} = 0.95$ which is why our posterior stops at that value. Confidence limits were calculated over the range of the simulation $\overline{x}_{\rm HI} = 0.01 - 0.95$.

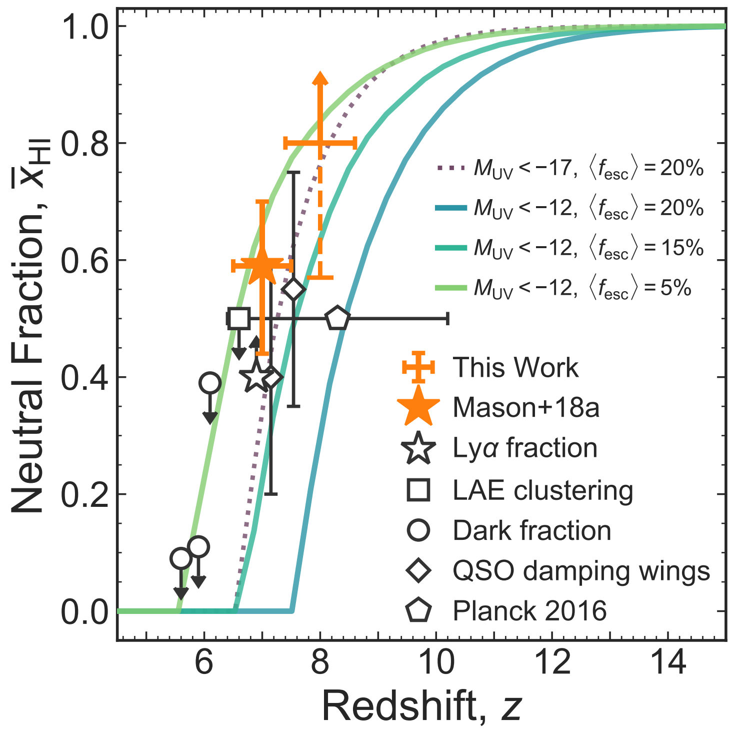

Figure 7.6: The redshift evolution of the volume average neutral hydrogen fraction of the IGM. Our new lower limit is shown in orange, with the horizontal errorbar at the 68% confidence level and the dashed vertical line extending to the 95% confidence level. We also plot measurements derived from observations of: the evolving Lyα EW distribution at $z \sim 7$ (orange filled star M18) previous estimates from the fraction of LBGs emitting Lyα (open black star, Mesinger et al., 2015); the clustering of Lyα emitting galaxies (square, Ouchi et al., 2010; Sobacchi & Mesinger, 2015); Lyα and Lyβ forest dark fraction (circle, McGreer et al., 2015); and QSO damping wings (diamond, Greig & Mesinger, 2017b; Bañados et al., 2017). We offset the constraints at $z \sim 7$ by $\Delta z = 0.1$ for clarity. We also plot the Aghanim et al. (2012) redshift range of instantaneous reionization (black pentagon). We show median model reionization histories derived from the Mason et al. (2015b) UV luminosity function models as coloured lines. We plot models obtained from integrating the luminosity function down to two magnitude limits – $M_{UV} = -17$ (purple dashed line) and $M_{UV} = -12$ (darkest blue solid line) and drawing from uniform distributions for the ionizing photon escape fraction $10 - 30\%$ and clumping factor $C = 1 - 6$, and log-normal distribution for the ionizing efficiency ξ_{ion} with mean 25.2 and standard deviation 0.15 dex. Comparing reionization histories with ionizing escape fraction drawn from a uniform distribution $1 - 10\%$ (light green) and $10 - 20\%$ (medium teal), integrating LFs down to $M_{UV} = -12$ in both cases and using the same distribution for the clumping factor and ξ_{ion} as above.

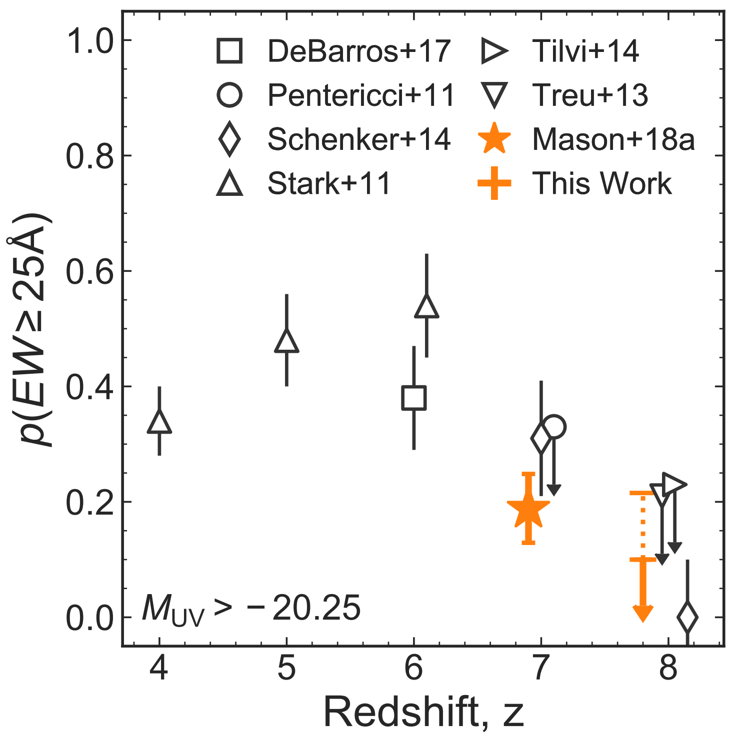

Figure 7.7: The redshift evolution of the 'Lyα fraction' for UV faint galaxies, the fraction of LBGs observed with Lyα EW ≥ 25 Å. We plot literature measurements from Stark et al. (2011); Pentericci et al. (2011); Treu et al. (2013); Tilvi et al. (2014); Schenker et al. (2014) and De Barros et al. (2017). We add small offsets in redshift for measurements at the same redshifts to ease the display of the data. We also plot the predicted Lyα fraction from M18 calculating $p(W > 25\mathring{A} | \overline{x}_{\rm HI}, M_{\rm UV})$ using $M_{\rm UV} = -20$ galaxies and the neutral fraction constraint $\overline{x}_{\rm HI} = 0.59^{+0.11}_{-0.15}$ ($16 - 84\%$ confidence intervals) as the orange star. We plot the upper limits recovered in this paper as orange lines, with the solid line showing our 68% confidence limit, and the dashed line extending to the 95% confidence limit. We calculate $p(W > 25\mathring{A} | \overline{x}_{\rm HI} > 0.80, M_{\rm UV})$ again using $M_{\rm UV} = -20$. Our constraint is consistent with literature values at the same redshift.

7.5.1 The timeline of reionization

We plot our new limit on the reionization timeline in Figure 7.6. We also plot other statistically robust constraints from Ouchi et al. (2010); McGreer et al. (2015); Sobacchi & Mesinger (2015); Mesinger et al. (2015); Greig & Mesinger (2017b); Bañados et al. (2017); Mason et al. (2018a) and the Aghanim et al. (2012). Our new limit, combined with the other recent $\overline{x}_{\rm HI}$ measurements at $z \sim 7$ provide increasing evidence for the bulk of hydrogen reionization occurring $z \sim 6 - 8$ (Greig & Mesinger, 2017b; Bañados et al., 2017; Mason et al., 2018a), late in the Aghanim et al. (2012) confidence range.

Accurate measurements of the reionization timeline can help constrain properties of early galaxies. In Figure 7.6 we show model reionization histories obtained from integrating the Mason et al. (2015b) UV luminosity functions, varying the typical reionization parameters: the minimum UV luminosity of galaxies, and the average ionizing photon escape fraction. We see that late reionization is most consistent with either a high minimum UV luminosity of galaxies ($M_{\rm UV} < -17$) and moderate escape fraction ($\langle f_{\rm esc} \rangle = 20\%$), or with including ultra-faint galaxies $M_{\rm UV} < -12$) with low escape fractions ($\langle f_{\rm esc} \rangle \lesssim 15\%$).

There are many degeneracies between these reionization parameters, and certainly the escape fraction is unlikely to be constant for all galaxies at all times (Trebitsch et al., 2017), but non-detections of high-redshift GRB host galaxies, and observations of lensed high-redshift galaxies, and local dwarfs, indicate galaxies fainter than $M_{\rm UV} = -17$ likely exist at $z \sim 8$ (e.g., Kistler et al., 2009; Tanvir et al., 2012; Trenti et al., 2012a; Alavi et al., 2014; Weisz & Boylan-Kolchin, 2017; Livermore et al., 2017; Bouwens et al., 2017b). If ultra-faint galaxies do contribute significantly to reionization our result suggests reionization can be completed with low escape fractions, consistent with low redshift estimates of the average escape fraction (Marchi et al., 2017; Rutkowski et al., 2017; Naidu et al., 2018; Steidel et al., 2018).

For comparison with previous high redshift Lyα spectroscopic surveys we plot the so-called 'Lyα fraction', the fraction of LBGs emitting Lyα with EW ≥ 25 Å in Figure 7.7. We compare our new upper limits on the Lyα fraction with literature measurements from

Stark et al. (2011); Pentericci et al. (2011); Treu et al. (2013); Tilvi et al. (2014); Schenker et al. (2014) and De Barros et al. (2017). We also plot the predicted Lyα fraction from M18. Using the M18 model EW distributions $p(W \,|\, \overline{x}_{\text{HI}}, M_{\text{UV}})$ we can calculate the Lyα fraction as the probability of EW $\geq 25\,$Å given our constraint on the neutral fraction.

As noted by M18 and Mason et al. (2018b) the Lyα EW distribution is likely a function of at least UV magnitude as well as the neutral fraction (see Oyarzún et al., 2017, for a thorough analysis of Lyα EW dependencies on galaxy properties), so it can be difficult to compare Lyα fraction from samples with different M_{UV}. Hence, when converting from the neutral fraction measurement in this work and M18 we use the model Lyα EW distribution for $M_{\text{UV}} = -20$ galaxies to compare more easily with the literature values for which that is the typical median UV magnitude. For $M_{\text{UV}} = -20$ our Lyα fraction limits are $f_{\text{Ly}\alpha} < 0.10$ (68%), < 0.22 (95%). Using our sample median magnitude, $M_{\text{UV}} = -18.2$, the limits are not significantly different: $f_{\text{Ly}\alpha} < 0.07$ (68%), < 0.19 (95%). Our measurements are consistent with the literature values.

We note that our inference assumes no evolution in the emitted Lyα EW distribution at fixed UV magnitude from $z \sim 6-8$, i.e. the only evolution in the *observed* EW distribution is due to reionization. Whilst there may be evolution in the amount of Lyα escaping the ISM of galaxies with increasing redshift, it is probably increasing as dust masses and HI covering fractions may decrease at higher redshifts and facilitate Lyα escape at fixed galaxy mass (Hayes et al., 2011; Oyarzún et al., 2016). In this case we expect our model to underestimate the observed EW distribution, which would suggest an even higher neutral hydrogen fraction given our non-detections. Our model also assumes no significant evolution in the dust spatial distribution and/or CGM opacity between $z \sim 6-8$, which could both reduce the Lyα EW before the photons reach the IGM. If these effects do significantly decreases Lyα EW between $z \sim 6-8$, this could lower our constraint on the neutral fraction. In modelling the emitted Lyα EW distribution we assume a Gaussian plus Dirac Delta function parameterisation, which has been shown to describe the Lyα EW distribution well (Oyarzún et al., 2017). However, choosing another functional form for the distribution will not significantly change the results (Treu et al., 2012; Schenker et al., 2014).

More accurate models of Lyα emerging from the $z > 6$ ISM are required to improve our inferences. Whilst it is impossible to directly observe the emitted Lyα from $z > 6$ galaxies, because of the intervening neutral gas, other emission lines could be used as a diagnostic of emerging Lyα. For example, Henry et al. (2018) showed that MgII emission line profiles and escape fractions closely trace those of Lyα in Green Peas, low-redshift analogues of high redshift galaxies. As the IGM optical depth to MgII is much lower than for Lyα, observations of MgII at $z > 6$ (which will possible with JWST) could be used infer the nature of Lyα emission at these redshifts.

We also assume the fraction of low redshift contaminants in our photometric sample is the same as our reference $z \sim 6$ sample from De Barros et al. (2017). Whilst the selection techniques for the two samples are different (ours is based on photometric redshifts, De Barros et al. (2017) uses a colour selection) our targets have extensive multi-wavelength photometry which help rule out low redshift contaminants (e.g., Vulcani et al., 2017; Livermore et al., 2018). Additionally, we use the full photometric redshift distribution from EAzY in our inference which will weight the most convincing high redshift candidates most strongly in our inference, and robustly account for contamination. With the final GLASS Lyα candidate sample it will be possible to use the same selections for both the $z \sim 6$ reference EW distribution and the $z > 6$ samples for reionization inferences (K. B. Schmidt et al., in prep.).

As our inference weights sources by their photometric redshift distribution, the tightest constraints on $\overline{x}_{\rm HI}$ will be obtained from samples with robust redshift estimates or, ideally, spectroscopic redshifts obtained from other emission lines, and deep Lyα EW limits. The prospects for large spectroscopic samples at these redshifts is increasing: ALMA is enabling spectroscopic confirmation of $z \gtrsim 7$ galaxies in the sub-mm (e.g., Bradač et al., 2017; Laporte et al., 2017; Smit et al., 2018; Hashimoto et al., 2018), and other UV emission lines have also been confirmed (Stark et al., 2015; Schmidt et al., 2016; Stark et al., 2017; Mainali et al., 2017; Mainali et al., 2018). Future observations with JWST slitless and slit spectroscopy will be able to build large and deep spectroscopic samples of $z \gtrsim 7$ galaxies, ideal for this type of analysis.

Understanding the differing evolution of Lyα emission as a function of galaxy properties and environment will be key to understanding how reionization progresses. Here we have shown that a sample of intrinsically UV faint systems at $z \sim 8$ (more likely to live in low density environments) show no significant Lyα emission, and favour a mostly neutral IGM. However, Lyα has been observed in a handful of UV bright galaxies at $z \gtrsim 7.5$ (Zitrin et al., 2015b; Oesch et al., 2015; Roberts-Borsani et al., 2016; Stark et al., 2017). Mason et al. (2018b) showed that the observed Lyα fraction for UV bright galaxies at $z \sim 8$ could not be reproduced with standard reionization models (using the EoS simulations, Mesinger, 2016), even when placing them in overdense regions (which reionize early) and giving them high Lyα velocity offsets to facilitate Lyα IGM transmission. Mason et al. (2018b) proposed those objects have detectable Lyα because they have unusually high emitted Lyα EW (they were certainly selected to have high optical line EW, Roberts-Borsani et al., 2016).

Fluctuations in the UV background during reionization, for example, due to the inhomogeneous distribution of ionizing sources, could also contribute to the differing evolution of Lyα emission from UV bright and UV faint galaxies by boosting the IGM opacity (transparency) in underdense (overdense) regions (Davies & Furlanetto, 2016; Becker et al., 2018). One important missing piece in our inference is the halo environment of the LBGs. This work assumes a simple mapping between UV luminosity and halo mass. This works well in an average sense (Mason et al., 2015b), but deep imaging with JWST could measure the clustering strength and scatter of galaxies in the reionization epoch (Ren et al., 2018), and be used to inform more realistic IGM simulations.

7.5.2 M1149_JD1 – Lyα emission at $z = 9.11$?

One target in our observations (known as M1149_JD1, Zheng et al., 2012) was recently spectroscopically confirmed at $z = 9.11$ via [[O III]]88 μm emission with ALMA observations (Hashimoto et al., 2018). Our EAzY photometric redshift distribution for this galaxy put it outside of our inference redshift range (all of the $p(z)$ is at $z > 9$, see Figure 7.4), so it was not used in our reionization inference. However, Hashimoto et al. (2018) also report a tentative

4σ detection of Lyα emission from this galaxy in X-shooter observations at 12271.5 Å with total line flux $(4.3 \pm 1.1) \times 10^{-18}$ erg s^{-1} cm^{-2}. We examined our KMOS cube and also find a tentative 3σ emission feature at this wavelength with flux $(1.7 \pm 0.6) \times 10^{-18}$ erg s^{-1} cm^{-2}, which appears spatially similar to the rest-frame UV imaging, lending more credence to the Lyα detection.

However, as noted by Hashimoto et al. (2018), if the line is Lyα, it is blueshifted by $\sim$ 450 km/s with respect to the [[O III]] emission. Hashimoto et al. (2018) suggest that Lyα photons scattered off inflowing gas, causing it to emerge blueshifted from the galaxy's systemic velocity. Whilst blueshifts due to inflows are expected and observed for Lyα (e.g., Verhamme et al., 2006; Dijkstra et al., 2006; Trainor et al., 2015), at $z > 6$ the IGM is opaque to emission < 1216 Å, thus no Lyα emitted bluer than its source galaxy's systemic redshift should be transmitted through the IGM (Dayal et al., 2011; Dijkstra et al., 2011).

Observing blueshifted Lyα requires the galaxy to sit in a large ionized bubble ($\gtrsim$500 km/s or $\gtrsim$400 kpc in radius, Haiman, 2002). Alternatively, the Lyα emission could arise in a different component or merging companion of the [[O III]] emitting galaxy, similar to a $z = 7.1$ galaxy observed by Carniani et al. (2017). The tentative emission we observe in our KMOS cube does appear spatially offset from the predicted position of the UV continuum and [[O III]] by $\sim$ 0$''$.4, which could provide evidence for the multi-component/merger scenario. However, the weakness of the detection and some general astrometric uncertainty in KMOS make a thorough analysis difficult. Deeper near-IR IFU observations of this galaxy would be extremely interesting to confirm and determine the nature of the Lyα emission, and will be possible in the near future with JWST NIRSpec.

We calculate the probability of observing Lyα emission from such an object in a mostly neutral IGM using the framework of M18, which modelled $p(W \,|\, \overline{x}_{\rm HI}, M_{\rm UV})$. Using $m_{\rm F160W} = 25.7$ (Zheng et al., 2012) we obtain $M_{\rm UV} = 19.2 - 2.5\log_{10}(10/\mu)$, $EW = 4 \pm 2$ Å for our measured flux and $EW = 11 \pm 3$ Å from the measurement by Hashimoto et al. (2018). Using these measurements we calculate $p(W = 4 \pm 2\,\text{Å} \,|\, \overline{x}_{\rm HI} > 0.80, M_{\rm UV} = -19.2) < 0.05$, while $p(W = 11 \pm 3\,\text{Å} \,|\, \overline{x}_{\rm HI} > 0.80, M_{\rm UV} = -19.2) < 0.03$. In fact, the total probability of observing Lyα from this galaxy with EW $> 4 \pm 2$ Å if $\overline{x}_{\rm HI} > 0.80$ is $\lesssim$0.5: low Lyα EW are expected and consistent with a mostly neutral IGM.

We note that our calculations assume the Lyα is emitted close to systemic velocity (i.e., assuming that the Lyα comes from another component). Obviously if the galaxy does sit in an ionized bubble the probability of seeing emission would be higher. But we note that assuming emission is emitted at systemic velocity the probability of detecting the emission is not negligible, and thus this detection is still consistent with a mostly neutral IGM at $z > 8$.

7.5.3 Other UV emission lines at $z \sim 8$

With Lyα increasingly suppressed at $z > 6$, rest-frame UV emission lines can be used to spectroscopically confirm high-redshift LBGs. These lines can also be used as diagnostics for the stellar populations and physical conditions present in these high-redshift galaxies. Our KMOS observations cover the wavelength range where NVλ1238 and CIVλ1558, 1551 can be observed, and we briefly discuss our upper limits on the EW of these lines.

NVλ1238, 1242 can arise due to stellar winds, particularly from very young stars (Shapley et al., 2003; Jones et al., 2012), or from HII regions if powered by an AGN or radiative shocks. Of the three $z > 7$ galaxies detected to-date with tentative NV emission ($S/N \sim 4$) all have been UV bright galaxies, where AGN activity could plausibly be powering NV emission (Tilvi et al., 2016; Laporte et al., 2017; Mainali et al., 2018). In our KLASS $7.2 < z_{\rm phot} < 8.8$ sub-sample (Section 7.4.2), the median NV EW upper limit is < 33 Å. As our sample comprises intrinsically faint galaxies, which are less likely to have strong AGN activity, it is not surprising we do not detect strong NV emission.

Nebular CIVλ1558, 1551 emission has been observed in two galaxies at $z > 6$ (Stark et al., 2015; Schmidt & Beutler, 2017; Mainali et al., 2017). We observed CIV in the $z = 6.11$ galaxy with KMOS and describe our observations in more detail in Appendix 7.7. The CIV emission can be powered by either AGN activity or extremely metal poor stars. Limits on other UV lines in these objects find low metallicity stars are a more likely source of the hard photons needed to produce CIV emission, rather than AGN. The two galaxies are also both UV faint galaxies ($M_{\rm UV} \lesssim -20.2$) and Mainali et al. (2018) has suggested that there is anti-correlation

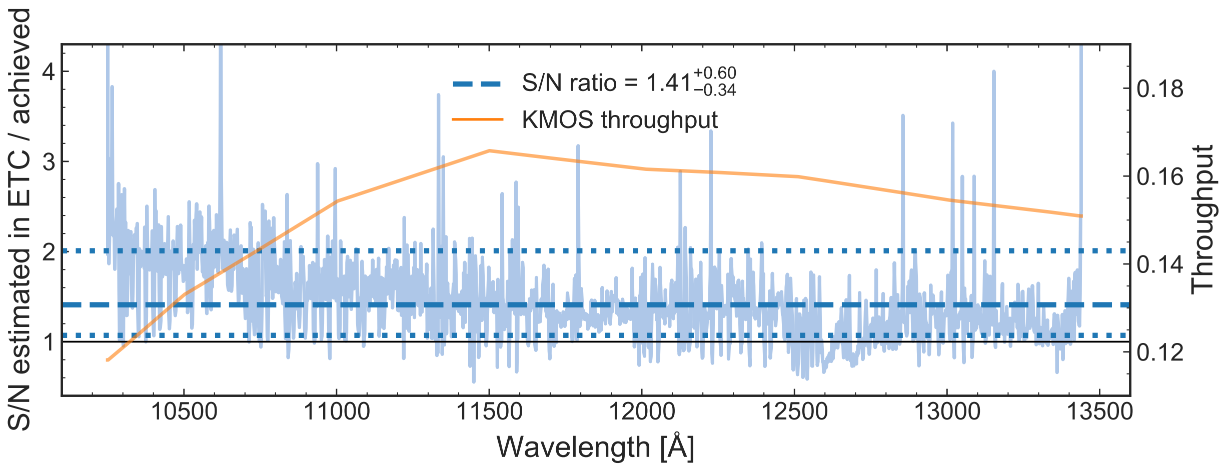

Figure 7.8: Comparison of our deepest exposure, 11 hours in in RXJ1347, with 450 second DITs, with the ESO KMOS ETC using the same exposure times. We compare the 5σ flux limits from our data and the ETC as a function of wavelength, assuming emission lines are spatially and spectrally unresolved. We divide the ETC estimated noise by $\sqrt{2}$ to account for the noise introduced by 'A-B' sky subtraction. The pale blue solid line shows the ratio of the ETC estimated S/N to our achieved S/N. The blue dashed (dotted) horizontal lines show the median ($16-84\%$ range) of the S/N ratio over the whole YJ range. The orange line shows the KMOS throughput for comparison.

between UV luminosity and CIV EW, which could arise if the lowest luminosity (mass) systems are more metal-poor.

Our KLASS observation provide a large additional sample of UV faint galaxies which can place new limits on CIV emission. In our KLASS $7.2 < z_{\rm phot} < 8.8$ sub-sample (Section 7.4.2), the median CIV EW upper limit is < 41 Å. In the three most UV faint systems with $P(7.2 < z_{\rm phot} < 8.8) > 0.6$, M0416_22746, RXJ1347_656, MACS0416_1997 (all with $M_{\rm UV} \sim -17.5$), the CIV upper limits are < 33 Å, < 12 Å, and < 26 Å respectively. These upper limits are below the CIV detection presented by Stark et al. (2015) in a $M_{\rm UV} \sim -19$ galaxy, and so suggest that the proposed anti-correlation between UV luminosity and CIV EW may not be so simple.

7.5.4 Background limited observations with KMOS

Optical and near-IR IFU observations have provided revolutionary 3D information about the structure and kinematics of galaxies out to $z \sim 2$ (Förster Schreiber et al., 2009; Epinat et al., 2009; Wisnioski et al., 2015; Stott et al., 2016; Genzel et al., 2017) and revealed diffuse Lyα halos around $z \lesssim 6$ galaxies (Bacon et al., 2014a; Karman et al., 2016; Wisotzki et al., 2016; Leclercq et al., 2017).

In KLASS we have provided the first deep NIR IFU observations of $z \gtrsim 7$ galaxy candidates. Whilst we did not make any 5σ detections of Lyα it is important to understand how this depended not only on the selection of our targets and the opacity of the IGM to Lyα at $z \sim 8$, but on the sensitivity of KMOS. In our long integrations we have pushed KMOS to the limits of its sensitivity to search for faint emission lines in near-IR IFU cubes, in wavelength regions dominated by OH sky emission lines. Using our deep observations we provide an assessment of the performance of KMOS for background-limited observations.

As described in Section 7.2.4 we performed additional sky subtraction routines after running the ESO pipeline to reduce residuals around bright OH lines. We also found the pipeline underestimated the noise in cubes by a factor ~ 1.2 and performed additional rescaling of the noise as a function of wavelength using the RMS noise obtained from the flux cubes.

One key question is how well the instrument performs relative to the predictions based on its instrumental capabilities. We can compare S/N estimated by the KMOS ETC[5] to our achieved S/N to assess its performance. We take the 5σ flux density limits as a function of wavelength for our deepest exposure, 11 hours in RXJ1347, (shown in Figure 7.2) and calculate the S/N as estimated by the ETC. We use our flux calibration based on observations of standard stars to convert flux to e^-/s and rescaled by the wavelength-dependent sky transmission and KMOS throughput curve (both obtained through the KMOS ETC webpage). We use the following ETC settings which are comparable to those of our observations: line $\mathrm{FWHM_{spec}} = 4\,\mathrm{\AA}$ (unresolved); point source; seeing $0\farcs6$; airmass: 1.50, Moon illumination FLI: 0.50, Moon-target separation: 45 degrees, PWV: $< 2.5\,\mathrm{mm}$. We calculate the S/N in an aperture with radius equal to the seeing FWHM $\sim 0\farcs6$.

[5]`https://www.eso.org/observing/etc/bin/gen/form?INS.NAME=KMOS+INS.MODE=lwspectr`

At every wavelength, the estimated S/N is:

$$\frac{S}{N} = \frac{\sqrt{NDIT} \times S_{\text{source}}}{\sqrt{S_{\text{source}} + S_{\text{bkg}} + n_{\text{spat}}(\text{DC} \times \text{DIT} + \text{RON}^2)}} \tag{7.7}$$

where for RXJ1347 NDIT = 88 is the number of DITs, of length DIT = 450 seconds. The KMOS dark current (DC) is 0.01 e^-/pixel/s and the read-out noise is 3.5 e^-/pixel/DIT. The aperture corresponds to $n_{\text{spat}} = 25$ spatial pixels and the calculation is done at the peak wavelength pixel. We use the online ETC to generate the background flux S_{bkg} in e^-/DIT as a function of wavelength, convolved with the instrumental resolution, given our input settings described above. We then calculate the estimated S/N using Equation 7.7 at every wavelength using our 5σ flux density limits as the source flux.

In Figure 7.8 we show a comparison of the ETC estimated S/N as a function of wavelength for the line fluxes corresponding to our 5σ limits. We plot the S/N estimated by the pipeline divided by 5 to show how the achieved S/N compares to the predicted S/N from the ETC. The public ETC does not account for noise due to sky subtraction routines. Assuming all DITs have equal noise σ, for 'A-B' frames the noise should be $\sqrt{2}\sigma$. Thus in Figure 7.8 we also divide the ETC estimate by a factor $\sqrt{2}$ for a fairer comparison with our data. We find that the ETC S/N is a median $\sim 1.4\times$ higher than our achieved values, and this overestimate is highest for wavelengths $\lesssim 11500$ Å, where the ETC estimate can be $\sim 1.6 - 1.8\times$ higher.

As shown in Figure 7.8, the KMOS YJ throughput is known to decrease at $\lesssim 11500$ Å but our results suggests that the YJ grating is less sensitive in the blue for background-limited observations than expected.

Unfortunately this corresponds to Lyα redshifts $z \lesssim 8.5$, where we expect to find the majority of our targets. Using the S/N estimated from the ETC in planning our observations likely led us to overestimate the line sensitivity of KMOS for our targets. Most of the GLASS Lyα candidates we assigned to KMOS IFUs had tentative detections in the *HST* grisms, hoping to confirm them with deeper KMOS observations. However, the deepest 1σ flux limit in our KMOS sample is 0.3×10^{-18} erg s^{-1} cm^{-2}, not much deeper than the 1σ flux limit in GLASS is 0.5×10^{-18} erg s^{-1} cm^{-2} (and the median flux limits for KLASS and GLASS are nearly equal), making it difficult to confirm the tentative GLASS Lyα candidates. A thorough comparison of the GLASS and KLASS observations, in combination with other follow-up at Keck, to determine the HST grism purity and completeness will be discussed in a future paper.

We advise any future KMOS users planning observations of faint targets to take into consideration both the additional noise from sky subtraction when using the KMOS ETC, and the lower than expected performance at the blue end of YJ. However, we find better agreement with the ETC estimates at redder wavelengths, demonstrating that KMOS YJ is performing well at $\gtrsim 11500\,\text{Å}$.

7.6 Summary and Conclusions

We have presented an analysis of reionization epoch targets from KLASS, a large ground-based ESO VLT/KMOS program following up sources studied in the HST grism survey GLASS. Our main conclusions are as follows:

1. The median 5σ flux limit of our survey is 2.4×10^{-18} erg s^{-1} cm^{-2}. We determine our spectroscopic survey to be 80% complete over the full wavelength range for $7.2 \lesssim z \lesssim 10.1$ spatially unresolved Lyα emission lines with flux $\gtrsim 5.7 \times 10^{-18}$ erg s^{-1} cm^{-2}, centred within $0\farcs8$ of the IFU centre and with emitted line rest-frame FWHM$_{\text{spec}} \lesssim 27$ km s^{-1}. Our observations are more complete to Lyα emission that may be spatially offset and/or extended compared to the UV continuum than typical slit-spectroscopy surveys.

2. Of the 52 $z \gtrsim 7$ candidate targets observed, none have confirmed Lyα emission, including those with candidate lines detected in the HST grisms. No other UV emission lines are detected at $z > 7$. We detect CIV emission in one image of a previously known CIV emitter at $z = 6.11$.

3. We define a sub-sample of 29 targets with a homogeneous photometric selection of $7.2 < z_{\text{phot}} < 8.8$ for a Bayesian inference of the IGM neutral hydrogen fraction. The median Lyα flux limit for our sample is 1.9×10^{-18} erg s^{-1} cm^{-2} and the median Lyα

EW upper limit is 31 Å. Combining our sub-sample with 8 previously observed $z \sim 8$ LBGs from the BoRG survey (Trenti et al., 2011; Treu et al., 2013; Schmidt et al., 2014a) we obtain a lower limit on the IGM neutral hydrogen fraction at $z = 7.9 \pm 0.6$, $\overline{x}_{\text{HI}} > 0.80$ (68%) and $\overline{x}_{\text{HI}} > 0.57$ (95%).

4. Our constraint favours a late reionization consistent with models where ultra-faint galaxies contribute significantly to reionization, with an ionizing photon escape fraction $\langle f_{\text{esc}} \rangle \lesssim 15\%$.

Our KMOS observations provide more evidence of a predominantly neutral IGM at $z \sim 8$. To make more precise constraints on the timeline of reionization will require larger samples of LBGs with precise photometric (or even better, spectroscopic) redshift estimates, and deep spectroscopic limits on Lyα. Forthcoming deep spectroscopic observations with JWST (e.g., Treu et al., 2017) will provide ideal samples for future inferences on reionization.

Acknowledgements

The authors thank Trevor Mendel and Owen Turner for useful discussions related to KMOS reductions for faint sources, and T. Mendel for sharing the readout correction code. We thank Andrei Mesinger for providing Lyα optical depths from the EoS simulations.

C.M. acknowledges support by NASA Headquarters through the NASA Earth and Space Science Fellowship Program Grant NNX16AO85H. This work was supported by the HST GLASS grant GO-13459, and the HST BoRG grants GO-12572, 12905, and 13767.

This work was based on observations collected at the European Organisation for Astronomical Research in the Southern Hemisphere under ESO program 196.A-0778; and on observations made with the NASA/ESA Hubble Space Telescope, obtained at STScI. We are very grateful to all ESO and STScI staff who have assisted in these observations.

This work utilises gravitational lensing models produced by PIs Bradač, Natarajan & Kneib (CATS), Merten & Zitrin, Sharon, Williams, Keeton, Bernstein and Diego, and the GLAFIC group. This lens modelling was partially funded by the HST Frontier Fields pro-

gram conducted by STScI. STScI is operated by the Association of Universities for Research in Astronomy, Inc. under NASA contract NAS 5-26555. The lens models were obtained from the Mikulski Archive for Space Telescopes (MAST).

Software: IPython (Pérez & Granger, 2007), matplotlib (Hunter, 2007), NumPy (Van Der Walt et al., 2011), SciPy (Oliphant, 2007), Astropy (Robitaille et al., 2013), QFitsView (`http://www.mpe.mpg.de/~ott/QFitsView/`).

7.7 Independent confirmation of CIV emission at $z = 6.11$

As well as Lyα candidates we also targeted 3 images of a multiply-imaged $z = 6.11$ galaxy in RXJ2248 to observe CIVλ1548,1551 emission. This multiple-image system has been detected with Lyα emission by Boone et al. (2013); Balestra et al. (2013); Monna et al. (2014); Karman et al. (2015); Schmidt et al. (2016) and Mainali et al. (2017). Detections of CIV and [O III]]λ1666 emission in one of the images were also presented by Mainali et al. (2017), and CIV detections and limits in all of the images by Schmidt & Beutler (2017). The presence of these highly ionised lines and lack of observed HeIIλ1640 indicate this object has a hard ionizing spectrum, but unlikely to be dominated by an AGN.

In Figure 7.9 we show our GLASS and KMOS spectra for the brightest image E. An emission line is seen in the KMOS data at the same wavelength as Mainali et al. (2017), and appears to be spatially compact with size approximately equal to our seeing ($\sim 0\farcs6$). However, due to the lower spectral resolution of our data ($R \sim 2700$ compared to $R \sim 6000$ in Mainali et al. (2017)) the emission line is overlapping with an adjacent skyline, adding some uncertainty to the extracted parameters.

We fit a model with 2 Gaussian emission lines to an extracted 1D spectrum, weighted by the inverse variance, fixing $\mathrm{FWHM_{spec}} = 5\,\mathrm{\AA}$ (close to the instrumental resolution, $4\,\mathrm{\AA}$) and allowing flux and the wavelength position of the doublet centre to vary. We note that the spatial aperture we use to extract the spectrum (1.2 sq arcsec) is slightly larger than the one used to plot Figure 7.9 (0.8 sq arcsec), to ensure we recover the full flux. We use the smaller aperture in the plot to maximise the plotted S/N and for comparison with the line

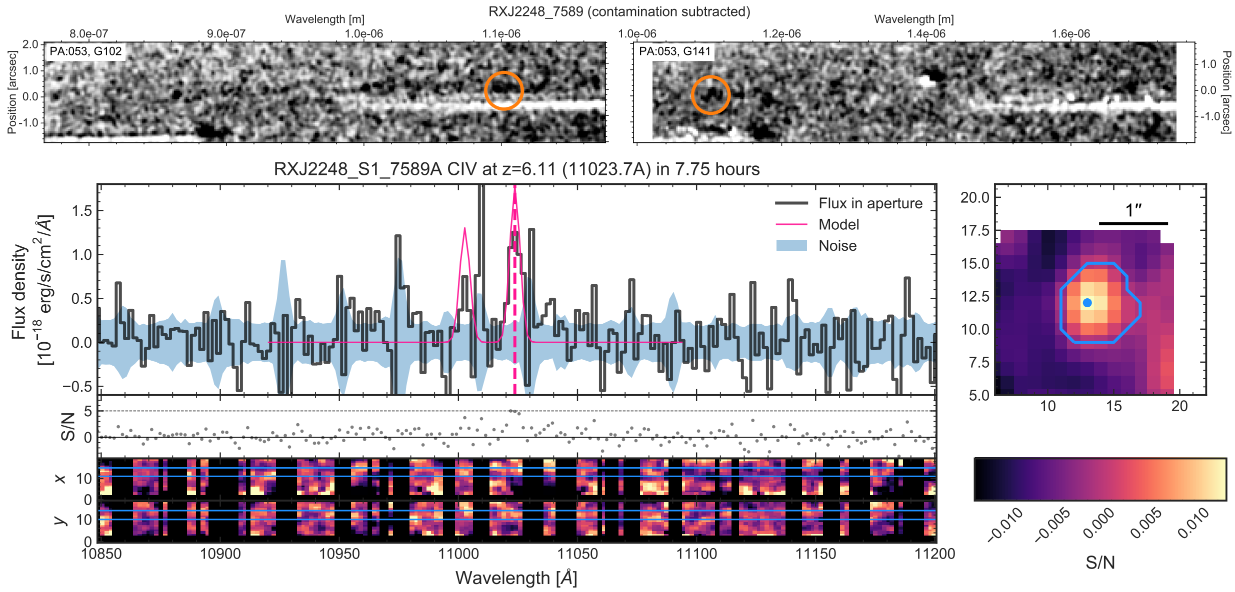

Figure 7.9: Upper panels: GLASS *HST* grism spectra taken at 2 position angles (PA) in G102 and G141. Positive flux is shown in black, white is negative flux. The candidate emission line is within the orange circle. **Lower left panel**: KLASS KMOS spectra of the same object, centred at the wavelength of the GLASS candidate emission. The top left panel shows a 1D spectrum (flux – black line, noise – blue shaded region) extracted in an aperture shown by the blue lines in the 2D postage stamp image on the right (an aperture containing the brightest 10% of pixels, with area 0.8 sq arcsec). The wavelength of the 1551 Å emission line is shown with the pink dashed vertical line. The model for the doublet using 2 Gaussians, extracting voxels in a 1.2 sq arcsec aperture (shown as the blue contour on the 2D image - lower right panel), is shown as a pink solid line. The middle panel shows the S/N at each wavelength pixel. The lower spectra show simulated slit spectra along the x and y directions, with the same aperture plotted as blue horizontal lines. Regions with strong sky emission are masked. The spectra are smoothed with a 3D Gaussian kernel with line spread function $\mathrm{FWHM_{spec}}$ equal to the instrumental resolution (4 Å) and point spread function $\mathrm{FWHM_{spat}}$ equal to the seeing (0.″6). **Lower right panel:** 2D flux postage stamp image of the emission summed over a 10 Å wavelength range centred at the wavelength shown by the pink dashed vertical line in the left panel. The emission is clearly spatially compact. The blue contour show the spatial aperture used to extract the 1D spectra. The S/N colourbar refers to the 2D slit spectra. We have performed an additional residual sky subtraction to the KLASS cube by subtracting a median spectrum obtained in spaxels away from the emission line.

identification technique described in Section 7.3.1 which also uses 0.8 sq arcsec apertures.

The strongest peak is fit at 11023.7 Å which Mainali et al. (2017) assigned to the 1551 Å emitted peak. There is a weaker peak at 11002.5 Å which would corresponds to the 1548 Å emitted peak. We note that in the 1D spectrum there does appear to be a peak redward of the strong peak, around 11040 Å which could alternatively be the 1551 Å emitted peak. However, by inspection of the 2D emission postage stamps in the KMOS cubes we see the 11002.5 Å flux is spatially coincident with the 11023.7 Å emission, whilst the 11040 Å flux is more spatially uniform and thus likely to be spurious noise peak. The peak separation to the 11040 Å line is also too low for it to be part of the doublet. Thus our assignment of the doublet wavelengths is consistent with the observations of Mainali et al. (2017).

Using our model we find a total line flux of $(1.6 \pm 0.3) \times 10^{-17}$ erg s^{-1} cm^{-2}. We find a flux ratio of CIVλ1548:CIVλ1551 = 0.7:1 which is much lower than the theoretically motivated expected value of 2:1 (e.g., Flower et al., 1979). Low mass metal-poor galaxies at $z \sim 2-3$ have been observed with flux ratios both comparable to the theoretical value (Vanzella et al., 2016; Caminha et al., 2016) and closer to a 1:1 ratio (Christensen et al., 2012; Stark et al., 2014).

However, the confusion with the adjacent skylines makes it difficult to measure an accurate flux. Our measured total flux is lower than those measured by Mainali et al. (2017) and Schmidt & Beutler (2017), but consistent with the value measured by Schmidt & Beutler (2017) within 2σ. We also find a tentative (S/N $\sim$ 3) detection at the wavelength where OIII]λ1666 was identified by Mainali et al. (2017) in our data (11837.1 Å).

7.8 Testing the selection function of our final sub-sample

As described in Section 7.4.2 we define a selection function based on the photometric redshift distributions to select a sub-sample of KLASS targets to use in the reionization inference. In this appendix we demonstrate the the sub-sample was not a biased selection from the final parent catalogues.

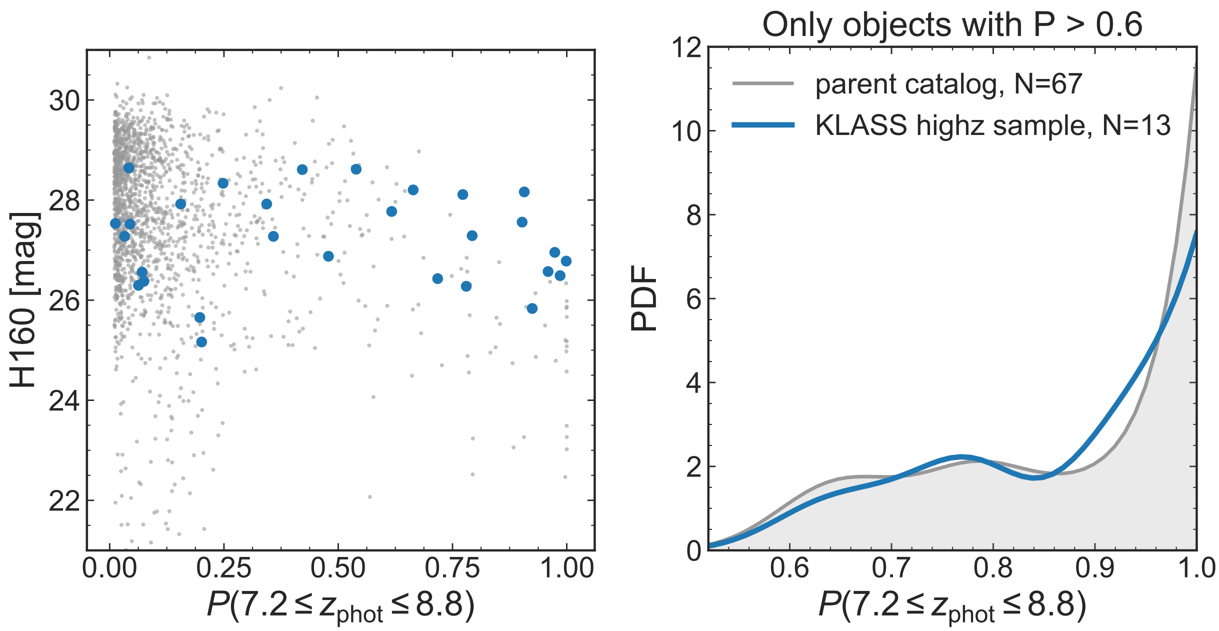

Figure 7.10: Left: Total probability (from the EAzY photometric redshift distributions) of objects being within our redshift range of interest ($P(7.2 \geq z_{\rm phot} \geq 8.8) > 0.01$) versus their F160W apparent magnitude. The KLASS sub-sample used for the inference is shown as large blue circles, objects from the full parent photometric catalogues are shown as small grey dots. Our sample is skewed towards higher probability of $7.2 \geq z_{\rm phot} \geq 8.8$ compared to the parent sample, with a smaller range in F160W magnitude. **Right**: Probability distribution functions of $P(7.2 \geq z_{\rm phot} \geq 8.8)$ values of all objects with $P(7.2 \geq z_{\rm phot} \geq 8.8) > 0.6$ from our KLASS sub-sample (blue) and the parent catalogues (grey). The distributions are plotted using a Gaussian kernel density estimator (Rosenblatt, 1956; Parzen, 1962). The two distributions are very similar, demonstrating our KLASS sub-sample is drawn randomly from the parent catalogue sample, and thus is not a biased sample in terms of photometric redshift distribution, despite being constructed after the observations were taken.

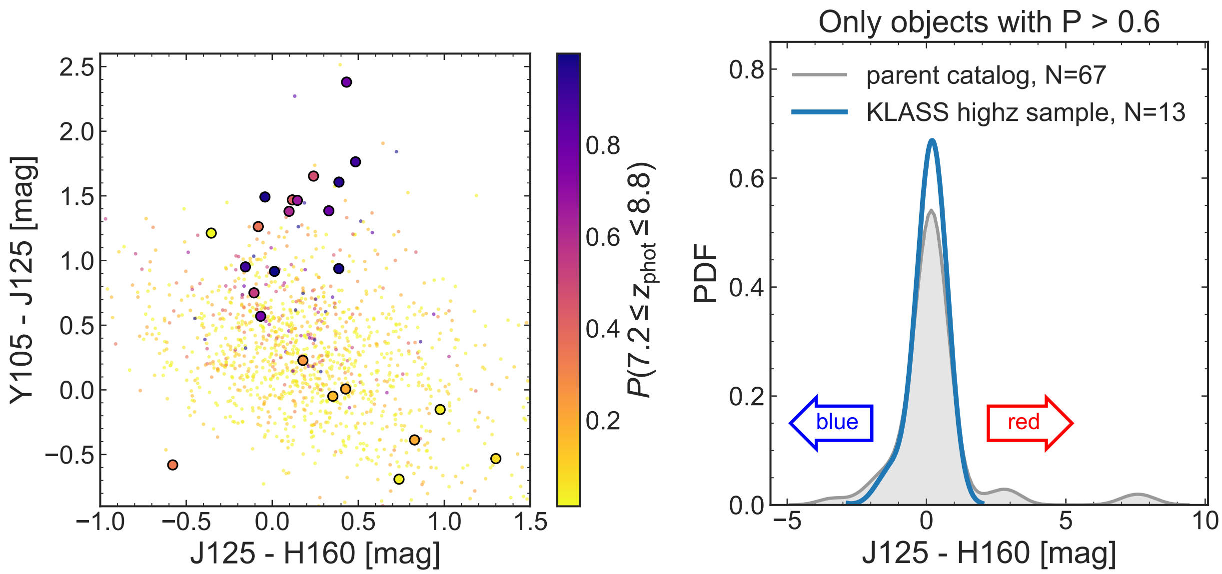

Figure 7.11: Left: F125W - F160W colour versus F105W - F125W colour for our KLASS inference sub-sample (large circles with black edges) and the parent catalogues (small points). The markers are colour-coded by their $P(7.2 \geq z_{\mathrm{phot}} \geq 8.8)$ so that the darkest points are the most likely to be within that redshift range. The most probable objects in the KLASS sub-sample appear to be in the same region of colour-colour space as the full parent catalogue. **Right**: Probability distribution functions of F125W - F160W colour values of all objects with $P(7.2 \geq z_{\mathrm{phot}} \geq 8.8) > 0.6$ from our KLASS sub-sample (blue) and the parent catalogues (grey). The distributions are plotted using a Gaussian kernel density estimator (Rosenblatt, 1956; Parzen, 1962). As in Figure 7.10 the two distributions are very similar, demonstrating our KLASS sub-sample is not a strongly biased sample in terms of colour, despite being constructed after the observations were taken. There are a few redder (F125W $-$ F160W > 0) objects in the full parent catalogue but these make up only a small fraction of the total ($< 10\%$) so given our small KLASS sample missing one of these objects is expected.

Objects in the sub-sample must have a match in our final deep photometric catalogues: for A2744, M0416 and M1149 we used the ASTRODEEP catalogues (Castellano et al., 2016; Merlin et al., 2016; Di Criscienzo et al., 2017). For M2129, RXJ1347 and RXJ2248 we created our own catalogues based on the ASTRODEEP methodology. And the objects must have $P(7.2 \geq z_{\rm phot} \geq 8.8) > 0.01$ based on photometric redshift probability distributions calculated using EAzY (Brammer et al., 2008). We use the full photometric redshift distribution in our inference to robustly weight objects based on their probability of being in our redshift range of interest (Section 7.4.1 and Appendix 7.9).

However, given that we construct this sub-sample *after* the observations were taken, we must check that the objects we observed were not a biased sample from the final catalogues. There are many more objects in the final catalogues which were not observed in KMOS so it could be that the KLASS targets are a biased sample of the final catalogue.

In Figure 7.10 we show the distribution of $P(7.2 \geq z_{\rm phot} \geq 8.8)$ values of our KLASS sub-sample and the parent catalogues. The parent catalogues have many more objects with low $P(7.2 \geq z_{\rm phot} \geq 8.8)$, showing that our sub-sample is skewed towards objects which are most likely to be within that redshift range, demonstrating that our initial $z_{\rm phot} > 7.2$ target selection was good. In the right panel we show the probability distribution of objects in the parent catalogues and our sub-sample, using only objects with $P(7.2 \geq z_{\rm phot} \geq 8.8) > 0.6$. As noted previously, we do not expect all the LBGs to have $P(7.2 \geq z_{\rm phot} \geq 8.8) = 1$ as there are often degeneracies in the photometry that make $z_{\rm phot} \sim 1 - 2$ solutions possible. Here we see that the distributions are consistent and demonstrate that the best targets in KLASS sub-sample (which weight most in the reionization inference) are drawn randomly from the best targets in the parent catalogues.

We also want to be sure our sub-sample is drawn randomly from the parent sample in terms of photometry. In particular, if we had selected only the reddest objects for our KMOS targets (based on F125W − F160W colours), our sub-sample could be biased towards dustier galaxies. As dust can significantly attenuate Lyα emission (Hayes et al., 2011) this would mean our non-detections of Lyα could be due to stronger dust attenuation as well as reionization. However, we demonstrate in Figure 7.11 that the F125W − F160Wcolour distribution our sub-sample is consistent with that of the final parent catalogues. The parent catalogues contain a small fraction ($< 10\%$) of redder objects that are not present in our KLASS sub-sample, but given the small number of objects in our sub-sample missing this small fraction of redder objects is expected.

7.9 Reionization Inference

This appendix derives the posterior distribution for the IGM neutral fraction, $\overline{x}_{\rm HI}$, extending the framework of M18 from single EW measurements to an input EW spectrum as a function of wavelength, and galaxy UV apparent magnitude and gravitational lensing magnification.

7.9.1 Likelihood at one spectral pixel

For simplicity, we assume lines are spectrally unresolved, so that an emission line produces flux at one spectral pixel d (at wavelength $\lambda_d = \lambda_\alpha(1 + z_d)$). Thus the rest-frame Lyα equivalent width at spectral pixel i is:

$$W_i = \begin{cases} 0 & \text{if } i \neq d \\ W & \text{if } i = d \end{cases} \tag{7.8}$$

Including Gaussian errors in the spectra (with error σ_i at spectral pixel i), the probability of measuring equivalent width W_i at spectral pixel i is given by a Gaussian distribution at each spectral pixel, with mean given by the 'true' value of W_i from Equation 7.8 and standard deviation σ_i:

$$p(W_i \,|\, W) = \begin{cases} \frac{1}{\sqrt{2\pi\sigma_i^2}} \exp\left(-\frac{W_i^2}{2\sigma_i^2}\right) & \text{if } i \neq d \\ \frac{1}{\sqrt{2\pi\sigma_i^2}} \exp\left(-\frac{(W_i - W)^2}{2\sigma_i^2}\right) & \text{if } i = d \end{cases} \tag{7.9}$$

Here we are assuming that the emission line is present at one wavelength pixel, and the spectrum is pure noise at every other pixel.

The likelihood of measuring Lyα EW W_i at wavelength λ_i given that the photons originate at z_d from a galaxy with apparent magnitude m and travel through an IGM with neutral fraction $\overline{x}_{\text{HI}}$ is

$$\begin{aligned} p(W_i \,|\, \overline{x}_{\text{HI}}, m, \mu, z_d) &= \int_0^\infty dW\, p(W_i \,|\, W)\, p(W \,|\, \overline{x}_{\text{HI}}, m, \mu, z_d) \\ &= \int_0^\infty dW\, p(W_i \,|\, W) \int_{-\infty}^{\infty} dM_{\text{UV}}\, p(W \,|\, \overline{x}_{\text{HI}}, M_{\text{UV}}) p(M_{\text{UV}} \,|\, m, \mu, z_d) \end{aligned} \tag{7.10}$$

where the second integral convolves the simulated $p(W \,|\, \overline{x}_{\text{HI}}, M_{\text{UV}})$ from M18 with the probability distribution of the absolute UV magnitude, M_{UV}, given our observed data:

$$p(M_{\text{UV}} \,|\, m, \mu, z_d) = \frac{1}{\sqrt{2\pi\sigma_M^2}} \exp\left[-\frac{(M_{\text{UV}} - M_{\text{UV,mod}}(\mu, z_d))^2}{2\sigma_M^2}\right] \tag{7.11}$$

where $M_{\text{UV,mod}}(\mu, z_d) = m - 5\log_{10}(D_L/10\,\text{pc}) + 2.5\log_{10}(1+z_d) + 2.5\log_{10}\mu$ converts observed magnitudes to rest-frame UV magnitudes, assuming the UV spectral slope $\beta = -2$ to calculate the K-correction (e.g., Blanton & Roweis, 2007). We assume the magnification distribution is log-normally distributed such that we can easily add the uncertainties in magnification and apparent magnitude: $\sigma_M^2 = \sigma_m^2 + (2.5\sigma_{\log\mu})^2$, where σ_m is the error on the observed apparent magnitude and $\sigma_{\log\mu}$ is the uncertainty in the logarithmic magnifications.

We note that the dependence on M_{UV} in $p(W \,|\, \overline{x}_{\text{HI}}, M_{\text{UV}})$ is weak compared to the dependence on $\overline{x}_{\text{HI}}$, and was parametrised with a smooth transition between two EW distributions for $M_{\text{UV}} > -20$ and $M_{\text{UV}} < -21$. Thus only the parameters which dominate changes in M_{UV} are important. We note that the distance modulus term changes the magnitude in our redshift range of interest, $z = 7.2 - 8.8$ ($\Delta M_{\text{UV}} \sim 0.5$) less than magnification ($\Delta M_{\text{UV}} \sim 0.75$ for $\mu = 2$), so for ease of computation we compute $p(W \,|\, \overline{x}_{\text{HI}}, m, \mu, z_d)$ ahead of time for each galaxy, setting $z_d = 8$, rather than having to redo this integral at every spectral pixel.

7.9.2 Likelihood for a full spectrum

For a full spectrum $\{W\} = W(\lambda_i)$ the likelihood is just the product of the likelihood at each wavelength pixel:

$$p(\{W\} \,|\, \overline{x}_{\text{HI}}, m, \mu, z_d) = \prod_{i \neq d} \frac{1}{\sqrt{2\pi}\sigma_i} e^{-\frac{W_i^2}{2\sigma_i^2}} \times \left[\int_0^\infty dW\, \frac{1}{\sqrt{2\pi}\sigma_d} e^{-\frac{1}{2}\left(\frac{W_d - W}{\sigma_d}\right)^2} p\left(W \,|\, \overline{x}_{\text{HI}}, m, \mu, z_d\right)\right] \tag{7.12}$$

where d is the index of the emission line, and $z_d = \lambda_d/\lambda_\alpha - 1$.

7.9.3 Likelihood for equivalent width upper limits

Often, one may provide only upper limits on the Lyα EW ($\{W\} < \{W_{\text{lim}}\}$). In these cases, the likelihood is obtained by integrating Equation 7.10 up to the upper limit in each pixel:

$$\begin{aligned} & p(\{W\} < \{W_{\text{lim}}\} \,|\, \overline{x}_{\text{HI}}, m, \mu, z_d) \\ &= \left[\int_{-\infty}^{W_{\text{lim},d}} dW_d \int_0^\infty dW \, \frac{1}{\sqrt{2\pi}\sigma_d} e^{-\frac{1}{2}\left(\frac{W_d - W}{\sigma_d}\right)^2} p(W \,|\, \overline{x}_{\text{HI}}, m, \mu, z_d) \right] \\ &\quad \times \prod_{i \neq d} \int_{-\infty}^{W_{\text{lim},i}} dW_i \, \frac{1}{\sqrt{2\pi}\sigma_i} e^{-\frac{W_i^2}{2\sigma_i^2}} \\ &= \left[\int_0^\infty dW \, \frac{1}{2} \operatorname{erfc}\left(\frac{W - W_{\text{lim},d}}{\sqrt{2}\sigma_d} \right) p(W \,|\, \overline{x}_{\text{HI}}, m, \mu, z_d) \right] \\ &\quad \times \prod_{i \neq d} \frac{1}{2} \operatorname{erfc}\left(-\frac{W_{\text{lim},i}}{\sqrt{2}\sigma_i} \right) \end{aligned} \tag{7.13}$$

where $\operatorname{erfc}(x)$ is the complementary error function:

$$\begin{aligned} \operatorname{erfc}(x) &= 1 - \operatorname{erf}(x) \\ &= \frac{2}{\pi} \int_x^\infty e^{-t^2} \, dt \end{aligned} \tag{7.14}$$

7.9.4 Posteriors

Using Bayes' Theorem the posterior distribution for $\overline{x}_{\text{HI}}$ and z_d is

$$p(\overline{x}_{\text{HI}}, z_d \,|\, \{W\}, m, \mu) = p(\{W\} \,|\, \overline{x}_{\text{HI}}, m, \mu, z_d) \times p(z_d) p(\overline{x}_{\text{HI}}) \tag{7.15}$$

We use a uniform prior on $\overline{x}_{\text{HI}}$ between 0 and 1, and use the photometric redshift for the prior $p(z)$. As we are only interested in the posterior probability of $\overline{x}_{\text{HI}}$ we can marginalise over z_d:

$$\begin{aligned} p(\overline{x}_{\text{HI}} \,|\, \{W\}, m, \mu) &= \int dz_d \, p(\overline{x}_{\text{HI}}, z_d \,|\, \{W\}, m, \mu) \\ &\propto \int dz_d \, p(\{W\} \,|\, \overline{x}_{\text{HI}}, m, \mu, z_d) p(z_d) p(\overline{x}_{\text{HI}}) \end{aligned} \tag{7.16}$$

To account for the incomplete wavelength coverage, we make use of the fact if the object has Lyα outside of the wavelength range (covering $[z_{\text{min}}, z_{\text{max}}]$) we would measure a non-detection in our data:

$$\begin{aligned} p(\overline{x}_{\text{HI}}\,|\,\{W\}, m, \mu) \propto &\int_{z_{\min}}^{z_{\max}} dz_d\; p(\{W\}|\overline{x}_{\text{HI}}, m, \mu, z_d) p(z_d) \\ &+ \prod_i p(\{W\}=0)\left(1 - \int_{z_{\min}}^{z_{\max}} dz_d\; p(z_d)\right) \end{aligned} \tag{7.17}$$

We assume all galaxies observed are independent, so that the final posterior is the product of the normalised posteriors (Equation 7.17) for each object.

CHAPTER 8

Conclusions

The evolution of galaxies and the reionization of intergalactic hydrogen within the universe's first billion years are intimately linked, thus understanding one of these processes requires us to understand the other. In my thesis I have used observations of galaxies at our current frontiers ($z \sim 6 - 8$) to ask what we can learn about the reionization process, and the evolution of early galaxies.

I have developed a method to remove the magnification bias in high redshift luminosity functions (Chapter 3) and shown that LF evolution can be easily modeled using the evolution of the underlying dark matter halo mass function (Chapter 2). Using the LF evolution model in combination with large scale reionization simulations and ISM models I developed statistical inference frameworks to measure the timeline of reionization from observations of Lyα emission from galaxies (Chapters 4, 5 and 7). This hybrid modeling is important for treating the multi-scale radiative transfer of Lyα through to our telescopes.

The key results, and the remaining questions, I see from this thesis are:

- The observed evolution of the luminosity function of galaxies, and the luminosity/star formation rate density can be simply modeled by assuming star formation rates are proportional to halo mass accretion rates, moderated by a mass-dependent, but redshift-independent efficiency. Does this hold at higher redshifts?

- Wide-area high-redshift luminosity functions will be dominated by gravitational lensing magnification bias. The predicted upturn from lensing was clearly observed recently by Ono et al. (2017), though magnification bias likely cannot account for all of the observed boost. How does the bright end of the luminosity function evolve at the highest redshifts? What does that tell us about feedback in high mass galaxies?

- The transmission of Lyα photons through the IGM depends on their emitted properties, which are probably correlated with their source galaxy's properties. We showed that a relation between galaxy halo mass and the emitted Lyα velocity offset from systemic accelerates the extinction of Lyα emission from low mass, UV faint galaxies, and slows the decline of Lyα emission in UV bright galaxies in massive halos. Lyα emission from UV bright galaxies may then be visible even in a highly neutral IGM. But how can we best model the emitted Lyα line properties? How reasonable is it to extrapolate emitted properties from $z \sim 6$ to higher redshifts?

- Observations of Lyα emission from Lyman Break galaxies favor late reionization (predominantly neutral IGM by $z \sim 8$). This is consistent with independent measurements from quasar spectra, and models of reionization driven by ultra-faint galaxies ($M_{\rm UV} < -12$) with a low average ionizing photon escape fraction ($\lesssim 15\%$). How robust are these estimates and what are the implications for galaxy evolution at $z \gtrsim 8$?

Within the past year, our work and new observations and analyses of Lyα damping wings in $z > 7$ quasar spectra (Greig et al., 2017; Bañados et al., 2017), have provided evidence favoring late reionization (with a half reionized universe at $z \sim 7$). However, all of these analyses are model-dependent and to make more precise measurements of the neutral fraction will require careful assessment of the models.

In particular, modeling Lyα emission *before* it reaches the IGM is important. Are there physical processes which cause emitted Lyα to rapidly decrease with redshift around $z \sim 7$ which could mimic a decline due to reionization (Bolton & Haehnelt, 2013; Dijkstra et al., 2014)? Multiple observations have shown Lyα emission properties depend on galaxy properties, such as dust attenuation, UV luminosity, star formation rate, spatial extent etc., but how do these properties relate to each other? Holistic models of Lyα emission, in particular, the distributions of Lyα EW and velocity offset as a function of galaxy properties and redshift are needed to make more realistic models of the emitted Lyα properties to compare with observations. At the same time, we must assess the reionization simulations we use for the inferences – how do different implementations of reionization impact our expected observations? Performing the inference with a range of reionization simulations will be important in understanding the robustness of our results.

Of course, all of our current inferences about reionization using Lyα emission rely on photometric redshifts. *JWST* will quickly establish the true population of high redshift galaxies by spectroscopically confirming them via other emission lines which are not affected by reionization, e.g. [O II] λ3727. We will soon know how many of these galaxies are really at high redshift.

Is star formation different at high redshift? It is somewhat remarkable that observations of the evolving luminosity function with redshift seem so consistent with simply tracing the accretion of dark matter onto halos, with a redshift-independent, but mass-dependent, efficiency. The feedback processes which are expected to govern star formation efficiency: supernova feedback, photoionization heating and AGN feedback all have some timescale for becoming important. How far back in time must we go before these feedback processes stop slowing star formation? If reionization does occur relatively late, this may indicate that the bulk of 'normal' galaxy formation happened at $z \lesssim 8$: at higher redshifts star formation may proceed differently. Upcoming observations with *JWST* (e.g., Treu et al., 2017) could provide answers to some of these questions. In particular, we will be able to measure the LF at $z > 8$ and compare to our predictions from the model in Chapter 2.

We are now at an observational frontier. The Hubble Space Telescope (HST) can observe galaxies in reionizations late stages, $\lesssim$ Myr after the Big Bang ($z \sim 6 - 10$). The James Webb Space Telescope (JWST) will expand our horizon to Cosmic Dawn ($z > 10$). There will be a radical shift from mostly counting photometrically-selected galaxy candidates to detailed spectral studies. Within a similar timeframe, the first generation of 21 cm intensity mapping experiments sensitive enough to detect the signals of reionization (e.g. HERA) will come online, providing the first maps of the reionizing IGM. We must be prepared to ask fundamental questions about what our new observations tell us about the early universe.

Bibliography

Aghanim, N., Arnaud, M., Ashdown, M., et al. 2012, A&A, 543, A102

Alavi, A., Siana, B., Richard, J., et al. 2014, ApJ, 780, 143

Alvarez, M. A., Finlator, K., & Trenti, M. 2012, ApJL, 759, L38

Arnouts, S., Schiminovich, D., Ilbert, O., et al. 2005, ApJ, 619, L43

Atek, H., Richard, J., Jauzac, M., et al. 2015a, ApJ, 814, 69

Atek, H., Richard, J., Kneib, J.-P., et al. 2015b, ApJ, 800, 18

Auger, M. W., Treu, T., Bolton, A. S., et al. 2010, ApJ, 724, 511

Bacon, R., Brinchmann, J., Richard, J., et al. 2014a, A&A, 575, A75

—. 2014b, A&A, 575, A75

Balestra, I., Vanzella, E., Rosati, P., et al. 2013, A&A, 559, L9

Balestra, I., Mercurio, A., Sartoris, B., et al. 2016, ApJS, 224, 33

Baltz, E. A., Marshall, P., & Oguri, M. 2009, J. Cosmol. Astropart. Phys., 2009, 015

Bañados, E., Venemans, B. P., Mazzucchelli, C., et al. 2017, Nature, doi:10.1038/nature25180

Barkana, R., & Loeb, A. 1999, ApJ, 523, 54

Barkana, R., & Loeb, A. 2004, ApJ, 601, 64

Barone-Nugent, R. L., Wyithe, J. S. B., Trenti, M., et al. 2015, MNRAS, 450, 1224

Barone-Nugent, R. L., Trenti, M., Wyithe, J. S. B., et al. 2014, ApJ, 793, 17

Barone-Nugent, R. L., Sonnenfeld, A., Wyithe, J. S. B., et al. 2015, MNRAS, 453, 3068

Becker, G. D., Bolton, J. S., Madau, P., et al. 2015, MNRAS, 447, 3402

Becker, G. D., Davies, F. B., Furlanetto, S. R., et al. 2018, ArXiv e-prints, arXiv:1803.08932

Behroozi, P. S., Marchesini, D., Wechsler, R. H., et al. 2013a, ApJ, 777, L10

Behroozi, P. S., & Silk, J. 2015, ApJ, 799, 32

Behroozi, P. S., & Silk, J. 2015, ApJ, 799, 32

Behroozi, P. S., Wechsler, R. H., & Conroy, C. 2013b, ApJ, 762, L31

—. 2013c, ApJ, 770, 57

Belli, S., Newman, A. B., & Ellis, R. S. 2014a, ApJ, 783, 117

Belli, S., Newman, A. B., Ellis, R. S., & Konidaris, N. P. 2014b, ApJ, 788, L29

Benítez, N., Ford, H., Bouwens, R., et al. 2004, ApJS, 150, 1

Bershady, M. A., Verheijen, M. A. W., Swaters, R. A., et al. 2010, ApJ, 716, 198

Bezanson, R., Franx, M., & van Dokkum, P. G. 2015, ApJ, 799, 148

Bezanson, R., van Dokkum, P., & Franx, M. 2012, ApJ, 760, 62

Bezanson, R., van Dokkum, P. G., van de Sande, J., et al. 2013, ApJ, 779, L21

Bezanson, R., van Dokkum, P. G., Franx, M., et al. 2011, ApJ, 737, L31

Blaizot, J., Wadadekar, Y., Guiderdoni, B., et al. 2005, MNRAS, 360, 159

Blandford, R. D., & Narayan, R. 1992, ARAA, 30, 311

Blanton, M. R., & Roweis, S. 2007, Astron. J., 133, 734

Bolton, J. S., & Haehnelt, M. G. 2013, MNRAS, 429, 1695

Bond, J. R., Cole, S., Efstathiou, G., & Kaiser, N. 1991, ApJ, 379, 440

Boone, F., Clément, B., Richard, J., et al. 2013, A&A, 559, L1

Bouché, N., Carfantan, H., Schroetter, I., Michel-Dansac, L., & Contini, T. 2015, Astron. J., 150, 92

Bouwens, R. J., Illingworth, G. D., Franx, M., & Ford, H. 2007, ApJ, 670, 928

Bouwens, R. J., Illingworth, G. D., Oesch, P. A., et al. 2017a, ApJ, 843, 41

—. 2015a, ApJ, 811, 140

Bouwens, R. J., Oesch, P. A., Illingworth, G. D., Ellis, R. S., & Stefanon, M. 2017b, ApJ, 843, 129

Bouwens, R. J., Smit, R., Labbé, I., et al. 2016a, ApJ, 831, 176

Bouwens, R. J., Illingworth, G. D., Rosati, P., et al. 2003, ApJ, 595, 589

Bouwens, R. J., Illingworth, G. D., Oesch, P. A., et al. 2011, ApJ, 737, 90

Bouwens, R. J., Illingworth, G. D., Oesch, P., et al. 2012, ApJ, 754, 83

Bouwens, R. J., Illingworth, G. D., Oesch, P. A., et al. 2014, ApJ, 793, 115

Bouwens, R. J., Illingworth, G. D., Oesch, P. A., et al. 2014, ApJ, 793, 115

—. 2015b, ApJ, 803, 34

Bouwens, R. J., Aravena, M., Decarli, R., et al. 2016b, ApJ, 833, 72

Bowler, R. A. A., Dunlop, J. S., McLure, R. J., et al. 2014, MNRAS, 440, 2810

—. 2015, MNRAS, 452, 1817

Bradač, M., Treu, T., Applegate, D., et al. 2009, ApJ, 706, 1201

Bradač, M., Vanzella, E., Hall, N., et al. 2012, ApJ, 755, L7

Bradač, M., Garcia-Appadoo, D., Huang, K.-H., et al. 2017, ApJ, 836, L2

Bradač, M., Garcia-Appadoo, D., Huang, K.-H., et al. 2017, ApJ, 836, L2

Bradley, L., Trenti, M., Oesch, P. A., et al. 2012, ApJ, 760, 108

Bradley, L. D., Zitrin, A., Coe, D., et al. 2014, ApJ, 792, 76

Brammer, G. B., van Dokkum, P. G., & Coppi, P. 2008, ApJ, 686, 1503

Bromm, V., Yoshida, N., Hernquist, L., & McKee, C. F. 2009, Nature, 459, 49

Bruzual, G., & Charlot, S. 2003, MNRAS, 344, 1000

Bundy, K., Ellis, R. S., & Conselice, C. 2005, ApJ, 625, 621

Bundy, K., Treu, T., & Ellis, R. S. 2007, ApJ, 665, L5

Bunker, A. J., Stanway, E. R., Ellis, R. S., & McMahon, R. G. 2004, MNRAS, 355, 374

Burgarella, D., Pérez-González, P. G., Tyler, K. D., et al. 2006, A&A, 450, 69

Cai, Z.-Y., Lapi, A., Bressan, A., et al. 2014, ApJ, 785, 65

Calvi, V., Trenti, M., Stiavelli, M., et al. 2016, ApJ, 817, 120

Calzetti, D., Armus, L., Bohlin, R. C., et al. 2000, ApJ, 533, 682

Caminha, G. B., Karman, W., Rosati, P., et al. 2016, A&A, 595, A100

Caminha, G. B., Grillo, C., Rosati, P., et al. 2017, A&A, 600, A90

Capak, P. L., Carilli, C., Jones, G., et al. 2015, Nature, 522, 455

Cappellari, M., Bacon, R., Bureau, M., et al. 2006, MNRAS, 366, 1126

Cardelli, J. A., Clayton, G. C., & Mathis, J. S. 1989, ApJ, 345, 245

Carniani, S., Maiolino, R., Pallottini, A., et al. 2017, A&A, 605, A42

Caruana, J., Bunker, A. J., Wilkins, S. M., et al. 2012, MNRAS, 427, 3055

—. 2014, MNRAS, 443, 2831

Cassata, P., Tasca, L. A. M., Le Fèvre, O., et al. 2015, A&A, 573, A24

Castellano, M., Yue (), B., Ferrara, A., et al. 2016, ApJ, 823, L40

Castellano, M., Amorín, R., Merlin, E., et al. 2016, A&A, 590, A31

Chabrier, G. 2003, PASP, 115, 763

Chae, K. H. 2010, MNRAS, 402, 2031

Charlot, S., & Fall, S. M. 2000, ApJ, 539, 718

Choi, Y.-Y., Park, C., & Vogeley, M. S. 2007, ApJ, 658, 884

Chonis, T. S., Blanc, G. A., Hill, G. J., et al. 2013, ApJ, 775, 99

Choudhury, T. R., Puchwein, E., Haehnelt, M. G., & Bolton, J. S. 2015, MNRAS, 452, 261

Christensen, L., Laursen, P., Richard, J., et al. 2012, MNRAS, 427, 1973

Coe, D., Benítez, N., Sánchez, S. F., et al. 2006, Astron. J., 132, 926

Coe, D., Bradley, L., & Zitrin, A. 2015, ApJ, 800, 84

Cole, S., Lacey, C. G., Baugh, C. M., & Frenk, C. S. 2000, MNRAS, 319, 168

Coles, P., & Jones, B. 1991, MNRAS(ISSN 0035-8711), 248, 1

Collett, T. E., Marshall, P. J., Auger, M. W., et al. 2013, MNRAS, 432, 679

Conselice, C. J. 2014, ARAA, 52, 291

Conselice, C. J., Bundy, K., Ellis, R. S., et al. 2005, ApJ, 628, 160

Contini, T., Epinat, B., Bouché, N., et al. 2016, A&A, 591, A49

Cooray, A., & Milosavljevic, M. 2005, ApJ, 627, 4

Courteau, S. 1997, Astron. J., 114, 2402

Cullen, F., Cirasuolo, M., Kewley, L. J., et al. 2016, MNRAS, 460, 3002

Curtis-Lake, E., McLure, R. J., Pearce, H. J., et al. 2012, MNRAS, 422, 1425

Davies, F. B., & Furlanetto, S. R. 2016, MNRAS, 460, 1328

Davies, R. I. 2007, MNRAS, 375, 1099

Davies, R. I., Agudo Berbel, A., Wiezorrek, E., et al. 2013, A&A, 558, A56

Dayal, P., Ferrara, A., Dunlop, J. S., & Pacucci, F. 2014, MNRAS, 445, 2545

Dayal, P., Maselli, A., & Ferrara, A. 2011, MNRAS, 410, 830

de Barros, S., Schaerer, D., & Stark, D. P. 2014, A&A, 563, A81

De Barros, S., Pentericci, L., Vanzella, E., et al. 2017, A&A, 608, A123

De Burgh-Day, C. O., Taylor, E. N., Webster, R. L., & Hopkins, A. M. 2015, MNRAS, 451, 2161

Decarli, R., Walter, F., Venemans, B. P., et al. 2017, Nature, 545, 457

Di Criscienzo, M., Merlin, E., Castellano, M., et al. 2017, A&A, 607, A30

Di Teodoro, E. M., Fraternali, F., & Miller, S. H. 2016, A&A, 594, A77

Dijkstra, M. 2014, PASA, 31, e040

Dijkstra, M., Haiman, Z., & Spaans, M. 2006, ApJ, 649, 37

Dijkstra, M., Lidz, A., & Wyithe, J. S. B. 2007, MNRAS, 377, 1175

Dijkstra, M., Mesinger, A., & Wyithe, J. S. B. 2011, MNRAS, 414, 2139

Dijkstra, M., & Wyithe, J. S. B. 2012, MNRAS, 419, 3181

Dijkstra, M., Wyithe, S., Haiman, Z., Mesinger, A., & Pentericci, L. 2014, MNRAS, 440, 3309

Dunlop, J. S., McLure, R. J., Robertson, B. E., et al. 2012, MNRAS, 420, 901

Dunlop, J. S., Rogers, A. B., McLure, R. J., et al. 2013, MNRAS, 432, 3520

Ellis, R., Santos, M. R., Kneib, J.-P., & Kuijken, K. 2001, ApJ, 560, L119

Epinat, B., Amram, P., Balkowski, C., & Marcelin, M. 2010, MNRAS, 401, 2113

Epinat, B., Amram, P., & Marcelin, M. 2008a, MNRAS, 390, 466

Epinat, B., Amram, P., Marcelin, M., et al. 2008b, MNRAS, 388, 500

Epinat, B., Contini, T., Fevre, O. L., et al. 2009, A&A, 546, A118

Erb, D. K. 2015, Nature, 523, 169

Erb, D. K., Steidel, C. C., Shapley, A. E., et al. 2006, ApJ, 646, 107

Erb, D. K., Steidel, C. C., Trainor, R. F., et al. 2014, ApJ, 795, 33

Faber, S. M., & Jackson, R. E. 1976, ApJ, 204, 668

Faisst, A. L., Capak, P., Carollo, C. M., Scarlata, C., & Scoville, N. 2014, ApJ, 788, 87

Fan, X., Narayanan, V. K., Lupton, R. H., et al. 2001, Astron. J., 122, 2833

Fan, X., Strauss, M. A., Becker, R. H., et al. 2006, Astron. J., 132, 117

Fassnacht, C. D., Moustakas, L. A., Casertano, S., et al. 2004, ApJ, 600, L155

Fialkov, A., & Loeb, A. 2015, ApJ, 806, 256

Finkelstein, S. L., Papovich, C., Ryan, R. E., et al. 2012a, ApJ, 758, 93

Finkelstein, S. L., Papovich, C., Salmon, B., et al. 2012b, ApJ, 756, 164

Finkelstein, S. L., Papovich, C., Dickinson, M., et al. 2013, Nature, 502, 524

Finkelstein, S. L., Song, M., Behroozi, P., et al. 2015a, ApJ, 814, 95

Finkelstein, S. L., Ryan, R. E., Papovich, C., et al. 2015b, ApJ, 810, 71

Finlator, K., Oppenheimer, B. D., & Davé, R. 2011, MNRAS, 410, 1703

Flores, H., Hammer, F., Puech, M., Amram, P., & Balkowski, C. 2006, A&A, 455, 107

Flower, D. R., Nussbaumer, H., & Schild, H. 1979, A&A, 72, L1

Fontana, A., Vanzella, E., Pentericci, L., et al. 2010, ApJ, 725, L205

Foreman-Mackey, D., Hogg, D. W., Lang, D., & Goodman, J. 2013, PASP, 125, 306

Forster Schreiber, N. M., Genzel, R., Lehnert, M. D., et al. 2006, ApJ, 645, 1062

Förster Schreiber, N. M., Genzel, R., Bouché, N., et al. 2009, ApJ, 706, 1364

Franx, M., Illingworth, G. D., Kelson, D. D., van Dokkum, P. G., & Tran, K.-V. 1997, ApJ, 486, L75

Furlanetto, S. R., & Oh, S. P. 2005, MNRAS, 363, 1031

Furlanetto, S. R., Zaldarriaga, M., & Hernquist, L. 2006, MNRAS, 365, 1012

Furlong, M., Bower, R. G., Theuns, T., et al. 2015, MNRAS, 450, 4486

Gardner, J. P., Mather, J. C., Clampin, M., et al. 2006, Space Sci. Rev., 123, 485

Gene, S., Vogelsberger, M., Springel, V., et al. 2014, MNRAS, 445, 175

Genzel, R., Newman, S., Jones, T., et al. 2011, ApJ, 733, 101

Genzel, R., Schreiber, N. M. F., Übler, H., et al. 2017, Nature, 543, 397

Giallongo, E., Grazian, A., Fiore, F., et al. 2015, A&A, 578, A83

Giocoli, C., Moreno, J., Sheth, R. K., & Tormen, G. 2007, MNRAS, 376, 977

Glazebrook, K. 2013, PASA, 30, e056

Gnerucci, A., Marconi, A., Cresci, G., et al. 2011, A&A, 528, A88

González, V., Labbé, I., Bouwens, R. J., et al. 2011, ApJ, 735, L34

Grazian, A., Castellano, M., Fontana, A., et al. 2012, A&A, 547, A51

Grazian, A., Fontana, A., Santini, P., et al. 2015, A&A, 575, A96

Grazian, A., Giallongo, E., Paris, D., et al. 2017, A&A, 602, A18

Green, A. W., Glazebrook, K., McGregor, P. J., et al. 2013, MNRAS, 437, 1070

Greene, Z. S., Suyu, S. H., Treu, T., et al. 2013, ApJ, 768, 39

Greig, B., & Mesinger, A. 2015, MNRAS, 449, 4246

Greig, B., & Mesinger, A. 2017a, MNRAS, 472, 2651

—. 2017b, MNRAS, 465, 4838

Greig, B., Mesinger, A., Haiman, Z., & Simcoe, R. A. 2017, MNRAS, 466, 4239

Grillo, C., Suyu, S. H., Rosati, P., et al. 2015, ApJ, 800, 38

Grillo, C., Karman, W., Suyu, S. H., et al. 2016, ApJ, 822, 78

Grogin, N. A., Kocevski, D. D., Faber, S. M., et al. 2011, ApJS, 197, 35

Gronke, M., Bull, P., & Dijkstra, M. 2015a, ApJ, 812, 123

Gronke, M., & Dijkstra, M. 2016, ApJ, 826, 14

Gronke, M., Dijkstra, M., McCourt, M., & Peng Oh, S. 2016, ApJ, 833, L26

Gronke, M., Dijkstra, M., Trenti, M., & Wyithe, S. 2015b, MNRAS, 449, 1284

Guaita, L., Talia, M., Pentericci, L., et al. 2017, A&A, 606, A19

Gunn, J. E., & Peterson, B. A. 1965, ApJ, 142, 1633

Guo, Q., White, S., Boylan-Kolchin, M., et al. 2011, MNRAS, 413, 101

Haiman, Z. 2002, ApJL, 576, L1

Haiman, Z., & Spaans, M. 1999, ApJ, 518, 138

Hall, N., Bradač, M., Gonzalez, A. H., et al. 2012, ApJ, 745, 155

Harikane, Y., Ouchi, M., Ono, Y., et al. 2016, ApJ, 821, 123

—. 2017, PASJ, 00, 1

Hashimoto, T., Ouchi, M., Shimasaku, K., et al. 2013, ApJ, 765, 70

Hashimoto, T., Verhamme, A., Ouchi, M., et al. 2015, ApJ, 812, 157

Hashimoto, T., Laporte, N., Mawatari, K., et al. 2018, Nature, 557, 392

Hathi, N. P., Mobasher, B., Capak, P., Wang, W.-h., & Ferguson, H. C. 2012, ApJ, 757, 43

Hayes, M., Laporte, N., Pell??, R., Schaerer, D., & Le Borgne, J. F. 2012, MNRAS, 425, L19

Hayes, M., Schaerer, D., Östlin, G., et al. 2011, ApJ, 730, 8

Hayes, M., Östlin, G., Schaerer, D., et al. 2013, ApJ, 765, L27

Hayward, C. C., & Hopkins, P. F. 2017, MNRAS, 465, 1682

Henriques, B. M. B., White, S. D. M., Lemson, G., et al. 2012, MNRAS, 421, 2904

Henry, A., Berg, D., Scarlata, C., Verhamme, A., & Erb, D. 2018, ApJ, 855, 96

Henry, A., Scarlata, C., Martin, C. L., & Erb, D. 2015, ApJ, 809, 19

Herenz, E. C., Urrutia, T., Wisotzki, L., et al. 2017, A&A, 606, A12

Hilbert, S., Hartlap, J., White, S. D. M., & Schneider, P. 2009, A&A, 499, 31

Hilbert, S., White, S. D. M., Hartlap, J., & Schneider, P. 2007, MNRAS, 382, 121

Hinshaw, G., Larson, D., Komatsu, E., et al. 2012, ApJS, 192, 18

Hoag, A., Huang, K.-H., Treu, T., et al. 2016, ApJ, 831, 182

Hoag, A., Bradač, M., Trenti, M., et al. 2017, Nat. Astron., 1, 0091

Hopkins, A. M., & Beacom, J. F. 2006, ApJ, 651, 142

Huang, K.-H., Lemaux, B. C., Schmidt, K. B., et al. 2016a, ApJ, 823, L14

Huang, K.-H., Bradač, M., Lemaux, B. C., et al. 2016b, ApJ, 817, 11

Hunter, J. D. 2007, Comput. Sci. Eng., 9, 99

Ilbert, O., McCracken, H. J., Le Fèvre, O., et al. 2013, A&A, 556, A55

Iliev, I. T., Mellema, G., Ahn, K., et al. 2014, MNRAS, 439, 725

Illingworth, G. D., Magee, D., Oesch, P. A., et al. 2013, ApJS, 209, 6

Inoue, A. K., Tamura, Y., Matsuo, H., et al. 2016, Science, 352, 1559

Ishigaki, M., Kawamata, R., Ouchi, M., et al. 2015, ApJ, 799, 12

Jaacks, J., Nagamine, K., & Choi, J. H. 2012, MNRAS, 427, 403

Jaacks, J., Thompson, R., & Nagamine, K. 2013, ApJ, 766, 94

Jensen, H., Laursen, P., Mellema, G., et al. 2013, MNRAS, 428, 1366

Jones, T., Ellis, R. S., Richard, J., & Jullo, E. 2013a, ApJ, 765, 48

Jones, T., Stark, D. P., & Ellis, R. S. 2012, ApJ, 751, 51

Jones, T., Wang, X., Schmidt, K. B., et al. 2015, Astron. J., 149, 107

Jones, T. A., Ellis, R. S., Schenker, M. A., & Stark, D. P. 2013b, ApJ, 779, 52

Jones, T. A., Swinbank, A. M., Ellis, R. S., Richard, J., & Stark, D. P. 2010, MNRAS, 404, 1247

Juárez, Y., Maiolino, R., & Mújica, R. 2010, Rev. Mex. Astron. y Astrofis. Ser. Conf., 37, 163

Jung, I., Finkelstein, S. L., Livermore, R. C., et al. 2018, eprint arXiv:1803.01870

Kakiichi, K., & Dijkstra, M. 2017, ArXiv e-prints, arXiv:1710.10053

Karman, W., Caputi, K. I., Grillo, C., et al. 2015, A&A, 574, A11

Karman, W., Caputi, K. I., Caminha, G. B., et al. 2016, A&A, 599, 43

Kassin, S. A., Weiner, B. J., Faber, S. M., et al. 2007, ApJ, 660, L35

Keeton, C. R. 2001, ApJ, 562, 160

Keeton, C. R., Kuhlen, M., & Haiman, Z. 2005, ApJ, 621, 559

Kelly, B. C., Fan, X., & Vestergaard, M. 2008, ApJ, 682, 874

Kelly, P. L., Rodney, S. A., Treu, T., et al. 2015, Science, 347, 1123

Kennicutt, R. C. 1998, Annu. Rev. A&A, 36, 189

Kimm, T., Katz, H., Haehnelt, M., et al. 2017, MNRAS, 466, 4826

Kistler, M. D., Yüksel, H., Beacom, J. F., Hopkins, A. M., & Wyithe, J. S. B. 2009, ApJ, 705, L104

Kitzbichler, M. G., & White, S. D. M. 2007, MNRAS, 376, 2

Koekemoer, A. M., Faber, S. M., Ferguson, H. C., et al. 2011, ApJS, 197, 36

Konno, A., Ouchi, M., Shibuya, T., et al. 2017, PASJ, 00, 1

Kriek, M., van Dokkum, P. G., Labbé, I., et al. 2009, ApJ, 700, 221

Kriek, M., van Dokkum, P. G., Franx, M., et al. 2006, ApJL, 649, L71

Lacey, C., & Cole, S. 1993, MNRAS, 262, 627

Lacey, C. G., Baugh, C. M., Frenk, C. S., & Benson, A. J. 2011, MNRAS, 412, 1828

Laporte, N., Nakajima, K., Ellis, R. S., et al. 2017, ApJ, 851, 40

Laporte, N., Ellis, R. S., Boone, F., et al. 2017, ApJ, 837, L21

Laureijs, R., Amiaux, J., Arduini, S., et al. 2011, arXiv.org, 1110, 3193

Laursen, P., Sommer-Larsen, J., & Razoumov, A. O. 2011, ApJ, 728, 52

Law, D. R., Steidel, C. C., Erb, D. K., et al. 2007, ApJ, 669, 929

—. 2009, ApJ, 697, 2057

Leclercq, F., Bacon, R., Wisotzki, L., et al. 2017, A&A, 608, A8

Lee, B., Giavalisco, M., Williams, C. C., et al. 2013, ApJ, 774, 47

Lee, S.-K., Ferguson, H. C., Somerville, R. S., et al. 2014, ApJ, 783, 81

Leethochawalit, N., Jones, T. A., Ellis, R. S., et al. 2016a, ApJ, 820, 84

Leethochawalit, N., Jones, T. A., Ellis, R. S., Stark, D. P., & Zitrin, A. 2016b, ApJ, 831, 13

Lehnert, M. D., & Bremer, M. 2003, ApJ, 593, 630

Lidz, A., Zahn, O., Furlanetto, S. R., et al. 2009, ApJ, 690, 252

Liu, A., & Parsons, A. R. 2016, MNRAS, 457, 1864

Livermore, R. C., Finkelstein, S. L., & Lotz, J. M. 2017, ApJ, 835, 113

Livermore, R. C., Trenti, M., Bradley, L. D., et al. 2018, ArXiv e-prints, arXiv:1805.05038

Livermore, R. C., Jones, T. A., Richard, J., et al. 2015, MNRAS, 450, 1812

Lotz, J. M., Koekemoer, A., Coe, D., et al. 2017, ApJ, 837, 97

Ma, X., Kasen, D., Hopkins, P. F., et al. 2015, MNRAS, 453, 960

Madau, P., & Dickinson, M. 2014, Annu. Rev. A&A, 52, 415

Madau, P., Ferguson, H. C., Dickinson, M. E., et al. 1996, MNRAS, 283, 1388

Madau, P., & Haardt, F. 2015, ApJ, 813, L8

Madau, P., Haardt, F., & Rees, M. J. 1999, ApJ, 514, 648

Madau, P., Pozzetti, L., & Dickinson, M. 1998, ApJ, 498, 106

Mahler, G., Richard, J., Clément, B., et al. 2018, MNRAS, 473, 663

Mainali, R., Kollmeier, J. A., Stark, D. P., et al. 2017, ApJ, 836, L14

Mainali, R., Zitrin, A., Stark, D. P., et al. 2018, ArXiv e-prints, arXiv:1804.00041

Maiolino, R., Carniani, S., Fontana, A., et al. 2015, MNRAS, 452, 54

Malhotra, S., & Rhoads, J. E. 2004, ApJ, 617, L5

Manti, S., Gallerani, S., Ferrara, A., Greig, B., & Feruglio, C. 2016, MNRAS, 466, 1160

Maraston, C. 2005, MNRAS, 362, 799

Marchi, F., Pentericci, L., Guaita, L., et al. 2017, ArXiv e-prints, 1710, arXiv:1710.10184

Mashian, N., Oesch, P. A., & Loeb, A. 2016, MNRAS, 455, 2101

Mason, C. A., Trenti, M., & Treu, T. 2015a, ApJ, 813, 21

Mason, C. A., Treu, T., Dijkstra, M., et al. 2018a, ApJ, 856, 2

Mason, C. A., Treu, T., Schmidt, K. B., et al. 2015b, ApJ, 805, 79

Mason, C. A., Treu, T., Fontana, A., et al. 2017, ApJ, 838, 14

Mason, C. A., Treu, T., de Barros, S., et al. 2018b, ApJ, 857, L11

Masters, D., McCarthy, P., Siana, B., et al. 2014, ApJ, 785, 153

Mather, J. C., Cheng, E. S., Cottingham, D. A., et al. 1994, ApJ, 420, 439

McCully, C., Keeton, C. R., Wong, K. C., & Zabludoff, A. I. 2014, MNRAS, 443, 3631

McGreer, I. D., Mesinger, A., & D'Odorico, V. 2015, MNRAS, 447, 499

McLean, I. S., Steidel, C. C., Epps, H. W., et al. 2012, in Proc. SPIE, ed. I. S. McLean, S. K. Ramsay, & H. Takami, Vol. 8446, 84460J

McLeod, D. J., McLure, R. J., & Dunlop, J. S. 2016, MNRAS, 459, 3812

McLinden, E. M., Finkelstein, S. L., Rhoads, J. E., et al. 2011, ApJ, 730, 136

McLure, R. J., Dunlop, J. S., Cirasuolo, M., et al. 2010, MNRAS, 403, 960

McLure, R. J., Dunlop, J. S., Bowler, R. A. A., et al. 2013, MNRAS, 432, 2696

McQuinn, M., Hernquist, L., Zaldarriaga, M., & Dutta, S. 2007a, MNRAS, 381, 75

McQuinn, M., Lidz, A., Zahn, O., et al. 2007b, MNRAS, 377, 1043

McQuinn, M., Lidz, A., Zaldarriaga, M., Hernquist, L., & Dutta, S. 2008, MNRAS, 388, 1101

Merlin, E., Amorín, R., Castellano, M., et al. 2016, A&A, 590, A30

Mesinger, A. 2010, MNRAS, 407, 1328

Mesinger, A., ed. 2016, Astrophysics and Space Science Library, Vol. 423, Understanding the Epoch of Cosmic Reionization (Cham: Springer International Publishing), doi:10.1007/978-3-319-21957-8

Mesinger, A., Aykutalp, A., Vanzella, E., et al. 2015, MNRAS, 446, 566

Mesinger, A., & Furlanetto, S. R. 2008a, MNRAS, 385, 1348

—. 2008b, MNRAS, 386, 1990

Mesinger, A., Greig, B., & Sobacchi, E. 2016, MNRAS, 459, 2342

Meurer, G. R., Heckman, T. M., & Calzetti, D. 1999, ApJ, 521, 64

Meylan, G., Jetzer, P., North, P., et al., eds. 2006, Gravitational Lensing: Strong, Weak and Micro

Miller, S. H., Bundy, K., Sullivan, M., Ellis, R. S., & Treu, T. 2011, ApJ, 115, 115

Miralda-Escude, J. 1998, ApJ, 501, 15

Mirocha, J., Furlanetto, S. R., & Sun, G. 2016, MNRAS, 6, 1365

Mitra, S., Roy Choudhury, T., & Ferrara, A. 2015, MNRAS, 454, L76

Mo, H. J., Mao, S., & White, S. D. M. 1999, MNRAS, 304, 175

Monna, A., Seitz, S., Greisel, N., et al. 2014, MNRAS, 438, 1417

Monna, A., Seitz, S., Balestra, I., et al. 2017, MNRAS, 466, 4094

Morishita, T., Abramson, L. E., Treu, T., et al. 2017, ApJ, 846, 139

Morishita, T., Abramson, L. E., Treu, T., et al. 2017, ApJ, 835, 254

Mortlock, A., Conselice, C. J., Hartley, W. G., et al. 2013, MNRAS, 433, 1185

Mostardi, R. E., Shapley, A. E., Nestor, D. B., et al. 2013, ApJ, 779, 65

Moster, B. P., Naab, T., & White, S. D. M. 2017, ArXiv e-prints, arXiv:1705.05373

Muñoz, J. A. 2012, JCAP, 2012, 015

Muzzin, A., Marchesini, D., Stefanon, M., et al. 2013, ApJ, 777, 18

Naidu, R. P., Forrest, B., Oesch, P. A., Tran, K.-V. H., & Holden, B. P. 2018, arXiv:1804.06845 [astro-ph], arXiv:1804.06845

Newman, A. B., Ellis, R. S., Treu, T., & Bundy, K. 2010, ApJ, 717, L103

Newman, S. F., Genzel, R., Förster-Schreiber, N. M., et al. 2012, ApJ, 761, 43

Nipoti, C., Londrillo, P., & Ciotti, L. 2003, MNRAS, 342, 501

Oesch, P., Bouwens, R. J., Illingworth, G. D., et al. 2012, ApJ, 759, 135

Oesch, P. A., Bouwens, R. J., Carollo, C. M., et al. 2010, ApJ, 725, L150

Oesch, P. A., Labbé, I., Bouwens, R. J., et al. 2013, ApJ, 772, 136

Oesch, P. A., Bouwens, R. J., Illingworth, G. D., et al. 2013, ApJ, 773, 75

—. 2014, ApJ, 786, 108

Oesch, P. A., Dokkum, P. G. V., Illingworth, G. D., et al. 2015, ApJ, 804, L30

Oliphant, T. E. 2007, Comput. Sci. Eng., 9, 10

Ono, Y., Ouchi, M., Mobasher, B., et al. 2012, ApJ, 744, 83

Ono, Y., Ouchi, M., Harikane, Y., et al. 2017, PASJ, 00, 1

Onoue, M., Kashikawa, N., Willott, C. J., et al. 2017, ApJ, 847, L15

Ota, K., Walter, F., Ohta, K., et al. 2014, ApJ, 792, 34

Ota, K., Iye, M., Kashikawa, N., et al. 2017, ApJ, 844, 85

Ouchi, M., Mobasher, B., Shimasaku, K., et al. 2009, ApJ, 706, 1136

Ouchi, M., Shimasaku, K., Furusawa, H., et al. 2010, ApJ, 723, 869

Ouchi, M., Ellis, R., Ono, Y., et al. 2013, ApJ, 778, 102

Oyarzún, G. A., Blanc, G. A., González, V., Mateo, M., & Bailey, J. I. 2017, ApJ, 843, 133

Oyarzún, G. A., Blanc, G. A., González, V., et al. 2016, ApJ, 821, L14

Papovich, C., Finkelstein, S. L., Ferguson, H. C., Lotz, J. M., & Giavalisco, M. 2011, MNRAS, 412, 1123

Parsa, S., Dunlop, J. S., & McLure, R. J. 2018, MNRAS, 474, 2904

Parzen, E. 1962, Ann. Math. Stat., 33, 1065

Pei, Y. C. 1995, ApJ, 440, 485

Peng, C. Y., Ho, L. C., Impey, C. D., & Rix, H.-W. 2010, Astron. J., 139, 2097

Pentericci, L., Fontana, A., Vanzella, E., et al. 2011, ApJ, 743, 132

Pentericci, L., Vanzella, E., Fontana, A., et al. 2014, ApJ, 793, 113

Pentericci, L., Carniani, S., Castellano, M., et al. 2016, ApJ, 829, L11

Pérez, F., & Granger, B. E. 2007, Comput. Sci. Eng., 9, 21

Pérez-González, P. G., Rieke, G. H., Villar, V., et al. 2008, ApJ, 675, 234

Phillips, M. M. 1993, ApJ, 413, L105

Pizagno, J., Prada, F., Weinberg, D. H., et al. 2007, AJ, 134, 945

Planck Collaboration, Adam, R., Ade, P. A. R., et al. 2016a, A&A, 594, A1

Planck Collaboration, Adam, R., Aghanim, N., et al. 2016b, A&A, 596, A108

Postman, M., Coe, D., Benítez, N., et al. 2012a, ApJS, 199, 25

Postman, M., Coe, D., Benítez, N., et al. 2012b, ApJS, 199, 25

Price, S. H., Kriek, M., Shapley, A. E., et al. 2016, ApJ, 819, 80

Puech, M., Hammer, F., Hopkins, P. F., et al. 2012, ApJ, 753, 128

Raičević, M., Theuns, T., & Lacey, C. 2011, MNRAS, 410, 775

Ren, K., Trenti, M., & Mutch, S. J. 2018, ApJ, 856, 81

Reyes, R., Mandelbaum, R., Gunn, J. E., Pizagno, J., & Lackner, C. N. 2011, MNRAS, 417, 2347

Rhee, M.-H. 2004, Journal of Korean Astronomical Society, 37, 91

Roberts-Borsani, G. W., Bouwens, R. J., Oesch, P. A., et al. 2016, ApJ, 823, 143

Robertson, B. E., Ellis, R. S., Furlanetto, S. R., & Dunlop, J. S. 2015, ApJ, 802, L19

Robertson, B. E., Furlanetto, S. R., Schneider, E., et al. 2013, ApJ, 768, 71

Robitaille, T. P., Tollerud, E. J., Greenfield, P., et al. 2013, A&A, 558, A33

Rosenblatt, M. 1956, Ann. Math. Stat., 27, 832

Rutkowski, M. J., Scarlata, C., Henry, A., et al. 2017, ApJ, 841, L27

Salpeter, E. E. 1954, ApJ, 121, 161

Santos, M. R. 2004, MNRAS, 349, 1137

Schaerer, D., Boone, F., Zamojski, M., et al. 2015, A&A, 574, A19

Schechter, P. 1976, ApJ, 203, 297

Schenker, M. A., Ellis, R. S., Konidaris, N. P., & Stark, D. P. 2013a, ApJ, 777, 67

—. 2014, ApJ, 795, 20

Schenker, M. A., Stark, D. P., Ellis, R. S., et al. 2012, ApJ, 744, 179

Schenker, M. A., Robertson, B. E., Ellis, R. S., et al. 2013b, ApJ, 768, 196

Schmidt, F., & Beutler, F. 2017, Phys. Rev. D, 96, arXiv:1705.07843

Schmidt, K. B., Treu, T., Trenti, M., et al. 2014a, ApJ, 786, 57

Schmidt, K. B., Treu, T., Brammer, G. B., et al. 2014b, ApJ, 782, L36

Schmidt, K. B., Treu, T., Bradač, M., et al. 2016, ApJ, 818, 38

Schmidt, K. B., Huang, K.-H., Treu, T., et al. 2017, ApJ, 839, 17

Schneider, P., Ehlers, J., & Falco, E. E. 1992, Gravitational Lenses (Springer)

Schneider, P., Kochanek, C. S., & Wambsganss, J. 2006, Gravitational Lensing: Strong, Weak and Micro (Springer)

Schroeder, J., Mesinger, A., & Haiman, Z. 2013, MNRAS, 428, 3058

Shapley, A. E., Steidel, C. C., Adelberger, K. L., et al. 2001, ApJ, 562, 95

Shapley, A. E., Steidel, C. C., Pettini, M., & Adelberger, K. L. 2003, ApJ, 588, 65

Sharples, R., Bender, R., AgudoBerbel, A., et al. 2013, The Messenger, 151, 21

Sheth, R. K., Mo, H. J., & Tormen, G. 2001, MNRAS, 323, 1

Sheth, R. K., & Tormen, G. 1999, MNRAS, 308, 119

Sheth, R. K., Bernardi, M., Schechter, P. L., et al. 2003, ApJ, 594, 225

Shibuya, T., Ouchi, M., & Harikane, Y. 2015, ApJS, 219, 15

Shibuya, T., Ouchi, M., Nakajima, K., et al. 2014, ApJ, 788, 74

Shull, J. M., Harness, A., Trenti, M., & Smith, B. D. 2012, ApJ, 747, 100

Simons, R. C., Kassin, S. A., Weiner, B. J., et al. 2017, ApJ, 843, 46

Smit, R., Swinbank, A. M., Massey, R., et al. 2017, MNRAS, 467, 3306

Smit, R., Bouwens, R. J., Carniani, S., et al. 2018, Nature, 553, 178

Smith, A., Safranek-Shrader, C., Bromm, V., & Milosavljevi, M. 2015, MNRAS, 449, 4336

Sobacchi, E., & Mesinger, A. 2014, MNRAS, 440, 1662

—. 2015, MNRAS, 453, 1843

Sobacchi, E., Mesinger, A., & Greig, B. 2016, MNRAS, 459, 2741

Somerville, R. S., Gilmore, R. C., Primack, J. R., & Domínguez, A. 2012, MNRAS, 423, 1992

Somerville, R. S., Hopkins, P. F., Cox, T. J., Robertson, B. E., & Hernquist, L. 2008, MNRAS, 391, 481

Somerville, R. S., Primack, J. R., & Faber, S. M. 2001, MNRAS, 320, 504

Song, M., Finkelstein, S. L., Gebhardt, K., et al. 2014, ApJ, 791, 3

Song, M., Finkelstein, S. L., Ashby, M. L. N., et al. 2016, ApJ, 825, 5

Spergel, D., Gehrels, N., Breckinridge, J., et al. 2013, ArXiv e-prints, 190

Springel, V., White, S. D. M., Jenkins, A., et al. 2005, Nature, 435, 629

Stark, D. P., Ellis, R. S., Chiu, K., Ouchi, M., & Bunker, A. 2010, MNRAS, 408, 1628

Stark, D. P., Ellis, R. S., & Ouchi, M. 2011, ApJ, 728, L2

Stark, D. P., Schenker, M. A., Ellis, R., et al. 2013, ApJ, 763, 129

Stark, D. P., Richard, J., Siana, B., et al. 2014, MNRAS, 445, 3200

Stark, D. P., Walth, G., Charlot, S., et al. 2015, MNRAS, 454, 1393

Stark, D. P., Ellis, R. S., Charlot, S., et al. 2017, MNRAS, 464, 469

Steidel, C. C., Bogosavlevic, M., Shapley, A. E., et al. 2018, ArXiv e-prints, arXiv:1805.06071

Steidel, C. C., Rudie, G. C., Strom, A. L., et al. 2014, ApJ, 795, 165

Stiavelli, M., Fall, S. M., & Panagia, N. 2004, ApJ, 600, 508

Stiavelli, M., Lilly, S., Gardner, J., et al. 2007

Stott, J. P., Swinbank, A. M., Johnson, H. L., et al. 2016, MNRAS, 457, 1888

Straatman, C. M. S., Labbé, I., Spitler, L. R., et al. 2014, ApJL, 783, L14

Suyu, S. H., Marshall, P. J., Auger, M. W., et al. 2010, ApJ, 711, 201

Tacchella, S., Trenti, M., & Carollo, C. M. 2013, ApJ, 37, L37

Tanvir, N. R., Levan, A. J., Fruchter, A. S., et al. 2012, ApJ, 754, 46

Teodoro, E. M. D., & Fraternali, F. 2015, MNRAS, 451, 3021

Tiley, A. L., Stott, J. P., Swinbank, A. M., et al. 2016, MNRAS, 460, 103

Tilvi, V., Papovich, C., Finkelstein, S. L., et al. 2014, ApJ, 794, 5

Tilvi, V., Pirzkal, N., Malhotra, S., et al. 2016, ApJ, 827, L14

Toft, S., Gallazzi, A., Zirm, A., et al. 2012, ApJ, 754, 3

Tomczak, A. R., Quadri, R. F., Tran, K.-V. H., et al. 2014, ApJ, 783, 85

Trac, H., Cen, R., & Loeb, A. 2008, ApJ, 689, L81

Trac, H. Y., & Gnedin, N. Y. 2011, Adv. Sci. Lett., 4, 228

Trainor, R. F., Steidel, C. C., Strom, A. L., & Rudie, G. C. 2015, ApJ, 809, 89

Trebitsch, M., Blaizot, J., Rosdahl, J., Devriendt, J., & Slyz, A. 2017, MNRAS, 470, 224

Trenti, M., Perna, R., & Jimenez, R. 2015, ApJ, 802, 103

Trenti, M., Perna, R., Levesque, E. M., Shull, J. M., & Stocke, J. T. 2012a, ApJ, 749, L38

Trenti, M., & Stiavelli, M. 2008, ApJ, 676, 767

—. 2009, ApJ, 694, 879

Trenti, M., Stiavelli, M., Bouwens, R. J., et al. 2010, ApJ, 714, L202

Trenti, M., Bradley, L. D., Stiavelli, M., et al. 2011, ApJ, 727, L39

—. 2012b, ApJ, 746, 55

Treu, T., Ellis, R. S., Liao, T. X., & van Dokkum, P. G. 2005, ApJ, 622, L5

Treu, T., Schmidt, K. B., Trenti, M., Bradley, L. D., & Stiavelli, M. 2013, ApJ, 775, L29

Treu, T., Trenti, M., Stiavelli, M., Auger, M. W., & Bradley, L. D. 2012, ApJ, 747, 27

Treu, T., Schmidt, K. B., Brammer, G. B., et al. 2015, ApJ, 812, 114

Treu, T., Brammer, G., Diego, J. M., et al. 2016, ApJ, 817, 60

Treu, T., Abramson, L., Bradac, M., et al. 2017, JWST Proposal ID 1324. Cycle 0 Early Release Science

Treu,Tommaso, Auger,MatthewW., Koopmans,LéonV.E., et al. 2010, ApJ, 709, 1195

Turner, E. L., Ostriker, J. P., & Gott, J. R., I. 1984, ApJ, 284, 1

Vale, A., & Ostriker, J. P. 2004, MNRAS, 353, 189 van de Sande, J., Kriek, M., Franx, M., Bezanson, R., & van Dokkum, P. G. 2014, ApJ, 793, L31

van de Sande, J., Kriek, M., Franx, M., et al. 2013, ApJ, 771, 85

van der Burg, R. F. J., Hildebrandt, H., & Erben, T. 2010, A&A, 523, A74

Van Der Walt, S., Colbert, S. C., & Varoquaux, G. 2011, Comput. Sci. Eng., 13, 22

van der Wel, A., Holden, B. P., Zirm, A. W., et al. 2008, ApJ, 688, 48

van Dokkum, P. G., Kriek, M., & Franx, M. 2009, Nature, 460, 717

Vanzella, E., Pentericci, L., Fontana, A., et al. 2011, ApJ, 730, L35

Vanzella, E., Barros, S. D., Cupani, G., et al. 2016, ApJ, 821, L27

Vanzella, E., Castellano, M., Meneghetti, M., et al. 2017, ApJ, 842, 47

Vanzella, E., Nonino, M., Cupani, G., et al. 2018, MNRAS, 476, L15

Venemans, B. P., Bañados, E., Decarli, R., et al. 2015, ApJ, 801, L11

Vergani, D., Epinat, B., Contini, T., et al. 2012, A&A, 546, A118

Verhamme, A., Schaerer, D., Atek, H., & Tapken, C. 2008, A&A, 491, 89

Verhamme, A., Schaerer, D., & Maselli, A. 2006, A&A, 460, 397

Vrbanec, D., Ciardi, B., Jelić, V., et al. 2016, MNRAS, 457, 666

Vulcani, B., Trenti, M., Calvi, V., et al. 2017, ApJ, 836, 239

Walter, F., Decarli, R., Carilli, C., et al. 2012, ApJ, 752, 93

Wang, X., Jones, T. A., Treu, T., et al. 2016, ApJ, 837, 89

Weisz, D. R., & Boylan-Kolchin, M. 2017, MNRAS, 469, L83

Whitaker, K. E., Franx, M., Leja, J., et al. 2014, ApJ, 795, 104

Willott, C. J., Carilli, C. L., Wagg, J., & Wang, R. 2015, ApJ, 807, 180

Windhorst, R. A., Cohen, S. H., Jansen, R. A., Conselice, C., & Yan, H. 2006, New Astronomy Reviews, 50, 113

Windhorst, R. A., Cohen, S. H., Hathi, N. P., et al. 2011, ApJS, 193, 27

Wisnioski, E., Förster Schreiber, N. M., Wuyts, S., et al. 2015, ApJ, 799, 209

Wisotzki, L., Bacon, R., Blaizot, J., et al. 2016, A&A, 587, A98

Wuyts, S., Förster Schreiber, N. M., Nelson, E. J., et al. 2013, ApJ, 779, 135

Wyithe, J. S. B., Turner, E. L., & Spergel, D. N. 2001, ApJ, 555, 504

Wyithe, J. S. B., Yan, H., Windhorst, R. A., & Mao, S. 2011, Nature, 469, 181

Yan, H., & Windhorst, R. A. 2004, ApJ, 600, L1

Yan, H., Yan, L., Zamojski, M. A., et al. 2011, ApJ, 728, L22

Yang, H., Malhotra, S., Gronke, M., et al. 2016, ApJ, 820, 130

—. 2017, ApJ, 844, 171

Yue, B., Ferrara, A., Vanzella, E., & Salvaterra, R. 2014, MNRAS, 443, 1

Zheng, W., Postman, M., Zitrin, A., et al. 2012, Nature, 489, 406

Zheng, Z., Cen, R., Trac, H., & Miralda-Escudé, J. 2010, ApJ, 716, 574

Zheng, Z., & Miralda-Escude, J. 2002, ApJ, 578, 33

Zheng, Z.-Y., Wang, J., Rhoads, J., et al. 2017, ApJ, 842, L22

Zitrin, A., Fabris, A., Merten, J., et al. 2015a, ApJ, 801, 44

Zitrin, A., Labbé, I., Belli, S., et al. 2015b, ApJ, 810, L12